Magnetoresistance and Fermi Surface of Copper Single Crystals Containing Dislocations

Magnetoresistance and Fermi Surface of Copper Single Crystals Containing Dislocations

By

QIUPING BIAN, M.S.

A Thesis

Submitted to the School of Graduate Studies

in Partial Fulfillment of the Requirements

for the Degree of

Doctor of Philosophy

McMaster University

DOCTOR OF PHILOSOPHY (2010) McMaster University

(Department of Materials Science and Engineering) Hamilton, Ontario

TITLE: Magnetoresistance and Fermi Surface of Copper Single Crystals Containing Dislocations

AUTHOR: Qiuping Bian, M.S.

(Brock University)

SUPERVISORS: Dr. Marek Niewczas

NUMBER OF PAGES: xxiii, 290

Abstract

The galvanomagnetic properties and shape of the Fermi surface of copper single crystals containing different density of dislocations have been studied experimentally and theoretically through magnetoresistivity measurement and using effective medium theory respectively.

In experiments, two crystallographic orientations of copper single crystal samples with tensile axis parallel to $< 100 >$ and $< 541 >$ have been plastically strained to various stress levels to introduce different density N_d of dislocations. The experimental data of angle and field-dependent magnetoresistivity measured at temperature $T = 2K$ and in the magnetic filed up to 9 *Tesla* show that dislocations influence substantially the galvanomagnetic properties of copper crystal samples in the open, extended and closed orbit crystallographic orientations. The results reveal that the pure samples with resistivity ratio *RR* equal to or larger than 151 show quadratic dependence of transverse magnetoresistivity as a function of the magnetic field in the open-orbit orientation, which changes to linear variation of magnetoresistivity with magnetic fields in highly deformed samples with *RR* smaller than 138. A quadratic dependence of transverse magnetoresistivity as a function of the magnetic field is

significantly suppressed as the density of dislocations increases. The magnetoresistivity decrease with the increase of the density of dislocations was also observed in the closed-orbit crystallographic orientation. Such effect is independent upon the type of dislocations introduced to the crystal lattice.

Measurements of the de Hass-van Alphen effect in plastically deformed copper single crystals have been carried out with torque magnetometer and AC susceptibility options of Quantum Design PPMS-9 system. The oscillation frequencies for the extremal orbits normal to the principal crystallographic directions are obtained through Fourier transform of torque versus inversed field characteristics. By comparing these frequencies with the analogous frequencies obtained for undeformed copper crystals, the changes in the cross-sectional area of the Fermi surface corresponding to the extremal orbits are obtained and the shape of the dislocation-distorted Fermi surface is postulated based on measurements performed.

The effective-medium approximation and Green's function method are applied to model the magnetoresistivity data and to gain insight into the fundamental material properties responsible for the observed magnetoresistivity behavior. The effective magnetoresistivity calculated using a self-consistent method shows a good agreement with the experimental results.

Acknowledgements

Throughout my doctoral research career spanning almost four and a half years in the Department of Materials Science and Engineering, I wish to acknowledge all who have helped and inspired me with their kindness and passion.

Firstly, I am greatly indebted to my respectable supervisor, Dr. Marek Niewczas, for his constant encouragement and invaluable discussions in supervising me towards the goals of my Ph. D study; for his patience in training me in experimental techniques and for his generosity and kindness in financially supporting me to complete this Ph. D work and helping my life in Hamilton. I could not achieve anything without his kind help in many respects.

Secondly, I would like to express my sincere thanks to Dr. Kitai and Dr. Gaulin, the other two reputable professors in my supervisory committee, for their treasurable suggestions and inspiring discussions in my annual supervisory committee meeting, from which I benefited a lot in my research.

And then, I wish to extend my heartfelt thanks to Dr. Britten for his assistance in

X-ray examination and data analysis, and to Dr. Daters for his important comments on this thesis.

Also, many thanks will be given to the Department of Materials Science and Engineering for supplying me with a very pleasant environment of research; and to the Ontario Graduate Scholarship foundation for its one-year financial support.

Finally, special thanks are devoted to my family and my parents for their understanding and encouraging which spiritually support me a lot in pursuing my doctoral degree

Hamilton, August 2010

Qiuping Bian

Notation

0.1 Character Notation

Through this thesis, a character under a right arrow denotes a vector ($\vec{A}$, $\vec{B}$, $\vec{C}$ etc.) and the one under left and right arrow denotes a tensor ($\overleftrightarrow{\tau}$, $\overleftrightarrow{\sigma}$, $\overleftrightarrow{\gamma}$, etc.). Their spatial components are expressed by the characters with subscript(s) such as A_i and τ_{ij}. Letters without arrow or subscript notation are scalar quantities or the magnitude of vectors. Conventional expression for operators i.e., a character with a hat ($\hat{p}$,$\hat{\mathscr{H}}$, etc.) is used.

The following are the character notations used as consistently as possible throughout the thesis, their definition might be occasionally repeated. If any of them is denoted for some other quantity, it will be explained and defined in the context. In the bracket after the definition of each character notation are also given the unit(s) in the CGS or MKS system which depends on conventionality in literature and occasionally both and their relations are provided. We omit all dimensionless physical quantities.

$\overleftrightarrow{\tau}$: stress tensor ($1Pa = 10^{-5}MPa$).

$\overleftrightarrow{\varepsilon}$: strain tensor.

$\vec{r}$: position vector and its components $r_1 = x$, $r_2 = y$ and $r_3 = z$ ($1m = 10^{-2}cm$).

E: Young's modulus ($1Pa = 10^{-5}MPa = 10^{-9}GPa$).

ν: Poisson's ratio.

G: shear modulus ($1Pa = 10^{-5}MPa = 10^{-9}GPa$).

$\vec{u}$: atomic displacement vector and its components u_x, u_y and u_z ($1m = 10^{-10}\mathring{A}$).

θ and ϕ: polar and azimuthal angular coordinates to define the direction of a vector. ($1degree = 1^\circ = 0.017rad$).

$\vec{F}$: tensile load (N).

$\vec{\tau}_s$: resolved shear stress (Pa).

τ_c: critical resolved shear stress (Pa).

$\vec{k}$: electron wave vector (Bloch wave vector) ($1m^{-1} = 10^{-2}cm^{-1}$).

$\varepsilon(\vec{k})$: electron energy at state $\vec{k}$ ($1eV = 1.602176487 \times 10^{-19}J$).

μ: the electrochemical potential per electron or Fermi energy (occasionally ε_F) (eV or J).

K_B: Boltzmann's constant ($= 1.3806503 \times 10^{-23}m^2kg\,s^{-2}K^{-1}$)

f_0 and f: electron distribution function at equilibrium and non-equilibrium state.

e: positive electron charge ($= 1.602176487 \times 10^{-19}C$).

$\vec{E}$: electric field strength ($1NC^{-1} = 1Vm^{-1}$).

$\vec{B}$: magnetic field strength ($1T = 10^4G$).

T: absolute temperature (K).

t: time (s).

$\hbar$: reduced Plank constant ($= 1.054571628 \times 10^{-34} Js$).

$\vec{v}(\vec{k})$: electron velocity at state $\vec{k}$ (ms^{-1}).

$W(\vec{k},\vec{k'})$: probability of transition of an electron from state $\vec{k}$ to state $\vec{k'}$

τ: relaxation time (s).

n: electron density (occasionally n_e) (m^{-3}).

m^*: effective electron mass (kg).

$\psi_{\vec{k}}(\vec{r})$ wave function of an electron at state $\vec{k}$ in r-space.

$\vec{J}$: current density (Am^{-2}).

$\overleftrightarrow{\sigma}$: conductivity tensor (or magnetoconductivity tensor if a magnetic field is applied) (Sm^{-1}; note: S denotes *siemens*) .

σ_0: scalar conductivity for an isotropic crystal without $\vec{B}$ ($= ne^2\tau/m^*$) (Sm^{-1}).

$\overleftrightarrow{\rho}$: resistivity tensor (or magnetoresistivity tensor if a magnetic field is applied)(Ωm^{-1}).

ρ_0: scalar resistivity for an isotropic crystal without $\vec{B}$ ($= 1/\sigma_0$) (Ωm^{-1}).

w_c: cyclotron frequency or the angular velocity of an electron in $\vec{B}$ ($rads^{-1}$).

$\overleftrightarrow{\sigma}^{op}$: magnetoconductivity tensor in some crystal orientations in which electrons move on open-orbits (Sm^{-1}).

$\overleftrightarrow{\sigma}^{cl}$: magnetoconductivity tensor in some crystal orientations in which electrons move on closed-orbits (Sm^{-1}).

$\overleftrightarrow{\rho}^{op}$: magnetoresistivity tensor in some crystal orientations in which electrons move on open-orbits (Ωm^{-1}).

$\overleftrightarrow{\rho}^{cl}$: magnetoresistivity tensor in some crystal orientations in which electrons move on closed-orbits (Ωm^{-1}).

$\overleftrightarrow{\sigma}_m$: conductivity tensor for medium in which crystallites are embedded (Sm^{-1}).

$\vec{G}_n$: a reciprocal lattice (m^{-1}).

k_F: Fermi wave vector (m^{-1} or cm^{-1}) .

$\overleftrightarrow{\sigma}_{eff}$: effective conductivity tensor(Sm^{-1}).

σ_α: conductivity of α-th component (α= 1,2...) in a composite (Sm^{-1}).

f_α: volume fraction of α-th component in a composite.

$\vec{p}_\alpha$: electric dipole moment of a crystallite of α-th component in a composite (Cm).

$\vec{P}_\alpha$: polarization of a crystallite of α-th component in a composite (Cm^{-2}).

V: volume of a composite (m^3).

V_α: volume of α-th component in a composite (m^3).

$\Phi(\vec{r})$: scalar potential as a function of $\vec{r}$ (V).

$G(\vec{r},\vec{r}')$: Green function.

$\overleftrightarrow{\Gamma}$: depolarization tensor (Ωm).

l: mean free path (m).

R_B: radius of the conduction electron orbits in a field (m).

$\mathscr{H}$: Hamiltonian of an electron moving in the magnetic field (J).

L_i: sample dimension along i-direction ($i = x,y,z$) (m).

ρ_{dos}: density of states ((m^{-3}).

$\mathscr{D}$: degeneracy for each Landau level.

N_e: the number of electrons on each Landau level.

$\mathscr{P}$: the period of the dHvA oscillation ($1T^{-1} = 10^{-4}G^{-1}$).

$\mathscr{F}$: the frequency of the dHvA oscillation (T or G).

S_F: cross section area of Fermi surface in k-space (m^{-2}).

$\mathfrak{R}_d$: specific dislocation resistivity (Ωm^3).

N_d: density of dislocations ($1m^2 = 10^4 cm^2$).

$\vec{M}$: magnetization (Am^{-1}).

Ω: thermodynamic potential ($J \cdot mole^{-1}$) .

$\vec{\mathscr{T}}$: torque ($N \cdot m$).

f_v: volume fraction of crystallites with open-orbits.

f_e: fraction of electrons moving on open-orbits.

RR: residual resistivity ratio.

$\vec{e}_i$: unit vector along i-axis ($i = x,y,z$) (m).

0.2 Symbols and Crystallographic Notation

The used symbols for operators are:

$$\vec{\nabla} = \frac{\partial}{\partial x}\vec{e}_x + \frac{\partial}{\partial y}\vec{e}_y + \frac{\partial}{\partial z}\vec{e}_z \text{ (gradient in } r\text{-space)},$$

$$\vec{\nabla}_{\vec{k}} = \frac{\partial}{\partial k_x}\vec{e}_{k_x} + \frac{\partial}{\partial k_y}\vec{e}_{k_y} + \frac{\partial}{\partial k_z}\vec{e}_{k_z} \text{ (gradient in } k\text{-space)},$$

$$\nabla^2 = \vec{\nabla}\cdot\vec{\nabla} = \frac{\partial^2}{\partial x^2} + \frac{\partial^2}{\partial y^2} + \frac{\partial^2}{\partial z^2} \text{ (Laplace operator)},$$

which is consistent with traditional definition. The left and right triangle bracket denotes spatial average which is defined by

$$< g(\vec{r}) >= \frac{1}{V} \int_V g(\vec{r}) d\vec{r} \quad \vec{r} \in V,$$

where g is any function of $\vec{r}$.

A plane is denoted by Miller indices in round parentheses such as (hkl) with integers h, k and l. A set of equivalent planes in cubic crystals due to symmetry operations with this plane is expressed by $\{hkl\}$, for example, $\{100\}$ means the set of (100), (010), (001), ($\bar{1}$00), and so on.

The crystallographic direction is denoted in square brackets such as $[hkl]$. A set of equivalent directions which are related by symmetry operations is denoted by $< hkl >$. For instance, $< 100 >$ means [100], [010], [001] or opposite to any of those directions.

Contents

List of Figures

List of Tables

Chapter 1

Introduction

Lattice imperfections and crystal defects have a profound influence on the electronic and magnetic properties of metals and alloys. The lattice imperfections interact with free electrons and create some extra terms in the crystal Hamiltonian. This leads to a distinct change in the electron energy spectrum due to defect levels merging into the energy band of pure crystals. Secondly, lattice imperfections form the bound states of electrons in which one or more electrons can be trapped and permanently localized in the potential well. In some cases, lattice imperfections can accept electrons from or donate them to the crystal. This may change electron distribution function, which is directly related to the electrical and magnetic properties of the crystal.

A particular type of lattice imperfections in the crystal structure of all metals and alloys are dislocations. These defects are important for many reasons. They are

almost always present in any real material structure, they are fundamental carries of the plastic deformation, they determine the strength and ductility and many other physical properties of real crystalline materials (Taylor, 1934a,b). For the past few decades, the electron-dislocation scattering and its effect on the electrical properties of metals have attracted considerable interest (Mackenzie & Sondheimer, 1950; Hunter & Nabarro, 1953; Harrison, 1958; Bhatia & Gupta, 1970; Ackerman & Klemens, 1971; Terwilliger & Higgins, 1973; Sacks & Robinson, 1976; Brown, 1977b; Bross & Häerlen, 1993). The detailed review of the progress in understanding the contributions of dislocations to the residual electrical resistivity of metals can be found in the reference (Brown, 1982). Despite substantial efforts, no theory has yet been entirely successful in explaining the electrical resistivity produced by dislocations (Watts, 1987). For example, Basinski and Dugdale (Basinski & Dugdale, 1985) measured the specific dislocation resistivity in copper single crystals with low densities of dislocations $10^7 cm^{-2}$ (i.e. $10^7 cm$ of the dislocation line per $1 cm^3$ volume of crystal) introduced by bending and concluded that within the experimental error not greater than 10%, there is no anisotropy of resistivity parallel and perpendicular to the dislocation line. This quite surprising conclusion is a big disparity with the concept accepted on the theoretical grounds that if an electron travels in the direction of the dislocation line, it will not be scattered and consequently there should be a large anisotropy of electrical resistivity along different directions with respect to the direction of dislocation line (Hunter & Nabarro, 1953; Martin & Ziman, 1970; Dexter, 1952c). Chang and Higgins (Chang & Higgins, 1975) did the pioneering work by applying magnetic field to the system and measured the de Hass-van Alphen (dHvA) effect of the samples with controlled dislocation densities to investigate electron scattering in a dislocated lattice. Based on their experimental

results, these authors argued that electron-dislocation scattering is anisotropic and dominant by small-angle scattering, which has been a unsettled topic in this area for a long time (Brown, 1978). Their work sheld a new light on the baffling problem of electron scattering by dislocated lattices. Unfortunately, very few further systematic investigations were reported since then, mainly owing to the complexity of the problem.

In the present work we study the electrical properties of copper single crystals containing dislocations from different point of view. Instead of directly measuring the resistivity of dislocated single crystal samples, we apply the magnetic field to the system and measure magnetoresistivity of the samples. There are several advantages of applying magnetic field to investigate electrical properties of the metal system containing dislocations. First, detailed information on the electron-dislocation scattering, which is normally averaged out in bulk transport measurements, can be obtained by using microscopic tools such as the de Haas-van Alphen effect because such measurement is localized in k space. Second, the information on the topological features of the Fermi surface of metals can be determined by measuring the de Haas-van Alphen frequencies and it is well known that many physical properties of metals are related intimately to the shape of the Fermi surface. Third, some other physical properties might be observed in the high magnetic field such as the effect of magnetic breakdown in the dislocated crystals (Pippard, 1965).

One of the aims of this research is to investigate the effect of dislocations and their orientation on the electronic conduction in metals by applying a magnetic field to the crystal samples containing these defects. Another motivation of this research

is the so-called linear law of transverse magnetoresistance, first summarized by Kapitza in 1929 (Kapitza, 1929). The law states that transverse magnetoresistance of many metals in the form of polycrystalline wire shows almost a linear increment with the magnetic fields. However, the phenomenon that the transverse magnetoresistance varies linearly with the magnetic field violates the semiclassical theory of Lifshitz et al. (Lifshitz *et al.*, 1957). This theory predicts a quadratic variation of the magnetoresistance for uncompensated metals with the strength of the magnetic field in some orientations along which electrons move on open-orbits or long extended orbits, and a saturating behavior in other directions in which closed orbits occur. In 1958, Lifshitz and Peschanskii published another article and theoretically explained the linear characteristic of magnetoresistance with the applied field as a result of averaging over the orientations of the crystallites in which open orbit occurs in polycrystalline samples (Lifshitz & Peschanski, 1959). The same idea also appeared in Ziman's work (Ziman, 1958). It seems that the problem of the linear law had been solved. Unfortunately, with more experiments in this area done by many other researchers such as Garland et al. (Garland & Bowers, 1969); Babiskin et al. (Babiskin & Siebenmann, 1971) and Kesternich et al. (Kesternich & Ullmaier, 1971), it was found that this linear behavior is not only observed in many simple metals such as the alkalis but also in several free electron metals with a closed Fermi surface, such as K, In and Al, in which a saturating behavior of magnetoresistivity is expected, because no open orbits exist in these metals. So far, no experiments in the simple metals have been reported in which the phenomenon of a saturating magnetoresistivity has been observed. Such a big discrepancy between the theory and experiments led to a debate in the research society about whether the observed linear behavior of magnetoresistivity is intrinsic or extrinsic. One of the plausi-

ble arguments for potential intrinsic source is the model of charge-density wave suggested by Overhauser (Overhauser, 1971, 1978). In this model, charge-density waves or spin-density waves resulted from the exchange and correlation interactions among electrons in the observed metals can create an electrical field, which may displace the positive ions and leads to the formation of the energy gaps causing a big distortion of Fermi surface. The appearance of energy gaps and distortion of Fermi surface can qualitatively explain the magnetoresistivity results for potassium. The drawback of the Overhauser's model is the complexity of experimental verification, although these quantities are in equilibrium states and their change should be measurable (Falicov & Smith, 1972).

In favor for extrinsic sources in magnetoresistivity saturation, some researchers attributed the disagreement of the theory and experiments to sample geometry and macroscopic inhomogeneities of the material. For example, Stroud and Pan (Stroud, 1975; Stroud & Pan, 1976, 1979) theoretically studied the effect of the material inhomogeneities on the magnetoresistivity tensor using the effective medium theory. By applying the method of Green's function to boundary problems, they developed a general and strict formulation for galvanomagnetic properties of inhomogeneous media. Their results show that even a small fraction of spherical voids in the crystal will make magnetoresistivity of the crystal to increase linearly with the magnetic field without saturating. This prediction was confirmed in the experiment done by Beers et al. (Beers *et al.*, 1978). Esposito et al. (Esposito *et al.*, 1978) theoretically investigated the influence of cylindrical voids on the thermal magnetoresistance of a model metal and concluded that the presence of voids does not enhance the quadratic term and a non-zero lattice thermal conductivity sub-

stantially decreases the effect of the voids, resulting in a linear magnetoresistivity behavior and producing appreciable deviation from the linearity at high magnetic fields. However, later, Bruls and co-workers (Bruls *et al.*, 1981) argued that in carefully prepared samples, the contribution from voids, which was previously assumed to be the source of linearity, is much too small to yield the linear magnetoresistance observed experimentally, and there should be some other sources of this behavior. They suggested that macroscopic surface defects may be additional sources causing linear dependence of magnetoresistance with the magnetic field. Amundsen and co-workers pointed out the importance of dislocation substructure in the contribution to the magnetoresistance of aluminum single crystals after examining the effect of quenching and straining upon the magnetoresistivity in this metal (Amundsen & Jerstad, 1974). Unfortunately, little systematic work has been done to understand this effect in details. This is yet another motivation for us to undertake these studies both theoretically and experimentally using model metal system such as copper single crystals. We investigate the influence of the density and orientation of dislocations on the magnetoresistivity in copper single crystals and try to understand under what circumstances a linear magnetoresistivity as a function of magnetic field is observed.

In this work, we use two different orientations of copper single crystal samples and by deforming them to various stress levels, we introduce different densities of dislocations to the samples. Then we measure the angle-dependent magnetoresistivity of the samples in a constant magnetic field of $B = 9$ *Tesla*, to investigate the effect of the density and the type of dislocations on magnetoresistivity of single crystals. The quadratic variation of magnetoresistivity with the magnetic field in the

deformed samples has been studied for crystallographic orientation of the samples in which the open or long extended orbits of electrons are observed. The behavior of magnetoresistivity in the large magnetic fields in the crystallographic orientation of the closed orbit is also examined. To gain insight into the fundamental material properties responsible for the observed phenomena, we undertook a theoretical study of the magnetoresistivity by employing the method of Green function within the framework of the effective medium theory. The modeling permits magnetoresistivity values in the magnetic fields which far exceed field levels attainable in our measurement system.

De Haas-van Alphen (dHvA) experiments have been carried out using torque magnetometer technique; the oscillation frequencies of electron on a given orbit in deformed and non-deformed copper samples were studied and were used to estimate the distortion of the Fermi surface in crystals containing dislocations with respect to the pure copper samples.

The dissertation is comprised of ten chapters. Chapter one provided a brief description to the background and motivations of this research project. Chapter two is concerned with the basic knowledge about the structure and properties of dislocations and area of plastic deformation of FCC metals, and provides theoretical background for understanding how dislocations are introduced to the samples and how their type and orientation can be controlled. Chapter three introduces theory necessary to interpret experimental results. It covers the semiclassical theory of electronic conduction in crystalline metals in the presence of the external electrical and magnetic field and deals with a theoretical foundation to understand and

interpret galvanomagnetic phenomena when a quantum size effect is ignored in the system. A brief summary of the topology of the Fermi surface of copper and the nature of different electron orbits occurring in momentum space is also included in this chapter. Chapter four describes the effective medium theory which is used to simulate the galvanomagnetic behavior of deformed copper single crystals. Chapter five gives a short review on the investigation of the strain dependent quantum oscillation and presents the theory of dHvA effect to elucidate this quantum phenomenon. The objective of the thesis is formulated in chapter six. Chapters seven contains a brief introduction of Quantum Design PPMS-9 system used in the present studies and the experimental techniques such as four-point resistance measurement and torque measurement employed to investigate galvanomagnetic properties and the shape of Fermi surface in dislocated crystals. Chapter eight presents experimental results, provides interpretation of the results and discussion. In chapter nine, we develop a new methodology to model the magnetoresistivity of dislocated samples by applying the effective medium theory and the method of Green's function, and we compare the results of the experiments against the developed model. Chapter ten is the summary and conclusions of the important results obtained. The appendixes provide derivations of the equations and FORTRAN source code for numerical computations of magnetoresistivity.

Chapter 2

Dislocation Substructure in Copper Single Crystals

2.1 Introduction to Dislocations

It was reported as early as in 1880s that plastic deformation can result in the appearance of bands on the surface of metallic specimens (Müggе, 1883; Ewing & Rosenhain, 1898). With the progress in the theory of crystalline structure of metals, these bands were interpreted as being the consequence of the relative slip movement of one part of the specimen with respect to its neighboring parts under a shear stress. However, based on the model of perfect crystals, the theoretical strength of the crystal, which is interpreted as the resolved shear stress required to move one layer of atoms over the other layer along a slip band, has been estimated as

$\mu/30$ where: μ is shear modulus of the material. The theoretical value of the yield strength of materials showed enormous deviations of many orders of magnitude greater than the value of the resolved shear stress measured experimentally on well-annealed crystals. In 1934 Orowan, Polanyi and Taylor (Orowan, 1934; Polanyi, 1934; Taylor, 1934a,b) explained provided independently the reason of such a striking contradiction between theory and experiment by postulating that a crystal imperfections can exist within crystal lattices and that the movement of these imperfections at low shear stresses results in crystal yielding followed by deformation. The imperfections are known now as dislocations. A few years later in 1939, Burgers (Burgers, 1939) advanced the description of dislocations by introducing a fundamental property of a dislocation, the Burgers vector. The experimental verification of the existence of dislocations in crystals was provided in 1953 by Hedges and Mitchell (Hedges & Mitchell, 1953) who used a decoration technique to make dislocations visible in silver-halide crystals under a high resolution transmission optical microscope. Since then many techniques such as etch-pitting, decoration of dislocations with impurity precipitates, electron-microscopy, X-ray, and field-ion methods have been developed for the direct observation of dislocations in crystals. A detailed review about the development of these techniques and their applications in many areas of Materials Science and Solid State Physics can be found in work of Amelinckx (Amelinckx, 1964).

Over the past decades, the dislocation theory which encompasses the studies of the structure and properties of dislocations and their effect on material properties, has developed into an important branch of solid state physics and made many important contributions to understanding chemical and physical properties of real

materials. However, the development of dislocation theory has somewhat stagnated in last two-three decades. One reason is that properties of individual dislocation are different than the properties of dislocation network, whereas in most situations dislocations form very complicated microstructure in the crystal, which is difficult to understand and described. Another reason is that many phenomena involving dislocations such as phenomenon of work-hardening has not yet been fully understood and there is no good theory which describes this process. Finally, understanding the properties of real materials by theoretical methods, requires to incorporate properties of lattice defects, which is often difficult to formulate and add much complexity to the periodic system. Our research will focus on the electrical and magnetic properties of coper containing dislocations. The following describes basic structure and properties of dislocations in a crystal lattice.

2.2 Structure of Edge and Screw Dislocations

Dislocations are linear defects in crystals which differentiate between two main types, namely edge and screw dislocations. In real materials, dislocations are usually found to be of mixed type, which means they have the characteristics of both. The basic geometry of an edge and screw dislocation is illustrated in Figure 2.1.

The formation of a dislocation in a crystal can be demonstrated in the following way. Consider a lattice structure of a perfect cubic crystal shown in Figure 2.1(a). If one makes a cut to the perfect crystal along any direction and on any plane and

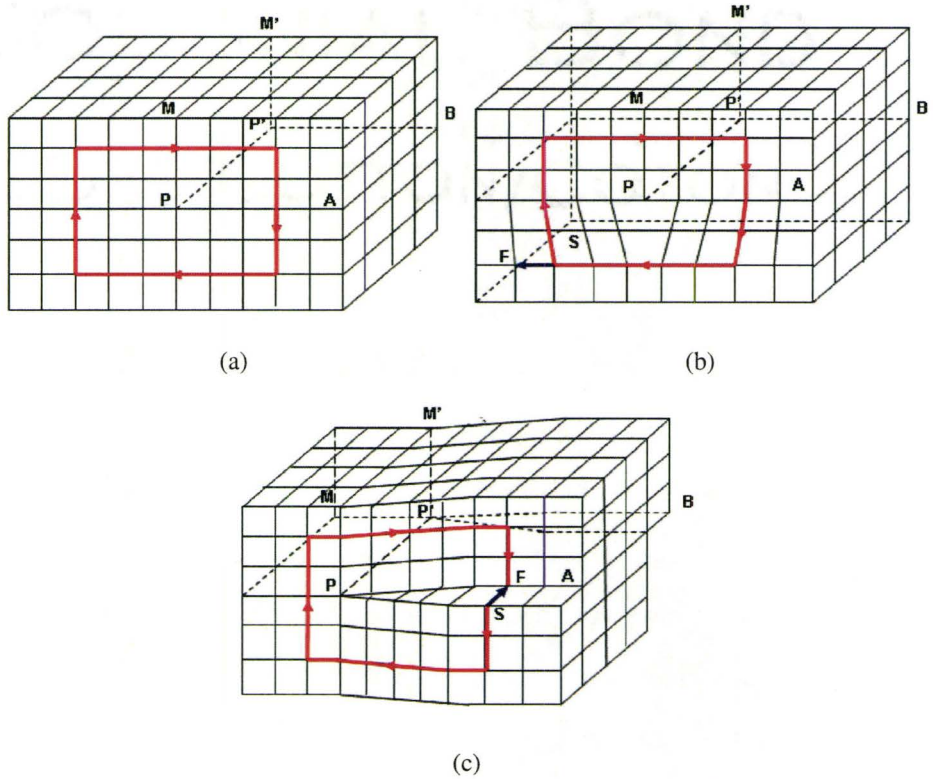

Figure 2.1: Schematics showing the structure of dislocations in a crystal lattice. (a) Perfect Crystal, (b) Edge dislocation, (c) Screw dislocation. The red lines represent the Burgers circuit and blue arrows indicate Burgers vector.

introduces extra-half plane, say a plane PABP' (Figure 2.1(b) and 2.1(c)), the surfaces of crystal will match perfectly everywhere, except the region near the cut line PP' i.e end of the extra-half plane (See Figure 2.1(b) and 2.1(c)). The extra-half plane PABP' represents a line imperfection called dislocation and the end of the extra-half plane represents a dislocation line. It is seen that in a lattice containing dislocation one part of the crystal is separated by the cut surface relative to the other part of the crystal by a translation vector of the lattice. If the part of the crystal over the cut surface shift in a direction perpendicular to dislocation line PP', an edge

dislocation is produced (Figure 2.1(b)). If the displacement occurs parallel to dislocation line PP', a screw dislocation is formed (Figure 2.1(c)). If the displacement is neither parallel nor perpendicular to the dislocation line but rather at certain angle, such a dislocation has the characteristics of both an edge and screw dislocation and is called mixed dislocation.

The Burgers vector of a dislocation marked as a blue arrow in Figure 2.1(b) and 2.1(c) is the most important property of this defect because a dislocation may be fully described, as long as its Burgers vector is known. The definition of the Burgers vector of a dislocation is not unique and depends on the convention which is used. Figure 2.1(a) shows a method to define the Burgers vector of a dislocation. A closed clockwise circuit (Burgers circuit) of atom-to-atom steps is defined in a perfect crystal starting at a lattice point S and finishing at a lattice point F, which coincide in the perfect crystal, as shown in Figure 2.1(a). If the same step-by-step circuit is made in an imperfect crystal, such that the dislocation is enclosed by the circuit, the ending lattice point F does not coincide with the starting lattice point S, as shown in Figure 2.1(b) (2.1(c)). Suppose that the positive direction of the dislocation is in the paper plane. Consequently, Burgers circuit is in the sense of a right-handed screw (RH) along the positive direction of the dislocation line. The vector (SF) connecting the starting point with the ending point is the Burgers vector of the dislocation. Such convention for the definition of a Burgers vector is referred as SF/RH (Start-Finish/Right-Hand) and this definition is adopted in this thesis. Under this definition, some characteristics of dislocations can be summarized: for an edge dislocation, its line is perpendicular to its Burgers vector and the dislocation moves on the slip plane in the direction of the Burgers vector;

for a screw dislocation, its line is parallel to its Burgers vector and the dislocation moves on the slip plane in the direction perpendicular to the Burgers vector.

2.3 Strain and Stress Field of Dislocations

The deformation of the lattice induced by the presence of a dislocation leads to a permanent internal strain and stress field in the vicinity of the dislocation line within a crystal. To describe these strain and stress fields is difficult because not only the interactions between the displaced atoms forming the dislocation but also the interaction with other non-displaced atoms must be taken into account. The mathematical treatment of the strain and stress field around a dislocation can be substantially simplified within a framework of isotropic and elastic continuous media. Although such a model may not reflect the exact properties of the dislocations, it is still a fairly good and powerful approximation. The reasoning is based on the following facts: First, the validity of Hook's law requires a linear variation of stresses with strains and linear relations between strains and stresses fails in the core region of a dislocation because of large displacements existing in that volume of the crystal. However, this does not cause a severe problem since in most practical cases the effects resulting from the core region of a dislocation can be neglected. Second, a real crystal can be viewed as a lattice containing defects embedded into the part of the crystal which is free of defects, or, in another word, the actual defect in a crystal generates deformation in an area of defect-free and such deformation is elastic up to the limit of crystal's elasticity. Therefore, the elastic stresses inside the crystal can be regarded as results of elastic strains produced by lattice defects in the ideal

matrix surrounding these defects. To describe mechanical properties of defect-free materials, the elastic continuum model, which avoids the plaguing mathematical complexity but yields fairly good results, can be employed. Here we will give brief introduction to the strain and stress fields of dislocations under the linear elasticity theory for isotropic media. The discussion how to treat the elastically anisotropic materials can be found in reference (Bacon *et al.*, 1980).

2.3.1 Fundamental equations

The state of stress at any point in a solid can be described in Cartesian coordinates by the Cauchy stress tensor

$$\overleftrightarrow{\tau} = \begin{pmatrix} \tau_{11} & \tau_{12} & \tau_{13} \\ \tau_{21} & \tau_{22} & \tau_{23} \\ \tau_{31} & \tau_{32} & \tau_{33} \end{pmatrix} = \begin{pmatrix} \tau_{xx} & \tau_{xy} & \tau_{xz} \\ \tau_{yx} & \tau_{yy} & \tau_{yz} \\ \tau_{zx} & \tau_{zy} & \tau_{zz} \end{pmatrix}, \tag{2.1}$$

where τ_{ij} $(i,j = 1(x),2(y),3(z))$, as a convention for this thesis) denotes the j-component of the acting force per unit area on a plane whose outward normal is parallel to the positive i direction. If the solid is in mechanical equilibrium, there is no net torque acting on each differential volume element of the solid, so that

$$\tau_{ij} = \tau_{ji}. \tag{2.2}$$

Let

$$r_1 = x, \quad r_2 = y, \quad r_3 = z. \tag{2.3}$$

At equilibrium there is no net force acting on the element, which yields:

$$\sum_{j=1}^{3} \frac{\partial \tau_{ij}}{\partial r_j} + f_i = 0, \quad (i = 1,2,3), \tag{2.4}$$

where f_i is the i-th component of the body force per unit volume. Equation(2.4) is called equilibrium equations of classical elasticity.

Solids will deform in response to the external stresses acting on them. Let u_i denote the i -th component of the displacement at a point $\vec{r}$. Each component of the strain tensor at the point

$$\overleftrightarrow{\varepsilon} = \begin{pmatrix} \varepsilon_{11} & \varepsilon_{12} & \varepsilon_{13} \\ \varepsilon_{21} & \varepsilon_{22} & \varepsilon_{23} \\ \varepsilon_{31} & \varepsilon_{32} & \varepsilon_{33} \end{pmatrix} = \begin{pmatrix} \varepsilon_{xx} & \varepsilon_{xy} & \varepsilon_{xz} \\ \varepsilon_{yx} & \varepsilon_{yy} & \varepsilon_{yz} \\ \varepsilon_{zx} & \varepsilon_{zy} & \varepsilon_{zz} \end{pmatrix} \tag{2.5}$$

can be defined as

$$\varepsilon_{ij} = \frac{1}{2}\left(\frac{\partial u_i}{\partial r_j} + \frac{\partial u_j}{\partial r_i}\right). \tag{2.6}$$

For isotropic crystalline solids, Hook's law can be written as:

$$\varepsilon_{xx} = \frac{1}{E}\left[\tau_{xx} - \nu\left(\tau_{yy} + \tau_{zz}\right)\right], \tag{2.7a}$$

$$\varepsilon_{yy} = \frac{1}{E}\left[\tau_{yy} - \nu\left(\tau_{zz} + \tau_{xx}\right)\right], \tag{2.7b}$$

$$\varepsilon_{zz} = \frac{1}{E}\left[\tau_{zz} - \nu\left(\tau_{zz} + \tau_{yy}\right)\right], \tag{2.7c}$$

$$\varepsilon_{xy} = \frac{\tau_{xy}}{2G}, \quad \varepsilon_{yz} = \frac{\tau_{yz}}{2G}, \quad \varepsilon_{zx} = \frac{\tau_{zx}}{2G} \tag{2.7d}$$

where E is Young's modulus, ν Poisson's ratio and G shear modulus. Only two

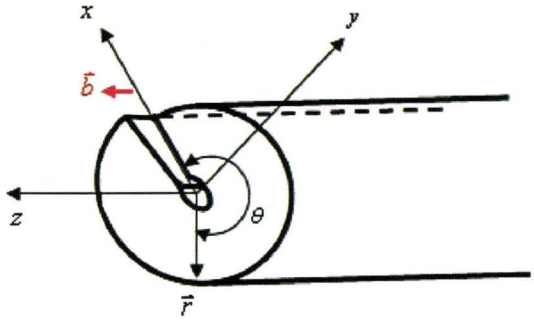

(a) Screw dislocation

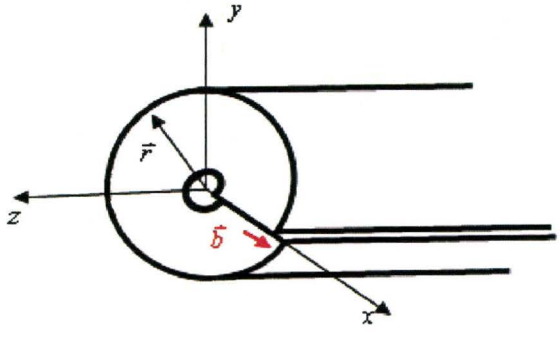

(b) Edge dislocation

Figure 2.2: Dislocations in continuum model.

elastic constants are independent, E and ν. Young's modulus and shear modulus are related by $E = 2G(1+\nu)$.

2.3.2 Strain and Stress Field of a Screw Dislocation

Volterra (Volterra, 1907) introduced a model to describe the internal stress and strain fields around a dislocation by making a cut into an elastic cylinder with a cylindrical core in its center and then reconnecting the cut surfaces after displacing them by a Burgers vector rigidly relative to each other. The reason to make such a hollow core in the center of the cylinder is to simplify the mathematical treatment and avoid the infinity of the stresses at the center of the dislocation core, which is a normal method in continuous medium. However, this does not happen in the real dislocations since the crystal lattice is periodic. Let the z-axis of Cartesian coordinate system coincides with the axis of the cylinder. If the direction of the displacement is parallel to the axis of the cylinder, a screw dislocation is produced (see figure 2.2(a)).

The components of the elastic displacement vector $\vec{u}$ for a screw dislocation have the simple forms in the continuum model

$$u_z = \frac{b\theta}{2\pi} = \frac{b}{2\pi}\arctan\left(\frac{y}{x}\right) \tag{2.8a}$$

$$u_x = u_y = 0. \tag{2.8b}$$

The elastic strain field around the screw dislocation can be easily determined by

substituting equation(2.8) into equation(2.6)

$$\varepsilon_{xz} = -\frac{b}{2\pi}\frac{y}{x^2+y^2}, \tag{2.9a}$$

$$\varepsilon_{yz} = \frac{b}{2\pi}\frac{x}{x^2+y^2}, \tag{2.9b}$$

$$\varepsilon_{xx} = \varepsilon_{yy} = \varepsilon_{zz} = \varepsilon_{xy} = 0. \tag{2.9c}$$

The stress field associated with this elastic strain field can be obtained through equations(2.7) and has the forms

$$\tau_{xz} = -\frac{Gb}{2\pi}\frac{y}{x^2+y^2}, \tag{2.10a}$$

$$\tau_{yz} = \frac{Gb}{2\pi}\frac{x}{x^2+y^2}, \tag{2.10b}$$

$$\tau_{xx} = \tau_{yy} = \tau_{zz} = \tau_{xy} = 0 \tag{2.10c}$$

It is straightforward to show that the internal stress from a dislocation satisfies the equilibrium equations.

2.3.3 Strain and Stress Field of an Edge Dislocation

An edge dislocation will be created if the direction of the displacement of cut surfaces of an elastic cylinder with a hollow discussed in the above section, is perpendicular to the axis of the cylinder (Figure 2.2(b)). Finding a solution to the stress field around an edge dislocation, which has to satisfy the equilibrium conditions, is done with analogy to a screw dislocation. However, the solution is more complicated and we do not go into details of it. More detailed derivation of the stress

field of an edge dislocation can be found in any advanced textbook on the theory of dislocations, such as the book of Hirth and Lothe (Hirth & Lothe, 1968).

The three components of the elastic displacement vector $\vec{u}$ around an edge dislocation can be written as:

$$u_x = \frac{b}{2\pi}\left[\arctan\left(\frac{y}{x}\right) + \frac{xy}{2(1-\nu)(x^2+y^2)}\right], \tag{2.11a}$$

$$u_y = -\frac{b}{2\pi}\left[\frac{1-2\nu}{4(1-\nu)}\ln\left(x^2+y^2\right) + \frac{x^2-y^2}{4(1-\nu)(x^2+y^2)}\right], \tag{2.11b}$$

$$u_z = 0. \tag{2.11c}$$

This displacement field gives rise to the strains

$$\varepsilon_{xx} = \frac{by}{4\pi(1-\nu)}\frac{(2\nu-3)x^2+(2\nu-1)y^2}{(x^2+y^2)^2}, \tag{2.12a}$$

$$\varepsilon_{yy} = \frac{by}{4\pi(1-\nu)}\frac{(2\nu+1)x^2+(2\nu-1)y^2}{(x^2+y^2)^2}, \tag{2.12b}$$

$$\varepsilon_{xy} = \frac{by}{4\pi(1-\nu)}\frac{x\left(x^2-y^2\right)}{(x^2+y^2)^2}, \tag{2.12c}$$

$$\varepsilon_{zz} = \varepsilon_{xz} = \varepsilon_{yz} = 0, \tag{2.12d}$$

and the associated stresses

$$\tau_{xx} = -\frac{Gb}{2\pi(1-\nu)}\frac{y(3x^2+y^2)}{(x^2+y^2)^2}, \tag{2.13a}$$

$$\tau_{yy} = \frac{Gb}{2\pi(1-\nu)}\frac{y(x^2-y^2)}{(x^2+y^2)^2}, \tag{2.13b}$$

$$\tau_{xy} = \frac{Gb}{2\pi(1-\nu)}\frac{x(x^2-y^2)}{(x^2+y^2)^2}, \tag{2.13c}$$

$$\tau_{zz} = -\frac{Gb\nu}{\pi(1-\nu)}\frac{y}{(x^2+y^2)^2}, \tag{2.13d}$$

$$\tau_{xz} = \tau_{yz} = 0. \tag{2.13e}$$

Information about the stress and strain field of a dislocation will be necessary to calculate scattering cross section and the relaxation time of conduction electrons scattered by dislocation, discussed in next sections.

2.4 Plastic Deformation of Single Crystals

2.4.1 Schmid's Law and Critical Resolved Shear Stress

Single crystals may respond elastically or plastically to external stress depending on the orientation and the magnitude of the applied stress. Plastic deformation in a crystal occurs by the movement or gliding of dislocations on well-defined crystallographic planes and in well-defined crystallographic directions. If the shear component of the acting stress resolved on a glide plane and glide direction reaches

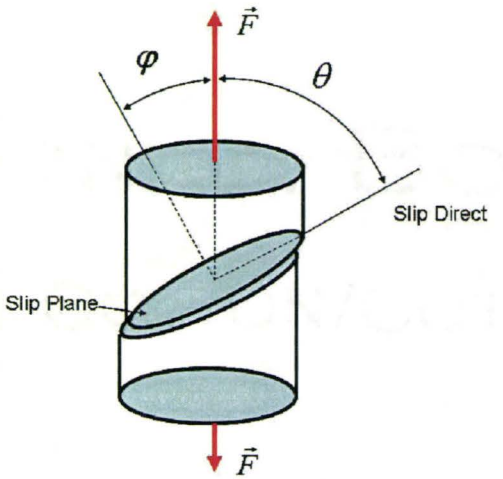

Figure 2.3: Geometry of a single slip in a single crystal sample.

a critical value, called the critical resolved shear stress, plastic deformation occurs by movement of dislocations in a given slip system. Figure 2.3 illustrates the quantitative determination of the critical shear stress by uniaxial tensile tests. A tensile load $\vec{F}$ acts on a metal specimen with a normal cross section area A. Let ϕ and θ denote the angles which the tensile axis makes with the normal to the slip plane and the slip direction respectively. A combination of the slip plane and slip direction constitute a slip system. The shear stress τ_s , resolved on the slip plane and in the slip direction, is

$$\tau_s = \frac{F}{A}\cos\phi\cos\theta = \tau_0 m \tag{2.14}$$

where $m\ (=\cos\phi\cos\theta)$ is *Schmid factor*. If the resolved shear stress τ_s attains the value of the critical resolved shear stress τ_c, the plastic deformation starts.

It was Schmid and co-workers (Schmid & Siebel, 1931; Schmid & Boas, 1950) who first attributed the large difference in the yield stresses of metallic sin-

gle crystals to the variation in the resolved shear stress. The statement proposed by these researchers that metal flows plastically when the resolved shear stress acting in the plane and along the direction of slip reaches a critical value is known as *Schmid's law*.

Table 2.1: Critical Resolved Shear Stress for *FCC* Metals (Reed-Hill & Abbaschian, 1992)

Metal	Purity	slip system	Critical Resolved Shear Stress (MPa)
Cu	99.999	$\{111\}\langle 110\rangle$	0.63
Ag	99.999	$\{111\}\langle 110\rangle$	0.37
Au	99.990	$\{111\}\langle 110\rangle$	0.91
Al	99.996	$\{111\}\langle 110\rangle$	1.02

The critical resolved shear stress for a given metal is affected by many factors such as the purity and composition of samples, the temperature at which sample testing is done, the load type (tension or compression), and others. Table 2.1 shows the critical resolved shear stress for some *FCC* metals measured at room temperature under tension.

2.4.2 Slip Systems in *FCC* Metals

Many experiments have verified that in metal crystals, slip occurs preferentially on the close-packed planes with the highest planar density of atoms along the close-packed directions having the highest linear density of atoms. The combination of a slip plane and one of its slip directions defines a slip system. For *FCC* metals, there are 4 close-packed $\{111\}$ octahedral planes, each octahedral plane containing 3

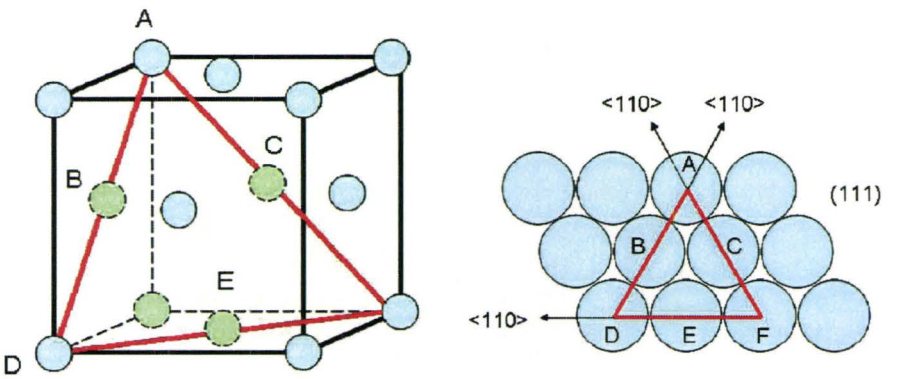

(a) (111) slip plane in a unit cell (b) ⟨110⟩ slip directions on (111) plane

Figure 2.4: Slip Systems in *FCC* Structure.

close-packed directions. Therefore, there are total 12 slip systems in *FCC* structure denoted by $\{111\}\langle 110\rangle$. Figure 2.4 illustrates slip systems $\{111\}\langle 110\rangle$ in *FCC* metals.

From Schmid's law, if, for any given *FCC* slip system, the resolved shear component of an acting stress on a crystal attains the critical value of the resolved shear stress (the value is $0.6MPa$ at room temperature for pure copper), this slip system is activated. In general, more than one slip systems can be simultaneously activated in a crystal, depending on the magnitude and orientation of external stress. In other words, one can make samples with specific distributions of dislocations by controlling the magnitude of the acting stress and the crystallographic orientation of the crystal. Figure 2.5 illustrates schematically two different orientations of copper single crystals used in our experiments. By applying the tensile loading to crystals with different crystallographic orientation of the tensile axis, one can activate different slip systems and induce different spatial distribution of dislocations in de-

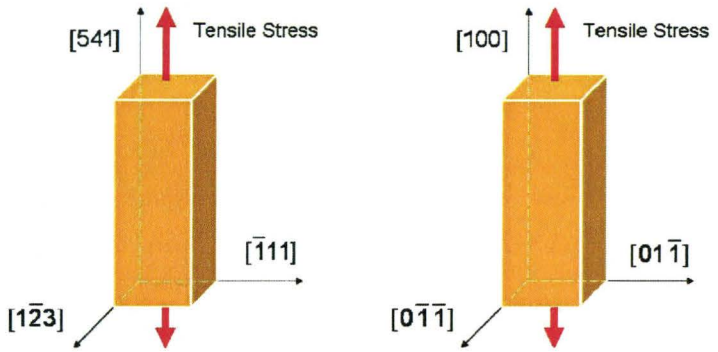

(a) Single crystal with tensile axis along ⟨541⟩

(b) Single crystal with tensile axis along ⟨100⟩

Figure 2.5: Crystallographic orientation of copper single crystals used in experiments.

formed samples. In one case (Figure 2.5(a)), the applied tensile loading is along [541], and in the other (Figure 2.5(b)), the loading is along [100] direction.

The application of the tensile stress in different crystallographic orientations to the crystal samples triggers different slip mechanisms in the deformed samples. The slip systems which are likely be activated can be theoretically predicted by computing Schmid factor for each slip system. Tables 2.2 and 2.3 list Schmid factors for all 12 different slip systems in *FCC* crystals oriented along ([541] and [100]). The Schmid factor is calculated from the formula ($m = \cos\phi \cos\theta$), where ϕ is the angle between the tensile axis and the plane normal, whereas θ is the angle between tensile axis and slip direction.

It is clear from tables 2.2 and 2.3 that during tensile deformation of the crystal

Table 2.2: The Schmid factors for different slip systems in crystal with tensile axis along [541]

slip system	Schmid factor	slip system	Schmid factor
$(111)[0\bar{1}1]$	-0.29	$(\bar{1}\bar{1}1)[011]$	-0.39
$(111)[10\bar{1}]$	0.39	$(\bar{1}\bar{1}1)[101]$	0.47
$(111)[\bar{1}10]$	0.10	$(\bar{1}\bar{1}1)[\bar{1}10]$	0.08
$(\bar{1}11)[101]$	0.0	$(\bar{1}1\bar{1})[011]$	-0.10
$(\bar{1}11)[0\bar{1}1]$	0.0	$(\bar{1}1\bar{1})[10\bar{1}]$	-0.08
$(\bar{1}11)[110]$	0.0	$(\bar{1}1\bar{1})[110]$	-0.17

Table 2.3: The Schmid factors for different slip systems in crystal with tensile axis along [100]

slip system	Schmid factor	slip system	Schmid factor
$(111)[0\bar{1}1]$	0.0	$(\bar{1}\bar{1}1)[011]$	0.0
$(111)[10\bar{1}]$	0.41	$(\bar{1}\bar{1}1)[101]$	-0.41
$(111)[\bar{1}10]$	-0.41	$(\bar{1}\bar{1}1)[\bar{1}10]$	0.41
$(\bar{1}11)[101]$	-0.41	$(\bar{1}1\bar{1})[011]$	0.0
$(\bar{1}11)[0\bar{1}1]$	0.0	$(\bar{1}1\bar{1})[10\bar{1}]$	-0.41
$(\bar{1}11)[110]$	-0.41	$(\bar{1}1\bar{1})[110]$	-0.41

oriented along $[541]$ the highest resolved shear stress will act on the $(\bar{1}\bar{1}1)[101]$ slip system, as it has the highest Schmid factor among all slip systems available. Thus, in a single crystal with tensile axis oriented along [541], the deformation will initiate dislocations activated by the $(\bar{1}\bar{1}1)[101]$ slip system i.e., on $(\bar{1}\bar{1}1)$ plane and in $[101]$ direction. This means that dislocation substructure introduced by such slip mechanism will consist of same-type dislocations in planar arrangement on a slip plane $(\bar{1}\bar{1}1)$ and having a/2[101] Burgers vector. However, in the sample oriented along $[100]$, many equivalent slip systems will be activated at simultaneously and on many intersecting planes. Such slip mechanism leads to a random distribution of dislocation lines and their Burgers vectors.

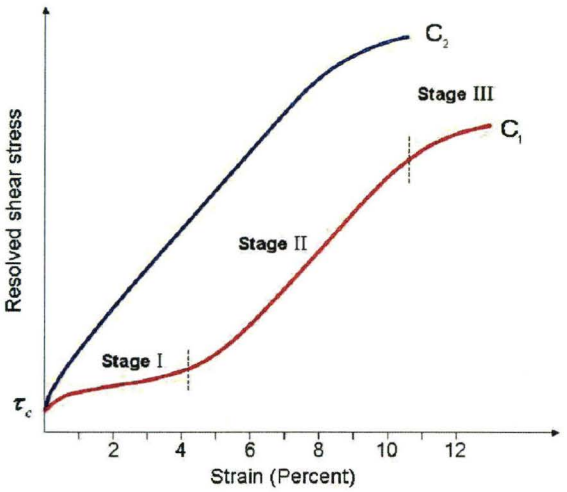

Figure 2.6: Typical strain-stress curves in *FCC* crystals.

Diversity of slip mechanisms in deformed crystals results in a significant change in microstructure which substantially affects the mechanical, electrical and magnetic properties of the deformed crystals. Figure 2.6 shows a typical tensile strain-stress curve of *FCC* metals. Curve C_2 corresponds to the sample oriented for multi-slip i.e. the orientation of the tensile axis is along [100]. In this sample, plastic deformation starts when the resolved shear stress reaches the critical value τ_c, and several slips systems are activated simultaneously on intersecting close-packed planes. This leads to strong interaction among the dislocations from different slip systems in the process called forest cutting, which makes further deformation more difficult and occurring at larger stresses. Consequently, this curve has a steep slope from the beginning of deformation. On the other hand, curve C_1 corresponds to the sample oriented for single slip i.e. orientation of the tensile axis along [541]. This curve is composed of three distinguished regions which are labeled *stage I*, *stage II* and *stage III*. *Stage I* the easy glide stage, is the region of the early beginning of

plastic deformation just after the resolved shear stress reaches the critical value and material yields in one slip system. In this stage a single slip plane $(\bar{1}\bar{1}1)$ is more highly stressed than the others, which means only one slip system $(\bar{1}\bar{1}1)\,[101]$ is activated, whereas others are inactive. Dislocations of active slip system interact with each other by a process called passing interactions which produces low work-hardening rate. Experimental observation shows that slip lines in stage I are very long (100-1000 μm), straight and uniformly spaced close to each other with a distance($10^2 - 10^3 \AA$) (Kovács & Zsoldos, 1973). Stage II of curve C_1 is a linear region and characteristic of a much steeper slope (work-hardening rate). In this stage deformed crystal hardens rapidly and linearly with strain, because secondary slip systems are activated on intersecting slip planes producing more effective obstacles for mobile dislocations. Experimental observations show the number of dislocations in this stage grows rapidly with increasing strain but their distribution is very inhomogeneous, a majority of dislocations are concentrated in small regions, which makes the density of dislocation very high in these areas, and separated by the regions with low dislocation density. The length of slip lines in this stage is much shorter (of the order of 10 μm). In the course of further deformation, *stageIII* begins. The features of this stage are a decreasing rate of work hardening and a smaller rate of increase of the dislocation density with increasing strain.

2.4.3 Dislocation Distribution in Copper Single Crystals

Dislocation substructure of deformed *FCC* metals and alloys has been studied thoroughly and there is large body of data available in the literature on this subject.

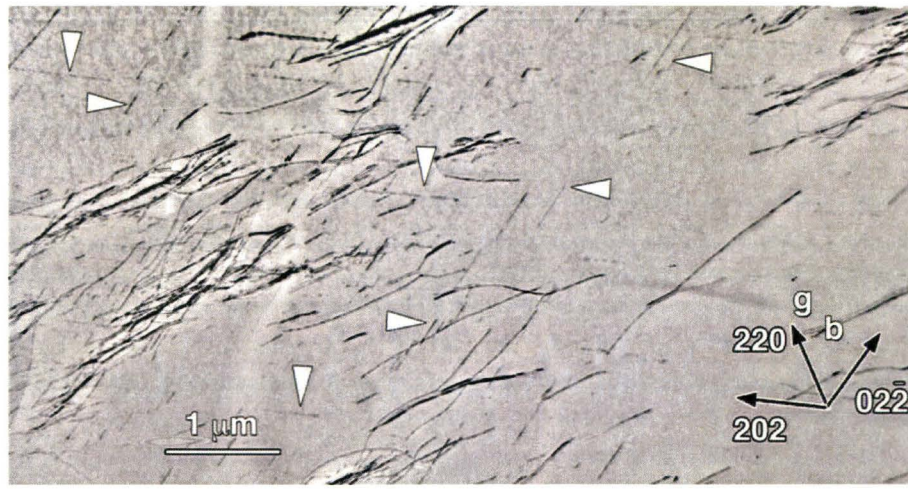

Figure 2.7: Primary dislocation bundles in *stage I*. The white arrowheads point to Frank dipoles (Veyssiére *et al.*, 2006)

Basinski (Basinski, 1964; Basinski & Basinski, 1964), Steeds (Steeds, 1966), Niewczas (Niewczas *et al.*, 2001; Niewczas, 2002) and Veyssiére *et al* (Veyssiére *et al.*, 2006) applied the techniques of transmission electron microscopy (TEM) to study the dislocation distribution in deformed copper single crystals at different stages of deformation at different temperatures. The following is a brief characterization of the dislocation substructure in deformed copper single crystals based on results of these researchers. The understanding of the nature of the dislocations will be helpful in interpreting the anisotropy of magnetoresistivity observed experimentally and in theoretical modeling of the magnetoresistivity in chapter 9.

Samples deformed into *stage I* show inhomogeneous dislocation arrangement at this stage. TEM observations carried out in section parallel to the primary glide plane reveal large areas completely free of dislocations separated by regions hav-

Figure 2.8: Stereo-pair of a primary dislocation bundle in *stage I*. Basinski (1964).

ing a relatively high dislocation density. The dislocation population is composed mainly of bundles of long edge dislocations produced by the primary slip system. The Figures 2.7 and 2.8 show the areas with high density of dislocations which forms the bundles of edge dislocations.

In the transition stage from *stage I* to *stage II*, the average density of dislocations in the bundle increases, but the width of bundles remains approximately constant. Figures 2.9 and 2.10 illustrate the arrangement of dislocations at the transition from *stage I* to *stage II*.

Samples deformed into *stage II* are characterized by the increase in the pro-

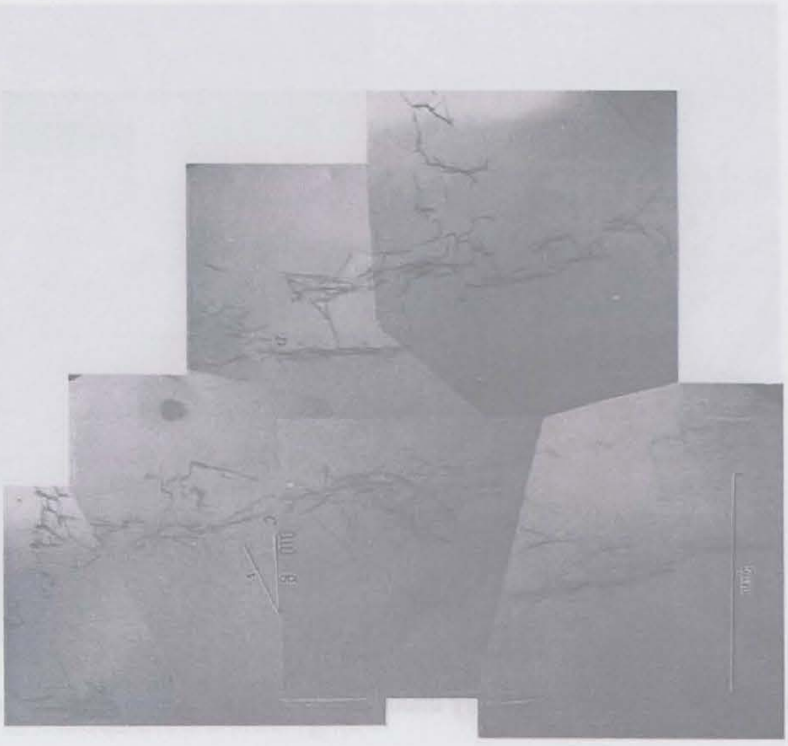

Figure 2.9: Dislocation arrays along the trace of the primary slip plane. Dipoles with the Burgers vectors are marked at C and D respectively (Steeds, 1966).

portion of dislocations activated in other non-coplanar slip systems. The primary edge dislocation bundles at this stage are chopped into segments of shorter length and the arrangement of dislocations is much less regular than in the previous stage. Another feature at this stage is that dislocation network is observed to be formed as a results of the interactions of dislocations from different sip systems. A characteristic feature is the formation of sessile Lomer-Cottrell dislocations. Figures 2.11 and 2.12 show the microstructure at this stage.

Figure 2.10: Formation of the dislocation bundles in the transition stage of $I-II$ (Niewczas, 2002).

The dislocation substructure in samples deformed to stage III is similar to the one deformed in stage II but with noticeable higher dislocation density and reduction of dislocation-free areas. One of the apparent features in this stage of deformation is the increase of local misorientations in magnitude and frequency and formation of the cell structure with high density cell boundaries (see picture 2.13) and lower density cell interiors. Figure 2.14 shows the alternately misoriented deformation bands in stage III. Figures 2.15 and 2.16 show dislocation substructure of copper single crystals developed in later stage III in $< 100 >$ (Figures 2.15) and $541 >$ (Figures 2.16) crystallographic orientation respectively. It is seen that these two TEM pictures show very similar dislocation substructure consisting of cells with very dense dislocation boundaries and somewhat less dense cell interiors, al-

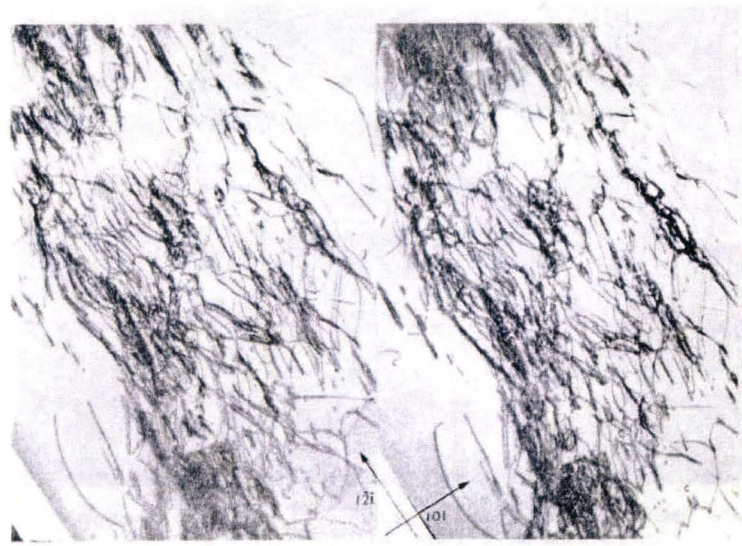

Figure 2.11: Microstructure of dislocation bundles in stage *II* Basinski (1964).

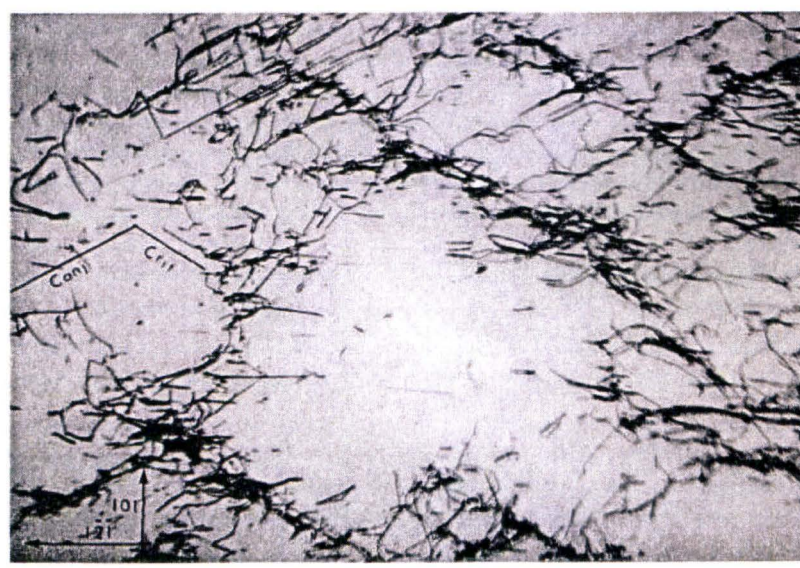

Figure 2.12: Dislocations in critical and conjugate planes interact in stage *II* Basinski (1964).

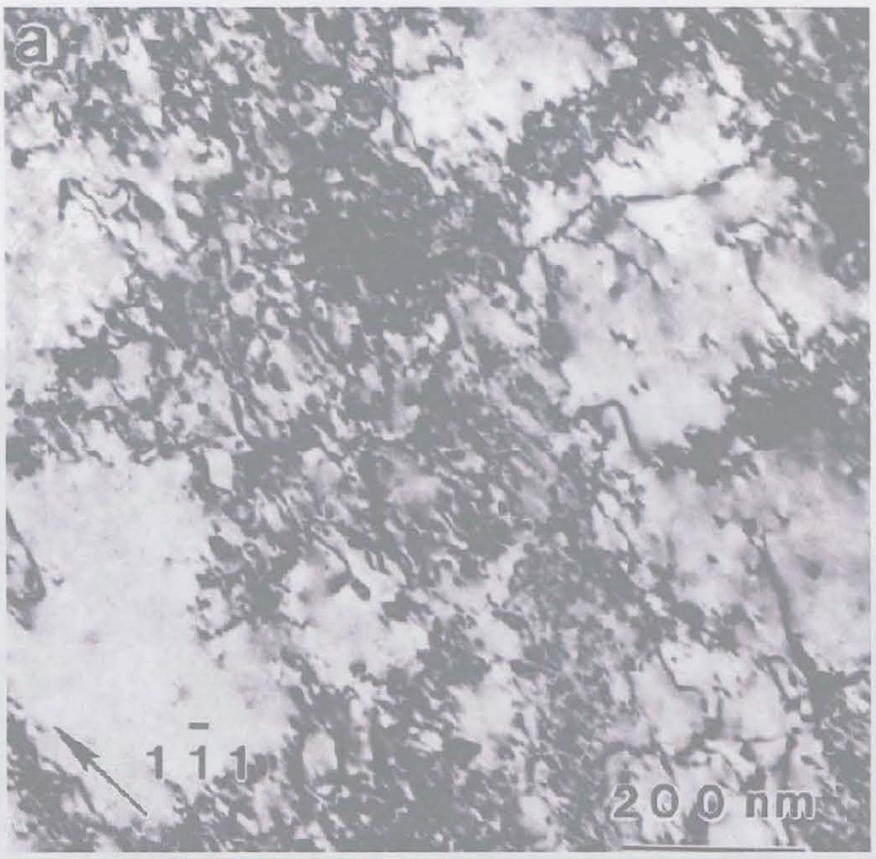

Figure 2.13: Cell structure and dislocation content in the wall in stage *III* (Niewczas *et al.*, 2001).

though it was produced in single crystals with different crystallographic orientation.

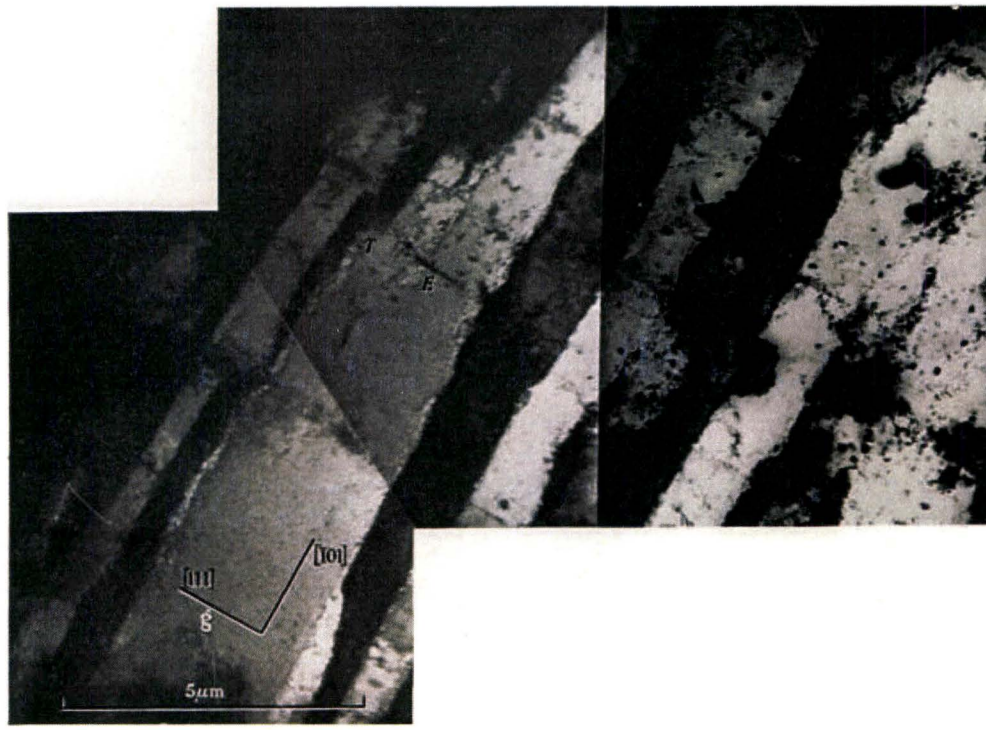

Figure 2.14: Dislocation boundaries formed by alternately misoriented regions in stage III (Steeds, 1966).

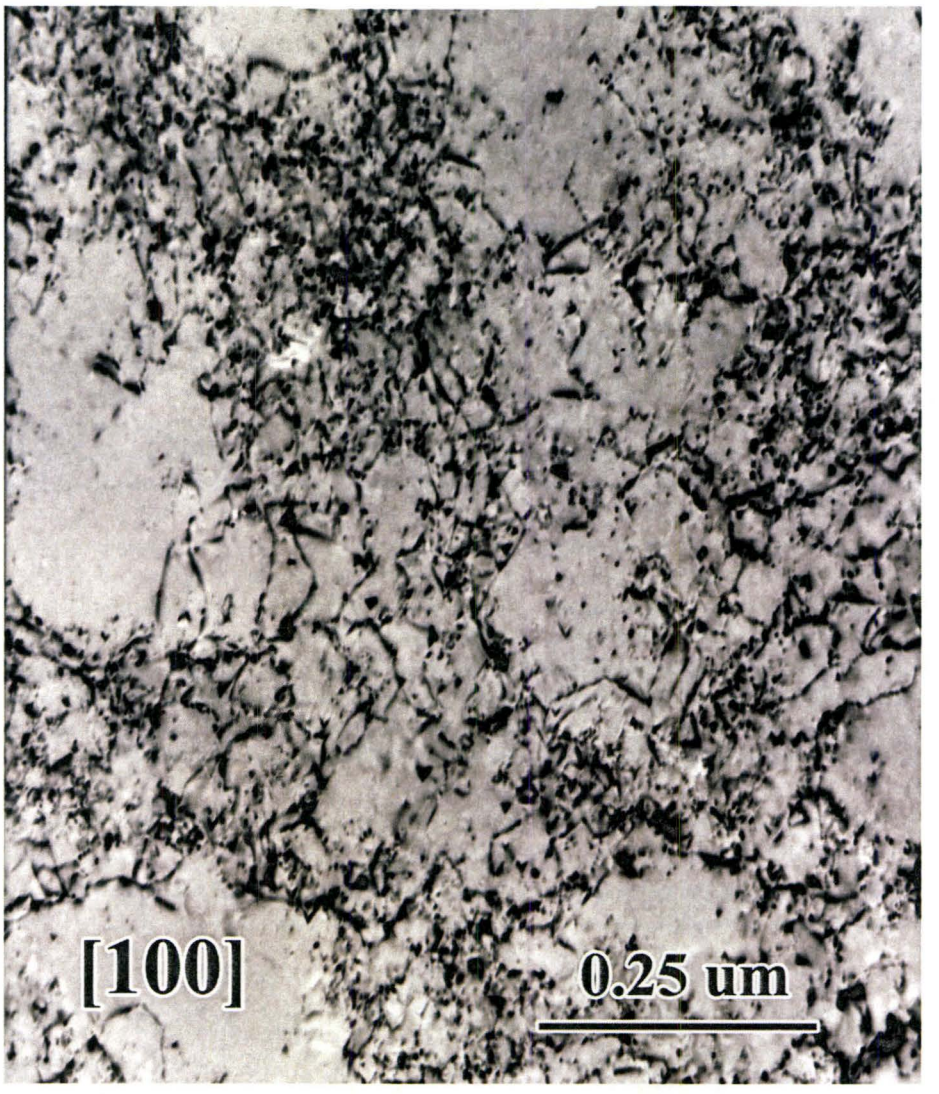

Figure 2.15: TEM observations of the dislocation substructure of $< 100 >$ copper single crystals deformed to later stage *III* at 4K by tension (Niewczas, 2003).

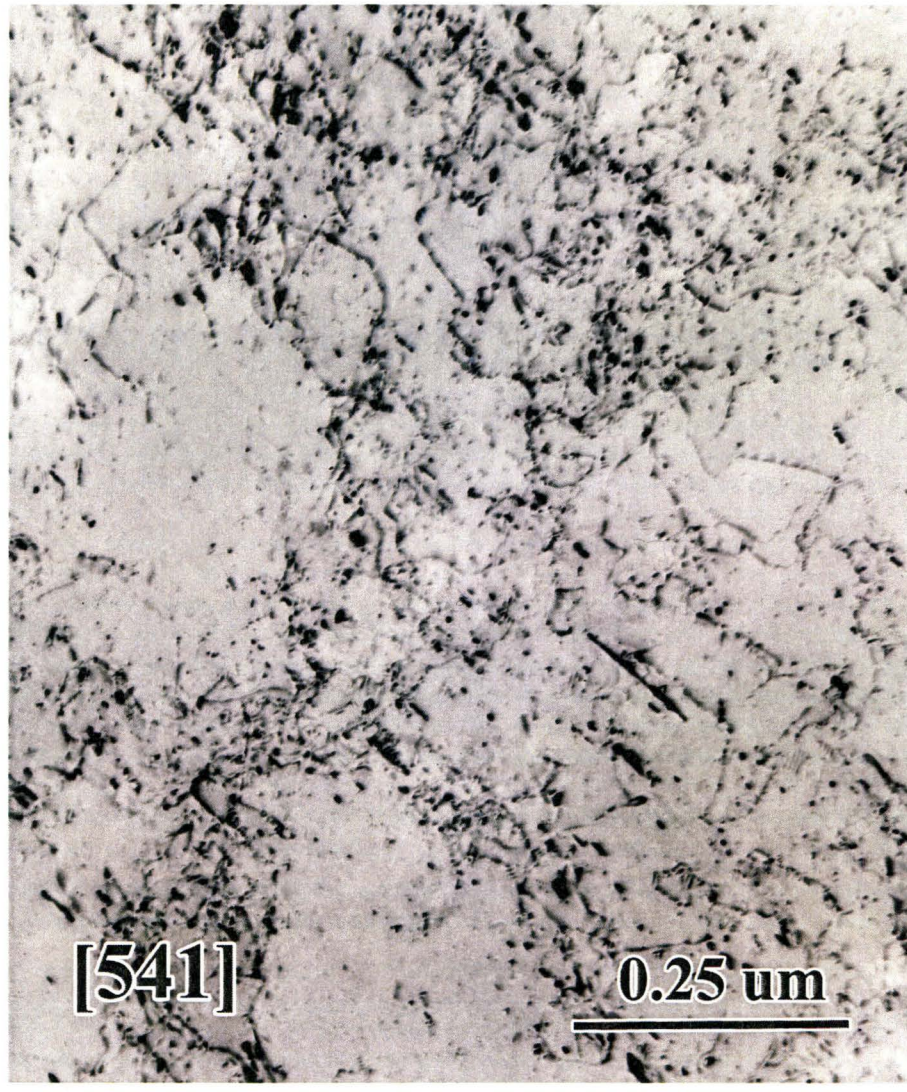

Figure 2.16: TEM observations of the dislocation substructure of $< 541 >$ copper single crystals deformed to later stage *III* at 4K by tension (Niewczas, 2003).

Chapter 3

The Semiclassical Theory of Electronic Conduction

3.1 The Boltzmann Transport Equation

The Boltzmann equation was established by Ludwig Boltzmann (Boltzmann, 1872). It represents a classical method in the kinetic theory dealing with non-equilibrium phenomena in dilute gases and yet it has had remarkable success in describing the conduction phenomena in metals and alloys after a change to semi-classical theory (Conwell, 1967; Callaway, 1991). The method may fail, though, if the physical size of an analyzed system is too small. A fully quantum mechanical transport theory is based on the linear response formalism due to Kubo (Kubo, 1957), but the application is too complicated. Therefore we choose the semi-classical Boltzmann's theory

which provides good approximation for determination of conductivity of bulk metals. Our samples for magnetoresistance measurements are large enough, so that the quantum size effect can be neglected and the semi-classical transport theory is applicable. In the following we provide a brief description of the semi-classical Boltzmann's equation.

Electrons are Fermions and obey the Fermi-Dirac statistics. For an electrical system at temperature T in equilibrium state, the average number of electrons at a given state $\vec{k}$ ($\vec{k}$ is the Bloch wave vector) is given by the distribution function $f_0[\varepsilon(\vec{k})]$:

$$f_0[\varepsilon(\vec{k})] = \frac{1}{e^{[\varepsilon(\vec{k})-\mu]/K_BT}+1}, \tag{3.1}$$

where $\varepsilon(\vec{k})$ is the energy of the electrons at state $\vec{k}$; μ the chemical potential per electron or Fermi energy and K_B the Boltzmann's constant.

In the presence of external fields or temperature gradient, the distribution function f will also be the function of time t and position $\vec{r}$ because of electron acceleration caused by external fields or diffusion by temperature gradient. Another way to change distribution function is the scattering of electrons by lattice imperfections such as phonons caused by ion thermal vibrations, impurities, volume disorder, crystal defects etc. Thus, Boltzmann's equation can be expressed as

$$\frac{df}{dt} = \left.\frac{\partial f}{\partial t}\right|_{diff} + \left.\frac{\partial f}{\partial t}\right|_{field} + \left.\frac{\partial f}{\partial t}\right|_{scat}. \tag{3.2}$$

If we restrict our attention to the conditions of homogeneity and steady-state problems under the influence of electrical field $\vec{E}$ and magnetic field $\vec{B}$, which may or

may not be time-dependent, the distribution function will only be the function of energy or wave vector $f(\vec{k})$. Therefore the Boltzmann's equation can be explicitly expressed as

$$-\frac{e}{\hbar}\left[\vec{E}+\vec{v}(\vec{k})\times\vec{B}\right]\cdot\vec{\nabla}_{\vec{k}}f=\left.\frac{\partial f}{\partial t}\right|_{scat}, \tag{3.3}$$

where e is the magnitude of electron charge, $\hbar$ is the Planck's constant divided by 2π, $\nabla_{\vec{k}}$ is the gradient operator in $\vec{k}$ space, $\vec{v}(\vec{k})$ is the electron velocity at state $\vec{k}$ and $\left.\frac{\partial f}{\partial t}\right|_{scat}$ is the rate of change of f due to the scattering of electrons. In derivation of equation (3.3), the following two equations of motion of electron in the electrical and magnetic field are used

$$\vec{v} = \frac{1}{\hbar}\vec{\nabla}_{\vec{k}}\varepsilon(\vec{k}) \tag{3.4a}$$

$$\frac{d\vec{k}}{dt} = -\frac{e}{\hbar}(\vec{E}+\vec{v}(\vec{k})\times\vec{B}). \tag{3.4b}$$

If $W(\vec{k},\vec{k}')$ denotes the probability of transition of an electron from state $\vec{k}$ to state $\vec{k}'$ per unit time, the rate of change of f due to the scattering reads (Blatt, 1968)

$$\left.\frac{\partial f}{\partial t}\right|_{scat}=\frac{V}{(2\pi)^3}\int\left\{W(\vec{k},\vec{k}')f(\vec{k}')\left[1-f(\vec{k})\right]-W(\vec{k}',\vec{k})f(\vec{k})\left[1-f(\vec{k}')\right]\right\}d\vec{k}' \tag{3.5}$$

where V is the crystal volume and the integral is in $\vec{k}$-space.

3.2 Conduction Electron Scattering in Metals

3.2.1 Relaxation Time Approximation

The Boltzmann's equation is an integro-differential equation and the solution to this equation is very complicated. Approximation has to be made to obtain the solution. The most common assumption is the relaxation time approximation which is defined by the following equation (Blatt, 1968)

$$\left.\frac{\partial f}{\partial t}\right|_{scat} = -\frac{f(\vec{k}) - f_0(\vec{k})}{\tau(k)} = -\frac{f_1(\vec{k})}{\tau(k)} \tag{3.6}$$

where $f_1(\vec{k})$ is the deviation of the distribution function at an instant from the equilibrium states and $\tau(k)$ is called relaxation time which may vary with the magnitude of $\vec{k}$ but not its direction and only depends on the scattering process but not on the external fields. In fact, if the scattering is elastic and the Fermi surface is spherical, the relaxation time approximation is quite accurate (Ashcroft & Mermin, 1976). Equation (3.6) implies that if a perturbed distribution $f(\vec{k})$ exists at a certain instant because of the effect of external fields, the equilibrium distribution will be re-established exponentially with a characteristic relaxation time $\tau(k)$ by scattering alone after switching off the external fields.

3.2.2 Electron Scattering

For elastic scattering, if we assume that the principle of microscopic reversibility or detailed balancing holds (Messiah, 1961; Rodberg & Thaler, 1976), then the condition for the probability of transition

$$W(\vec{k},\vec{k'}) = W(\vec{k'},\vec{k}) \tag{3.7}$$

must be met. We can rewrite equation (3.5) as

$$\left.\frac{\partial f}{\partial t}\right|_{scat} = \frac{V}{(2\pi)^3}\int W(\vec{k'},\vec{k})\left[f_1(\vec{k'}) - f_1(\vec{k})\right]d\vec{k'} \tag{3.8}$$

or

$$\left.\frac{\partial f}{\partial t}\right|_{scat} = f_1(\vec{k})\frac{V}{(2\pi)^3}\int W(\vec{k'},\vec{k})\left[\frac{f_1(\vec{k'})}{f_1(\vec{k})} - 1\right]d\vec{k'}. \tag{3.9}$$

Comparing equation (3.9) with the definition of the relaxation time in equation (3.6), we have

$$\frac{1}{\tau(k)} = \frac{V}{(2\pi)^3}\int W(\vec{k'},\vec{k})\left[1 - \frac{f_1(\vec{k'})}{f_1(\vec{k})}\right]d\vec{k'}. \tag{3.10}$$

Since $\tau(k)$ may depend on the magnitude of $\vec{k}$ but not its direction, so we can suppose

$$f_1(\vec{k}) = c\vec{k}\cdot\hat{x} \tag{3.11}$$

where c is a constant and $\hat{x}$ is the unit vector in the direction of the electrical field

(Ashcroft & Mermin, 1976). Substituting equation (3.10) in (3.11) gives

$$\frac{1}{\tau(k)} = \frac{V}{(2\pi)^3} \int W(\vec{k}', \vec{k}) \left[1 - \cos\theta_{\vec{k}\vec{k}'}\right] d\vec{k}', \tag{3.12}$$

where $\theta_{\vec{k}\vec{k}'}$ is the angle between Bloch wave vector $\vec{k}$ and $\vec{k}'$. Clearly, the relaxation time strongly depends on the scattering probability of elections. The relaxation time of electrons is a very important factor in determination of the electrical properties of metals. Therefore, the detailed information about electron scattering processes is required to understand electrical properties of metals.

3.2.3 Electron-Dislocation Scattering

Dislocations are one dimensional lattice imperfections, characterized by lines along which the lattice deviates from the crystal's periodic structure and associated with characteristic strain and stress fields (chapter 2). In metals dislocations are usually arranged in a complex three-dimensional dislocation substructure, which makes electron-dislocation scattering difficult to describe and no theory has been successful so far in explaining all experimental observations despite substantial research efforts by various groups. The following is a short overview of the development of electron-dislocation scattering theory.

Koehler (Koehler, 1949) did the pioneering work on the electron-dislocation scattering problem and theoretically discussed the reasons for the residual electrical resistance of metals produced by cold working. Mackenzie and Sondheimer (MS) (Mackenzie & Sondheimer, 1950) re-examined Koehler's work and refined it by

pointing out a few ambiguities. Based on the theory of a continuum model and assuming that the main part of the energy of a dislocation in a crystal is spread through the medium and stored as the potential energy of elastic strain, MS obtained the scattering potential encountered by conduction electrons when moving through the crystal containing dislocations. The derivation of the lattice potential was based on the fact that in the presence of a dislocation, the ions and consequently their screened coulomb fields are displaced from the perfect lattice position. Therefore, this perturbing potential was given as

$$\Delta V(\vec{r}) = \sum_{\alpha} \left\{ V_{\alpha}(\vec{r}, \vec{R}_{\alpha}^{0} + \vec{u}_{\alpha}) - V_{i}(\vec{r}, \vec{R}_{\alpha}^{0}) \right\} \approx \sum_{\alpha} \vec{u}_{\alpha} \cdot \vec{\nabla} V_{\alpha}(\vec{r}, \vec{R}_{\alpha}^{0}), \tag{3.13}$$

where the sum is over all lattice points; $V_{\alpha}(\vec{r}, \vec{R}_{\alpha}^{0})$ is the interacting potential energy of an electron at $\vec{r}$ with the α^{th} ion in an equilibrium state at $\vec{R}_{\alpha}$ and obviously this potential is a function of $\vec{r} - \vec{R}_{\alpha}$; $\vec{u}_{\alpha}$ is the displacement of the α^{th} ion from its perfect lattice position and its explicit expression suggested by MS is similar to the equation (2.11).

MS method which permits a direct calculation of resistivity based on the displacements of ions around the dislocation seems sound and elegant. However, the difficulties arise immediately because of the problem of convergence. In order to obtain a finite scattering cross section, it was necessary to take into account of the perturbation induced by a pair of dislocations of opposite sign which are situated at distance apart. Furthermore, Landauer (Landauer, 1951) pointed out that MS method did not consider the redistribution of electrons around the distortion.

Landauer and Dexter (LD) (Landauer, 1951; Dexter, 1952a,b,c) used a quite

different method to deal with the same subject. The authors assumed that electrons can redistribute themselves in the neighborhood of a dislocation line. That is possible because the Fermi level above the slip plane tends to be higher than that below the plane, causing some electrons above the slip plane to diffuse below the slip plane. As a result, there will be an extra electrical field formed in the crystal. Equilibrium will be attained when the Fermi levels in the different regions achieve equilibrium (Bardeen & Shockley, 1950). In LD model, the relative change in ionic density n around a dislocation was derived by using the stress field surrounding an edge dislocation suggested by Koehler (Koehler, 1941)

$$\frac{\Delta n}{n} = \frac{a}{2\pi}\frac{1-\nu-2\nu^2}{1-\nu^2}\frac{\sin\theta}{r}, \tag{3.14}$$

where a is lattice constant and ν is Poisson's ratio; z-axis in the polar coordinate system is parallel to the axes of the dislocations and the angle θ is measured with respect to the slip plane. Under free-electron approximation, the width of the filled portion of conduction band is

$$E = \frac{\hbar^2}{2m^*}(3\pi^2 n_e)^{2/3}, \tag{3.15}$$

where m^* is electronic effective mass and n_e is the density of electrons. Assuming that the change of electron density follows the change of the density of ions, Landauer and Dexter proposed the scattering potential in the form

$$\Delta V(\vec{r}) = \frac{\Delta E}{e} = \frac{aE}{3\pi e}\frac{1-\nu-2\nu^2}{1-\nu^2}\frac{\sin\theta}{r}. \tag{3.16}$$

This model is much simpler in mathematics and avoids the convergence difficulties. However, the free-electron assumption in LD model leads to the conclusion that the conduction electrons suffer no scattering by the shear components of the strain tensor. Apparently this is not true in reality.

Hunter and Nabarro (Hunter & Nabarro, 1953) also introduced a deformation potential to handle the problem of the electron-dislocation scattering. However, this model could not even qualitatively explain the increase of the electrical resistivity observed after cold work. The discrepancy is approximately a factor of 30 for Cu, Ag, Au and Al (Bross & Häerlen, 1993).

Harrison (Harrison, 1958) considered the problem of electron-dislocation scattering within the framework of pseudopotential theory. Supposing that the scatter is a long and straight empty core, which has a square-well potential of the order of fractional Fermi surface, he calculated electron scattering cross section area and obtained an expression for resistivity due to dislocations. However, the numerical solution for the actual hollow core structure is too small to account for the measured resistivity. Bhatia and Gupta (Bhatia & Gupta, 1970) refined Harrison's model by considering the core of the dislocation consisting of one atomic high row of vacancies. The resistivity numerically obtained for aluminum by these authors is near the experimental value. The important point was made that there should be non-zero electrical resistivity when the electrical field is applied parallel to a dislocation line.

Martin and Ziman (MZ) (Martin & Ziman, 1970) suggested an atomistic model to calculate resistivity for aluminum with edge dislocation along $\langle 112 \rangle$ direction. In their model, the scattering potential was taken as the difference in the crystal

potentials of dislocated and perfect crystals and was expanded in reciprocal lattice space. The advantage of such treatment is that the Fourier transform of the potential can be expressed into the product of a form factor and a structure factor in which the effect of dislocation is incorporated. The dislocation resistivity was evaluated by taking the pseudopotential from the literature. The results are in fairly good agreement with the experiment data. However, this model still fails to explain the isotropy of electrical resistivity in metals containing dislocations.

Watts (Watts, 1987, 1988) noticed the importance of the structure factor and argued that the underlying crystal structure should be taken into account to understand why the measured electrical resistivity is approximately isotropic in dislocated samples, even in those known to contain very anisotropic arrangement of dislocations. Watts showed how to calculate the amplitude of the electron wave scattered by the dislocation oriented along $\langle 211 \rangle$ direction in faced-centered cubic metals, by considering the effect from the underlying crystal structure. A slightly anisotropic resistivity was obtained which is physically acceptable. However no further calculation of resistivity in other orientations of samples was reported in the literature since then.

Using the partial-wave theory of scattering, Brown (Brown, 1977a,b,c) applied a different approach to the problem of electron-scattering and derived an expression for resistivity. Although his formulation is in a good agreement with experiment, it is rather implausible on theoretical grounds and contains too many arbitrary assumptions.

It is interesting to notice that Bausch *et al.*, (Bausch *et al.*, 1999) calculated, in

cylindrical coordinate system, a differential cross section area per unit length of a screw dislocation, by directly solving Schrödinger equation containing contribution of the type of a vector potential as well as of a repulsive scalar potential. The advantage of their method is that the exact far-field expression of an electron scattered by a screw dislocation was obtained and this avoids the free-electron assumption which is not valid because of long-range interaction potential. However, the method has limited applications to the case of edge dislocation, due to much more complicated strain field what makes it impossible to solve Schrödinger equation directly.

Here we have summarized a few basic models of electron scattering by dislocations in single crystals. Other details on this subject may be found in work of Watts (Watts, 1989). In addition, the treatment of electron-dislocation scattering in composites or compounds can be found in other references such as (Seeger, 1991). To the best of our knowledge, there is currently no theory of the electron-dislocation scattering, which explains all experimental results observed in single crystals. The theoretical understanding of this phenomenon is difficult due to the complexity of the process itself. Hopefully, this research can shed some new light and will help to understand this problem.

3.2.4 The Selection Rules

The transition probability of electron from initial state $\left|\vec{k}\right\rangle$ to the final $\left|\vec{k'}\right\rangle$ per unit time is given to the first order in perturbation theory (Schiff, 1968)

$$W(\vec{k},\vec{k'}) = \frac{2\pi}{\hbar}\left|\left\langle \vec{k'}\left|\hat{H'}\right|\vec{k}\right\rangle\right|^2 \delta(E_{\vec{k'}} - E_{\vec{k}}). \tag{3.17}$$

where $\hat{H'}$ is the perturbation potential and $\delta(x)$ is Dirac delta function . The transition matrix in $\vec{r}$ space is defined as

$$\left\langle \vec{k'}\left|\hat{H'}\right|\vec{k}\right\rangle = \int \psi^*_{\vec{k'}}(\vec{r})\hat{H'}(\vec{r})\psi_{\vec{k}}(\vec{r})d\vec{r}, \tag{3.18}$$

Equation (3.17) is also called Fermi's golden rule.

By using the selection rule, we can rewrite equation (3.12) as

$$\frac{1}{\tau(k)} = \frac{V}{4\pi^2\hbar}\int \left|\left\langle \vec{k'}\left|\hat{H'}\right|\vec{k}\right\rangle\right|^2 (1-\cos\theta_{\vec{k}\vec{k'}})\delta(E_{\vec{k'}} - E_{\vec{k}})d\vec{k'}. \tag{3.19}$$

For spherical band or under free-electron approximation, by carrying out the integral over k', the above equation can be expressed in another form

$$\frac{1}{\tau(k)} = \int (1-\cos\theta)\Gamma(k,\theta)d\Omega', \tag{3.20}$$

where $\Gamma(k,\theta)$ is called differential scattering cross section per scattering center and for simplicity, instead of $\theta_{\vec{k}\vec{k'}}$ we use θ to denote the angle between $\vec{k}$ and $\vec{k'}$.

3.3 Magnetoresistivity in Metals

In this section, we turn to magnetoresistance in pure metals and formulate the magnetoconductivity tensors in open and closed-orbit crystallographic orientations which will be needed to simulate the galvanomagnetic properties of deformed copper single crystals. The discussion in this section partly follows the reference (Smith *et al.*, 1967)

Under the approximation of the relaxation time, Boltzmann's equation can be simplified as

$$-\frac{e}{\hbar}\left[\vec{E}+\vec{v}(\vec{k})\times\vec{B}\right]\cdot\vec{\nabla}_{\vec{k}}f=-\frac{f_1}{\tau}. \tag{3.21}$$

Finding a solution to this equation is not trivial even in the relaxation time approximation and more assumptions have to be made in order to calculate magnetoresistivity tensor theoretically.

3.3.1 Parabolic Band Approximation

Suppose electrons have parabolic energy band structure

$$\varepsilon(\vec{k})=\frac{\hbar^2k^2}{2m^*}. \tag{3.22}$$

Noticing that f_1 is a small deviation from the equilibrium state caused by external fields, we can rewrite Boltzmann's equation as

$$\left[1+\tau\hat{X}\right] f_1 = -e\tau\vec{E}\cdot\vec{v}\frac{df_0}{d\varepsilon}, \tag{3.23}$$

where $\hat{X}$ is an operator defined by

$$\hat{X} = -\frac{e}{\hbar}(\vec{v}\times\vec{B})\cdot\frac{\partial}{\partial\vec{k}} = -\frac{e}{m^*}(\vec{v}\times\vec{B})\cdot\frac{\partial}{\partial\vec{v}}. \tag{3.24}$$

Assuming that (Ziman, 1960)

$$f_1 = \vec{C}\cdot\vec{v}, \tag{3.25}$$

where $\vec{C}$ is an unknown factor. By substituting equation (3.25) back into equation (3.23) and using vector identity

$$\vec{A}\times(\vec{B}\times\vec{C}) = \vec{B}(\vec{A}\cdot\vec{C}) - \vec{C}(\vec{A}\cdot\vec{B}). \tag{3.26}$$

we can determine $\vec{C}$ as

$$\vec{C} = -e\tau\frac{\partial f_0}{\partial\varepsilon}\frac{\vec{E}+(e\tau/m^*)\vec{B}\times\vec{E}+(e\tau/m^*)^2(\vec{B}\cdot\vec{E})\vec{B}}{1+(eB\tau/m^*)^2} \tag{3.27}$$

From the definition of the current density $\vec{j}$

$$\vec{j} = -\frac{e}{4\pi^3}\int\vec{v}(\vec{k})f(\vec{k},\vec{r})d\vec{k} = \overleftrightarrow{\sigma}\cdot\vec{E}, \tag{3.28}$$

we can obtain the expression for magnetoconductivity tensor

$$\sigma_{ij}(\vec{B}) = \frac{\sigma_0}{1+(eB\tau/m^*)^2}\left[\delta_{ij} - (e\tau/m^*)\varepsilon_{ijk}B_k + (e\tau/m^*)^2 B_i B_j\right], \tag{3.29}$$

where δ_{ij} and ε_{ijk} are *Kronecker delta* and *Lei – Civita* symbols respectively, and $\sigma_0 = ne^2\tau/m^*$. In the derivation of equation (3.29), we already used an approximate value for the integral expansion

$$-\int_0^\infty g(\varepsilon)\frac{\partial f_0}{\partial \varepsilon}d\varepsilon = g(\mu) + \frac{(\pi K_B T)^2}{6}g''(\mu) + \ldots \tag{3.30}$$

For a simple case of electric field $\vec{E}$ along x-axis and magnetic field $\vec{B}$ along z-axis, the transverse magnetoconductivity tensor has the form

$$\overleftrightarrow{\sigma} = \frac{\sigma_0}{1+(eB\tau/m^*)^2}\begin{pmatrix} 1 & -eB\tau/m^* & 0 \\ eB\tau/m^* & 1 & 0 \\ 0 & 0 & 1+(eB\tau/m^*)^2 \end{pmatrix} \tag{3.31}$$

Equation (3.31) will be used for modeling magnetoresistivity in chapter 9.

3.3.2 Jones-Zener Expansion - Weak Field Approximation

For arbitrary band shape, Boltzmann's equation (3.23) still holds, but the second sign of equality in equation (3.24) is not correct any more. However, the solution

to equation (3.23) can be obtained by taking operator expansion such as

$$\frac{1}{1+\hat{A}} = 1-\hat{A}+\hat{A}^2+\ldots(-\hat{A})^n+\ldots, \qquad \|\hat{A}\|<1, \tag{3.32}$$

therefore f_1 is given as

$$\begin{aligned} f_1 &= -\frac{1}{1+\hat{X}} e\tau\vec{E}\cdot\vec{v}\frac{df_0}{d\varepsilon} \\ &= -\left[1-\hat{X}+\hat{X}^2+\ldots(-\hat{X})^n+\ldots\right] e\tau\vec{E}\cdot\vec{v}\frac{df_0}{d\varepsilon} \\ &= -e\frac{df_0}{d\varepsilon}\vec{E}\cdot\left[\tau\vec{v}-\hat{X}\tau\vec{v}+\hat{X}^2\tau\vec{v}+\ldots(-\hat{X})^n\tau\vec{v}+\ldots\right], \end{aligned} \tag{3.33}$$

then substituting equation (3.33) into equation (3.28) to evaluate the current densities yields

$$\sigma_{ij}(\vec{B}) = \frac{e^2}{4\pi^3}\int\frac{df_0}{d\varepsilon}v_i\left[\tau v_j-\hat{X}\tau v_j+\hat{X}^2\tau v_j+\ldots(-\hat{X})^n\tau v_j+\ldots\right]d\vec{k}. \tag{3.34}$$

Above method is called Jones-Zener expansion, first proposed by Jones and Zener(Jones & Zener, 1934).

Equation (3.34) is merely Taylor expansions of $\sigma_{ij}(\vec{B})$ in argument $\vec{B}$, namely,

$$\sigma_{ij}(\vec{B}) = \sigma_{ij}(0)+\sum_k\left[\frac{\partial\sigma_{ij}(\vec{B})}{\partial B_k}\right]_{\vec{B}=0}B_k+\frac{1}{2!}\sum_{k,l}\left[\frac{\partial^2\sigma_{ij}(\vec{B})}{\partial B_k\partial B_l}\right]_{\vec{B}=0}B_kB_l+\ldots, \tag{3.35}$$

The requirement for the convergence of equation (3.35) is that the magnitude of the magnetic field should be small. The quantitative condition for convergence problem in equation (3.34) or (3.35) can be estimated roughly by expanding the denominator in equation (3.29) as a geometric series of argument $eB\tau/m^*$ and comparing it with

equation (3.35). The convergence condition is

$$eB\tau/m^* < 1. \tag{3.36}$$

More detailed discussion about the convergence problem can be found in the reference (Smith *et al.*, 1967) .

3.3.3 Lifshits' Theory - Strong Field Approximation

It is well known that conduction electrons in the electrical and magnetic fields experience not only the electrostatic forces, which make them travel in straight lines between collisions, but also the Lorentz forces which bend their paths into helices and are consequently responsible for conductivity change in metals. If we neglect quantum effects such as weak localization to cause a negative magnetoresistance (Altshuler *et al.*, 1980), in semiclassical approximation this force can be regarded as the reason to create magnetoresistance and lower conduction electron mobility in metals.

In general, a magnetic field can only have a significant effect on conductivity of metals if it is strong enough to bend the trajectory of an electron appreciably during a free path. Therefore, the magnetoresistance effect will be more easily detected in an intense magnetic field. The focus of this work is on the electronic behavior in a strong magnetic field, which has to satisfy following condition

$$w_c\tau = eB\tau/m^* \gg 1. \tag{3.37}$$

where w_c is the cyclotron frequency or the angular velocity of an electron in an external magnetic field B and again m^* is the effective mass of the electron.

For metals, the conductivity or resistivity is written as

$$\sigma_0 = \frac{ne^2\tau}{m^*} \quad or \quad \rho_0 = \frac{m^*}{ne^2\tau} \tag{3.38}$$

where n is the density of electrons. For copper with one electron per atom, n is about $8.5 \times 0^{28} m^{-3}$. Combining equation (3.37) and (3.38) gives

$$w_c\tau = \frac{B\sigma_0}{ne} = \frac{B}{\rho_0 ne}. \tag{3.39}$$

Equation (3.39) explicitly indicates that, for any specimen in a magnetic field, if equation (3.37) holds, the sample should have a high conductivity or a low resistivity. Usually, such a condition can be achieved when magnetoresistivity measurements are carried out at a low temperature on very high purity metals.

The magnetic field does no work on electrons because the Lorentz force is perpendicular to the velocity of electrons. The Lorentz force makes electrons to circle around in k -space in the different orbits on a surface of constant energy. The frequency of the orbital motion is proportional to the intensity of the magnetic field. This means that in a strong magnetic field an electron can travel a substantial arc of its orbit in k -space on the surface of constant energy before being scattered. Then the geometry of the orbit may be a more important factor needed to be considered in the motion of the electron in a strong magnetic field than the details of the scattering. For simplicity, suppose that the external magnetic field is along z -direction.

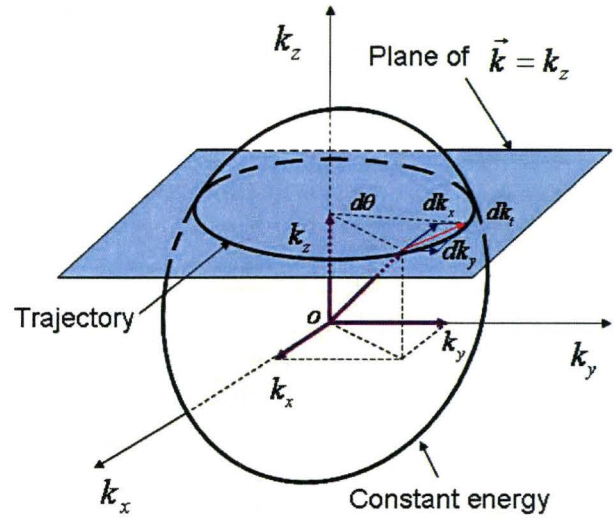

Figure 3.1: Schematic illustration for a trajectory of electrons in k-space and the definition of angular variable θ

Instead of the conventional set of variables such as (k_x, k_y, k_z), we will follow approach used in the reference (Smith *et al.*, 1967) and introduce $(\varepsilon, \theta, k_z)$ as the variables of the system. Here θ is an angular variable to describe the motion of an electron along the trajectory which is the curve of the surface of constant energy ε intersecting with the plane of $\vec{k} = k_z$. Figure 3.1 shows the definition of angular variable θ and dk_t is the tangential component of wave vector to the trajectory. Such definition gives, in the absence of the electrical field,

$$d\theta = w_c dt = \frac{eB}{m^*} dt. \tag{3.40}$$

In the relaxation time approximation, the Boltzmann equation can be written in

terms of ε, k_z and θ as

$$\dot{\varepsilon}\frac{\partial f}{\partial \varepsilon}+\dot{k}_z\frac{\partial f}{\partial k_z}+\dot{\theta}\frac{\partial f}{\partial \theta}=\left.\frac{\partial f}{\partial t}\right|_{scat}=-\frac{f(\vec{k})-f_0(\vec{k})}{\tau} \tag{3.41}$$

In the case of magnetoresistivity measurements the applied electric field is very small whereas the magnetic field is very large. Noticing equations (3.4) of the motion of electrons and bearing in mind that the magnitude of the electrical field is a small quantity and the terms with the second or higher order in the electrical field can be neglected, we can obtain

$$\dot{\varepsilon} = \nabla_{\vec{k}}\varepsilon\cdot\dot{\vec{k}}=-e\vec{v}\times\vec{E}, \tag{3.42a}$$

$$\dot{\vec{k}}_z = -(e/\hbar)E_z, \tag{3.42b}$$

$$\dot{\theta} = \frac{\hbar}{m^*}\left(\frac{\dot{k}_x^2+\dot{k}_y^2}{v_x^2+v_x^2}\right)^{1/2}\approx \frac{eB}{m^*}\left[1-\frac{v_xE_y-v_yE_x}{B(v_x^2+v_y^2)}\right]. \tag{3.42c}$$

Lets follow now the standard method and suppose that the solution of the Boltzmann equation (3.41) has the form

$$f=f_0+e\tau\vec{E}\cdot\vec{C}\frac{\partial f}{\partial \varepsilon}, \tag{3.43}$$

where $\vec{C}$ is an unknown constant to be determined. Submitting equations (3.42) and (3.43) into the Boltzmann's equation and simplifying the equation by dropping the quadratic and higher terms in the electrical field, we can obtain a new equation about $\vec{C}$

$$\vec{v}\cdot\vec{E}-\frac{e\tau B}{m^*}\vec{E}\cdot\frac{\partial\vec{C}}{\partial\theta}=\vec{E}\cdot\vec{C}. \tag{3.44}$$

Since the electric field is arbitrary, the above equation (3.44) is equivalent to

$$\frac{\partial \vec{C}}{\partial \theta} + \alpha_0 \vec{C} = \alpha_0 \vec{v}, \tag{3.45}$$

where $\alpha_0 = m^*/e\tau B$. It is clear that $\vec{C}$ is a function of θ.

To obtain the expression for magnetoconductivity tensor, we have to evaluate current density. By substituting equation (3.43) into equation (3.28) and considering the relation

$$dk_x dk_y dk_z = \frac{m^*}{\hbar^2} d\varepsilon dk_z d\theta \tag{3.46}$$

we can write the conductivity tensor as

$$\sigma_{ij} = -\frac{e^2 m^*}{4\pi^3 \hbar^2} \iiint \tau v_i C_j(\theta) \frac{\partial f_0}{\partial \varepsilon} d\varepsilon dk_z d\theta. \tag{3.47}$$

By means of the integral expansion equation (3.30), the expression for the conductivity tensor can be simplified by finishing the first integration over energy ε

$$\sigma_{ij} = \frac{e^2 m^*}{4\pi^3 \hbar^2} \iint_{\varepsilon=\mu} \tau v_i C_j(\theta) dk_z d\theta. \tag{3.48}$$

Equation (3.48) indicates that the remaining double integrals will be evaluated along some certain trajectories on the Fermi surface in one Brillouin zone for each k_z. This means that the value of the integral depends substantially on the geometries of orbits or on the topology of the Fermi surface and also implies that only those electrons on the Fermi surface can have contributions to magnetoconductivity of materials.

From equation (3.48) it is straightforward that the analytical expression for mag-

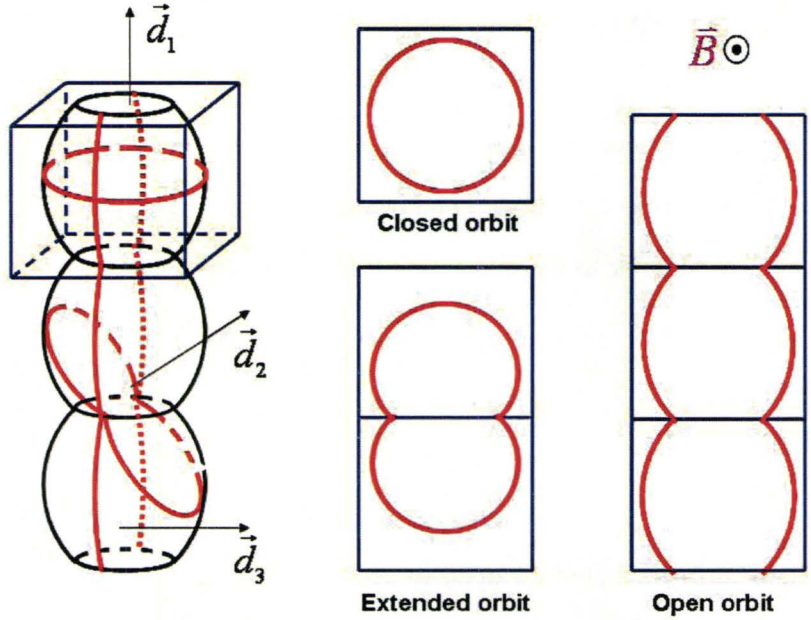

Figure 3.2: Illustration of different types of electron orbits for the magnetic field oriented along different directions in the sample with the Fermi surface of corrugated cylindrical type.

netoconductivity tensor is on the condition that $\vec{C}$ is known. Therefore, the question how to calculate this magnetoconductivity tensor reduces to the question how to find the unknown vector $\vec{C}$.

Lifshitz *etal* (Lifshitz *et al.*, 1957) proposed a method, which permits to find the unknown vector $\vec{C}$. Here we give a brief description of this method.

Although the geometries of the Fermi surface of materials are so diverse, in general one can differentiate between three types of electron orbits on the Fermi surface in reciprocal space when the magnetic field is turned on. Figure 3.2 shows the features of these three types of electron orbits for the sample with the Fermi

surface of corrugated cylindrical type (left). The blue cubic cell represents the Brillouin zone in reciprocal space for the material. When the magnetic field is along direction $\vec{d}_1$, electrons under the action of Lorentz force will circulate along the trajectory (red round circle) which is the intersection of the Fermi surface with the plane perpendicular to the magnetic field. This electron orbit is totally within the Brillouin zone and hence called closed orbit. If the magnetic field orients in $\vec{d}_2$, the electron orbit will extend several Brillouin zones (two zones in Figure 3.2) and is named extended orbit. Finally, if the magnetic field coincides in $\vec{d}_3$, the electron orbit will spread out through the length of the whole sample and never be closed. This kind of orbit is called an open orbit. In terms of their structure or shape, extended orbits are between closed and open orbits and they represent a transition region from closed to an open orbit. This implies that when we try to calculate magnetoconductivity tensor, only two extreme cases, i.e., closed and open orbits have to be considered.

In a strong magnetic field, $\alpha_0 \ll 1$, in order to find the solution to equation (3.45), we can expand the component of $\vec{C}$ into a series of α_0

$$C_i = \sum_{\beta=0}^{\infty} b_\beta^i \alpha_0^\beta . \tag{3.49}$$

The average value of any function u of argument θ is defined in the following way:

$$\bar{u} = \frac{1}{\theta_0}\int_0^{\theta_0} u(\theta)d\theta \quad \textit{closed orbit} \tag{3.50a}$$

$$\bar{u} = \lim_{\theta_0\to\infty}\frac{1}{\theta_0}\int_0^{\theta_0} u(\theta)d\theta \quad \textit{open orbit}, \tag{3.50b}$$

where θ_0 is cyclic period of angle θ for closed orbits and for open orbits this period can be regarded as infinity. The advantage of such definition is that we can now use the features of these two extreme types of electron orbits. For example, applying equation (3.50) and taking the average from both sides of equation (3.45) yields

$$\bar{C}_i = \bar{v}_i, \qquad i = x,\ y, \tag{3.51}$$

which is true for both closed and open orbits.

Because $\vec{C}$ is independent of α_0, we can obtain the following equivalent coupling equations by substituting equation (3.49) into equation (3.45) and letting the coefficients of the same power in α_0 in both side of the equation

$$\frac{\partial b_0^i}{\partial \theta} = 0, \tag{3.52a}$$

$$\frac{\partial b_i^i}{\partial \theta} + b_0^i = v_i, \tag{3.52b}$$

$$\frac{\partial b_\beta^i}{\partial \theta} + b_{\beta-1}^i = 0, \quad \beta \geq 2. \tag{3.52c}$$

The conditions for the coefficients, obtained directly from equation (3.51) are:

$$b_0^i = \bar{v}_i, \quad \bar{b_\beta^i} = 0, \quad \beta \geq 1,\ i = x,y. \tag{3.53}$$

Suppose the considered open orbit is along k_y direction. Noticing that:

$$\bar{v}_x = \bar{v}_y = 0, \quad \textit{closed orbit}, \tag{3.54a}$$

$$\bar{v}_x \neq 0,\ \bar{v}_y = 0, \quad \textit{open orbit}, \tag{3.54b}$$

we can solve the coupling equations (3.52) by means of the equation of motion and equation (3.54). The solution for closed orbits is

$$C_x = \frac{\hbar k_y}{m^*}\alpha_0 + b_2^x\alpha_0^2 + ..., \tag{3.55a}$$

$$C_y = -\frac{\hbar k_x}{m^*}\alpha_0 + b_2^y\alpha_0^2 + ..., \tag{3.55b}$$

$$C_z = b_0^z + ..., \tag{3.55c}$$

and for open orbits in k_y direction

$$C_x = \bar{v}_x + b_1^x\alpha_0 + ..., \tag{3.56a}$$

$$C_y = -\frac{\hbar}{m^*}(k_y - \bar{k}_y)\alpha_0 + b_2^y\alpha_0^2 + ..., \tag{3.56b}$$

$$C_z = b_0^z + ... \tag{3.56c}$$

The magnetoconductivity tensors in uncompensated metals corresponding to closed and open orbits, obtained from equations (3.55) and (3.56) are (Abrikosov, 1972; Smith *et al.*, 1967)

$$\overleftrightarrow{\sigma}^{cl} = \begin{pmatrix} \alpha_0^2 a_{xx} & \alpha_0 a_{xy} & \alpha_0 a_{xz} \\ \alpha_0 a_{yx} & \alpha_0^2 a_{yy} & \alpha_0 a_{yz} \\ \alpha_0 a_{zx} & \alpha_0 a_{zy} & a_{zz} \end{pmatrix} \tag{3.57}$$

and

$$\overleftrightarrow{\sigma}^{op} = \begin{pmatrix} a_{xx} & \alpha_0 a_{xy} & a_{xz} \\ \alpha_0 a_{yx} & \alpha_0^2 a_{yy} & \alpha_0 a_{yz} \\ a_{zx} & \alpha_0 a_{zy} & a_{zz} \end{pmatrix}, \tag{3.58}$$

here $a_{ij}(i,j=x,y,z)$ are constants. Taking the inverse of equation (3.57) and (3.58), we can obtain magnetoresistivity tensors

$$\overleftrightarrow{\rho}^{cl} = \begin{pmatrix} e_{xx} & \alpha_0^{-1} e_{xy} & e_{xz} \\ \alpha_0^{-1} e_{yx} & e_{yy} & e_{yz} \\ e_{zx} & e_{zy} & e_{zz} \end{pmatrix} \tag{3.59}$$

and

$$\overleftrightarrow{\rho}^{op} = \begin{pmatrix} e_{xx} & \alpha_0^{-1} e_{xy} & e_{xz} \\ \alpha_0^{-1} e_{yx} & \alpha_0^{-2} e_{yy} & \alpha_0^{-1} e_{yz} \\ e_{zx} & \alpha_0^{-1} a_{zy} & e_{zz} \end{pmatrix}, \tag{3.60}$$

where $e_{ij}(i,j=x,y,z)$ are constants.

Lifshitz' theory predicts that for uncompensated metals if the magnetic field tilts to some direction (say z -direction) and only closed orbits occur, the magnetoresistivity tensor shows only Hall effect and ρ_{ii} will approach to some constants at large fields which are independent of B (diagonal elements). Hence, ρ_{ii} will saturate. If, on the other hand, there is an open orbit in a certain direction (say, in k_y -direction), ρ_{ii}(ρ_{yy}) will increase as B^2 without limit. This prediction has been proved by many experimental observations since then.

In Lifshitz's theory, the effect of the magnetic field is introduced as a perturba-

tion in electronic structure and the only assumption made about the relaxation time is that it is independent of the magnetic field. Generally speaking, such treatment has no limitation for the theory to apply to any shape of the Fermi surface which, in fact, determines the type of electron orbits in momentum space in the presence of the magnetic field. In order to get better understanding about the galvanomagnetic property of copper, it is necessary to know the full details of the geometry of copper Fermi surface.

3.4 The Fermi Surface and Electron Orbits in Copper

3.4.1 Schrödinger's Equation and Energy Bands

The Fermi surface of a crystal is an extremely important concept in solid state physics because its topology determines the linear response of the material to an electrical, magnetic and thermal field. In theory, the shape of the Fermi surface is a direct result of electronic energy band structure mapping into the momentum space, which can be obtained under single-particle approximation by solving Schrödinger's equation

$$-\frac{\hbar^2}{2m}\nabla^2\psi(\vec{r}) + V(\vec{r})\psi(\vec{r}) = \varepsilon\psi(\vec{r}), \tag{3.61}$$

where $\psi(\vec{r})$ is electronic wave function and $V(\vec{r})$ is the potential that the electron is exposed to. Since $V(\vec{r})$ is a periodic function of the Bravais lattice of the crystal, such feature requires the solution to equation (3.61) $\psi(\vec{r})$ to take the form

$$\psi(\vec{r}) = exp(-i\vec{k}\cdot\vec{r})u_{\vec{k}}(\vec{r}), \tag{3.62}$$

where $u_{\vec{k}}(\vec{r})$ is also a periodic function with the same periodicity as $V(\vec{r})$. Equation (3.62) is more commonly called Bloch's theorem. It can be shown that eigenvalue ε of equation (3.61) is a function of electron wave vector $\vec{k}$ and forms a set called electronic energy bands, labeled by $\varepsilon_\alpha(\vec{k})$ ($\alpha = 1,2,3....$).

Let ε_c be a constant and

$$\varepsilon(\vec{k}) = \varepsilon_c. \tag{3.63}$$

The pictorial representation of equation (3.63) in k-space gives constant energy surface. If this constant ε_c is equal to Fermi energy μ defined in equation (3.1), thus

$$\varepsilon(\vec{k}) = \mu, \tag{3.64}$$

the constant energy surface in reciprocal space described by equation (3.64) is called the Fermi surface.

It is clear that the existence of a Fermi surface in a crystal is a direct consequence of the Pauli exclusion principle and such surface marks the boundary in reciprocal space between occupied and unoccupied states.

In real crystals, band structure calculations to probe the Fermi surface is a very

complicated task because of the difficulties to determine a reliable expression for potential $V(\vec{r})$ and to find the solution to Schrödinger's equation. Several approximated approaches have been developed such as the tight-binding method, Wigner-Seitz and cellular method, orthogonalized plane wave (OPW) and augmented plane wave(APW), Green's function and pseudopotentials. The development and application of these approaches can be found in other references for example (Crachnell & Wong, 1973; Cracknell, 1971)

3.4.2 Topology of the Fermi Surface of Copper

In free-electron approximation, the solution to equation (3.61) is simplified as

$$\psi_{\vec{k}}(\vec{r}) = exp\left[-i(\vec{k}+\vec{G}_n)\cdot\vec{r}\right] \tag{3.65}$$

and energy bands

$$\varepsilon(\vec{k}) = \frac{\hbar^2}{2m}|\vec{k}+\vec{G}_n|^2, \tag{3.66}$$

where $\vec{G}_n$ is a vector of the reciprocal lattice which can be taken as zero in extended zone scheme. Equation (3.66) graphically describes a set of constant energy surfaces in reciprocal space. The Fermi surface determined by letting $\varepsilon(\vec{k}) = \varepsilon_F$ is a sphere. The value of Fermi energy ε_F depends on the density of conduction electrons n_e in the crystal and is defined by the following equation

$$\varepsilon(\vec{k}) = \frac{\hbar^2}{2m}(3\pi^2 n_e)^{2/3}. \tag{3.67}$$

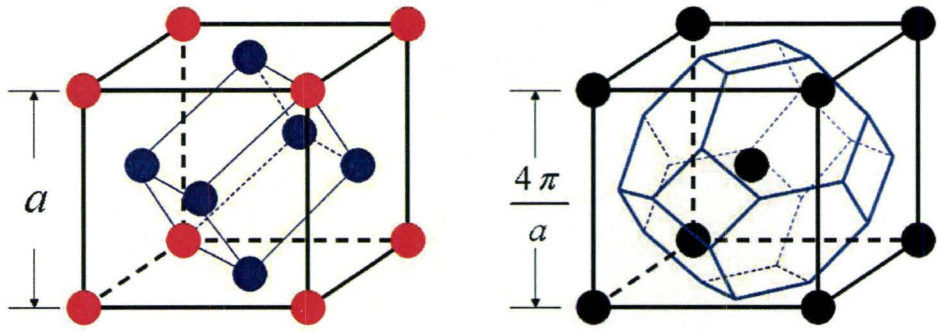

(a) A conventional unit cell with lattice constant a and a primitive unit cell of Bravais lattice

(b) The first Brillouin zone,a truncated octahedron, in reciprocal space for *FCC* crystals

Figure 3.3: Space lattice and Brillouin zone for *FCC* crystals

Copper has *FCC* crystal structure and its Bravais lattice is shown in Figure 3.3(a). The lattice constant of copper is $a = 3.61\mathring{A}$. Figure 3.3(b) indicates the reciprocal lattice of copper having a *BCC* structure and its first Brillouin zone-a truncated octahedron. The length R from the center of the truncated octahedron to each center of the eight hexagonal faces is

$$R = \frac{\sqrt{3}}{4}\frac{4\pi}{a} \approx 0.433\frac{4\pi}{a}. \tag{3.68}$$

Copper electronic configuration is $1s^2 2s^2 2p^6 3s^2 3p^6 3d^{10} 4s^1$ which is characteristic of a full $3d$ band with one electron per atom in the conduction band. Consequently, the Fermi surface or the radius of Fermi sphere k_F in the reciprocal space can be obtained by combining equation (3.67) with (3.68) which gives

$$k_F = (3\pi^2 n_e)^{1/3} = (\frac{3}{16\pi})^{1/3}\frac{4\pi}{a} \approx 0.391\frac{4\pi}{a}. \tag{3.69}$$

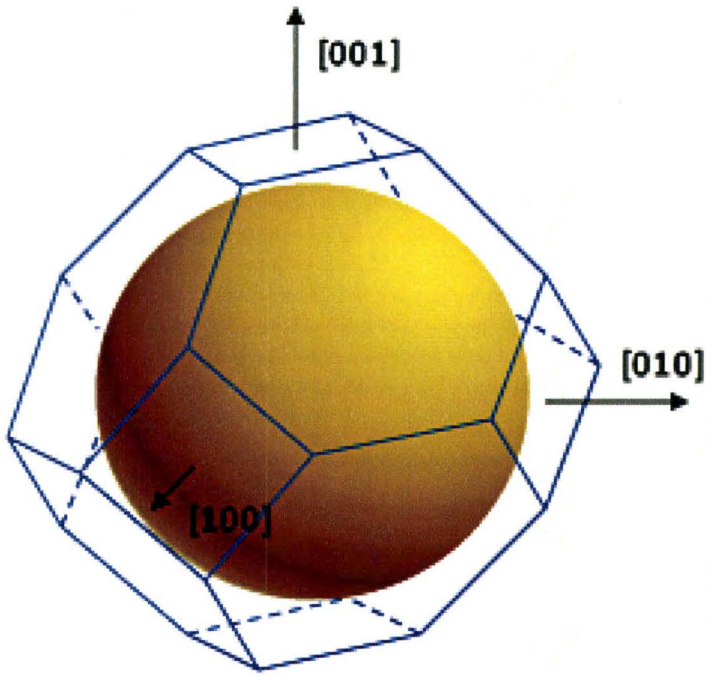

Figure 3.4: Schematic illustration of the spherical copper Fermi surface in free-electron model which is entirely contained within the first Brillouin zone and untouched zone boundary

Comparing equation (3.69) with equation (3.68) indicates that copper Fermi surface in the free-electron approximation is completely contained within the first Brillouin zone without touching zone boundary. Figure 3.4 shows the spherical Fermi surface of copper within the first Brillouin zone in free-electron model.

However, many experimental results and more precise calculations all indicate that the Fermi surface of copper single crystal is distorted from a sphere and touches the Brillouin zone boundary at each center of eight hexagonal faces or $\{111\}$ planes (detailed review on the historical development of copper Fermi surface can be found

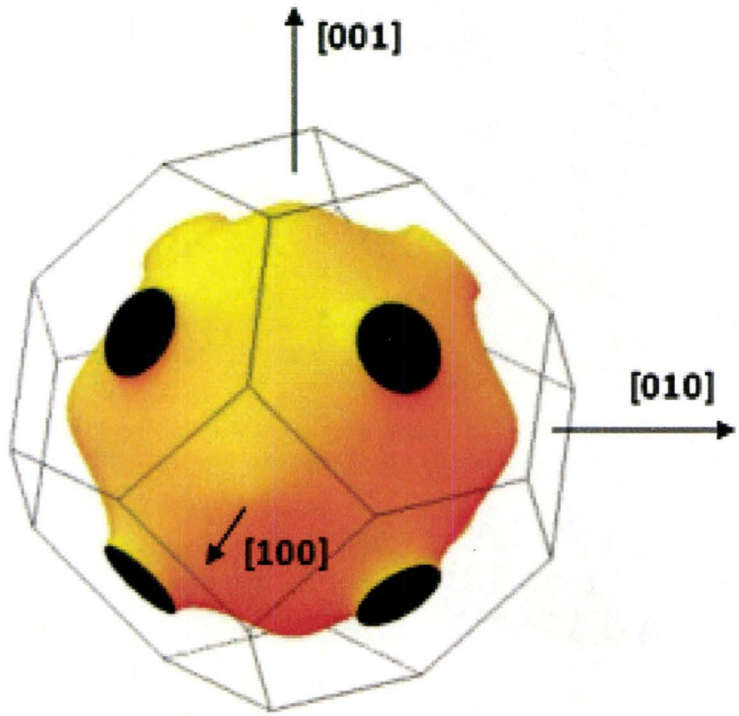

Figure 3.5: 3D plotting of energy band structure for copper single crystal from tight-binding calculation Choy (2007)

in the reference (Crachnell & Wong, 1973; Cracknell, 1971)). Today the shape of Fermi surface of copper is well known because of substantial efforts both in theory and experiment in last few decades. Figure 3.5 is a 3D plotting of energy band structure calculation to illustrate the Fermi surface of a real copper single crystal.

Figure 3.6: Open Fermi surface of copper in repeated zone scheme, from a model by Shoenberg (1960)

3.4.3 Electron Orbits in the Reciprocal Space of Copper

The topology of copper Fermi surface can be precisely constructed through more refined experiments and more accurate calculations both of which are in a very good agreement, so that the contour of copper Fermi surface can be regarded as known with good accuracy. If we use repeated zone scheme to image the Fermi surface of copper, the space will be filled with the Brillouin zones and the Fermi surface form an open surface multiply connected by necks along $< 111 >$ directions. Figure 3.6 shows schematically the open Fermi surface of copper in repeated zone scheme (Shoenberg, 1960). As we already discussed it, such features of copper Fermi sur-

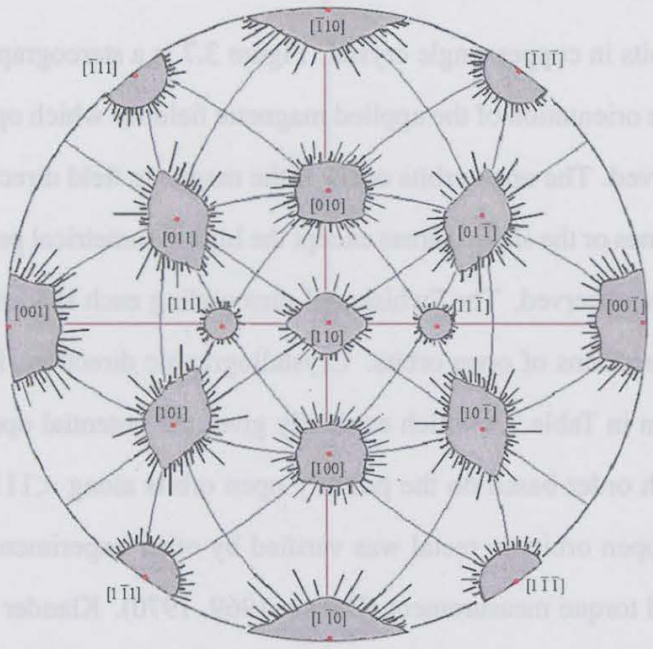

Figure 3.7: Stereographic representation for electron orbits in copper. The open orbits occur as the magnetic field $\vec{B}$ is oriented in the direction which is on the lines or in the shaded areas except the higher symmetrical points (red points). Redrawn from the reference (Klauder *et al.*, 1966)

face can generate a variety of electron orbits as the orientation of the magnetic field is changed and will, to a large degree, determine the galvanomagnetic properties of copper single crystal.

In the presence of the magnetic field $\vec{B}$, electron orbits are defined by the sections of the Fermi surface by the planes normal to $\vec{B}$. Any electron orbit can be identified as long as the orientation of the magnetic field is known. However, technically it is an arduous work because of the complexity of the problem especially for higher order open orbits. Klauder *et al*. (Klauder *et al.*, 1966) collected a vast of experimental data by measuring magnetoresistance and Hall effect to determine

the electron orbits in copper single crystal. Figure 3.7 is a stereographic projection representing the orientation of the applied magnetic field for which open and closed orbits are observed. The open orbits occur if the magnetic field direction coincides with the solid lines or the shaded areas except the high symmetrical points for which closed orbits are observed. The "whiskers" surrounding each shaded area are also the pertinent directions of open orbits. Crystallographic directions for some open orbits are shown in Table 3.1 which explicitly gives the potential open orbit directions up to sixth order based on the primary open orbits along <111> directions. Present of the open orbits in metal was verified by other experimental techniques such as induced torque measurement (Datars, 1969, 1970). Klauder *et al.* pointed out an interesting fact that the indices for the direction of higher order open orbits are possibly the simple combination of the ones for primary directions in various arrangements. If true, such a rule can significantly reduce the experimental work to find open orbits in copper single crystal.

Table 3.1: The observed directions of potential open orbits in copper (Retabulated from the reference (Klauder *et al.*, 1966))

Order	Family of possible open orbit directions
1	<111>
2	<100>, <110>
3	<113>, <133>
4	<012>, <112>, <122>
5	<115>, <135>, <155>, <335>, <355>
6	<013>, <023>, <123>, <223> , <233>

The experimental observation of open orbits which correspond to high peaks of magnetoresistance measurement is limited by conduction electron scattering, although there might be many open orbits which in principle should be observed in

magnetoresistance measurement. If the sample is not pure enough so that electron mean free path is very short, which means electrons can not travel a substantial distance without being scattered, the open orbits would not be revealed in the magnetoresistance measurements.

Chapter 4

Effective Medium Theory

In chapter 3, Lifshitz's theory was introduced, which describes the galvanomagnetic phenomena in metals. Based on the semiclassical theory of electron conduction in the presence of the electrical and magnetic fields, magnetoconductivity tensor in large field approximation is formulated and shows a strong dependence on the value of the path integral along electron trajectories. However, one important point worthy to mention here is the applicability of the theory which is usually limited to pure crystals because of the strict condition in large field approximation given by equation (3.37). Furthermore, to successfully perform the integral (equation 3.48) one needs the detailed information on the electron orbits, which makes it a quite complicated task.

Unfortunately, it turns out a difficult task that theoretically to calculate magnetoconductivity tensor for the samples with high density of defects through equation

(3.48) and based on this to develop understanding about behavior of magnetoresistivity of deformed samples. A challenge is to describe the details of the crystal structure containing dislocations, in k-space. In addition, the Fermi surface for deformed samples must be distorted since dislocations introduced by deformation induce some additional potential field in the crystal and little is known about this distortion both in theory and experiment. In other words, it is impossible to carry out the integrals in equation (3.48) for crystals containing dislocations in the way proposed in Lifshits' theory. Consequently, to describe magnetoresistivity of samples containing dislocations, a new theory has to be developed.

The effective medium theory has been successfully used to describe the macroscopic properties of spatially inhomogeneous materials and composites, to which our deformed samples can be categorized. We will apply this theory to undertake theoretical investigation of the galvanomagnetic properties of the deformed samples and to gain better insight into the fundamental material properties responsible for the observed effect . First, we describe a historical development of effective medium theory.

4.1 Introduction and Literature Review

The effective medium theory is a powerful method to evaluate transport properties of macroscopically inhomogeneous (disordered) media consisting of the spatial variation of some physical properties such as the conductivity, dielectric function or elastic modulus. The central concept of the effective medium theory is based on

Maxwell-Garnett (MG) equation, first derived by Maxwell and Garnett, to explain and predict the permittivity of glasses having spherical particles and the permittivity of films of silver, gold, potassium and sodium (Maxwell-Garnett, 1904). Maxwell-Garnett model is viewed as a traditional frame work of the effective medium theory by some researchers in this area (Choy, 1999). A significant improvement to the effective medium theory was made by Bruggeman (Bruggeman, 1935). Later, the topic was quantitatively studied in a different context by Landauer who termed it the effective medium theory (Landauer, 1952).

The main contribution of Bruggeman to the development of effective theory was following: Consider a random medium having two components which are denoted by A and B, and characterized by different scalar conductivities σ_A and σ_B, as schematically illustrated in Figure 4.1. Since it is impossible to obtain the conductivity for such a random and infinite system through the exact calculation, approximation was made in Bruggeman's approach by assuming that one of grains (say a grain of component A), instead of being embedded in its real random environment, is immersed in a homogeneous medium characterized by a yet undetermined effective conductivity σ_{eff}. Figure 4.2 illustrates this concept by showing a single inclusion embedded in a homogeneous medium with uniform conductivity σ_{eff} .

In the presence of an electrical field, the single inclusion in the homogeneous medium will be polarized. Suppose that the applied electrical field far away from the inclusion equals to $\vec{E}_0$. Its dipole moment $\vec{p}_A$, under the approximation of

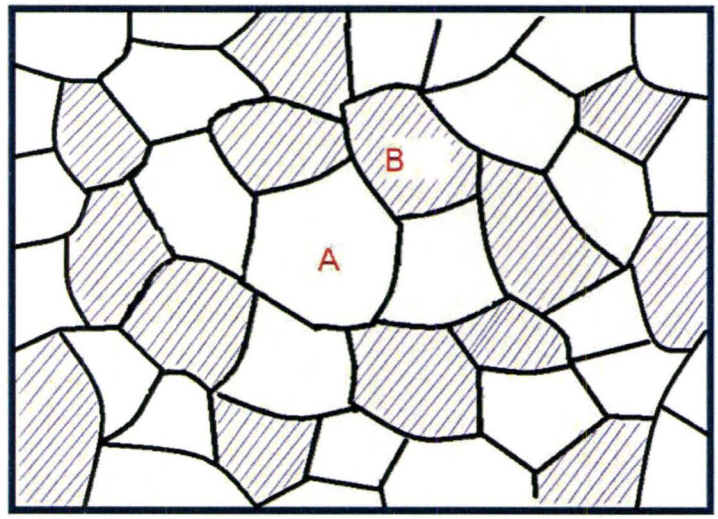

Figure 4.1: Schematic illustration of a random composite.

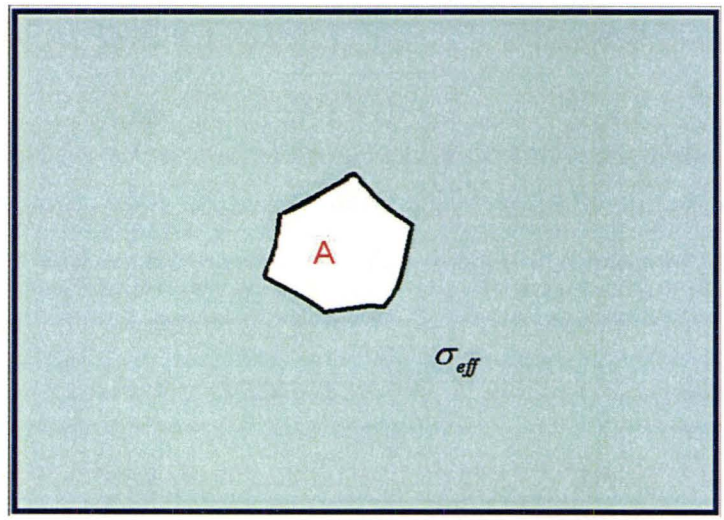

Figure 4.2: A single grain of component *A* embedded in a homogeneous medium.

spherical shape inclusion, can be written as

$$\vec{p}_A = \frac{3}{4\pi} V \frac{\sigma_A - \sigma_{eff}}{\sigma_A + 2\sigma_{eff}} \vec{E}_0, \tag{4.1}$$

where V is the volume of the region under consideration. The polarization $\vec{P}_A$ is

$$\vec{P}_A = \frac{3}{4\pi}\frac{\sigma_A - \sigma_{eff}}{\sigma_A + 2\sigma_{eff}}\vec{E}_0. \tag{4.2}$$

The resulting field $\vec{E}_A$ at the center of the spherical inclusion due to this polarization is parallel to $\vec{P}_A$, and the magnitude, after space integral, has

$$\vec{E}_A = \frac{\sigma_A - \sigma_{eff}}{\sigma_A + 2\sigma_{eff}}\vec{E}_0. \tag{4.3}$$

The dipole polarization field $\vec{E}_A$ is different from the applied field $\vec{E}_0$. Repeating the same calculation with a grain of component B results in another dipole polarization field which is

$$\vec{E}_B = \frac{\sigma_B - \sigma_{eff}}{\sigma_B + 2\sigma_{eff}}\vec{E}_0. \tag{4.4}$$

Bruggeman's effective theory requires that the total volume average dipole polarization field summed over the two types of inclusions must vanish. That is

$$f_A\frac{\sigma_A - \sigma_{eff}}{\sigma_A + 2\sigma_{eff}} + f_B\frac{\sigma_B - \sigma_{eff}}{\sigma_B + 2\sigma_{eff}} = 0, \tag{4.5}$$

where f_A and f_B are the volume fraction of component A and B respectively with the condition

$$f_A + f_B = 1. \tag{4.6}$$

Equation (4.5) can be easily generalized to the composites having any number

of components such that

$$\sum_{\alpha} f_{\alpha} \frac{\sigma_{\alpha} - \sigma_{eff}}{\sigma_{\alpha} + 2\sigma_{eff}} = 0, \tag{4.7a}$$

$$\sum_{\alpha} f_{\alpha} = 1, \tag{4.7b}$$

where σ_{α} is the conductivity tensor of component α .

Over the years, Bruggeman's effective theory has further been developed. Detailed review of the early developments of the effective medium theory can be found in references (Landauer, 1977; Milton, 1985), the recent progress is described in the work of Stroud (Stroud, 1998).

Here we focus our attentions to the galvanomagnetic properties of inhomogeneous media and will discuss the applications of the effective medium theory in this area. As mentioned in Chapter 1, Kapitza in 1929 showed that the resistance of many metals in the form of polycrystalline wires varied linearly with the transverse magnetic field (Kapitza, 1929), which is known as the Kapitza's linear law. This interesting phenomenon has been remaining a mystery for many years, since the Lifshitz' theory (Lifshitz *et al.*, 1957) predicted that magnetoresistance for single crystals is dependent on the geometry of electron orbits in momentum space and it should saturate or show a quadratic behavior at high fields, which has been discussed in Chapter 3.3.2. In order to understand the linear dependence of the resistance of polycrystalline metals in high magnetic fields, in late 50s, several authors (Ziman, 1958; Lifshitz & Peschanski, 1959; Lüthi, 1960; Alekseyevsky & Gaidukov, 1959) theoretically attacked this problem starting with the conjecture

that the polycrystalline magnetoresistance could be obtained by spatially averaging the resistivity or conductivity of crystallites over all possible orientations of the crystal axes with respect to the magnetic field. Herring (Herring, 1960) was the first to give a full description of the effect of random inhomogeneities on galvanomagnetic properties of materials without any arbitrary assumptions. In Herring's model, a modestly but continuously variable fluctuation in electrical properties was assumed, which is unlike the traditional treatment of the effective conductivity of a medium consisting of two or more distinct phases and separated by sharp boundaries. Perturbation theory was applied by taking the first order fluctuation of the Fourier expansion in electrical conductivity. The explicit forms of the effective conductivity tensor and the expressions at low and high field approximation were obtained. Herring showed that inhomogeneity can give rise to a magnetoresistance which does not saturate with increasing magnetic field as it would be expected for homogeneous free-electron like media. In his work, Herring also gave a very brief discussion about the possible application in the crystals with dislocations. It is clear that the restriction on the applicability of Herring's model is that the fluctuations in electrical properties in media should be weak, but this is often violated in real crystals. Stachowiak (Stachowiak, 1964, 1967a,b, 1970, 1973) published a series of papers on the galvanomagnetic properties of inhomogeneous media to extend Herring's model to the case where the small fluctuation in the electrical properties is not satisfied. His work was based on the effective theory with two assumptions: each crystallite has a spherical shape and behaves like being embedded in a homogeneous medium with an effective conductivity. By solving the boundary problem for the crystallite with the open orbits, general equations for effective conductivity tensor of polycrystalline mixtures were obtained. His results showed

that in the presence of open orbits and extended orbits, magnetoresistance tends to be linear as the magnetic fields increase. Stroud and Pan (Stroud, 1975; Stroud & Pan, 1976, 1978, 1979) generalized the effective medium approach to treat inhomogeneous media with crystallites of arbitrary shape, size and orientation whose conductivity tensors are of arbitrary symmetry. By applying the method of Green's function to the boundary problem for the crystallite with open orbits embedded in the effective medium, Stroud and Pan developed a general and strict formulation for galvanomagnetic properties of inhomogeneous media. We will provide a detailed discussion of Stroud and Pan's approach in the next section.

4.2 Method of Green's Functions

4.2.1 The Effective Conductivity

Here we introduce Huberman and Overhauser's (Huberman & Overhauser, 1981) method to formulate the effective conductivity tensor. Consider an inhomogeneous medium consisting of the randomly distributed crystallites or grains of the pure components, and assume that the linear dimensions of the typical crystallite are large enough comparing to the mean free path characteristic of a current carrier and fairly small to the dimension of the sample itself. In such inhomogeneous medium, the current density $\vec{j}(\vec{r})$, electrical field $\vec{E}(\vec{r})$ and the conductivity tensor $\overleftrightarrow{\sigma}(\vec{r})$ of the pure component at any position $\vec{r}$ are related by the differential form of Ohm's

law

$$\vec{j}(\vec{r}) = \overleftrightarrow{\sigma}(\vec{r}) \cdot \vec{E}(\vec{r}). \tag{4.8}$$

Suppose that the medium, having a volume of V and bounded by a surface S , is composed of m components and let v_α denote the volume occupied by the crystallites of component α ; f_α the volume fraction and $\overleftrightarrow{\sigma}_\alpha(\vec{r})$ the conductivity tensor at the point $\vec{r}$ for this component. Since the crystallites fill the whole space, it is clear we will have

$$\sum_{\alpha=1}^{m} \frac{v_\alpha}{V} = \sum_{\alpha=1}^{m} f_\alpha = 1 \tag{4.9}$$

In order to calculate the conductivity for such a random medium, we will be concerned with the ensemble average of vector or scalar fields taken over a certain region in space. For a given function $g(\vec{r})$ which is integrable over volume V, the ensemble average of function $g(\vec{r})$ over volume V is

$$< g(\vec{r}) >= \frac{1}{V} \int_V g(\vec{r}) d\vec{r}. \tag{4.10}$$

The average is independent of $\vec{r}$ because of a random medium.

The macroscopically measurable electrical properties of the conductor are determined by an effective conductivity $\overleftrightarrow{\sigma}_{eff}$ and it may be defined as

$$< \vec{j}(\vec{r}) >= \overleftrightarrow{\sigma}_{eff} \cdot < \vec{E}(\vec{r}) >, \tag{4.11}$$

where $< \vec{j}(\vec{r}) >$ and $< \vec{E}(\vec{r}) >$ are the spatial average of the current density and the electrical field respectively. It is clear that $\overleftrightarrow{\sigma}_{eff}$ is independent of the sample

geometry or boundary condition.

Suppose a uniform external electrical field $\vec{E}_{ext}$ is applied to the sample. In principle, the effective conductivity can be obtained from equation (4.11), provided that the average current density $< \vec{j}(\vec{r}) >$ and average electrical field $< \vec{E}(\vec{r}) >$ are calculated. Unfortunately, it is impossible to get the solution exactly because of the nature of random inhomogeneity. In order to compute the effective conductivity of such a random medium, we may refer to the mean field approximations. We assume that each crystallite in the sample has an ellipsoidal shape and, instead of being immersed in the actual environment surrounded by the crystallites of other components, it is embedded in a uniform infinite medium of conductivity tensor $\overleftrightarrow{\sigma}_m$. Within the above assumptions, for a single crystallite embedded in such uniform infinite medium, the electrical field inside the crystallite is proportional to the external electrical field and it can be written as

$$\vec{E}_{\alpha}^{in}(\vec{r}) = \overleftrightarrow{\eta}_{\alpha}\left[\overleftrightarrow{\sigma}_m, \overleftrightarrow{\sigma}_{\alpha}(\vec{r})\right] \cdot \vec{E}_{ext}, \quad \alpha = 1,2,...m. \tag{4.12}$$

where $\overleftrightarrow{\eta}_{\alpha}\left[\overleftrightarrow{\sigma}_m, \overleftrightarrow{\sigma}_{\alpha}(\vec{r})\right]$ is a tensor depending on the conductivities of the medium $\overleftrightarrow{\sigma}_m$ and conductivities of inhomogeneity $\overleftrightarrow{\sigma}_{\alpha}(\vec{r})$. The current density inside the crystallite will be

$$\begin{aligned} \vec{j}_{\alpha}^{in}(\vec{r}) &= \overleftrightarrow{\sigma}_{\alpha}(\vec{r}) \cdot \vec{E}_{\alpha}^{in}(\vec{r}) \\ &= \overleftrightarrow{\sigma}_{\alpha}(\vec{r}) \cdot \overleftrightarrow{\eta}_{\alpha}\left[\overleftrightarrow{\sigma}_m, \overleftrightarrow{\sigma}_{\alpha}(\vec{r})\right] \cdot \vec{E}_{ext}, \quad \alpha = 1,2,...m. \end{aligned} \tag{4.13}$$

For simplicity of mathematical formalism, we will drop off argument $\vec{r}$ in the following equations.

If the currents and fields generated by the crystallites do not overlap with each other, the averages of total current density and electrical field will be

$$<\vec{J}>=<\sum_{\alpha=1}^{m}\vec{j}_{\alpha}^{in}>=<\sum_{\alpha=1}^{m}\overleftrightarrow{\sigma}_{\alpha}\cdot\overleftrightarrow{\eta}_{\alpha}>\cdot\vec{E}_{ext}, \tag{4.14}$$

$$<\vec{E}>=<\sum_{\alpha=1}^{m}\vec{E}_{\alpha}^{in}>=<\sum_{\alpha=1}^{m}\overleftrightarrow{\eta}_{\alpha}>\cdot\vec{E}_{ext}, \tag{4.15}$$

Combining equations (4.14) and (4.15) with equation (4.11), the effective conductivity may be written as

$$\overleftrightarrow{\sigma}_{eff}=<\sum_{\alpha=1}^{m}\overleftrightarrow{\sigma}_{\alpha}\cdot\overleftrightarrow{\eta}_{\alpha}>\cdot<\sum_{\alpha=1}^{m}\overleftrightarrow{\eta}_{\alpha}>^{-1}. \tag{4.16}$$

Replacing $\overleftrightarrow{\sigma}_{\alpha}=\delta\overleftrightarrow{\sigma}_{\alpha}+\overleftrightarrow{\sigma}_{m}$ in equation (4.16) and noticing that $\overleftrightarrow{\sigma}_{m}$ is a constant tensor, leads to the more popular expression for the effective conductivity

$$\begin{aligned}\overleftrightarrow{\sigma}_{eff} &= <\sum_{\alpha=1}^{m}(\delta\overleftrightarrow{\sigma}_{\alpha}+\overleftrightarrow{\sigma}_{m})\cdot\overleftrightarrow{\eta}_{\alpha}>\cdot<\sum_{\alpha=1}^{m}\overleftrightarrow{\eta}_{\alpha}>^{-1}\\ &= \overleftrightarrow{\sigma}_{m}+<\sum_{\alpha=1}^{m}\delta\overleftrightarrow{\sigma}_{\alpha}\cdot\overleftrightarrow{\eta}_{\alpha}>\cdot<\sum_{\alpha=1}^{m}\overleftrightarrow{\eta}_{\alpha}>^{-1}.\end{aligned} \tag{4.17}$$

The choice of $\overleftrightarrow{\sigma}_{m}$ is not unique and depends on the problems under consideration. The benefit of equation (4.17) is that the effective conductivity can be computed in a self-consistent way. The procedure is following: select an initial $\overleftrightarrow{\sigma}_{m}$; calculate the effective conductivity tensor $\overleftrightarrow{\sigma}_{eff}$ using equation (4.17); let this calculated $\overleftrightarrow{\sigma}_{eff}$ equal to a new $\overleftrightarrow{\sigma}_{m}$ and repeat the calculation till a self-consistent

solution is obtained.

We will model the behavior of magnetoresistance for dislocated samples through iterations by applying the above equation.

4.2.2 Formalism for Green's Function Approach

The discussion in this section is based on the approach proposed by Stroud and Pan. It is known that the effective conductivity can be solved through a self-consistent method. However, so far we have not discussed the approach to calculate tensor $\overleftrightarrow{\eta}_\alpha\left[\overleftrightarrow{\sigma}_m, \overleftrightarrow{\sigma}_\alpha(\vec{r})\right]$, which is an important step to successfully apply the self-consistent method through equation (4.17). In order to achieve this goal, let us review our problem again. A crystallite of volume v'; bounded by surface s' and characterized by a spatial varying conductivity tensor $\overleftrightarrow{\sigma}'_\alpha$ is embedded in a uniform infinite medium of conductivity tensor $\overleftrightarrow{\sigma}_m$. If a uniform electrical field $\vec{E}_{ext}$ is applied, the problem reduces to calculate the magnitude of the electrical field inside the crystallite. This is an electrostatic problem which can be solved by using the basic electrostatic equations

$$\vec{\nabla}\cdot\vec{j}(\vec{r}) = 0, \tag{4.18a}$$

$$\vec{\nabla}\times\vec{E}(\vec{r}) = 0. \tag{4.18b}$$

Introducing scalar potential $\Phi(\vec{r})$ which is

$$\vec{E}(\vec{r}) = -\vec{\nabla}\Phi(\vec{r}) \tag{4.19}$$

and combining the above equations with Ohm's law, we can arrive to an equation for the electrostatic potential

$$\vec{\nabla} \cdot \overleftrightarrow{\sigma}(\vec{r}) \cdot \vec{\nabla}\Phi(\vec{r}) = 0, \quad \vec{r} \in V \tag{4.20}$$

where V is the volume of the uniform medium.

Letting

$$\overleftrightarrow{\sigma}(\vec{r}) = \overleftrightarrow{\sigma}_m + \delta\overleftrightarrow{\sigma}(\vec{r}), \tag{4.21}$$

substituting this relation into equation (4.20) and noticing the boundary condition for the system which require that on the surface S of the medium, the electrostatic potential is $\Phi_0(\vec{r}) = -\vec{E}_{ext} \cdot \vec{r}$, we can establish differential equations for the boundary problem to find the electrical field inside the crystallite. The equations read

$$\vec{\nabla} \cdot \overleftrightarrow{\sigma}_m \cdot \vec{\nabla}\Phi(\vec{r}) = -\vec{\nabla} \cdot \delta\overleftrightarrow{\sigma}(\vec{r}) \cdot \vec{\nabla}\Phi(\vec{r}), \ \vec{r} \in V, \tag{4.22a}$$

$$\Phi(\vec{r}) = \Phi_0(\vec{r}) = -\vec{E}_{ext} \cdot \vec{r}, \ \ \vec{r}\ on\ S. \tag{4.22b}$$

It is clear that the electrical field inside the crystallite can be obtained through equation (4.19) after boundary value problem has been solved.

It is well known that the method of Green's functions is a useful tool to boundary problems. Stroud and Pan did the pioneering work to apply such approach to equations (4.22) of the boundary problem. With the introduction of the Green's

function $G(\vec{r},\vec{r}')$ defined by

$$\vec{\nabla}\cdot\overleftrightarrow{\sigma}_m\cdot\vec{\nabla}G(\vec{r},\vec{r}') = -\delta(\vec{r}-\vec{r}'),\ \vec{r}\in V, \tag{4.23a}$$

$$G(\vec{r},\vec{r}') = 0,\ \vec{r}' \text{ on } S. \tag{4.23b}$$

The solution to equation (4.22) will be

$$\begin{aligned}\Phi(\vec{r}) &= \Phi_0(\vec{r}) + \int_V G(\vec{r},\vec{r}')\vec{\nabla}'\cdot\delta\overleftrightarrow{\sigma}(\vec{r}')\cdot\vec{\nabla}'\Phi(\vec{r}')d\vec{r}' \\ &= \Phi_0(\vec{r}) - \int_V \left\{\vec{\nabla}'G(\vec{r},\vec{r}')\right\}\cdot\delta\overleftrightarrow{\sigma}(\vec{r}')\cdot\vec{\nabla}'\Phi(\vec{r}')d\vec{r}'. \end{aligned}\tag{4.24}$$

Appendix A (A.1) provides formal derivation of above equation.

Taking the negative gradient from the both sides of the above equation with respect to $\vec{r}$ yields the electrical field

$$\begin{aligned}\vec{E}(\vec{r}) &= -\vec{\nabla}\Phi(\vec{r}) \\ &= \vec{E}_{ext} + \int_V \left\{\vec{\nabla}\vec{\nabla}'G(\vec{r},\vec{r}')\right\}\cdot\delta\overleftrightarrow{\sigma}(\vec{r}')\cdot\vec{E}(\vec{r}')d\vec{r}'. \end{aligned}\tag{4.25}$$

Let

$$\overleftrightarrow{g}(\vec{r},\vec{r}') = \vec{\nabla}\vec{\nabla}'G(\vec{r},\vec{r}'). \tag{4.26}$$

Its component are

$$\overleftrightarrow{g}_{ij}(\vec{r},\vec{r}') = \frac{\partial}{\partial r_i}\frac{\partial}{\partial r_j}G(\vec{r},\vec{r}'). \tag{4.27}$$

Here again we have used our conventional notations

$$i,j,k \equiv 1,2,3 \quad and \quad r_1 = x,\ r_2 = y,\ r_3 = z. \tag{4.28}$$

Substituting equation (4.26) into equation (4.25) yields

$$\vec{E}(\vec{r}) = \vec{E}_{ext} + \int_V \overleftrightarrow{g}(\vec{r},\vec{r}') \cdot \delta\overleftrightarrow{\sigma}(\vec{r}') \cdot \vec{E}(\vec{r}')d\vec{r}'. \tag{4.29}$$

Equation (4.29) represents a feasible way to find the electrical field and further to obtain the effective conductivity tensor for the inhomogeneous materials consisting of crystallites of any arbitrary shape and of the conductivity tensors of arbitrary symmetry, but the formidability of applications is pretty daunting because of the complexity of equation (4.29). One have to provide more approximations, to compute the electrical field inside the crystallite and then to obtain the coefficient in equation (4.12). If the crystallites are composed of pure components, this means that the spatially varying conductivity tensor $\overleftrightarrow{\sigma}'_\alpha(\vec{r})$ can be replaced by a different constant conductivity tensor $\overleftrightarrow{\sigma}'_\alpha$ for each grain; and if the crystallites have the ellipsoidal shapes, it can be shown that, inside the crystallites, the electrical field $\vec{E}^{in}$ and current density $\vec{j}^{in}$ are both uniform (Kunin & Sosnina, 1971; Landau *et al.*, 1984; Moon, 1986). Noticing that

$$\delta\overleftrightarrow{\sigma}(\vec{r}') = \delta\overleftrightarrow{\sigma} = \overleftrightarrow{\sigma}' - \overleftrightarrow{\sigma}_m,\ \vec{r}' \in v'\ (inside\ the\ crystallite), \tag{4.30a}$$

$$\delta\overleftrightarrow{\sigma}(\vec{r}') = \overleftrightarrow{\sigma}_m - \overleftrightarrow{\sigma}_m = 0, \quad \vec{r}' \notin v'\ (otherwise), \tag{4.30b}$$

and letting the center of the crystallite at $\vec{r}=0$, we can write equation (4.29) as

$$\begin{aligned}\vec{E}(\vec{r}=0) &= \vec{E}^{in}=\vec{E}_{ext}+\int_V \overleftrightarrow{g}(\vec{r}=0,\vec{r}')\cdot\delta\overleftrightarrow{\sigma}(\vec{r}')\cdot\vec{E}(\vec{r}')d\vec{r}' \\ &= \vec{E}_{ext}+\int_{v'} \overleftrightarrow{g}(\vec{r}=0,\vec{r}')\cdot\delta\overleftrightarrow{\sigma}(\vec{r}')\cdot\vec{E}(\vec{r}')d\vec{r}' \\ &= \vec{E}_{ext}+\left\{\int_{v'} \overleftrightarrow{g}(\vec{r}=0,\vec{r}')d\vec{r}'\right\}\cdot\delta\overleftrightarrow{\sigma}\cdot\vec{E}^{in} \\ &= \vec{E}_{ext}+\overleftrightarrow{\Gamma}\cdot\delta\overleftrightarrow{\sigma}\cdot\vec{E}^{in}, \end{aligned} \tag{4.31}$$

where $\overleftrightarrow{\Gamma}$ is called depolarization tensor and defined as

$$\begin{aligned}\overleftrightarrow{\Gamma} &= \int_{v'} \overleftrightarrow{g}(\vec{r}=0,\vec{r}')d\vec{r}'=\int_{v'}\vec{\nabla}'\vec{\nabla}'G(\vec{r}')d\vec{r}' \\ &= \int_{v'}\vec{\nabla}'\vec{n}'\frac{d}{dr'}G(\vec{r}')dr'dS'=\oint_{S'}\left\{\vec{\nabla}'G(\vec{r}')\right\}\vec{n}'dS', \end{aligned} \tag{4.32}$$

here $\vec{n}'$ in the area integral is the outward normal direction on the surface S' of the crystallite. Its component is

$$\Gamma_{ij}=\int_{v'}\frac{\partial}{\partial r_i'}\frac{\partial}{\partial r_j'}G(\vec{r}')d\vec{r}'=\oint_{S'}\left\{\frac{\partial}{\partial r_i'}G(\vec{r}')\right\}n_j'dS'. \tag{4.33}$$

It is straightforward that equation (4.31) gives

$$\vec{E}^{in}=(\mathbf{1}-\overleftrightarrow{\Gamma}\cdot\delta\overleftrightarrow{\sigma})^{-1}\cdot\vec{E}_{ext} \tag{4.34}$$

which means

$$\overleftrightarrow{\eta}=(\mathbf{1}-\overleftrightarrow{\Gamma}\cdot\delta\overleftrightarrow{\sigma})^{-1}. \tag{4.35}$$

To generalize the above expression to different components, we can simply add a

label for each component i.e.,

$$\overleftrightarrow{\eta}_{\alpha} = (\mathbf{1} - \overleftrightarrow{\Gamma}^{\alpha} \cdot \delta\overleftrightarrow{\sigma}_{\alpha})^{-1}. \tag{4.36}$$

Then the effective conductivity tensor can be explicitly rewritten in a more popular form

$$\overleftrightarrow{\sigma}_{eff} = \overleftrightarrow{\sigma}_{m} + < \sum_{\alpha=1}^{m} \delta\overleftrightarrow{\sigma}_{\alpha}(\mathbf{1} - \overleftrightarrow{\Gamma}^{\alpha} \cdot \delta\overleftrightarrow{\sigma}_{\alpha})^{-1} > \cdot < \sum_{\alpha=1}^{m} (\mathbf{1} - \overleftrightarrow{\Gamma}^{\alpha} \cdot \delta\overleftrightarrow{\sigma}_{\alpha})^{-1} >^{-1}. \tag{4.37}$$

Equation (4.37) was first deduced through the method of Green's functions by Stroud and Pan and it has a wide application to the calculation of the effective conductivity of inhomogeneous media. The option on the conductivity tensor of the medium $\overleftrightarrow{\sigma}_{m}$ depends on the problem under consideration and it may be guided by specific geometry of crystallites in the sample. A common choice of $\overleftrightarrow{\sigma}_{m}$ is to let it be equal to $\overleftrightarrow{\sigma}_{eff}$ and this will yield the self-consistency condition

$$< \sum_{\alpha=1}^{m} \delta\overleftrightarrow{\sigma}_{\alpha}(\mathbf{1} - \overleftrightarrow{\Gamma}^{\alpha} \cdot \delta\overleftrightarrow{\sigma}_{\alpha})^{-1} >= 0 \tag{4.38}$$

The application of Stroud and Pan's approach in different areas can be found in the references (Koss & Stroud, 1985; Fisher & Stroud, 1997; Bergman & Stroud, 2000; Barabash & Stroud, 2001; Guttal & Stroud, 2005). In chapter 9 we apply this theory to model the behavior of magnetoresistance in copper single crystals containing different distribution of dislocations.

Chapter 5

De Hass-van Alphen Effect and the Fermi Surface

5.1 Introduction and Literature Review

The de Hass-van Alphen (dHvA) effect is a quantum oscillatory phenomenon which was first observed in 1930 by de Hass and van Alphen when they measured the field-dependent magnetization M of a sample of bismuth in the high magnetic field B at temperature $T = 14.2K$. The researchers found that the magnetic susceptibility M/B is a periodic function of the reciprocal of the magnetic field (de Hass & van Alphen, 1930). However, the significant importance of dHvA effect had not gained recognition till about 1952 when Onsager applied semiclassical treatment to quantize electron motion in a magnetic field and deduced a formula (commonly

called Onsager's relation) explicitly indicating that dHvA oscillatory frequency F is directly proportional to the extremal cross-section area S_F of the Fermi surface (Onager, 1952). This interpretation uncovered the physical nature hidden behind the dHvA effect and provided theoretical base to design a tool for accurate measurement of the Fermi surface. Based on Onsager's relation, Schoenberg made a significant contribution to refine the dHvA effect into a practical and powerful tool to probe the Fermi surface (Shoenberg, 1965). Nowadays, many different techniques (such as torque and pulsed field methods) to measure the dHvA oscillatory frequency has been developed with the advent of superconducting magnets and the dHvA measurements have become one of the most popular and powerful methods to investigate the Fermi surface of many material systems. A detailed description on the development of this topic can be found in the book by Schoenberg (Shoenberg, 1984)

The dHvA studies of the strain and stress effect on the Fermi surface have been attracting a lot of attention because they can provide valuable information about the dependence of band structure energy on the lattice parameter. The experimental measurements to examine the strain/stress dependence of the Fermi surface can be performed in two ways. One way is to apply external tension or compression directly to the sample and then check the change of the Fermi surface under the stress by measuring the change of the dHvA frequency. In the other way, the change in the Fermi surface can be indirectly inferred from the measurement of the oscillatory magnetostriction i.e., the oscillatory strain or sound velocity determined by the elastic stiffness tensor, because these two physical quantities depend upon the stress derivative of logarithmic dHvA frequency.

The experimental study of the measurement of the Fermi surface under the applied strain and stress started in 1950s. Verkin *et al.* did the first measurement of the strain dependence of the Fermi surface on bismuth with the pressure bomb technique (Verkin *et al.*, 1956). Schoenberg and Stiles developed a new method by applying phase shift technique which can measure very small change in frequency caused by a stress acted on the samples (Shoenberg & Stiles, 1964). The first direct measurement of uniaxial tension dependence of the Fermi surface on noble metals was performed by Schoenberg and Watts (Shoenberg & Watts, 1964) and later by other researchers such as Gamble and Watts (Gamble & Watts, 1973), Gerstein and Elbaum (Gerstein & Elbaum, 1973) and Mayers and Watts (Mayers & Watts, 1978). The first observation of oscillatory magnetostriction in bismuth was done by Green and Chandrasekhar (Green & Chandrasekhar, 1963) and the oscillation in the velocity of sound also on bismuth by Mavroides *et al.*, (Mavroides *et al.*, 1962). The measurements of oscillatory magnetostriction and magnetic torque was developed to study the strain dependence of the Fermi surface of other crystals by Grienssen *et al.*, (Griessen & Olsen, 1971; Griessen & Kündiga, 1972; Griessen & Sorbello, 1972; Griessen *et al.*, 1976) and Posternak *et al.*, (Posternak *et al.*, 1975). Testardi *et al.*, (Testardi & Condon, 1970) and Lee *et al.*, (Lee *et al.*, 1976) used the measurement data of oscillatory sound velocity with magnetization and torque measurements to investigate the strain dependence of the Fermi surface of beryllium and tungsten respectively. More recently, these techniques have been employed to study the Fermi surface of composites (Sirenko *et al.*, 2009).

So far the investigations of the stress and strain dependence of the Fermi surface have been carried out on moderately deformed crystals within the elastic strain

limit. To satisfy conditions for the occurrence of dHvA effect, the experiments have to be performed on very pure samples, in a very strong magnetic field and at very low temperatures so that (Lifshitz *et al.*, 1973)

$$l \gg R_B, \tag{5.1a}$$

$$\varepsilon_F \gg \hbar w_c \gg K_B T, \tag{5.1b}$$

where l is the mean free path of conduction electrons and R_B the radius of the conduction electron orbits in the field. Other constants in equation (5.1) are defined in earlier chapters. However, as we mentioned before, dislocations exists in almost every real crystal and their existence introduces a permanent strain and elastic stress fields inside the crystal. Consequently, the Fermi surface of dislocated crystals will be distorted and the degree of topological distortion of the Fermi surface may depends upon amount of deformation and the density of dislocations that are stored in the lattice. The effect may be more apparent than that observed in elastically deformed crystals. In this sense, the investigation of the distortion of the Fermi surface of plastically deformed crystals is significant from both fundamental and practical point of view.

The requirement for the purity of the samples to observe the dHvA effect, i.e. equation (5.1a) is equivalent to condition (3.37). In chapter 7, we will discuss the limits for the density of dislocations stored in the samples that need to satisfy condition (3.37) in order to observe galvanomagnetic properties of deformed samples in the presence of the magnetic field $B = 9\ Tesla$. If the sample is deformed to a strain of $2 \sim 4\%$ percent, the density of dislocations produced in the deformed sample is

approximately about $10^{10}/cm^2$, therefore, the condition (3.37) will be satisfied if the applied field is 9 *Tesla* . This means that the dHvA effect in such deformed samples should exhibit an appreciable signal, which can easily be detected.

In the present work we will investigate the distortion of the Fermi surface of plastically deformed copper single crystal by measuring the dHvA oscillatory frequency of the magnetic torque in the presence of a magnetic field B. The following is the basic theory of the dHvA effect.

5.2 Theory of the dHvA Effect

5.2.1 Free Electron in a Magnetic Field

The dHvA effect is the direct consequence of quantization of electron motion in a magnetic field which has to be discussed in the framework of quantum mechanics. Consider a simple case: free electrons moving in a uniform magnetic field $\vec{B}$ along z-direction. The Hamiltonian is

$$\mathscr{H} = \frac{1}{2m}(\vec{p}+q\vec{A})^2 = \frac{1}{2m}(\vec{p}-e\vec{A})^2, \tag{5.2}$$

where $\vec{p}$ is the canonical momentum of the electron and the vector potential in the Landau gauge is $\vec{A} = (-yB, 0, 0)$ which satisfies the relation

$$\vec{B} = \vec{\nabla} \times \vec{A} = B\vec{e}_3. \tag{5.3}$$

Under the Landau gauge, Schrödinger's equation for electron wave function $\Psi(\vec{r})$ satisfies

$$\hat{\mathscr{H}}\Psi(\vec{r}) = \frac{1}{2m}\left[(\hat{p}_x + eB\hat{y})^2 + \hat{p}_y^2 + \hat{p}_z^2\right]\Psi(\vec{r}) = \varepsilon\Psi(\vec{r}), \tag{5.4}$$

where canonical momentum operator $\hat{p}_i$ is defined as

$$\hat{p}_i = \frac{\hbar}{i}\frac{\partial}{\partial r_i} \tag{5.5}$$

and satisfies the commutation relation

$$\left[\hat{p}_i, r_j\right] = \frac{\hbar}{i}\delta_{ij}, \quad (i,j = 1,2,3). \tag{5.6}$$

since the only explicit position dependence in equation (5.4) is through the y coordinate, we expect the solution to have the form

$$\Psi(\vec{r}) = e^{i(k_x x + k_z z)}\phi(y). \tag{5.7}$$

Substituting equation (5.5) in equation (5.4) and noticing the fact that $\Psi(\vec{r})$ is the eigenfunction for operators $\hat{p}_x$ and $\hat{p}_z$, i.e.

$$\hat{p}_x\Psi(\vec{r}) = \hbar k_x\Psi(\vec{r}), \tag{5.8a}$$

$$\hat{p}_z\Psi(\vec{r}) = \hbar k_z\Psi(\vec{r}), \tag{5.8b}$$

hence, we obtain

$$\frac{1}{2m}\left[(\hbar k_x + eBy)^2 + \hat{p}_y^2 + \hbar^2 k_z^2\right]\phi(y) = \varepsilon\phi(y), \tag{5.9}$$

or specifically

$$\left[-\frac{\hbar^2}{2m}\frac{\partial^2}{\partial y^2} + \frac{1}{2m}(\hbar k_x + eBy)^2\right]\phi(y) = (\varepsilon - \frac{\hbar^2 k_z^2}{2m})\phi(y). \tag{5.10}$$

Let

$$w_c = \frac{eB}{m}, \qquad y_0 = -\frac{\hbar k_x}{eB}, \qquad \varepsilon' = \varepsilon - \frac{\hbar^2 k_z^2}{2m}. \tag{5.11}$$

Equation (5.10) can be simplified as

$$\left[-\frac{\hbar^2}{2m}\frac{\partial^2}{\partial y^2} + \frac{m}{2}w_c^2(y - y_0)^2\right]\phi(y) = \varepsilon'\phi(y) \tag{5.12}$$

which is similar to the Schrödinger's equation for one dimensional harmonic oscillator centered at y_0 with angular frequency w_c. The solution to the harmonic oscillator is well known and its eigenfunction is

$$\phi_n(y - y_0) = \sqrt{\frac{1}{2^n n!}}\left(\frac{mw_c}{\pi\hbar}\right)^{1/4} e^{-\frac{mw_c}{2\hbar}(y-y_0)^2} H_n\left[\sqrt{\frac{mw_c}{\hbar}}(y - y_0)\right], (n = 0, 1, 2, ...) \tag{5.13}$$

where functions $H_n(x)$ are the Hermite polynomials. The corresponding eigenvalues are

$$\varepsilon' = (n + \frac{1}{2})\hbar w_c. \tag{5.14}$$

Subsequently, the energy levels for equation (5.4) can be expressed as

$$\varepsilon_{nk_z} = (n+\frac{1}{2})\hbar w_c + \frac{\hbar^2 k_z^2}{2m}, \qquad (n = 0,1,2,...) \tag{5.15}$$

which is characterized by two quantum numbers, n and k_z.

Equation (5.15) clearly indicates the energy of electron movement in z-direction is $\hbar^2 k_z^2/2m$ which is unaffected by the magnetic field because of Lorentz force having no component along $\vec{B}$. However, the energy of electron cyclotron movement on the plane perpendicular to the magnetic field is quantized, which would be $\hbar^2(k_x^2+k_y^2)/2m$ without the magnetic field. The step between the neighboring energy levels is uniform and equal to $\hbar w_c$. Such phenomenon is called orbit quantization and the discrete energy levels denoted by equation (5.15) are known as Landau levels.

One point worthy to emphasize is that equation (5.15) is deduced in free-electron approximation. In a crystal, an electron moves in a potential $V(\vec{r})$ which is a periodic function of Bravais lattice of the crystal. In the presence of the magnetic field $\vec{B}$, the Hamiltonian will be

$$\mathscr{H} = \frac{1}{2m}(\vec{p} - e\vec{A})^2 + V(\vec{r}). \tag{5.16}$$

Unfortunately, exactly solving the corresponding Schrödinger's equation defined by the Hamiltonian (5.16) is extremely formidable. However, under effective mass approximation (Smith *et al.*, 1967), the effect of the periodic potential of Bravais lattice on the motion of a single electron can be absorbed into electron mass which is

different from the free-electron mass and determined directly by the second derivative of energy eigenvalue with respect to wavevector. Such electron mass is called the effective mass and labeled as m^*. Accordingly, the equation (5.16) can be simplified as

$$\mathscr{H} = \frac{1}{2m^*}(\vec{p} - e\vec{A})^2. \tag{5.17}$$

Equation (5.17) indicates an electron in a crystal is like a free-electron but with the effective mass m^*. Such approximation tremendously simplifies the problem of conduction electrons in crystals in the presence of the external fields which is true on the condition that the external field is sufficiently small so that the electron always remains in a single band.

5.2.2 Degeneracy and Onsager's Relation

Consider the motion of electrons in a crystalline sample with dimensions $L_x \times L_y \times L_z$ without the field. The wave vector of a single electron is quantized under the periodic boundary condition and its components have the form

$$k_x = n_x\frac{2\pi}{L_x},\quad k_y = n_y\frac{2\pi}{L_y},\quad k_z = n_z\frac{2\pi}{L_z},\quad (n_x, n_y, n_z = 0, \pm1, \pm2, ...). \tag{5.18}$$

For a fixed k_z (suppose $k_z = 0$ for simplicity) which mathematically corresponds to the case of 2 dimensions, the density of states ρ_{dos} at an energy ε inside an interval $(\varepsilon, \varepsilon + d\varepsilon)$ on the k_xk_y plane is

$$\rho_{dos} = \frac{m^*L_xL_y}{\pi\hbar^2}. \tag{5.19}$$

When a uniform magnetic field $\vec{B}$ along k_z-direction turns on, the cyclotron motion of electrons under the action of Lorentz force is quantized and the energy for each quantized orbital movement is determined by Landau levels (5.15) which are highly degenerate. The degeneracy $\mathscr{D}$ for each Landau level is

$$\mathscr{D} = \hbar w_c \cdot \rho_{dos} = \frac{L_x L_y}{\pi\hbar} eB \tag{5.20}$$

which is explicitly proportional to the magnitude of $\vec{B}$.

Let the number of electrons in a system be equal to N_e. Suppose that the Landau levels for such system are filled up to a quantum number n and all energy levels above n are empty when the applied field is B_1, so that,

$$n\mathscr{D} = N_e \quad \Rightarrow \quad \frac{1}{B_1} = n\frac{L_x L_y}{\pi\hbar N_e}. \tag{5.21}$$

If the magnetic field decreases, the electrons start to occupy the $(n+1)th$ Landau level since degeneracy for each quantized orbitals is decreasing. This leads to the change of the total energy of the system. With the magnetic field decreasing to B_2 at which the exact $n+1$ Landau levels are coincidently filled up and the above levels are empty, it can be shown that the total energy of the system changes back to the quantity at $B = B_1$, and

$$n\mathscr{D} = N_e \quad \Rightarrow \quad \frac{1}{B_2} = (n+1)\frac{L_x L_y}{\pi\hbar N_e}. \tag{5.22}$$

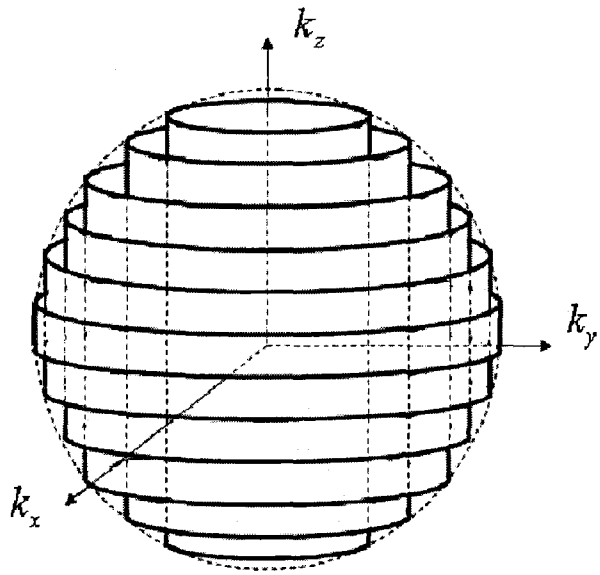

Figure 5.1: The intersections of Landau tubes with the spherical Fermi surface indicate the quantized electron orbitals on the planes perpendicular to the field

Subtracting equation (5.21) from equation (5.22) gives

$$\mathscr{P} = \Delta\left(\frac{1}{B}\right) = \frac{1}{B_2} - \frac{1}{B_1} = \frac{L_x L_y e}{\pi \hbar N_e} = \frac{2\pi e}{\hbar S_F}, \tag{5.23}$$

where $\mathscr{P}$ is the period of the dHvA oscillation in $B^{-1}(Tesla^{-1})$ and S_F is the cross section area (Fermi circle area) and defined by

$$S_F = 2\pi^2 \frac{N_e}{L_x L_y}. \tag{5.24}$$

If k_z is not fixed, the electrons can move freely along the field direction and their energies are determined by equation (5.15). Subsequently, electron states will lie

on the Landau tubes and the intersection of each tube with the Fermi surface gives a quantized orbit on the planes perpendicular to the field. Figure 5.1 is a schematic illustration of Landau tubes for spherical Fermi surface. It can be shown that the density of states of n-th Landau subband per unit volume $\mathcal{N}_n$ is

$$\mathcal{N}_n(\varepsilon) = 2eB\sqrt{2m^*}\frac{1}{(2\pi\hbar)^2}\left[\varepsilon - (n+\frac{1}{2})\hbar w_c\right]^{-1/2} \tag{5.25}$$

and the total density of states per unit volume is given by summing over all occupied Landau levels

$$\mathcal{N}(\varepsilon) = \sum_{n=0}^{n_{max}} \mathcal{N}_n(\varepsilon) = \frac{1}{4\pi^2}\left(\frac{2m^*}{\hbar^2}\right)^{3/2}\hbar w_c \sum_{n=0}^{n_{max}}\left[\varepsilon - (n+\frac{1}{2})\hbar w_c\right]^{-1/2} \tag{5.26}$$

where integer n_{max} is defined by

$$(n_{max}+\frac{1}{2})\hbar w_c \leq \varepsilon. \tag{5.27}$$

Similar to the 2-dimensional case, when the magnitude of the magnetic field decreases, the electron states accommodated in each Landau subband will also decrease and some electrons will transfer to the new higher Landau level because the total number of electrons is unchanged. This will lead to the oscillations of the total energy of the system. The main contribution to the oscillation of the total energy is from the electrons moving along the extremal orbitals while the contributions from electrons moving along the nonextremal orbitals are canceled out because of phase cancellation (Kittel, 1986). The oscillatory period is also determined by equation (5.23) but S_F is the extremal cross section area on the planes perpendicular to the

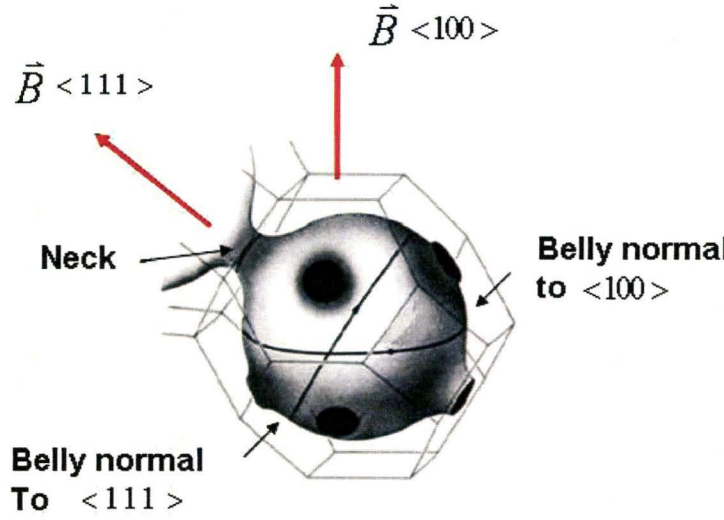

Figure 5.2: The Fermi surface of copper in a single zone with a neck connecting to an adjacent zone. Three extremal orbits (one neck and two different belly orbits) are indicated for $\vec{B}$ along $< 111 >$ and $< 100 >$ directions respectively.

field direction and satisfies by the condition

$$\frac{\partial S_F(k_z)}{\partial k_z} = 0. \tag{5.28}$$

Equation (5.23) is the so-called Onsager relation. Besides the total energy, any physical quantity of a metal which is related to the motion of electrons such as electrical resistivity, magnetic susceptibility, heat capacity, thermal conductivity etc., will also oscillate as the magnetic field is varied.

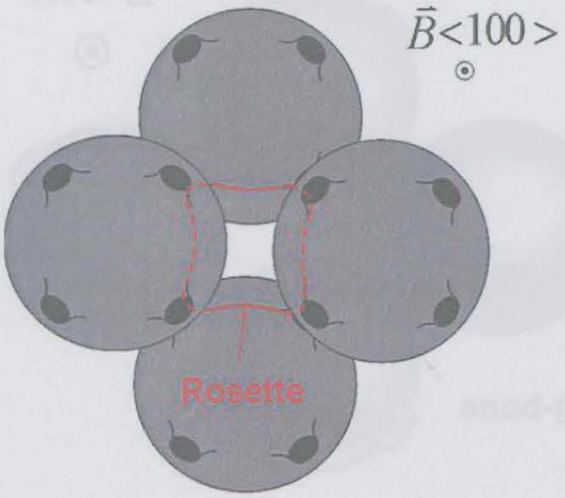

Figure 5.3: The Fermi surface of copper in extended zone scheme. The extremal hole orbit (four-cornered rosette) is indicated as $\vec{B}$ tilts in $< 100 >$ direction.

5.2.3 Extremal Orbits and Oscillatory Frequencies in Copper

In chapter 3, we have discussed the form of the Fermi surface of copper: a distorted sphere jointed by eight necks on the $< 111 >$ faces of the Brillouin zone. It is straightforward to obtain extremal orbits for electrons in such a simple model. Figures 5.2, 5.3 and 5.4 show schematically the extremal orbits normal to high symmetry directions ($< 100 >$, $< 110 >$ and $< 111 >$) which are the focus of the most experimental studies.

So far much effort has been made to measure the dHvA oscillatory frequencies to determine the Fermi surface of metals and metallic compounds through the On-

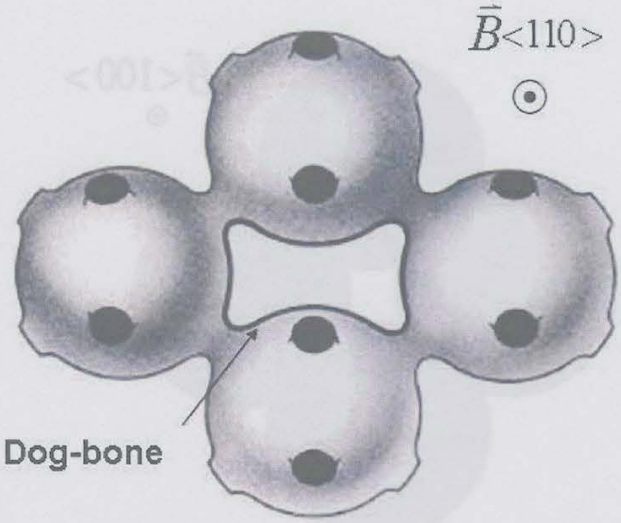

Figure 5.4: The Fermi surface of copper in extended zone scheme. The extremal hole orbit (dogs-bone) is indicated as $\vec{B}$ tilts in $< 110 >$ direction.

sager relation. The first systematic studies of the dHvA effect in copper were carried out by Schoenberg (Shoenberg, 1959). Other scientists who also contributed to this research area are listed in table 5.1.

Table 5.1: de Hass-van Alphen frequencies in copper (all in units of 10^3 *G*). A (Jan & Templeton, 1966), B (O'Sullivan & Schirber, 1967, 1968), C (Halse, 1969),D (Lee, 1969), E (Coleridge *et al.*, 1971)

	$< 111 >$		$< 100 >$		$< 110 >$
	Belly	Neck	Belly	Rosette	Dog-bone
A	580900 ± 600	21740 ± 20	—	—	—
B	581400 ± 600	21770 ± 20	599800 ± 600	246200 ± 300	251400 ± 300
C	580700	21735	599400	245900	250800
D	581010 ± 600	21747 ± 20	599600 ± 100	246210 ± 50	251000 ± 200
E	580730 ± 10	21737.6 ± 0.4	599550 ± 10	246040 ± 10	250965 ± 10

It should be emphasized that the oscillatory frequencies obtained by different

researchers and listed in the table 5.1 are very close to each other, a difference is of the order of 10^{-3}. These values are considered in the literature as highly reliable. The specimens which were used in these measurements were of the highest purity available, with resistivity ratio RR close to 10^4 or higher. Therefore, the frequencies listed in the table 5.1 can be used as a benchmark against which our results can be compared.

Chapter 6

Objective of the Thesis

The objective of the thesis is to develop a better understanding of the effect of dislocation substructure on galvanomagnetic properties of copper single crystals and to investigate the distortion of the Fermi surface of copper produced by the presence of dislocations.

The objectives will be accomplished by both theoretical and experimental efforts which include:

- systematic studies of the effect of the type, density and dislocation distribution on the galvanomagnetic properties of deformed samples, by means of magnetoresistance measurements

- studies of the distortion of the Fermi surface due to dislocations by means of de Haas-van Alphen experiments

- modeling the transverse magnetoresistivity using mean field theory.

The remaining part of the thesis consists of four chapters: the next chapter (7) introduces the experimental techniques used in this work including sample deformation experiments, magnetoresistance and de Hass-van Alphen measurements. Chapter 8 presents the experimental results and provides the discussion of the results. Chapter 9 deals with theoretical modeling of the field-dependent and angular dependent transverse magnetoresistance for deformed samples with different density of dislocations. Chapter 10 provides summary and conclusions arising from this work.

Chapter 7

Experimental Procedures

7.1 Materials and Deformation Procedure

Copper single crystals in the form of rectangular prism with dimensions $3mm \times 3mm \times 65mm$ were grown by a modified Bridgeman technique from 99.9995% copper in split graphite moulds from pre-oriented nucleus (Niewczas *et al.*, 2001). The crystallographic orientation of the samples was veryfied by Laue method. One crystal had the initial crystallographic orientations of the tensile axis along [541] and two mutually perpendicular lateral faces oriented parallel to $(1\bar{2}3)$ and $(1\bar{1}\bar{1})$ plane. The other crystal had the initial crystallographic orientations of the tensile axis along [100] and two mutually perpendicular lateral faces oriented parallel to $(0\bar{1}\bar{1})$ and $(01\bar{1})$ plane. The crystals were deformed in tension with an initial strain rate of $1.7 \times 10^{-4}s^{-1}$ to different deformation stages at temperature of $78K$. A

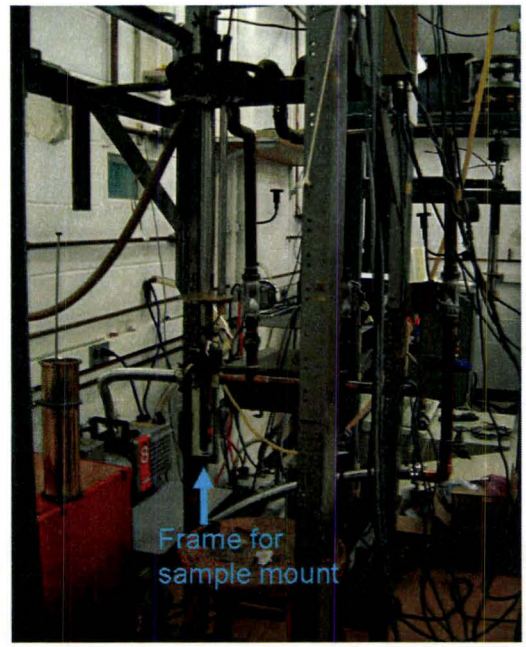

Figure 7.1: Picture of the equipment for sample deformation

bath of liquid nitrogen was used to maintain a temperature of $78K$ during deformation and data for load and extension of the sample were acquired and stored in a pc-computer. The density of dislocations in the deformed samples was controlled by deforming the same orientation of the single crystals to different strains. After desired amount of deformation, the part of deformed crystal was spark-cut and subjected to all characterization. The remaining part of the crystal was re-mounted and deformed further to induce higher density of dislocations. The procedure was repeated after subsequent deformation to obtain samples with higher dislocations density for further studies. The dislocation microstructures of deformed copper single crystals were discussed in chapter 2. Figure 7.1 shows the tensile tester equipped with a cryostat used in deformation experiments.

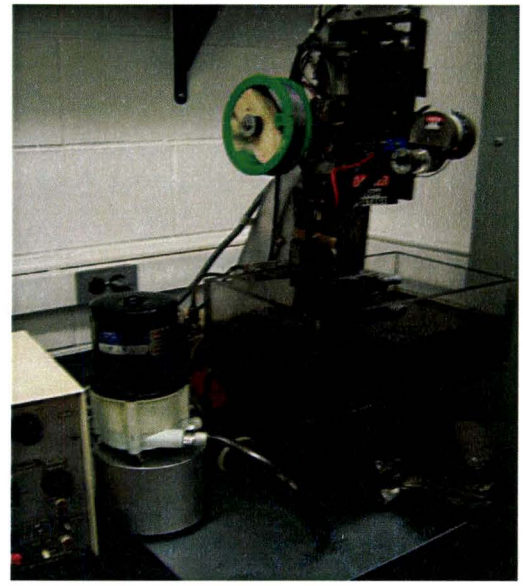

Figure 7.2: Picture of the equipment for sample sectioning

7.2 Sample Sectioning

For the measurements of electrical and magnetic properties, smaller size samples were prepared from deformed single crystals. Spark cutter (Figure 7.2) was used to cut the deformed crystals into different geometries to meet different experimental requirements. For the measurements of de Haas-van Alphen effect by torque magnetometry, the sample size of dimensions $1.5mm \times 1.5mm \times 0.5mm$ was used. For magnetoresistivity and Hall effect measurements, the sample dimensions was about $2.0mm \times 2.0mm \times 20.0mm$. To remove damage by spark-cutting all cut samples were chemically polished on a cloth with Mitchell solution consisting of supersaturated solution of CuCl2 in HCl.

7.3 Dislocation Density in Magnetoresistivity Measurements

It was discussed in Chapter 3 that, in order to measure the change of resistance of the sample in the magnetic field, the field has to be strong enough to bend electron orbits appreciably. Hence, it is important to estimate the necessary conditions for the observation of a measurable magnetoresistance effect in copper samples with dislocations before performing any experiment.

Equation (3.37) in chapter 3 provides the condition for strong fields. Suppose the applied field during magnetoresistivity measurements is 9 *Tesla.* After substituting all room temperature constants ($n = 8.5 \times 10^{28} m^{-3}$; $e = 1.6 \times 10^{-19} C$ and $\rho_0 = 1.72 \times 10^{-8} \Omega m$), the equation (3.39) yields $\omega_c \tau = 0.038$, which is much smaller than one. This means that the field of 9 *Tesla* is not strong enough to observe magnetoresistance phenomena at room temperature for copper samples. However, situation is quite different if measurement is carried out at the temperature $T = 2K$ at which phonon vibration is suppressed. Under these conditions dislocations and other lattice defects are sole source of electron scattering. If we assume that only dislocations are present, we can write the resistivity as

$$\rho_0 = N_d \Re_d, \tag{7.1}$$

where $\Re_d$ is called specific dislocation resistivity and for copper its value is approximately $1 \times 10^{-25} \Omega m^3$ (Watts, 1989) , N_d is the density of dislocations of samples. Substituting equation (7.1) with the value of specific dislocation resistivity back

into equation (3.39), we have

$$\omega_c \tau = \frac{6.6 \times 10^{15}}{N_d}. \tag{7.2}$$

It is clear from equation (7.2) that the saturation magnetoresistance in copper samples is expected at the density of dislocations higher than $6.6 \times 10^{15} m^{-2}$ or $6.6 \times 10^{11} cm^{-2}$.

All magnetoresistivity measurements have to be carried out at a low temperatures to measure a weak scattering effects from dislocations and change of the resistivity under applied magnetic field.

7.4 Magnetoresistivity and de Haas-van Alphen Measurements

Quantum Design Physical Property Measurement System (PPMS-9), which offers broad range of experimental capabilities was used in this work. The PPMS-9 System (Figure 7.3) consists of a measurement probe with a 9 *Tesla* magnet and cylindrical sample chamber of 2.5cm diameter, incorporated into a liquid helium dewar. The hardware is controlled by microprocessor electronic circuitry and PPMS MultiVu windows-based software, which provides all functions essential for different measurement applications. The combination of hardware and software provides a versatile system which can perform highly sophisticated and accurate measure-

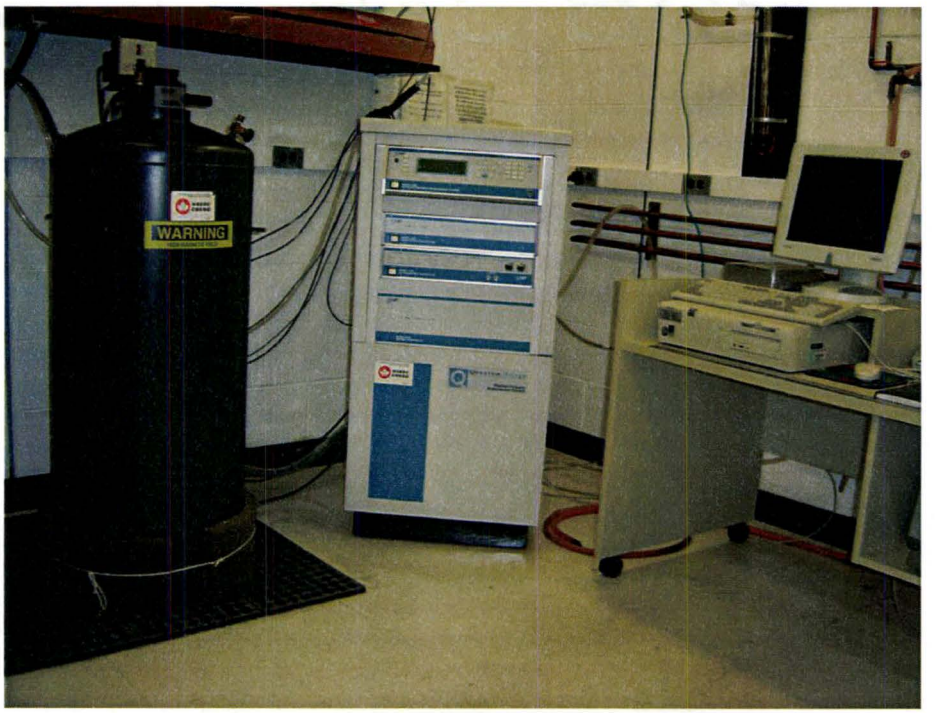

Figure 7.3: The model PPMS-9 Physical Properties Measurement System

ments of physical properties of materials in a temperature range from $1.9K$ to $400K$ and a magnetic field from $0-9$ *Tesla*. The configuration of the system installed in our laboratory permits to measure broad range of electrical and magnetic properties as well as heat capacity of materials.

Figure 7.4 shows the schematic view of a sample chamber. In resistivity and magnetoresistivity studies four-point method of measuring potential drop across the sample is used. In this method a known current is passed through the circuit and the resulting potential drop is measured by the system. Potential and current leads are spot welded to the samples and samples are mounted on printed-circuit platforms or pucks (Figure 7.5(a)). Four leads are soldered to the pads on the plat-

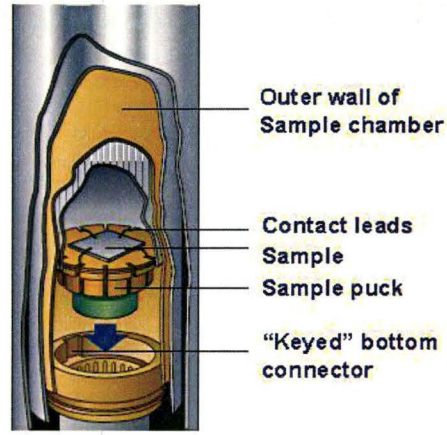

Figure 7.4: Cut away view of sample chamber. The picture is taken from web page: http://www.lotoriel.de/site/site_down/qd_ppms_deen.pdf

forms and then the pucks are inserted into the rotator probe (Figure 7.5(b)). The rotator allows to rotate samples by 360 degree around one axis of rotation. During measurements the rotator probe is inserted into the sample chamber of PPMS-9 system. To eliminate Thermal Electromotive Force (EMF), the current is reversed many times and the average of potential drops in both directions is calculated. In all resistivity and magnetoresistivity measurements the current was $100mA$ and 100 reversals per each measurement point was used, giving accuracy of resistivity better than 1%. Magnetoresistivity masurements were done under a magnetic field of 9 *Tesla*.

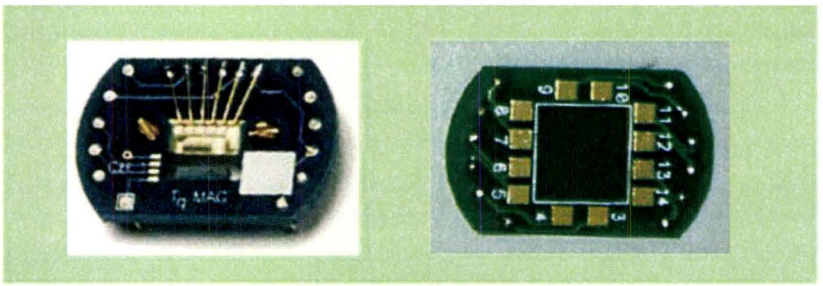

(a) Pucks for torque (left) and resistivity (right) measurement

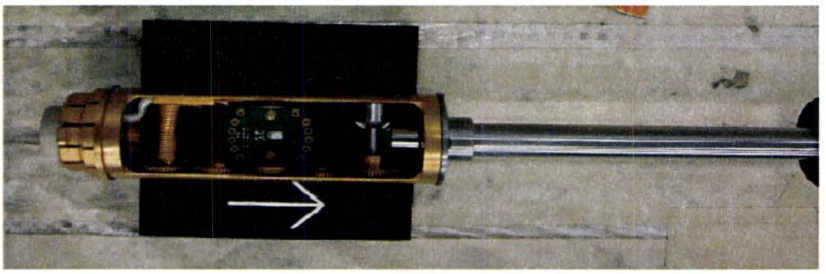

(b) Horizontal and vertical sample rotator probe

Figure 7.5: Pictures for sample pucks and rotator probe

7.4.1 De Haas-van Alphen Effect

The magnetization $\vec{M}$ of metals in the magnetic field can be obtained by calculating the thermodynamic potential Ω

$$\Omega = -K_B T \sum_{\alpha} ln[1 + e^{(\mu - \varepsilon_\alpha)/K_B T}] \tag{7.3}$$

where the summation runs over all quantum states, and then using the relation

$$\vec{M} = -\frac{\partial \Omega}{\partial \vec{B}}. \tag{7.4}$$

Lifshitz *et al.*, (Lifshitz & Kosevich, 1956) first derived an expression for the oscillatory magnetization given by

$$M = -\frac{\sqrt{2}T}{B^{1/2}}\left(\frac{e\hbar}{\pi}\right)^{3/2}\sum_{\alpha} S_F^{\alpha}\left|\frac{\partial^2 S_F}{\partial k_z^2}\right|_{\alpha}^{-1/2} exp\left(-\frac{2\pi^2 T m^*}{\hbar e B}\right)\sin\left(\frac{S_F^{\alpha}\hbar}{eB}\pm\frac{\pi}{4}\right)\cos\left(\frac{\pi m^*}{m_e}\right), \tag{7.5}$$

where the summation extends over all cross section areas of the Fermi surface, and the phase is taken $-\pi/4$ if $\partial S_F/\partial k_z > 0$ and $\pi/4$ if $\partial S_F/\partial k_z < 0$. The period of the magnetization oscillation (or intervals between the zeros of the function) is determined by the extremal cross section of the Fermi surface, as per equation (5.23).

One of the most popular methods to determine the dHvA oscillatory frequency is torque measurement, which relies on the phenomenon that metallic samples in an external magnetic field are magnetized and then they interact with the magnetic field. Consequently, there is a torque $\vec{\mathscr{T}}$ acting on the sample, which depends on the intensity of the magnetic field:

$$\vec{\mathscr{T}} = V\vec{M}\times\vec{B}. \tag{7.6}$$

where V is the sample volume. Equation (7.6) indicates that $\mathscr{T}$ has the same oscillatory features as magnetization M. Accordingly, the dHvA oscillatory frequency can be determined by measuring torque as a function of the magnetic field, plotting torque as a function of the inverse of the field $(1/B)$ and then making Fourier transform of this data to obtain the oscillatory frequency. The following describes

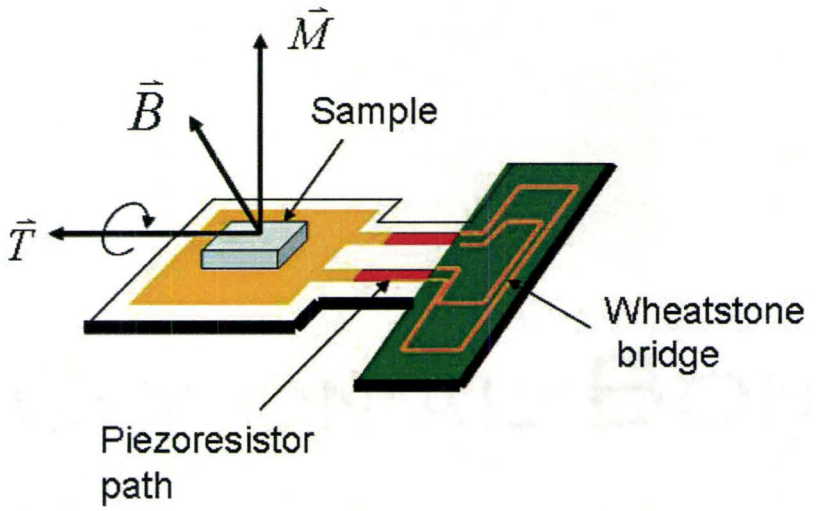

Figure 7.6: Schematic diagram of the torque-lever chip. The two legs of the chip connect with two piezoresistor grids which is incorporated into an integrated wheatstone bridge circuit

sample preparation and measurements of dHvA effect.

7.4.2 Oscillatory Magnetization and Torque Measurements

Deformed or undeformed single crystals are spark-cut into the small samples of dimensions: $1.5mm \times 1.5mm \times 0.5mm$. To remove spark damage the samples are chemically polished in Mitchell solution in the same way as samples for magnetoresistivity measurements, described in chapter 7.2.

For torque measurements, the samples are mounted on the torque-lever chip, which is subsequently placed into the rotator probe and inserted to the system.

To probe magnetic moment of the sample, the torque-lever chip utilizes a high-sensitivity detection circuit in a Wheatstone bridge configuration through the piezoresistor paths connecting with the two legs of the chip. Figure 7.6 is a schematic diagram of the components on the torque-lever chip. When a magnetic field is applied to the sample, the torque lever twists inducing the resistance change in each leg. The change in the resistance of the piezoresistive path is precisely measured with the Wheatstone bridge, by the electronic circuitry. For angle-dependent torque measurement, the applied field is fixed at $B = 9$ *Tesla* and the sample is rotated around one axis and the torque is measured every 2 degree in a range of rotation angles 0 - 360 deg. For field-dependent torque measurements, the position of the sample is fixed and the field is increased from 8.5 to 8.6 *Tesla* with a step of 2 *Gauss*. The torque versus magnetic field characteristics are subsequently processed using external software to obtain dHvA oscillatory frequencies.

Chapter 8

Experimental Results and Discussion

8.1 Plastic Deformations of Single Crystals and Dislocation Density Measurements

To examine the effect of dislocation density and substructure on magnetoresistivity, two orientations of copper single crystal samples were deformed in tension at 78K, using the following procedure. A small sample of about $1.5cm$ in length was spark-cut from a virgin copper single crystal with initial length of about $7cm$. The cut sample was subjected subsequently to full characterization and through this thesis is denoted as undeformed material. The larger virgin crystal, termed parent sample, was mounted to the tensile tester and deformed at 78K by few percent of strain. From deformed crystal a smaller sample of about $1.5cm$ in length was spark-cut and used for measurements of resistivity and magnetoresistivity. Parent sample

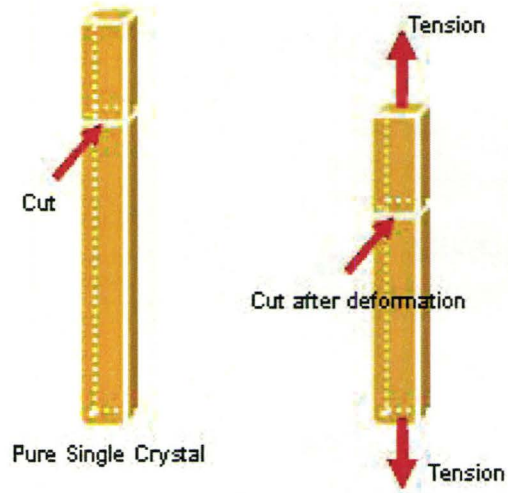

Figure 8.1: Samples are obtained from the same single crystal deformed to different stress levels, by cutting part of deformed crystal.

was deformed to the next stress level at $78K$ and the next smaller piece of sample was spark-cut to obtain a sample with higher dislocation density. The procedure was repeated few times to obtain the samples with different dislocation density for magnetoresistivity studies. Figure 8.1 illustrates schematically the sectioning of the crystal to obtain series of deformed samples.

With the above method, six samples were obtained for analysis; three from 733B crystal with initial orientation of the tensile axis along [100] and three from 749A crystal with initial orientation of the tensile axis along [541]. In the subsequent part of the thesis these samples are denoted as $733B1 < 100 >$, $733B2 < 100 >$, $733B3 < 100 >$, $749A1 < 541 >$, $749A2 < 541 >$ and $749A3 < 541 >$. The dimension of samples used in magnetoresistivity measurements was $2mm \times 2mm \times 15mm$.

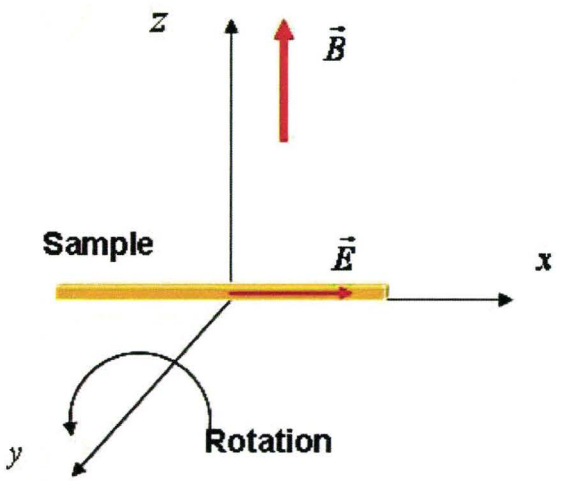

Figure 8.2: Samples rotate along y-axis in the magnetic field fixed in z-axis but the electrical current rotates with samples

$733B1 < 100 >$ and $749A1 < 541 >$ denote undeformed samples. Two other single crystal samples grown in the same melt, $733C < 100 >$ and $700H < 541 >$ respectively, were deformed to large strains to obtain samples with highest dislocation density. In every experiment, the crystallographic orientation of the samples was controlled by Laue and EBSD methods. Table 8.1 gives the orientation of the samples defined with respect to the coordinate system shown in Figure 8.2.

Figures 8.3 and 8.4 shows stress-strain characteristics of [100] and [541] single crystals deformed at 78K to larger stresses. It is seen that the flow stress in samples with crystallographic orientation of the tensile axis along $< 100 >$ increases faster than those along $< 541 >$ i.e. the work hardening of $< 100 >$ orientation is larger than $< 541 >$ crystal. This is because $< 100 >$ orientation deforms by

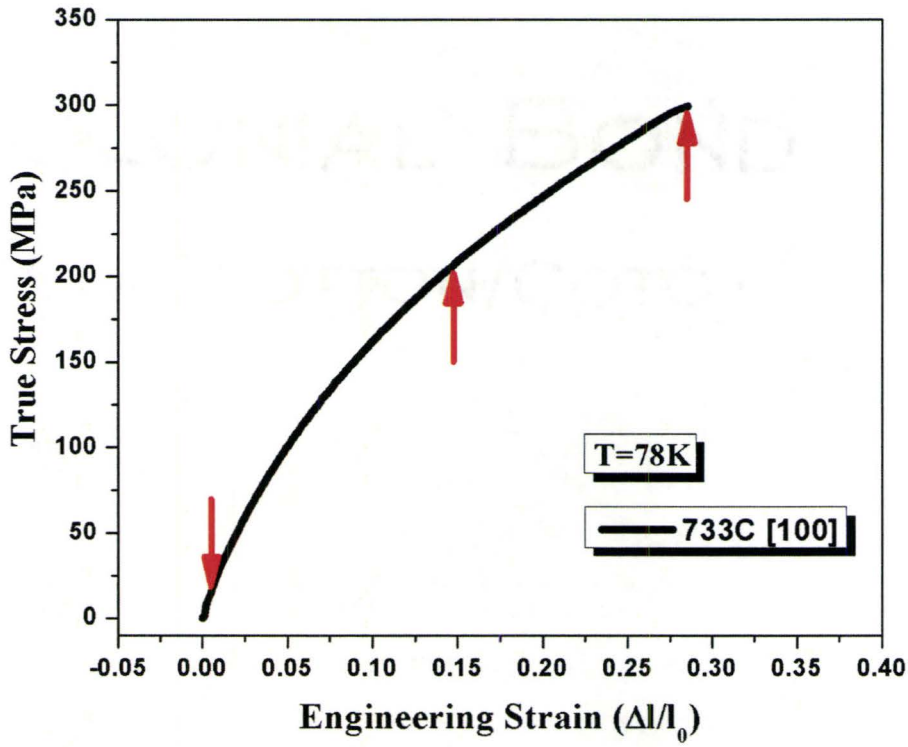

Figure 8.3: Strain-stress characteristic of $< 100 >$ single crystal deformed at 78K. The arrows point to the deformation stages of the specimens used in studies of the magnetic and electrical properties.

many non-coplanar slip system, activated right from the beginning of deformation causing the dislocations of these slip systems to intersect each other in the process called forest hardening. On the other hand, sample with the orientation of the tensile axis $< 541 >$ deforms predominantly in one slip system and mobile dislocations do not intersect many forest dislocations, which automatically leads to lower work-hardening rate during the deformation (see Chapter 2.4.2). The arrows on the stress-strain characteristics point to the deformation stages where the samples

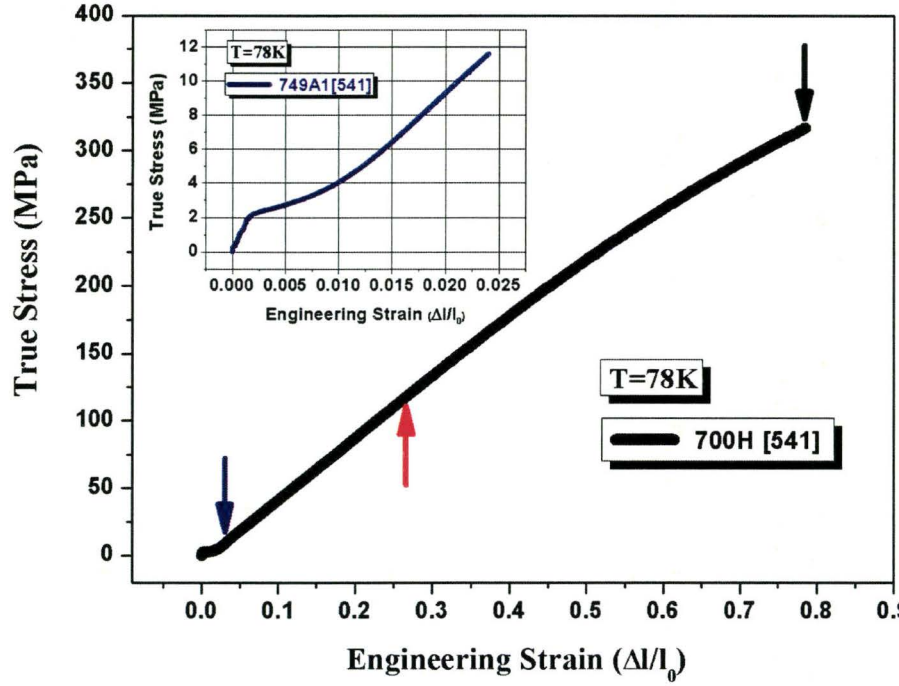

Figure 8.4: Strain-stress characteristic of $< 541 >$ single crystal deformed at 78K. The arrows point to the deformation stages of the specimens used in studies of the magnetic and electrical properties. Inset diagram shows the details of the deformation of 749A2 sample.

for electrical and magnetic properties were obtained. Sample 749A2 was deformed to *stage I*, sample 749A3 to the middle of *stage II* and sample 700H to the early *stage III*. Deformation of sample 733B2, 733B3 and 733C was carried out also to different stages marked in Figures 8.3. The resulting dislocation density developed in particular specimen has been evaluated by measuring resistivity ratios.

Table 8.2 list the results of the strain, stress and resistance measurements as well as dislocation density values in samples tested. For comparison, data for other single crystals deformed to higher stress levels and for copper polycrystals are in-

Table 8.1: Sample orientations determined form EBSD data

Sample	X	Y	Z
733B1<100>	[100]	[$\bar{1}\bar{7}5$]	[057]
733B2<100>	[100]	[$\bar{1}\bar{7}5$]	[057]
733B3<100>	[100]	[$\bar{1}\bar{6}6$]	[056]
733C<100>	[$\bar{1}$00]	[0$\bar{5}\bar{2}$]	[025]
749A1<541>	[6$\bar{1}\bar{5}$]	[$\bar{2}5\bar{3}$]	[111]
749A2<541>	[$\bar{1}\bar{5}$6]	[5$\bar{3}\bar{2}$]	[111]
749A3<541>	[$\bar{3}5\bar{2}$]	[$\bar{6}\bar{2}$5]	[345]
700H<541>	[26$\bar{3}$]	[$\bar{6}$32]	[326]

Table 8.2: The resistivity ratio and dislocation density for samples deformed to different tensile stress σ and strain ε levels.

Sample	$R_{298K}(10^{-4}\Omega)$	$R_{2K}(10^{-6}\Omega)$	RR	$N_d(10^{10}cm^{-2})$	σ_T (MPa)	$\varepsilon(10^{-2})$
733B1<100>	1.396	0.335	418	4.1	-	-
733B2<100>	0.827	0.330	251	6.8	15.6	0.63
733B3<100>	1.083	0.714	151	11.4	211.8	17.3
733C <100>	1.864	1.351	138	12.5	299.1	28.6
749A1<541>	1.487	0.372	400	4.3	-	-
749A2<541>	0.938	0.422	222	7.7	11.6	2.4
749A3<541>	1.348	0.809	166	10.4	110.2	19.2
700H <541>	2.381	2.285	104	16.5	317.0	78.4
Poly43micron	0.894	1.341	67	25.7	636.2	124

cluded in table 8.2. It is seen that, as expected, samples deformed to higher stresses exhibit smaller resistivity ratio and therefore have higher dislocation density.

8.2 Magnetoresistivity Results

8.2.1 Normal Magnetoresistivity

In the first set of experiments magnetoresistivity was measured by rotating the sample around y axis, as shown in Figure 8.2. The rotation axis is placed in the center of the stereographic projections in Figures 8.5 and 8.6. The crystallographic orientations which are scanned during sample rotation are located on the great circle at the circumference of the stereographic projection. It is easy to make such plots for other sample orientations, since the crystallographic orientations for these samples are known from EBSD data (see table 8.1) and therefor we omit these graphs. From geometry of the experimental setup it is seen that the applied current is also rotating with the sample during measurement i.e. the applied electrical field is neither exactly parallel nor perpendicular to the fixed magnetic field. We call this normal magnetoresistivity or just magnetoresistivity to differentiate it from longitudinal and transverse magnetoresistivity discussed later in section 8.2.2. Normal magnetoresistivity considered in this section is much more complicated than transverse and longitudinal magnetoresistivity because it has both components of normal and parallel to the magnetic field. In this thesis we present magnetoresistivity measurements for samples rotating along y axis without theoretical development of this subject due to its substantial complexity. We also study field-dependent normal magnetoresistance by fixing the crystallographic orientation of the sample with respect to the direction of the magnetic field vector and increasing magnetic field in the range from 0 to 9 *Tesla*.

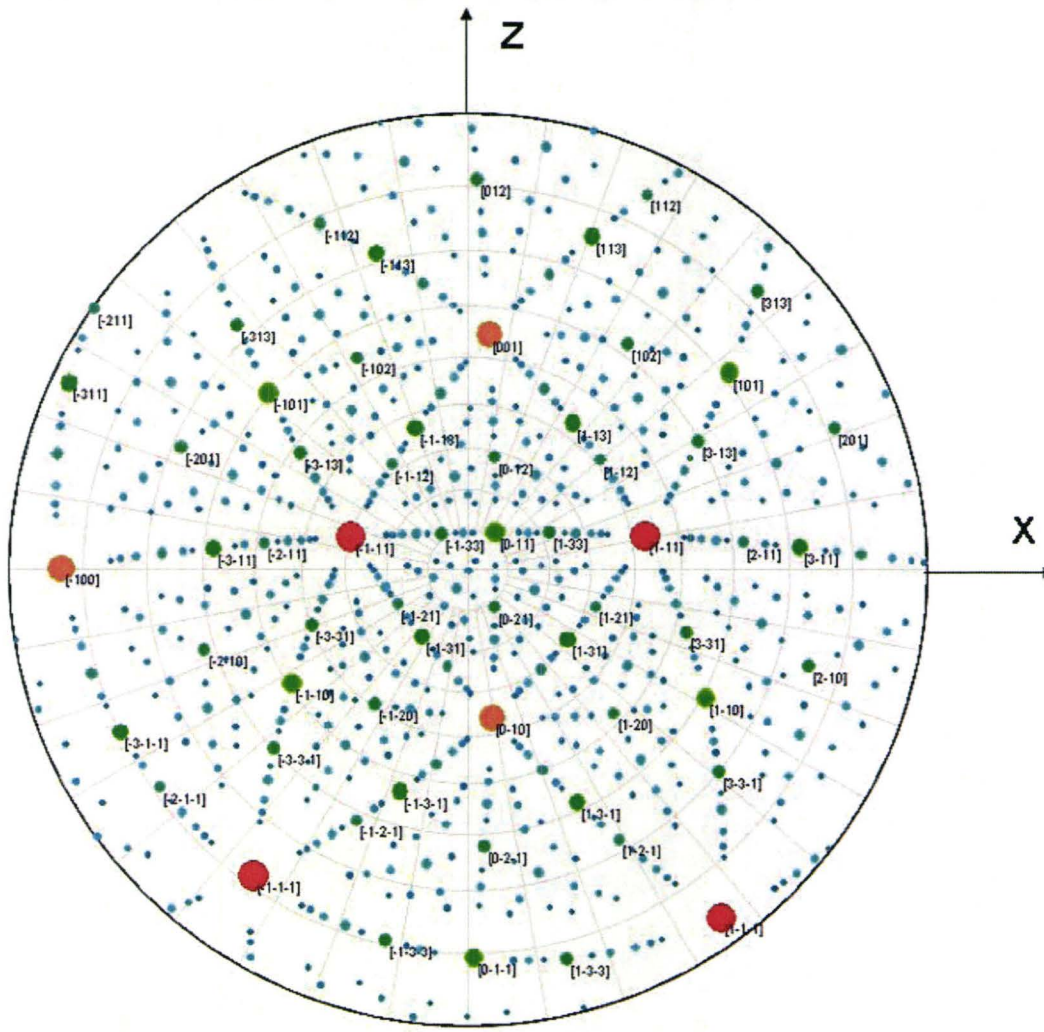

Figure 8.5: Standard stereographic projection around y axis placed in the center of the projection for sample 733B1. Crystallographic directions parallel to the applied field during sample rotation, are located on the great circle on the circumference of the projection.

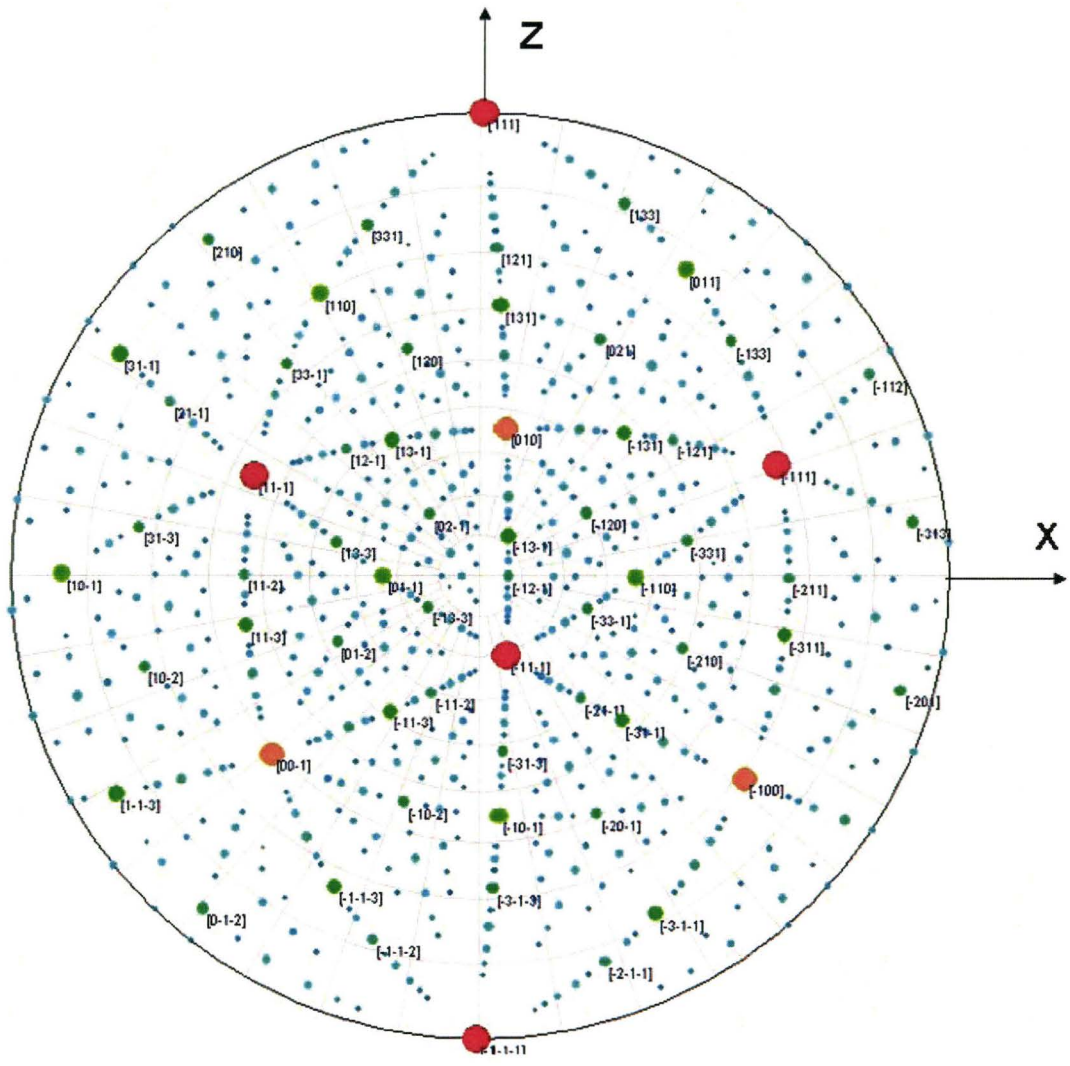

Figure 8.6: Standard stereographic projection around *y* axis placed in the center of the projection for sample 749A1. Crystallographic directions parallel to the applied field during sample rotation, are located on the great circle on the circumference of the projection.

Figures 8.7 show angular dependence of magnetoresistivity in a constant magnetic field of 9 *Tesla* (Figure 8.7(a)) and field-dependence of magnetoresistivity (Figure 8.7(b)) along field directions corresponding to high peaks marked in Figure 8.7(a) in which electrons move on open or long extended orbits for non-deformed sample 733B1 (the labels of the field orientations to high peaks in this figure or others thereafter are based on stereographic projection or calculation). It is clear from Figure 8.7(b) that the curves of field-dependence magnetoresistivity for open or long extended orbits show a quadratic behavior. The increase of resistivity with magnetic field is larger for sample orientations, which exhibit higher peaks in Figure 8.7(a).

Figures 8.8, 8.9 and 8.10 show angular and field dependence of magnetoresistivity for $< 100 >$ samples 733B2, 733B3 and 733C, deformed to higher stresses, therefore containing higher dislocation density of randomly distributed dislocations, characterized by lower resistivity ratio *RR*. It can be seen in Figures 8.7(a), 8.8(a), 8.9(a) and 8.10(a) that the curves of angle-dependent magnetoresistivity for the samples with different density of dislocations have qualitatively similar characteristics. Also, it is seen that the magnitude of peaks decreases with increasing dislocation density in the samples (*RR* is smaller). The variation of magnetoresistivity with the field for open or long extended orbits plotted in Figures 8.7(b) and 8.8(b), shows quadratic dependence in non-deformed or slightly deformed samples (flow stress equal $15.6MPa$). On the other hand, the behavior of magnetoresistivity for the largely deformed samples 733B3 and 733C (flow stress equal $211.8MPa$

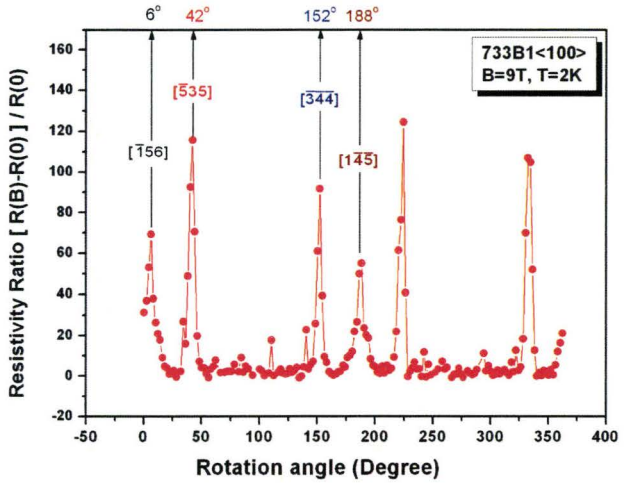

(a) Resistivity ratio $(R(\vec{B}) - R(0))/R(0)$ against rotation angle around y-axis in the constant magnetic field of 9 *Tesla* for non-deformed sample 733B1. The crystallographic orientation of the sample parallel to the magnetic field is marked in the figure for selected rotation angles.

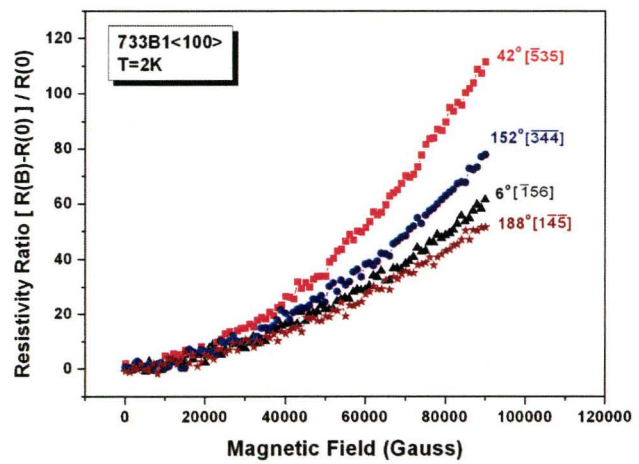

(b) Resistivity ratio as a function of the magnetic field for non-deformed sample 733B1. Each curve corresponds to the different orientation of the sample parallel to the magnetic field, marked in Figure 8.7(a) and the electrical field has a constant angle with the magnetic field in each measurement.

Figure 8.7: Magnetoresistivity characteristics for non-deformed sample 733B1 in y-axis rotation in the magnetic field.

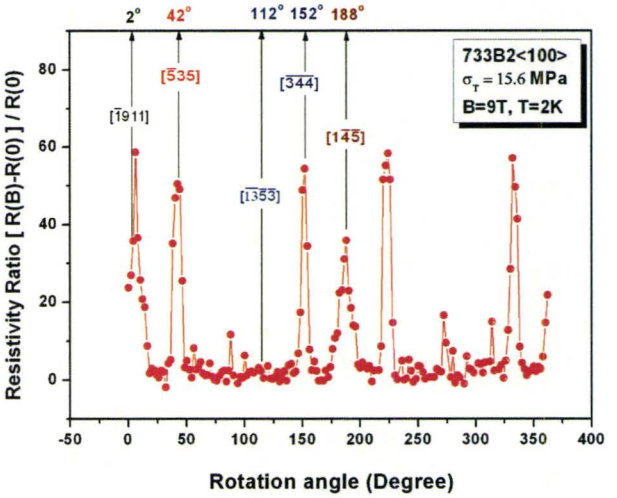

(a) Resistivity ratio $(R(\vec{B}) - R(0))/R(0)$ against rotation angle around y-axis in the constant magnetic field of 9 *Tesla* for 733B2 sample deformed to 15.6 *MPa*. The crystallographic orientation of the sample parallel to the magnetic field is marked in the figure for selected rotation angles.

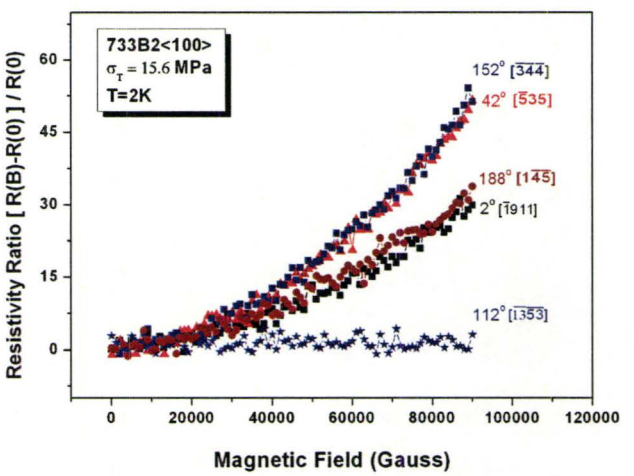

(b) Resistivity ratio as a function of the magnetic field for 733B2 sample deformed to 15.6 *MPa*. Each curve corresponds to the different orientation of the sample parallel to the magnetic field, marked in Figure 8.8(a). The electrical field has a constant angle with the magnetic field in each measurement.

Figure 8.8: Magnetoresistivity characteristics for 733B2 sample deformed to 15.6 *MPa*, in y-axis rotation in the magnetic field.

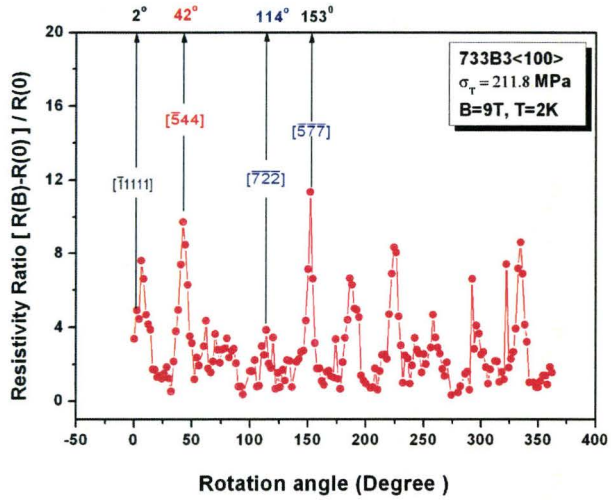

(a) Resistivity ratio $(R(\vec{B}) - R(0))/R(0)$ against rotation angle around y-axis in the constant magnetic field of 9 *Tesla* for 733B3 sample deformed to 211.8 *MPa*. The crystallographic orientation of the sample parallel to the magnetic field is marked in the figure for selected rotation angles.

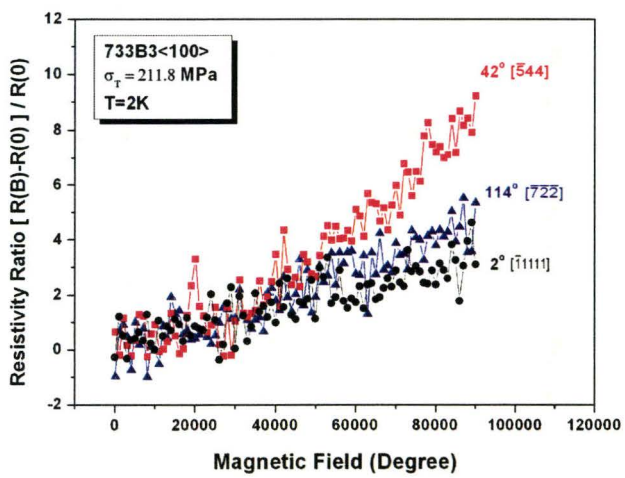

(b) Resistivity ratio as a function of the magnetic field for 733B3 sample deformed to 211.8 *MPa*. Each curve corresponds to the different orientation of the sample parallel to the magnetic field, marked in Figure 8.9(a). The electrical field has a constant angle with the magnetic field in each measurement.

Figure 8.9: Magnetoresistivity characteristics for 733B3 sample deformed to 211.8 *MPa*, in y-axis rotation in the magnetic field.

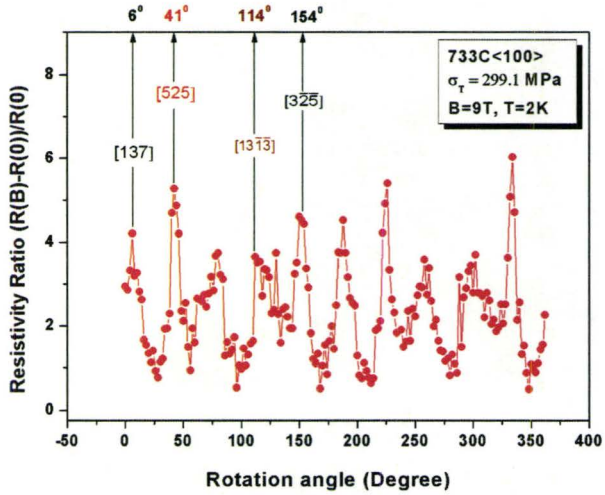

(a) Resistivity ratio $(R(\vec{B}) - R(0))/R(0)$ against rotation angle around y-axis in the constant magnetic field of 9 *Tesla* for 733C sample deformed to 299.1 *MPa*. The crystallographic orientation of the sample parallel to the magnetic field is marked in the figure for selected rotation angles.

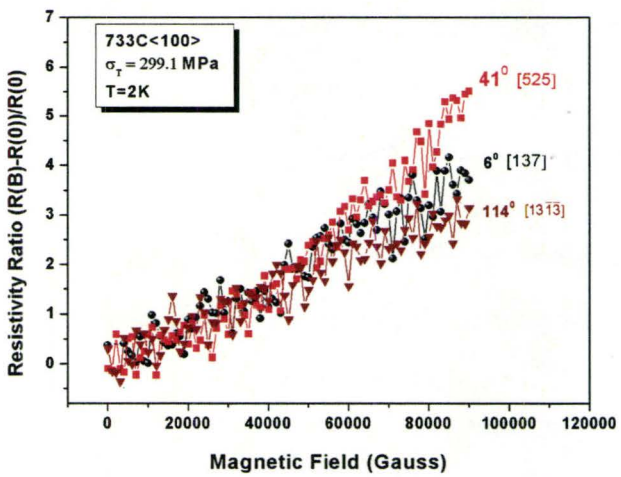

(b) Resistivity ratio as a function of the magnetic field for 733C sample deformed to 299.1 *MPa*. Each curve corresponds to the different orientation of the sample parallel to the magnetic field, marked in Figure 8.10(a). The electrical field has a constant angle with the magnetic field in each measurement.

Figure 8.10: Magnetoresistivity characteristics for 733C sample deformed to 299.1 *MPa*, in y-axis rotation in the magnetic field.

and 299.1MPa respectively) is more like linear at the high fields, as demonstrated in Figures 8.9(b) and 8.10(b).

For another type of dislocations that are induced in samples 749A1, 749A2, 749A3 and 700H by straining single crystals along $< 541 >$ crystallographic orientation of the tensile axis, similar behavior of magnetoresistivity, as in crystals 733B's oriented along $< 100 >$, is observed . The angular dependence of magnetoresistivity exhibits similar pick pattern at the position of open or long extended orbits and the magnitude of peaks is reduced as the resistivity ratio RR decreases (see Figures 8.11(a), 8.12(a), 8.13(a) and 8.14(a)). The variation of magnetoresistivity with the field is quadratic for non-deformed and slightly deformed samples (Figure 8.11(b) and 8.12(b)), and almost linear at the high fields for largely deformed samples (Figures 8.13(b) and 8.14(b)).

In all magnetoresistivity measurements as the samples rotate around y-axis, we have not observed appreciable difference in the form and character of the magnetoresistivity and field-dependent magnetoresistivity data between two crystal orientations, $< 541 >$ and $< 100 >$. This suggest that magnetoresistivity properties depend strongly upon the density of dislocations but not on the type of dislocation substructure accumulated in the sample.

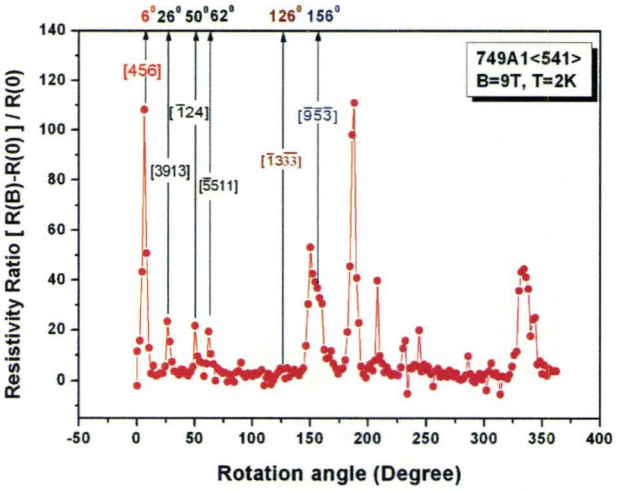

(a) Resistivity ratio $(R(\vec{B}) - R(0))/R(0)$ against rotation angle around y-axis in the constant magnetic field of 9 *Tesla* for non-deformed sample 749A1. The crystallographic orientation of the sample parallel to the magnetic field is marked in the figure for selected rotation angles.

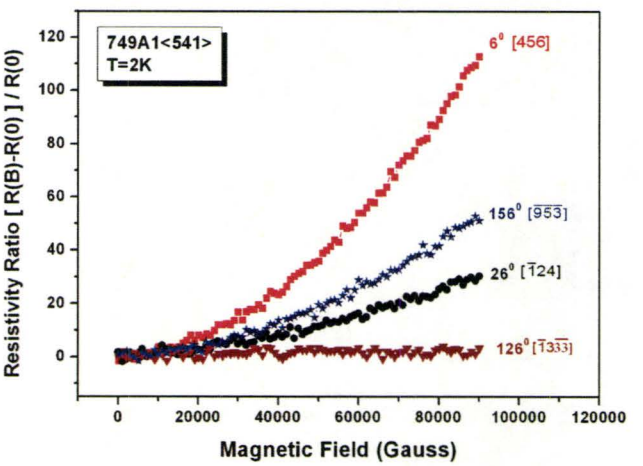

(b) Resistivity ratio as a function of the magnetic field for non-deformed sample 749A1. Each curve corresponds to the different orientation of the sample parallel to the magnetic field, marked in Figure 8.11(a). The electrical field has a constant angle with the magnetic field in each measurement.

Figure 8.11: Magnetoresistivity characteristics for non-deformed sample 749A1 in y-axis rotation in the magnetic field.

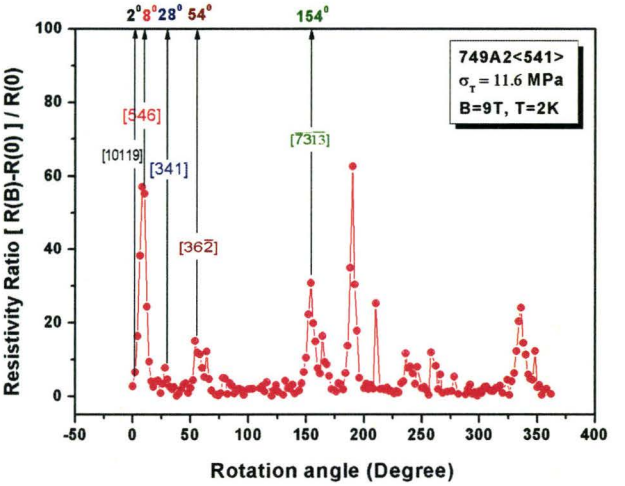

(a) Resistivity ratio $(R(\vec{B}) - R(0))/R(0)$ against rotation angle around y-axis in the constant magnetic field of 9 *Tesla* for 749A2 sample deformed to 11.6 *MPa*. The crystallographic orientation of the sample parallel to the magnetic field is marked in the figure for selected rotation angles.

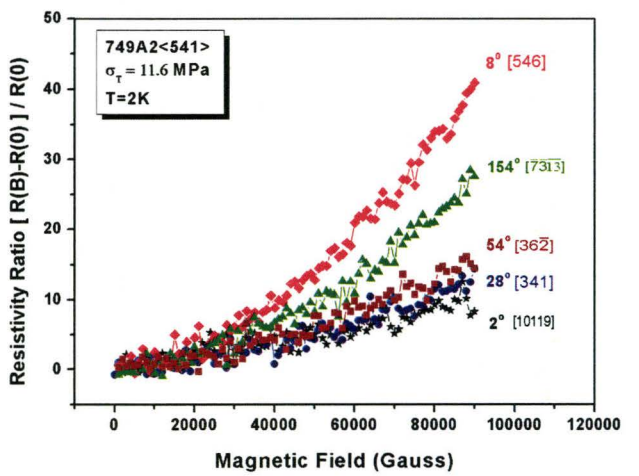

(b) Resistivity ratio as a function of the magnetic field for sample 749A2 deformed to 11.6 *MPa* . Each curve corresponds to the different orientation of the sample parallel to the magnetic field, marked in Figure 8.12(a) and the electrical field has a constant angle with the magnetic field in each measurement.

Figure 8.12: Magnetoresistivity characteristics for 749A2 sample deformed to 11.6 *MPa*, in y-axis rotation in the magnetic field.

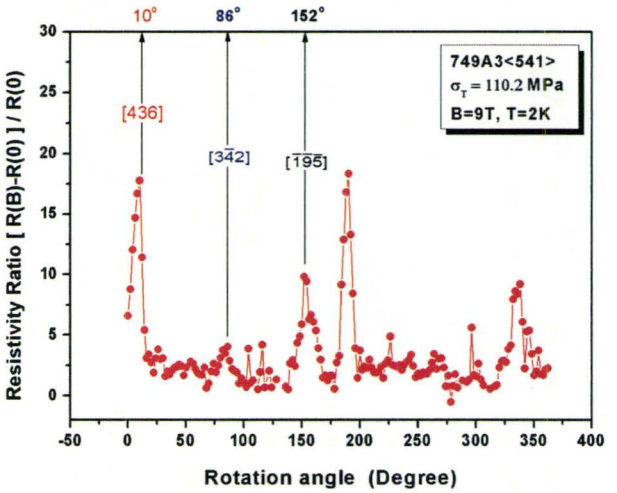

(a) Resistivity ratio $(R(\vec{B}) - R(0))/R(0)$ against rotation angle around y-axis in the constant magnetic field of 9 *Tesla* for 749A3 sample deformed to 110.2 *MPa*. The crystallographic orientation of the sample parallel to the magnetic field is marked in the figure for selected rotation angles.

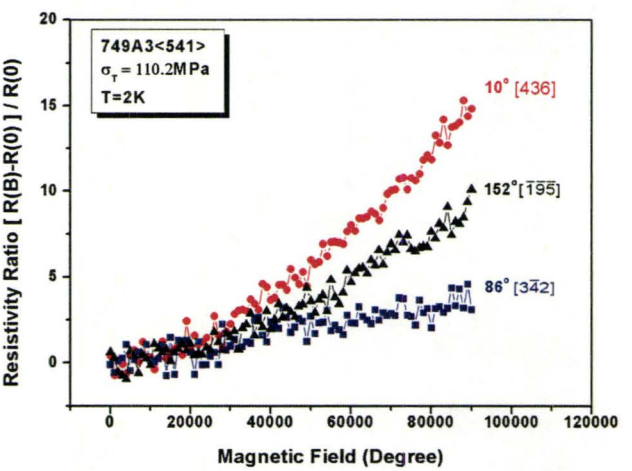

(b) Resistivity ratio as a function of the magnetic field for 749A3 sample deformed to 110.2 *MPa*. Each curve corresponds to the different orientation of the sample parallel to the magnetic field, marked in Figure 8.13(a). The electrical field has a constant angle with the magnetic field in each measurement.

Figure 8.13: Magnetoresistivity characteristics for 749A3 sample deformed to 110.2 *MPa*, in y-axis rotation in the magnetic field.

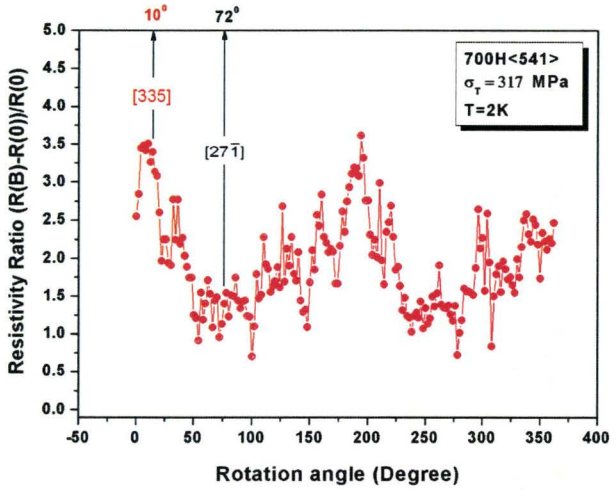

(a) Resistivity ratio $(R(\vec{B}) - R(0))/R(0)$ against rotation angle around y-axis in the constant magnetic field of 9 *Tesla* for 700H sample deformed to 317 *MPa*. The crystallographic orientation of the sample parallel to the magnetic field is marked in the figure for selected rotation angles.

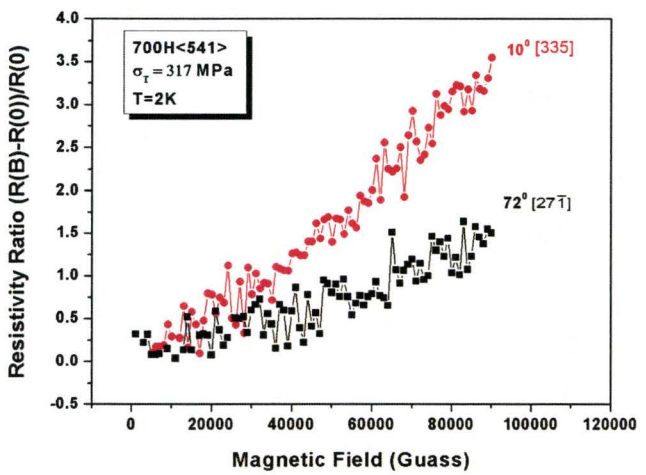

(b) Resistivity ratio as a function of the magnetic field for 700H sample deformed to 317 *MPa*. Each curve corresponds to the different orientation of the sample parallel to the magnetic field, marked in Figure 8.14(a) and the electrical field has a constant angle with the magnetic field in each measurement.

Figure 8.14: Magnetoresistivity characteristics for 700H sample deformed to 317 *MPa*, in y-axis rotation in the magnetic field.

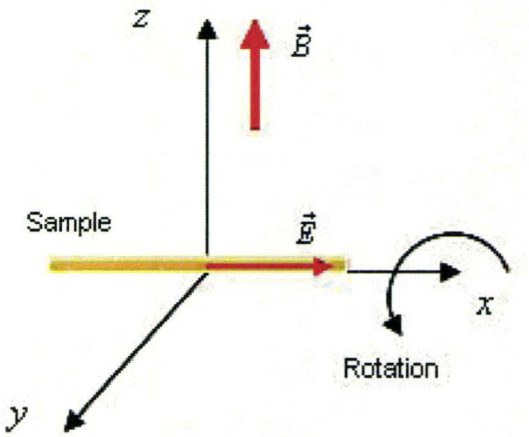

Figure 8.15: Geometrical setup for measurement of transverse magnetoresistance. Samples rotate along x-axis in the magnetic field fixed in z-axis, which is perpendicular to the electrical field.

8.2.2 Transverse Magnetoresistivity

Transverse magnetoresistance is determined under conditions of a magnetic field perpendicular to electrical field. Transverse magnetoresistance was measured by rotating the samples around x-axis in the constant magnetic field of 9 *Tesla*, as shown in Figure 8.15. The rotation axis, x axis of the samples, is placed in the center of the stereographic projections in Figures 8.16 and 8.17 for samples 733B1 and 749A1 respectively. The crystallographic orientations scanned during sample rotation are located on the great circle at the circumference of the stereographic projection. As in previous case, we studied field-dependent magnetoresistance by fixing the crystallographic orientation of the sample with respect to direction of magnetic field and increasing magnetic field in the range from 0 to 9 *Tesla*.

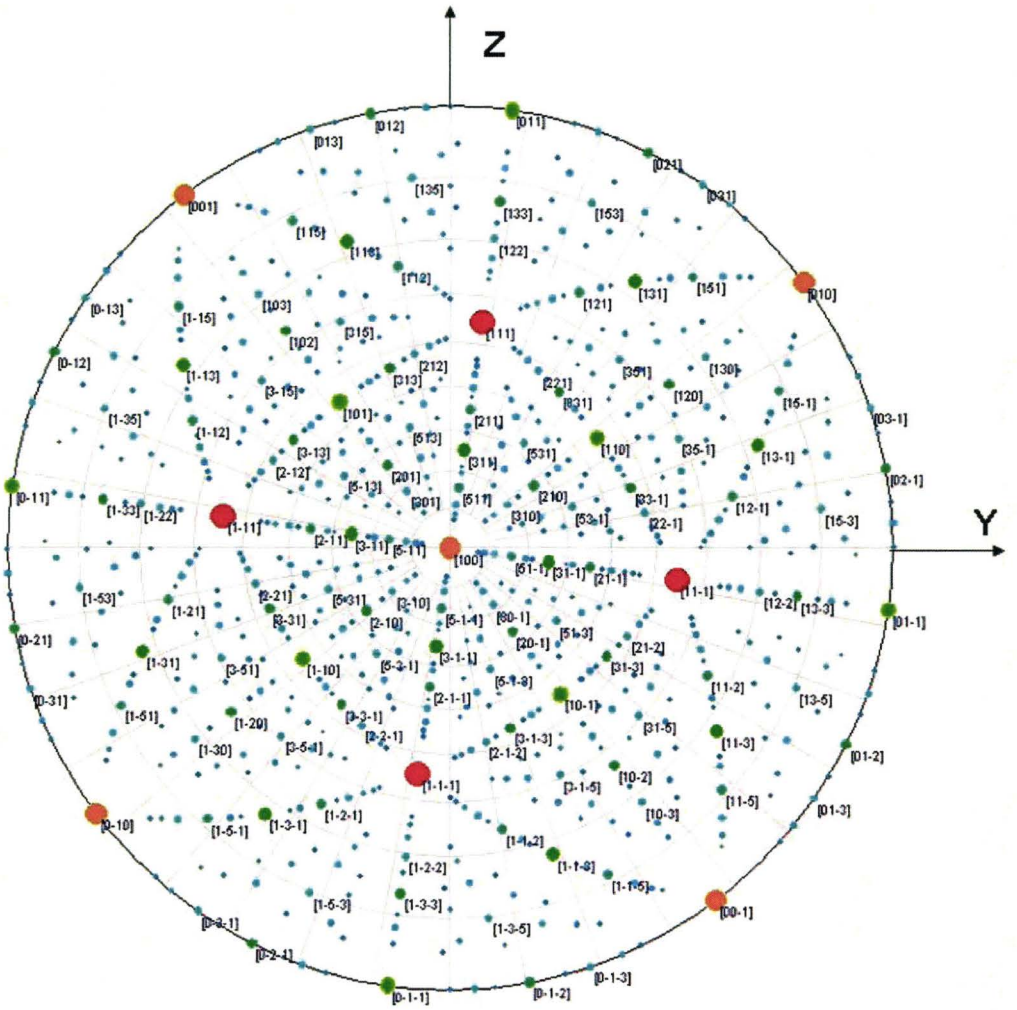

Figure 8.16: Standard stereographic projection around x axis placed in the center of the projection for sample 733B1. Crystallographic directions parallel to the applied field during sample rotation, are located on the great circle on the circumference of the projection.

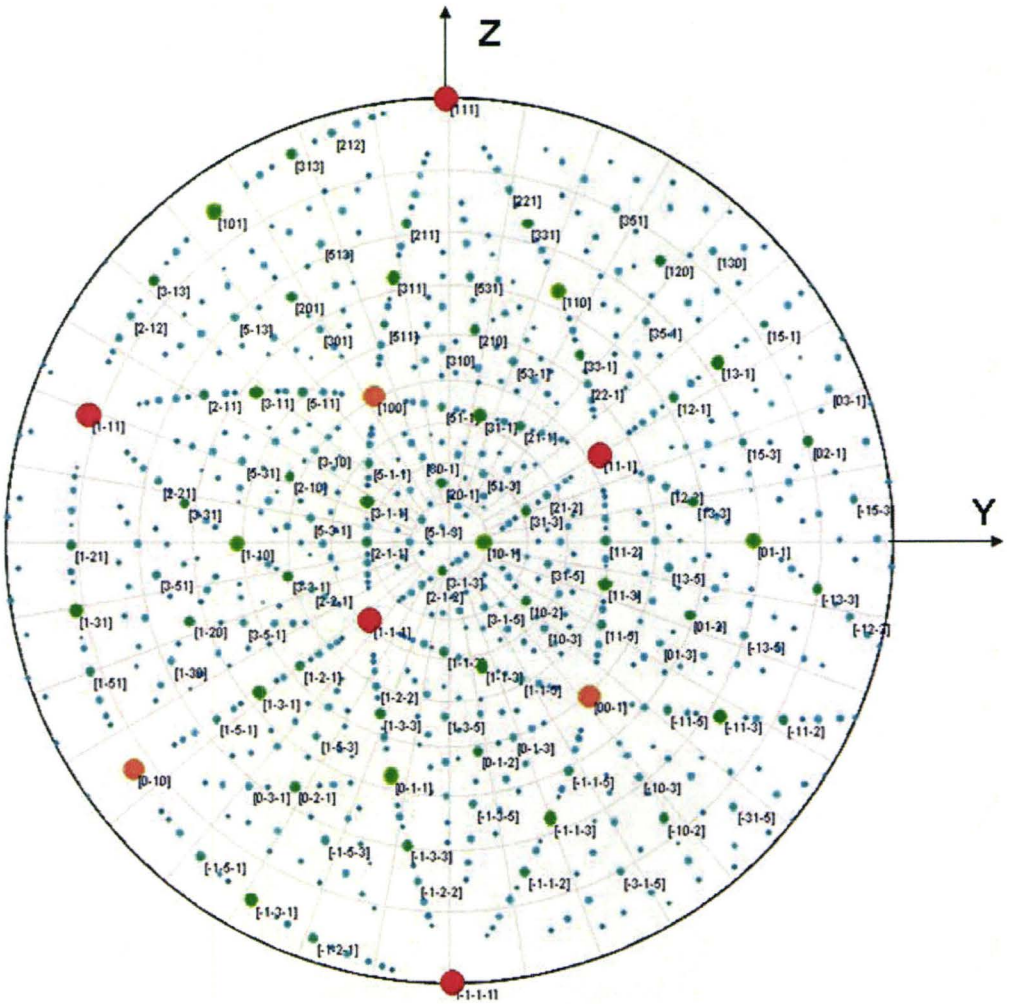

Figure 8.17: Standard stereographic projection around x axis placed in the center of the projection for sample 749A1. Crystallographic directions parallel to the applied field during sample rotation, are located on the great circle on the circumference of the projection.

Figure 8.18(a) is the plot of transverse magnetoresistivity as a function of sample rotation angle around $< 100 >$ pole for sample 733B1 ($RR = 418$). As seen in the stereographic projection 8.16 for the sample, in this set of measurements the magnetic field sweeps through four $< 110 >$ and four $< 100 >$ crystallographic directions in a complete 360 degree revolution of the sample. The adjacent $< 110 >$ or $< 100 >$ directions are spaced by 45 degrees. Electrons move on closed orbits when the sample rotates to the position in which the field is along $< 110 >$ and/or $< 100 >$ crystallographic directions (see Figure 3.7). Eight $< 013 >$ directions also correspond to closed-orbit orientation and are also spaced by 45 degree from each other. They are separated by $< 110 >$ and/or $< 100 >$ closed orbit directions (Figure 8.18(a)). Consequently, magnetoresistivity will have minimum values at the rotation angles corresponding exactly to $< 100 >$, $< 110 >$ and $< 013 >$. It is seen in Figure 8.18(a) that each lowest point marking exact orientation of the closed orbit is associated with two peaks corresponding to open or long extend orbits when the sample orientation deviates in both sides slightly from exact position of the closed orbit. This experimental observation is in agreement with the statement that if the magnetic field continuously deviates from the closed-orbit orientation, the electron orbit will smoothly change to extended or open orbits (Abrikosov, 1972; Lifshitz *et al.*, 1973). Therefore, there are totally sixteen peaks in a 360-degree rotation of the sample around $< 100 >$ pole, associated with sixteen $< 110 >$, $< 100 >$ and $< 013 >$ orientations parallel to the magnetic field to cause closed-orbits. Figure 8.18(a) displays such features, consistent with experimental observations made by other researchers (Klauder *et al.*, 1966).

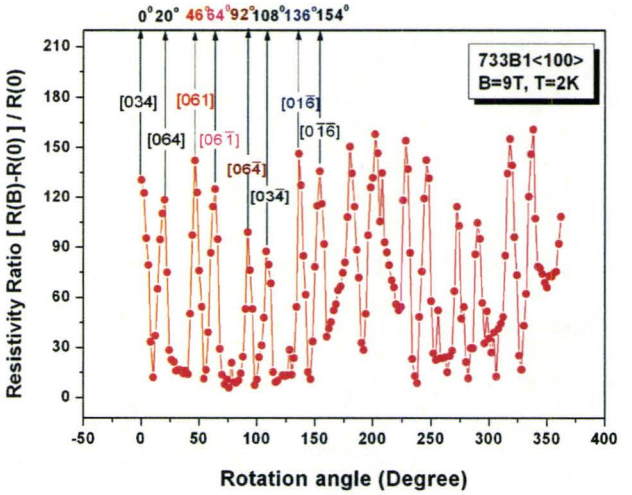

(a) Resistivity ratio $(R(\vec{B}) - R(0))/R(0)$ against rotation angle around x-axis in the constant magnetic field of 9 *Tesla* for non-deformed sample 733B1. The crystallographic orientation of the sample parallel to the magnetic field is marked in the figure for selected rotation angles.

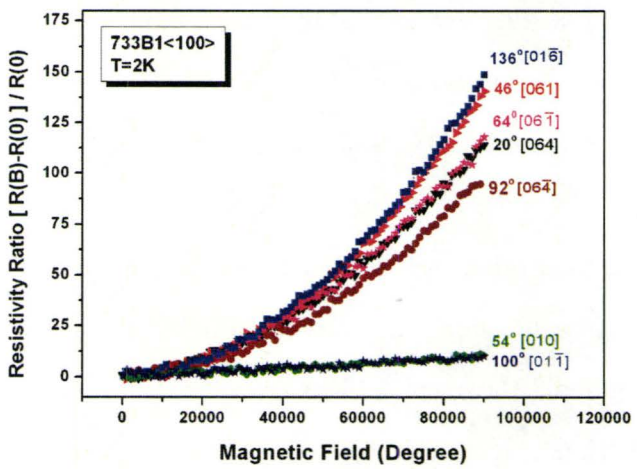

(b) Resistivity ratio as a function of the magnetic field for non-deformed sample 733B1. Each curve corresponds to the different orientation of the sample parallel to the magnetic field, marked in Figure 8.18(a) and the electrical field is perpendicular to the magnetic field in each measurement.

Figure 8.18: Transverse magnetoresistivity characteristics for non-deformed sample 733B1 in x-axis rotation in the magnetic field.

Figure 8.18(b) is the plot of field-dependent transverse magnetoresistivity for open or long extended orbits and for closed orbits corresponding to rotation angles labeled in Figure 8.18(a). It is seen that magnetoresistivity versus the field has a quadratic behavior for open or long extended orbits and linear for closed orbits.

Figures 8.19, 8.20 and 8.21 show angle and field-dependent transverse magnetoresistivity for $< 100 >$ samples; 733B2 ($RR = 251$), 733B3 ($RR = 151$) and 733C ($RR = 138$) deformed to larger strains. It can be seen by comparison of Figures 8.18(a), 8.19(a), 8.20(a) and 8.21(a) that dislocations induced in the samples substantially reduce magnetoresistivity for open or long extended orbits. For the strongly deformed samples 733B3 and 733C, the high and sharp peaks disappear, instead smooth and flat curves are observed. It is interesting to note that the troughs corresponding to closed orbits still remain for the magnetic field oriented along $< 100 >$ and $< 110 >$ directions. In the plots of field-dependent transverse magnetoresistivity, Figures 8.18(b) and 8.19(b) show the quadratic variation for open or long extended orbits. Figure 8.21(b) displays a linear change at large fields for highly deformed sample 733C, whereas sample 733B3 deformed to stage *II* and thus containing less dislocations than 733C sample shows behavior somewhere between quadratic and linear (Figure 8.20(b)). In general, it can be concluded that magnetoresistivity for open or long extended orbits decreases in the samples containing higher content of dislocations.

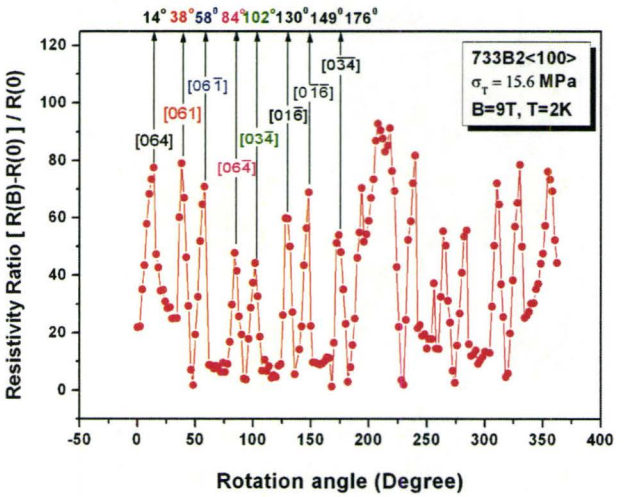

(a) Resistivity ratio $(R(\vec{B}) - R(0))/R(0)$ against rotation angle around x-axis in the constant magnetic field of 9 *Tesla* for 733B2 sample deformed to 15.6 *MPa*. The crystallographic orientation of the sample parallel to the magnetic field is marked in the figure for selected rotation angles.

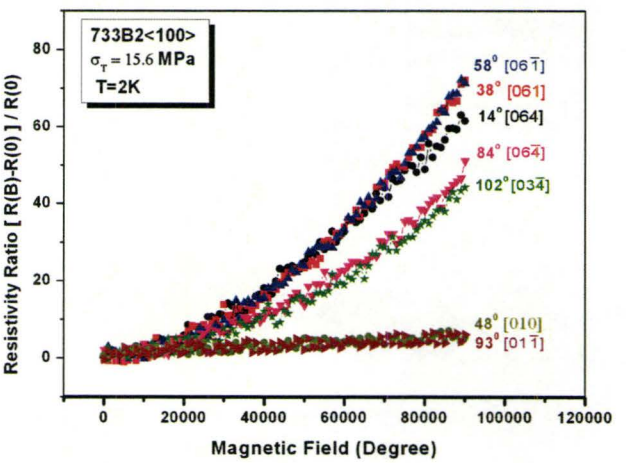

(b) Resistivity ratio as a function of the magnetic field for 733B2 sample deformed to 15.6 *MPa*. Each curve corresponds to the different orientation of the sample parallel to the magnetic field, marked in Figure 8.19(a). The electrical field is perpendicular to the magnetic field in each measurement.

Figure 8.19: Transverse magnetoresistivity characteristics for 733B2 sample deformed to 15.6 *MPa*, in x-axis rotation in the magnetic field.

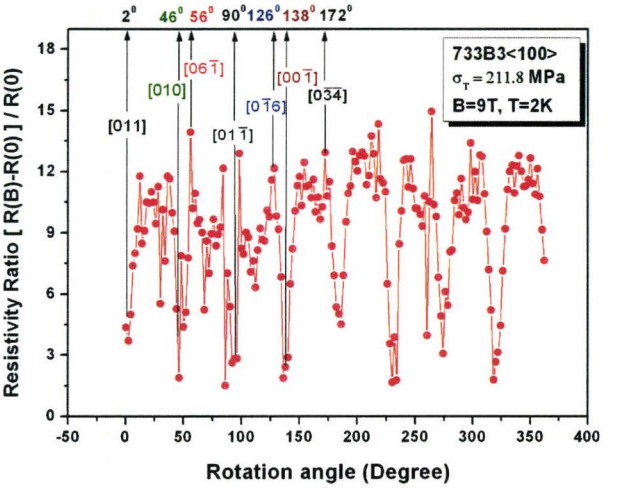

(a) Resistivity ratio $(R(\vec{B}) - R(0))/R(0)$ against rotation angle around x-axis in the constant magnetic field of 9 *Tesla* for sample 733B3 deformed to 211.8 *MPa*. The crystallographic orientation of the sample parallel to the magnetic field is marked in the figure for selected rotation angles.

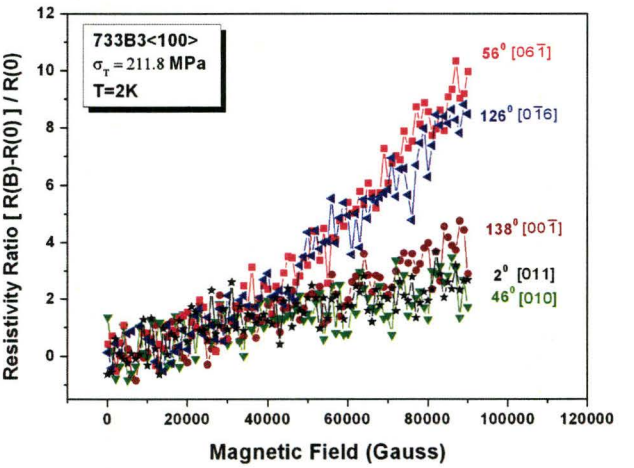

(b) Resistivity ratio as a function of the magnetic field for sample 733B3 deformed to 211.8 *MPa*. Each curve corresponds to the different orientation of the sample parallel to the magnetic field, marked in Figure 8.20(a) and the electrical field is perpendicular to the magnetic field in each measurement.

Figure 8.20: Transverse magnetoresistivity characteristics for sample 733B3 deformed to 211.8 *MPa*, in x-axis rotation in the magnetic field.

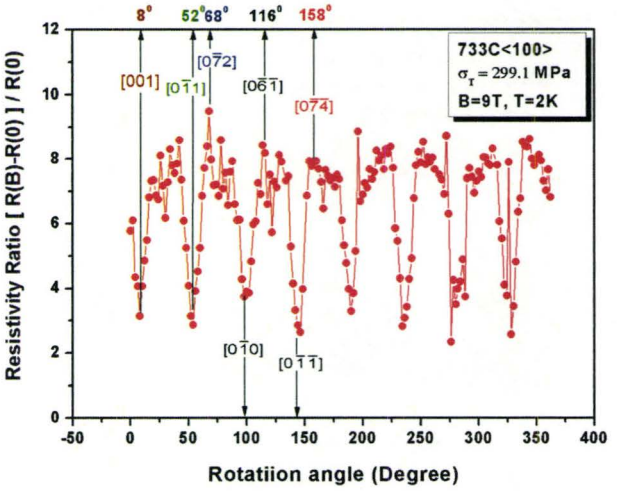

(a) Resistivity ratio $(R(\vec{B}) - R(0))/R(0)$ against rotation angle around x-axis in the constant magnetic field of 9 *Tesla* for 733C sample deformed to 299.1 *MPa*. The crystallographic orientation of the sample parallel to the magnetic field is marked in the figure for selected rotation angles.

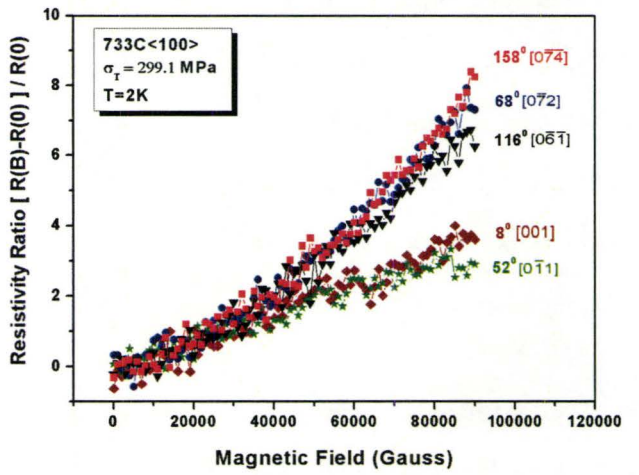

(b) Resistivity ratio as a function of the magnetic field for 733C sample deformed to 299.1 *MPa*. Each curve corresponds to the different orientation of the sample parallel to the magnetic field, marked in Figure 8.21(a). The electrical field is perpendicular to the magnetic field in each measurement.

Figure 8.21: Transverse magnetoresistivity characteristics for 733C sample deformed to 299.1 *MPa*, in x-axis rotation in the magnetic field.

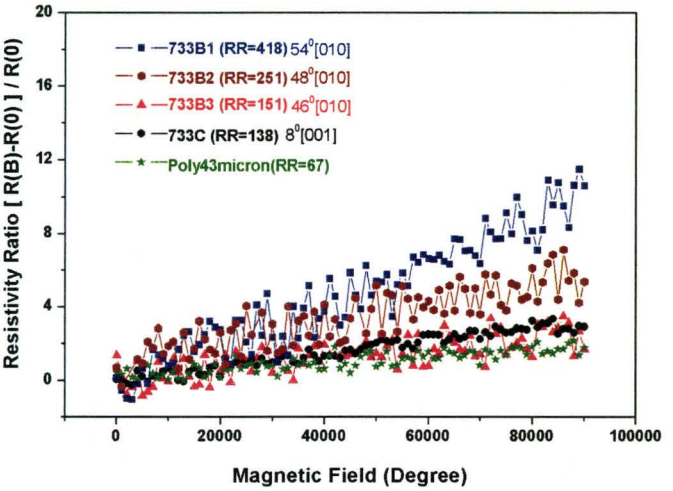

Figure 8.22: Transverse magnetoresistivity characteristics for closed orbits for sample 733B's, 733C and poly43micron in x-axis rotation in the magnetic field.

In order to make a better comparison of transverse magnetoresistivity for closed orbits, we plotted experimental data in Figure 8.22 for the samples with different density of dislocations characterized by value of *RR*. It is clear that the variation of transverse magnetoresistivity with the magnetic field for closed orbits is linear and with more dislocation introduced to the samples represented by decreasing value of resistivity ration *RR*, the slope of these characteristics decreases.

In case of samples deformed along $< 541 >$ the transverse magnetoresistivity data show quantitative similarity to the characteristics of $< 100 >$ 733B's samples discussed above. From Figures 8.23(a), 8.24(a), 8.25(a) and 8.26(a) it can be seen that magnetoresistivity corresponding to open or long extended orbits are largely reduced as resistivity ratio *RR* decreases. It is clear from stereographic projection 8.17 that the magnetic field will sweep through two $< 111 >$ crystallographic planes

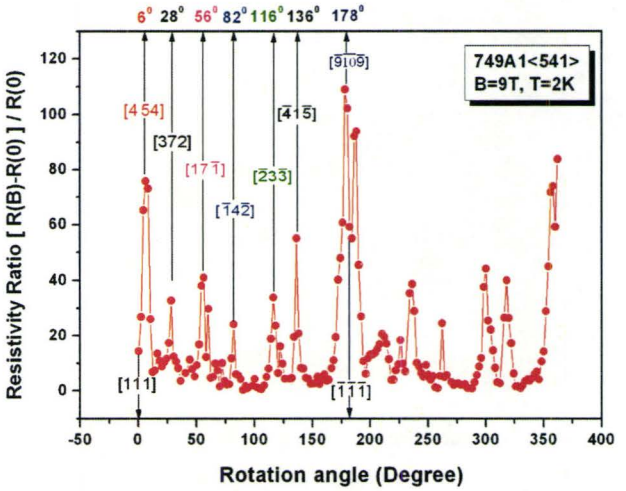

(a) Resistivity ratio $(R(\vec{B}) - R(0))/R(0)$ against rotation angle around x-axis in the constant magnetic field of 9 *Tesla* for non-deformed deformed sample 749A1. The crystallographic orientation of the sample parallel to the magnetic field is marked in the figure for selected rotation angles.

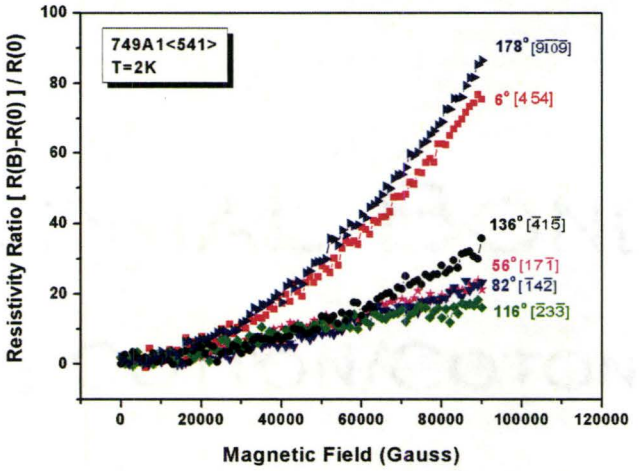

(b) Resistivity ratio as a function of the magnetic field for non-deformed sample 749A1. Each curve corresponds to the different orientation of the sample parallel to the magnetic field, marked in Figure 8.23(a) and the electrical field is perpendicular to the magnetic field in each measurement.

Figure 8.23: Transverse magnetoresistivity characteristics for non-deformed sample 749A1 in x-axis rotation in the magnetic field.

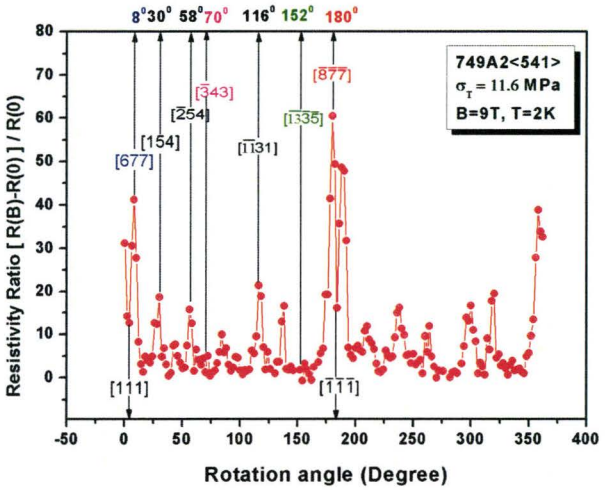

(a) Resistivity ratio $(R(\vec{B}) - R(0))/R(0)$ against rotation angle around x-axis in the constant magnetic field of 9 *Tesla* for 749A2 sample deformed to 11.6 *MPa*. The crystallographic orientation of the sample parallel to the magnetic field is marked in the figure for selected rotation angles.

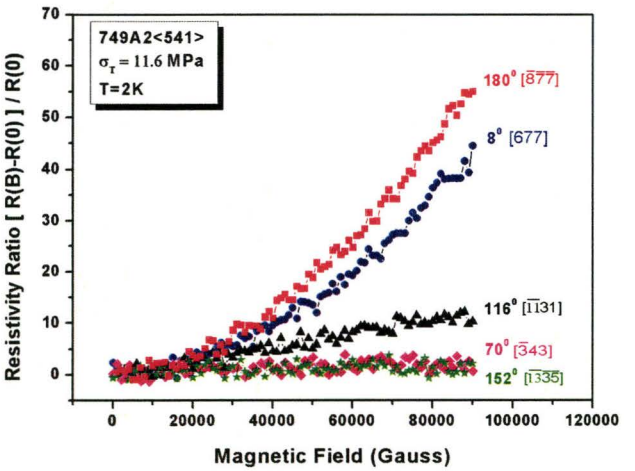

(b) Resistivity ratio as a function of the magnetic field for 749A2 sample deformed to 11.6 *MPa*. Each curve corresponds to the different orientation of the sample parallel to the magnetic field, marked in Figure 8.24(a). The electrical field is perpendicular to the magnetic field in each measurement.

Figure 8.24: Transverse magnetoresistivity characteristics for 749A2 sample deformed to 11.6 *MPa*, in x-axis rotation in the magnetic field.

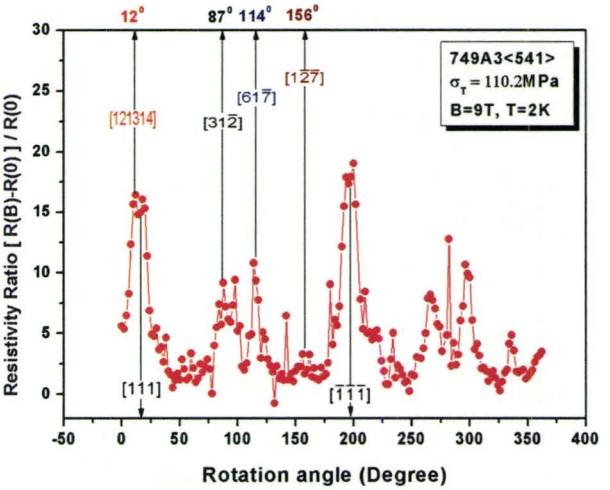

(a) Resistivity ratio $(R(\vec{B}) - R(0))/R(0)$ against rotation angle around x-axis in the constant magnetic field of 9 *Tesla* for 749A3 sample deformed to 110.2 *MPa*. The crystallographic orientation of the sample parallel to the magnetic field is marked in the figure for selected rotation angles.

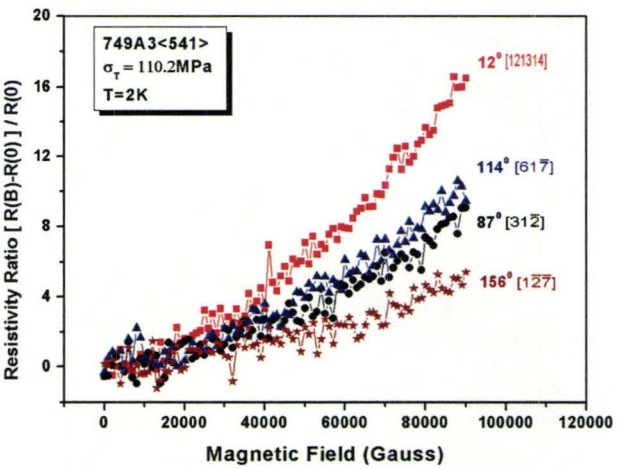

(b) Resistivity ratio as a function of the magnetic field for 749A3 sample deformed to 110.2 *MPa*. Each curve corresponds to the different orientation of the sample parallel to the magnetic field, marked in Figure 8.25(a) and the electrical field is perpendicular to the magnetic field in each measurement.

Figure 8.25: Transverse magnetoresistivity characteristics for 749A3 sample deformed to 110.2 *MPa*, in x-axis rotation in the magnetic field.

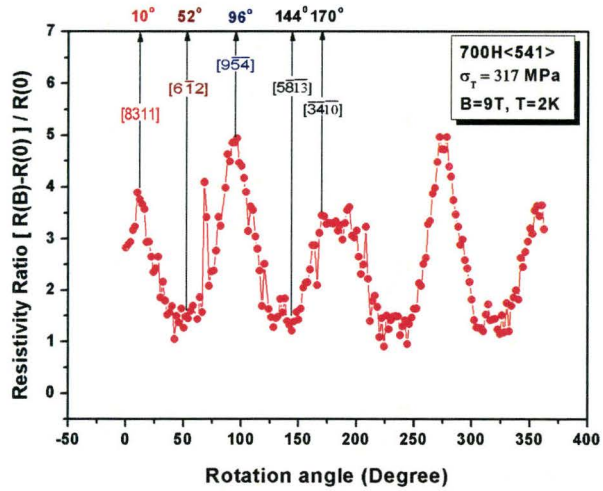

(a) Resistivity ratio $(R(\vec{B}) - R(0))/R(0)$ against rotation angle around x-axis in the constant magnetic field of 9 *Tesla* for sample 700H deformed to 317 *MPa*. The crystallographic orientation of the sample parallel to the magnetic field is marked in the figure for selected rotation angles.

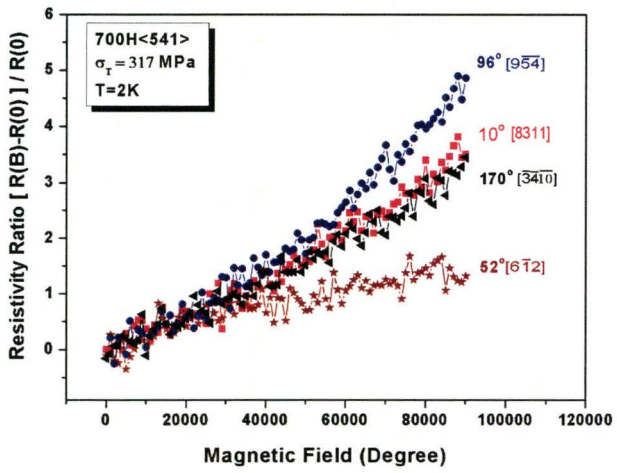

(b) Resistivity ratio as a function of the magnetic field for sample 700H deformed to 317 *MPa*. Each curve corresponds to the different orientation of the sample parallel to the magnetic field, marked in Figure 8.26(a) and the electrical field is perpendicular to the magnetic field in each measurement.

Figure 8.26: Transverse magnetoresistivity characteristics for sample 700H deformed to 317 *MPa*, in x-axis rotation in the magnetic field.

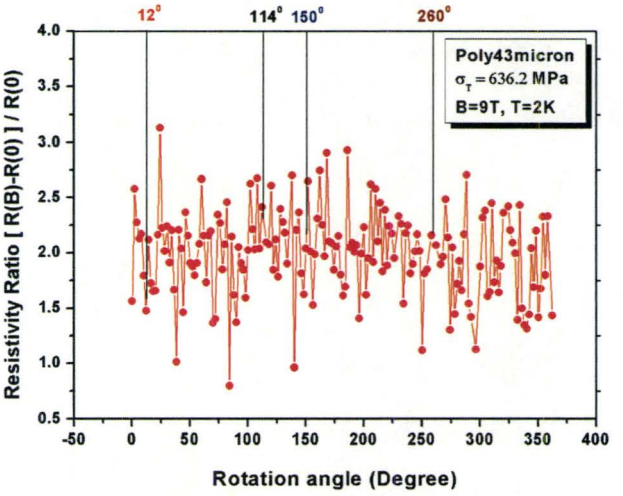

(a) Resistivity ratio $(R(\vec{B}) - R(0))/R(0)$ against rotation angle around x-axis in the constant magnetic field of 9 *Tesla* for polycrystalline copper sample with the grain size of 43 microns, deformed to 636.2*MPa* of tensile stress. The crystallographic orientation of the sample parallel to the magnetic field is marked in the figure for selected rotation angles.

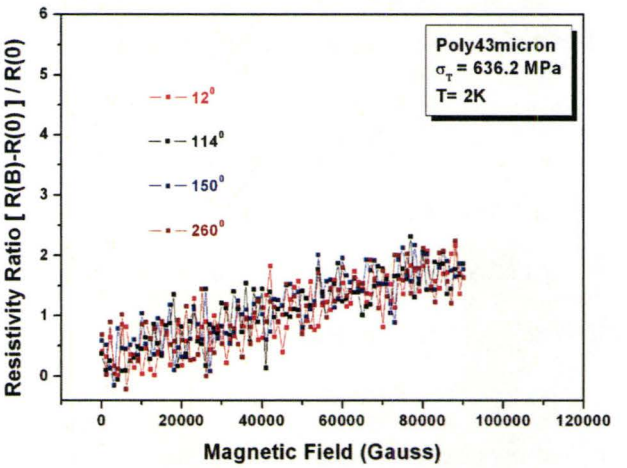

(b) Resistivity ratio as a function of the magnetic field for polycrystalline sample with the grain size of 43 microns, deformed at 4K to the flow stress of 636.2 *MPa*. Each curve corresponds to the different orientation of the sample parallel to the magnetic field, marked in Figure 8.27(a) and the electrical field is perpendicular to the magnetic field in each measurement.

Figure 8.27: Transverse magnetoresistivity characteristics for polycrystalline copper sample with the grain size of 43 microns, deformed at 4K to the flow stress of 636.2 *MPa*, in x-axis rotation in the magnetic field.

of the samples in $< 541 >$ deformation. Consequently, high peaks occurs when the magnetic field is oriented close to $< 111 >$ crystallographic direction, corresponding to closed orbits. It is found that the high and sharp peaks in pure or slightly deformed samples are replaced by the smoother peaks in largely deformed samples. Present observations are compatible with the data published by other researchers (Klauder *et al.*, 1966). Figures 8.23(b), 8.24(b), 8.25(b) and 8.26(b) reveal that that field-dependent transverse magnetoresistivity substantially decreases as more dislocations is stored in the samples, a behavior observed previously in $< 100 >$ samples. A non-deformed and slightly deformed samples 749A1 and 749A2 show a quadratic dependence of magnetoresistivity with the field, whereas a linear variation at large fields is observed in highly deformed sample 700H. Similar to the conclusions drawn from normal magnetoresistivity data, present experiments also indicate that there is no difference between two types of dislocation substructure stored in the $< 541 >$ and $< 100 >$ samples on transverse magnetoresistance properties.

The transverse magnetoresistivity in all deformed samples tested in this work, including highly deformed samples with the tensile stress approaching 317 *MPa*, is still very anisotropic. Deformed single crystal samples have however different galvanomagnetic properties from deformed polycrystalline samples. As a comparison, Figures 8.27 shows experimental data for highly deformed polycrystalline sample, where a large and frequent oscillation of angle-dependent transverse magnetoresistivity are observed (Figure 8.27(a)). At the same time the samples exhibit a linear behavior of field-dependent transverse magnetoresistivity, but have a smaller constant slope for different rotation angles, which can be viewed as an ev-

idence of isotropy of transverse magnetoresistivity in polycrystalline samples (Figure 8.27(b)).

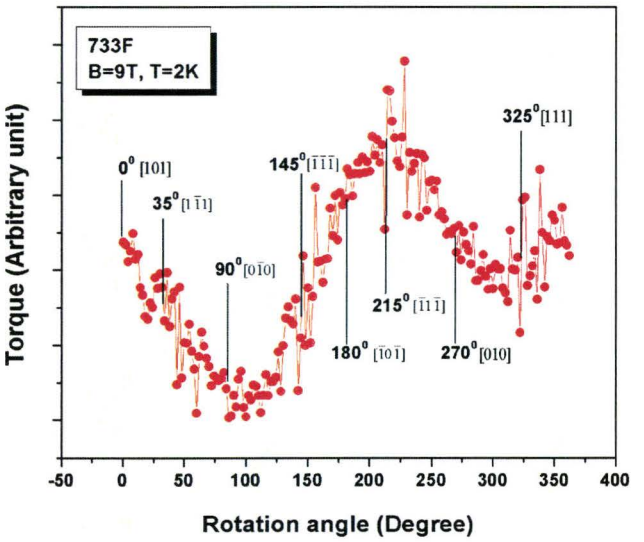

Figure 8.28: Torque as a function of rotation angle for non-deformed sample 733F measured at a constant magnetic field $B = 9\ Tesla$ and at temperature $T = 2K$. Rotation axis is along $< 10\bar{1} >$.

8.3 De Haas-van Alphen Results

Figures 8.28, 8.29, 8.30 and 8.31 show torque versus rotation angle characteristics for a non-deformed crystal and the crystals deformed to stress level of 3.34 *MPa*, 299.1 *MPa* and 317 *MPa*, respectively, measured at a constant magnetic field of 9 *Tesla*. In general, all figures display a sinusoidal variation of torque with rotation angle as described by equation 7.6. However, Figures 8.28 and 8.29 reveal strong quantum oscillations of the torque observed at $< 111 >$ orientations corresponding to the sample position in which closed orbits occur. On the other hand, Figures

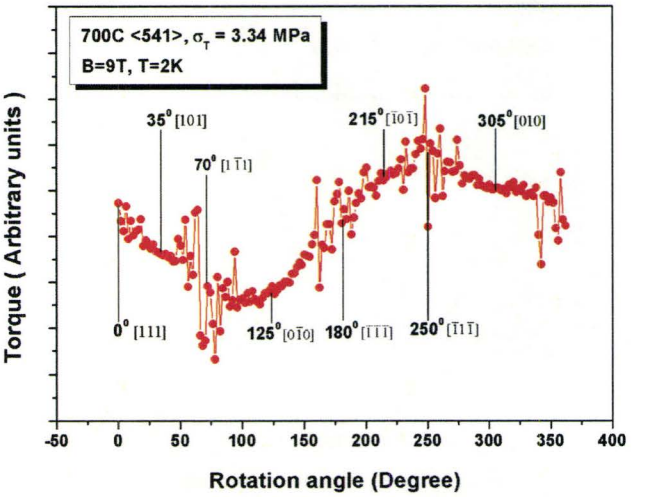

Figure 8.29: Torque as a function of rotation angle for $< 541 >$ sample 700C, deformed to 3.34 *MPa*, measured at a constant magnetic field $B = 9$ *Tesla* and at temperature $T = 2K$. Rotation axis is along $< 10\bar{1} >$.

8.30 and 8.31 show a smooth change of torque as a function of rotation angle, indicating that quantum oscillations disappear in largely deformed samples. Such observation is consistent with theoretical prediction that more defects in the sample, corresponding to smaller relaxation time or mean free path, will make quantum phenomena disappeared.

Here we follow the discussion of Chapter 5 and use free-electron approximation and equation (5.1) to make a quantitative estimation of the dislocation density limit for the occurrence of the dHvA effect in deformed samples at temperature $T = 2K$. We first consider the case of small deformations and assume that the distribution of dislocations in slightly deformed samples is uniform and dislocations are separated by dislocation means free path l , which can be viewed also as the mean free

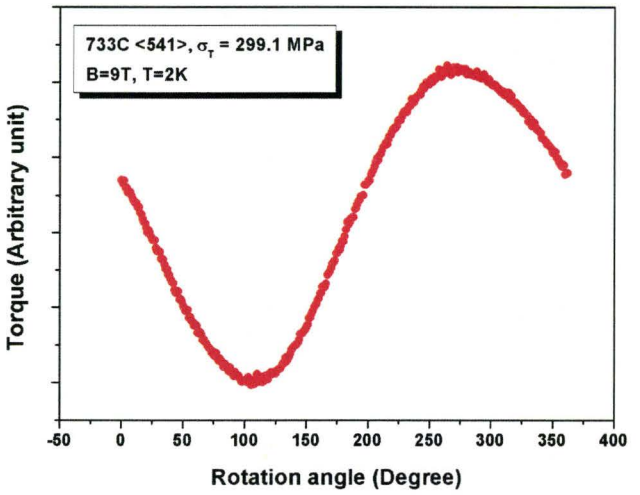

Figure 8.30: Torque as a function of rotation angle for $< 100 >$ sample 733C, deformed to 299.1 *MPa*, measured at a constant magnetic field $B = 9$ *Tesla* and at temperature $T = 2K$. Rotation axis is along $< 101 >$ direction

path of electrons scattered on dislocations. To observe the dHvA effect in samples with dislocations requires that electron cyclotron movements in the magnetic field be within the dislocation-free area, without reaching the boundaries, otherwise the dHvA quantum effect will be smeared out by electron-dislocation scattering. Figure 8.32 shows schematically this concept: electrons circulate in the dislocation-free area and they might get scattered by dislocations separated by dislocation means free path l, if the applied magnetic field is small enough. This is because the radius R_B of electron circular movements is proportional to the inverse intensity of the applied magnetic field, which has the form

$$R_B = \frac{m^* v}{eB}, \tag{8.1}$$

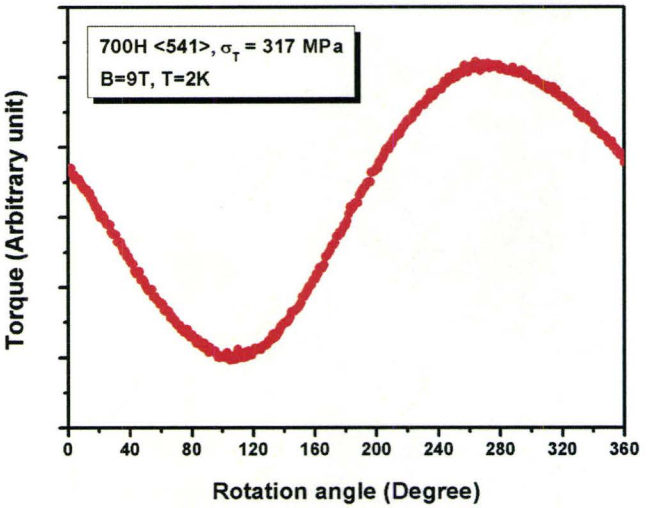

Figure 8.31: Torque as a function of rotation angle for $< 541 >$ sample 700H, deformed to 317 *MPa*, measured at a constant magnetic field $B = 9$ *Tesla* and at temperature $T = 2K$. Rotation axis is along $< 101 >$ direction.

where m^* is electron effective mass; v electron velocity; e electron charge and B the intensity of the applied magnetic field.

Replacing v in equation (8.1) by the average electron velocity equal to electron mean free path l over relaxation time τ, we can write the ratio of electron mean free path over the radius of electron circular movements as

$$\frac{l}{R_B} = \frac{1}{ne\Re_d} \times \frac{B}{N_d}, \tag{8.2}$$

where n, $\Re_d$, and N_d are electron density, specific resistivity of and density of dislocations respectively. Substituting the physical constants into equation (8.2), we

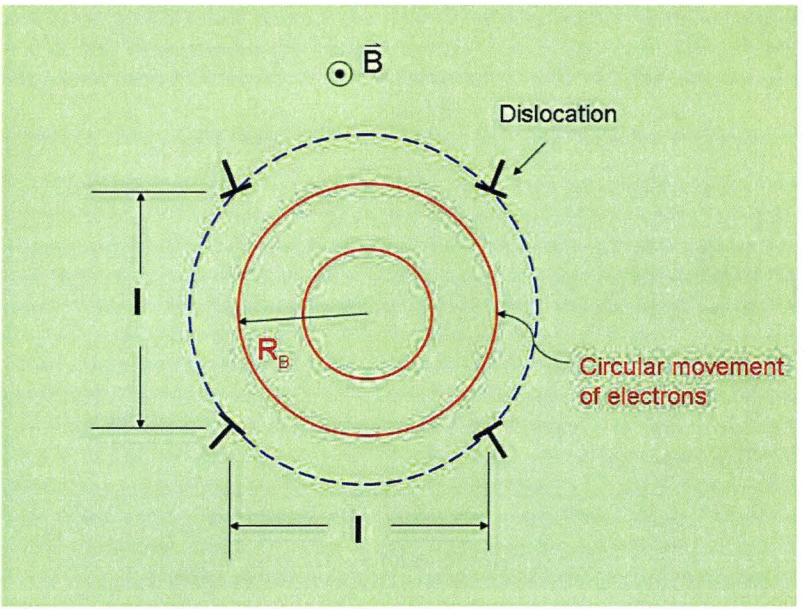

Figure 8.32: Schematic illustration of circular movements of conduction electrons in the dislocation-free area of a sample having a uniform distribution of dislocations. The radius R_B of the circle increases as the applied field decreases and the electrons moving on the blue dash circle are scattered by dislocations, if the applied field is small enough.

obtain

$$\frac{l}{R_B} = 7.35 \times 10^{14} \times \frac{B}{N_d}. \tag{8.3}$$

According to equation (5.1), the ratio $\frac{l}{R_B}$ must be much larger than one in order to observe the dHvA effect in copper samples containing dislocations. If the applied magnetic field is 9 *Tesla* and $\frac{l}{R_B}$ ratio is 10, to satisfy the condition of equation (5.1) and to be able to observe the dHvA quantum effect in deformed samples, the maximum density of dislocations in the samples is $6.6 \times 10^{14} m^{-2}$ or $6.6 \times 10^{10} cm^{-2}$. This corresponds to a small deformation of a few percent. The estimation of the maximum dislocation density for the occurrence of dHvA quantum effect, although

very rough, agrees well with experimental observations (Figure 8.28 and 8.29).

For samples deformed into stage *II* and *III*, the dislocation substructure is characterized by the formation of cell substructure, with high dislocation density in cell boundaries (or cell walls) and lower dislocation density in cell interiors (e.g. Figures 2.12, 2.13, 2.15 and 2.16). The experimental observations show that the average cell size is temperature dependent and in samples deformed at $T = 78K$ to stage *II*, the cell size is approximately $0.7 \times 10^{-6}m$ (Niewczas, 2002). If we take the velocity of conduction electrons in copper samples as Fermi velocity, which is $1.57 \times 10^{6}m/s$ (Ashcroft & Mermin, 1976), and the intensity of the magnetic field as 9 *Tesla*, we can easily find from equation (8.1) that $R_B \approx 1.0 \times 10^{-6}m$, which is larger than the average cell size in highly deformed samples. Additionally, as the deformation increases more dislocations is stored in the cell interiors (Niewczas, 2002). This means that conduction electrons in largely deformed samples will be constantly scattered by dislocation walls or by dislocations stored in the cell interiors and the electrons will not be able to develop circular movements, even in the field of 9 *Tesla*. Consequently, the dHvA quantum effect will disappear in samples containing higher dislocation densities. Figure 8.33 depicts schematically the movement of conduction electrons in the sample containing dislocation cell substructure, under condition of the magnetic field applied perpendicular to the plane of the paper. Instead of cyclotron movement (red dash circle with radius R_B), conduction electrons will be constantly scattered by dislocations located in the walls or cell interiors and presumably will move along random arcs trajectories, shown schematically by the solid red lines in Figure 8.33. Thus, it is expected that the dHvA effect in largely deformed sample such as 733C containing approximately $1.25 \times 10^{11}cm^{-2}$ dislo-

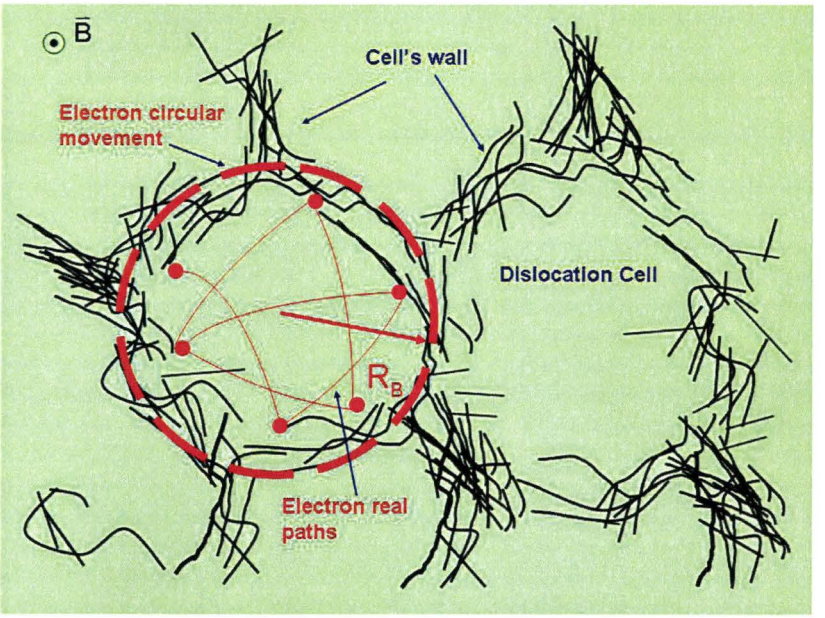

Figure 8.33: Schematic illustration of a paths of conduction electrons moving in a highly deformed sample containing dislocation cell structure. The red dash circle with radius R_B show electron cyclotron trajectory in the applied magnetic field coinciding with the size of dislocation cell boundaries. The red solid lines show the paths of conduction electrons in the magnetic field caused by constant electron-dislocation scattering.

cation density and in sample 700H containing $1.65 \times 10^{11} cm^{-2}$ dislocations will be smoothed out. This conclusion is consistent with experimental results shown in Figure 8.30 and 8.31. Therefore, our experimental efforts will focus on studying the dHvA effect in slightly deformed sample 700C and comparing its behavior against the dHvA effect observed in undeformed samples.

Figure 8.36(a), 8.37(a) and 8.38(a) show quantum oscillations of the torque as a function of the inverse magnetic field for slightly deformed sample 700C, for the orientation of the applied magnetic field along $< 100 >$, $< 111 >$ and $< 110 >$ directions respectively. Quantum oscillation frequencies are obtained by taking

Table 8.3: de Hass-van Alphen frequencies (in units of 10^3 G) in copper crystal 700C containing dislocations in comparison with the frequencies measured in pure, non-deformed samples 733F and frequencies reported in the literature

	< 111 >		< 100 >		< 110 >
	Belly	Neck	Belly	Rosette	Dog-bone
*Average** $\mathscr{F}_0$	581000	21748	599600	246100	251067
$\mathscr{F}_{733F}$	583926	21898	598899	248324	–
$\mathscr{F}_{700C}$	584483	21918	599095	248405	248405
$\delta\mathscr{F}_{733F} = \mathscr{F}_{733F} - \mathscr{F}_0$	2926	150	-701	2224	–
$\delta\mathscr{F}_{700C} = \mathscr{F}_{700C} - \mathscr{F}_0$	3483	170	-505	2305	-2662
$\delta\mathscr{F}_{733F}/\mathscr{F}_0(10^{-3})$	5.036	6.897	-1.170	8.956	–
$\delta\mathscr{F}_{700C}/\mathscr{F}_0(10^{-3})$	5.994	7.817	-0.842	9.366	-10.603

∗:Figures in each column represent the average value of the literature data given in table 5.1

Fourier transform of the torque versus the inverse magnetic field for a given orientation of the sample with respect to applied magnetic field, as shown in Figures 8.36(b), 8.37(b) and 8.38(b). Figure 8.34 and 8.35 are the same plots of quantum oscillations of the torque against the inversed magnetic field and their Fourier transformation for non-deformed sample 733F. The analysis of these data is provided in the next section.

8.4 Data Analysis

Table 8.3 shows the dHvA frequency $\mathscr{F}$ of the extremal orbits normal to high symmetry directions in non-deformed sample 733F and slightly deformed sample 700C. For comparison, table 8.3 also lists the average value of oscillation frequencies $\mathscr{F}_0$ for very pure copper single crystal samples (label '0' denotes the state of samples without applied stress, measured by other researchers and given in table 5.1). We take these figures as benchmark values with which the results obtained in this work are compared. It is straightforward to calculate the ratio of frequency difference $\mathscr{F} - \mathscr{F}_0$ over the benchmark values $\mathscr{F}_0$ for each extremal orbit. Through the Onsager relation such ratio corresponds to the percent changes of extremal cross-section area of the Fermi surface normal to the applied field direction which is caused by other defects in non-deformed sample 733F or the stress field produced by dislocations present in slightly deformed sample 700C. The results in table 8.3 show quantitatively that the extremal cross section areas of the neck orbit, four-cornered rosette and belly orbits normal to $< 111 >$ are expanded with different ratios while the area of the extremal orbits of dogbone normal to $< 100 >$ are reduced. However, the area change (especially the sign) with density of defects in samples for belly extremal orbits normal to $< 100 >$ can not be determined and this is because such change is too small to be measured in our present PPMS system. It is clear that the dogbone and four-cornered rosette orbits have larger ratio of the change of the cross section area than the other orbits and this may be explained by the fact that these two extremal orbits are connected with four necks and each neck has the same contribution to the area change.

Based on the above analysis, the contour of deformed Fermi surface can be qualitatively postulated. Figure 8.38(a) and 8.38(b) show schematically the change of the dogbone and four cornered rosette orbits due to the strain field inside the dislocated copper sample. Figure 8.41 is a schematic sketch of the distortion of the Fermi surface in one Brillouin zone and the red solid curves represent the two extremal belly orbits. The belly orbit normal to $< 100 >$ has a small negative ratio of the area change approximately 8 parts per 10^{-4} while the belly orbit normal to $< 111 >$ have a large positive ratio round 6 parts per 10^{-3}, which is almost eight times larger than the area change ratio of belly orbit normal to $< 100 >$. The more detailed information of the distortion of Fermi surface of copper requires collection of a large body of dHvA oscillation frequencies along different crystallographic orientations of the sample, which was beyond the scope of the present work.

It is interesting and of much significance to compare the present results of the dHvA oscillatory frequencies of the copper samples containing dislocations with dHvA frequencies observed in the samples subjected to elastic stress, as studied by Templeton (Templeton, 1974). Tables 8.4 and 8.5 show the effect of hydrostatic compressive and uniaxial tensile stress applied along the principal symmetry directions on the Fermi surface of copper. The change of the cross-sectional area of the Fermi surface per unit stress is given by

$$\frac{\partial \ln S_F}{\partial p} = \frac{\delta S_F}{S_F^0}\frac{1}{\delta p} = \frac{\delta \mathscr{F}}{\mathscr{F}_0}\frac{1}{\delta p}, \tag{8.4}$$

where S_F is the cross section area of the Fermi surface normal to the applied field

Table 8.4: Distortion of the Fermi surface of copper caused by hydrostatic pressure applied along the high symmetry directions. $\partial \ln S_F/\partial p$ is in units of $10^{-12}\ cm^2/dyn$ (Templeton, 1974)

	< 111 >		< 100 >		< 110 >
	Belly	Neck	Belly	Rosette	Dog-bone
$\frac{\partial \ln S_F}{\partial p}$	0.421 ± 0.03	1.98 ± 0.05	0.442 ± 0.003	0.442 ± 0.003	0.404 ± 0.002

and p is the applied stress.

Table 8.5: Distortion of the Fermi surface of copper caused by the uniaxial tensile stress applied along the high symmetry directions

	$\partial \ln S_F/\partial p$ ($10^{-12}\ cm^2/dyn$)				
	< 111 >		< 100 >		< 110 >
*	Belly	Neck	Belly	Rosette	Dog-bone
a	-0.113 ± 0.007	6.26 ± 0.11	-0.346 ± 0.012	0.23 ± 0.04	2.17 ± 0.06
b	-0.09 ± 0.003	6.9 ± 1.5	-0.38 ± 0.08	0.33 ± 0.13	—
c	—	8.8 ± 0.8	—	—	—
d	—	7.5 ± 2.0	—	—	—

*: *a* (Ruesink & Perz, 1983), *b* (Shoenberg & Watts, 1967), *c* (Slavin, 1973), *d* (Aron, 1972)

From table 8.4 it is seen that compressive stress results in the expansion of the cross sectional area of the Fermi surface normal to the principal symmetry directions. The stress derivative $\partial \ln S_F/\partial p$ in these directions are all positive and the rate of expansion of the neck cross sectional area with the applied compressive stress is much larger than in the other directions. For the case of uniaxial tension, the data in table 8.5 indicate that the rate of increase of the cross section area with the applied tensile stress for neck orbit is still much larger than for the other or-

bits, similar to the case of hydrostatic pressure. However, a significant difference is that the rate of increase with tensile stress for the belly orbits normal to $< 100 >$ and $< 111 >$ directions is negative. This means that the two corresponding cross sectional areas shrink under the action of uniaxial tension. More surprising conclusions emerge after comparing the data of elastically deformed samples in table 8.5 with plastically deformed samples in table 8.3. First, the rate of increase of the cross sectional area is quite different in these two cases. Here we provide an estimation of the rate of increase of the cross section of Fermi surface for the elastically deformed samples at the critical state of elasticity and compare it with plastically deformed samples. The critical resolved shear stress to initiate dislocation glide in copper is 0.63 MPa (chapter 2.4.1, table 2.1). Assuming that the applied tensile stress is along $< 100 >$ direction, the tensile stress (normal stress, defined also as the yield stress of copper) to start plastic deformation is 1.54 MPa or 1.54×10^7 dyn/cm^2. In the case of Shoenberg and Watts (Shoenberg & Watts, 1967), such applied stress will give a ratio -5.8×10^{-6} of cross sectional area change for $< 100 >$ belly orbit and 5.1×10^{-6} for rosette orbit (1.54×10^7 dyn/cm^2 multiplied by line b in table 8.5 yields the two numbers). These are much smaller than the corresponding figures -8.42×10^{-4} and 9.366×10^{-3} obtained in the present work for plastically deformed copper single crystal along $< 541 >$ when the field orients in $< 100 >$(Table 8.3). Similar calculations for other orbits yields the same conclusions. Second, the rate of increase for dogbone orbit in two cases has the opposite sign. In plastically deformed sample, the cross sectional area for dogbone shrinks with relatively substantial rate but expands in elastically deformed sample with a relatively small rate. To understand the reasons of these differences more work needs to be done in this topic.

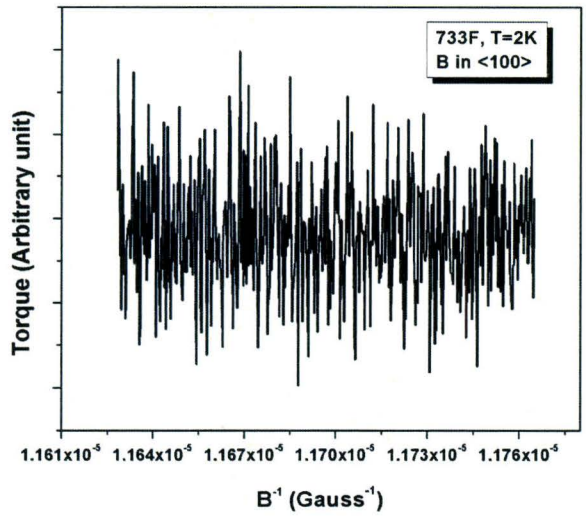

(a) Torque oscillations as a function of the inverse of the applied magnetic field, measured at temperature $T = 2K$ and orientation of the magnetic filed along $< 100 >$.

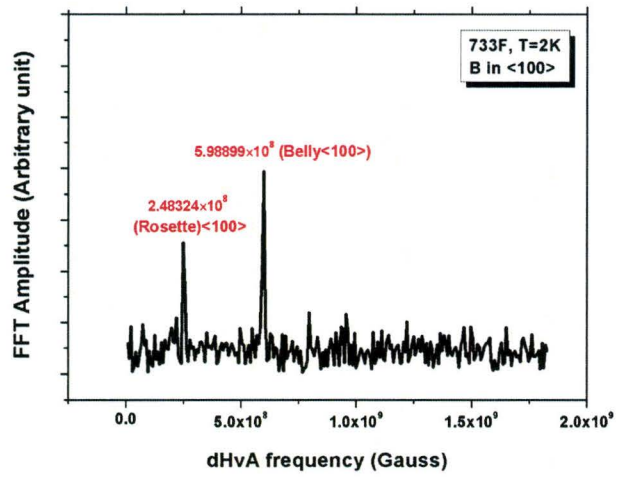

(b) Fourier spectrum of the torque as a function of B^{-1} from Figure 8.35(a), at $T = 2K$ and the magnetic field along $< 100 >$. The two peaks correspond to the dHvA oscillation frequencies of the neck and belly orbits normal to $< 100 >$ direction respectively

Figure 8.34: The dHvA effect and oscillatory frequency for non-deformed sample 733F for the orientation of the magnetic field along $< 100 >$ direction.

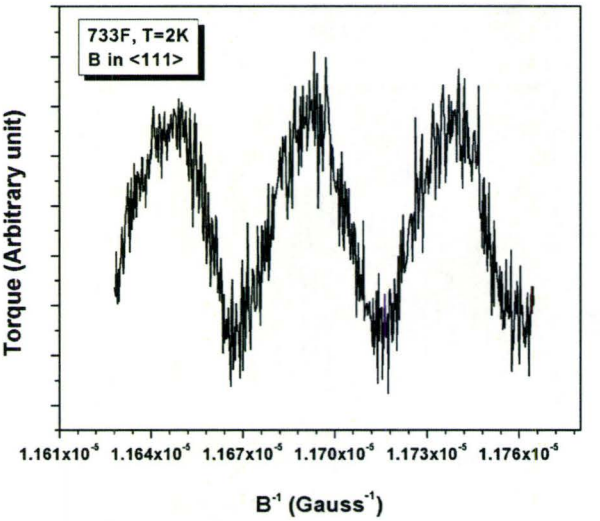

(a) Torque oscillations as a function of the inverse of the applied magnetic field, measured at temperature $T = 2K$ and orientation of the magnetic filed along $< 111 >$.

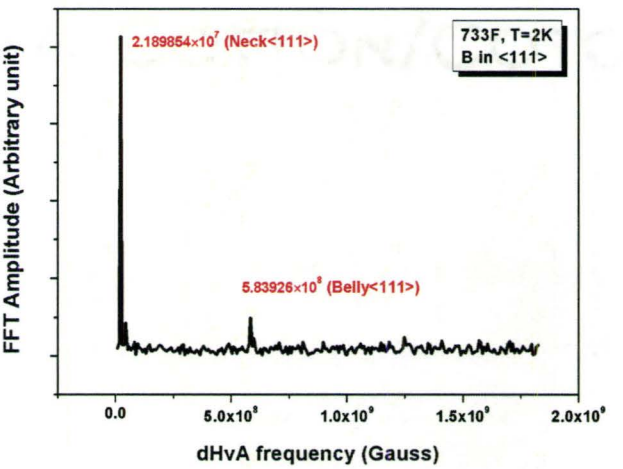

(b) Fourier spectrum of the torque as a function of B^{-1} from Figure 8.35(a), at $T = 2K$ and the magnetic field along $< 111 >$. The two peaks correspond to the dHvA oscillation frequencies of the neck and belly orbits normal to $< 111 >$ direction respectively

Figure 8.35: The dHvA effect and oscillatory frequency for non-deformed sample 733F for the orientation of the magnetic field along $< 111 >$ direction.

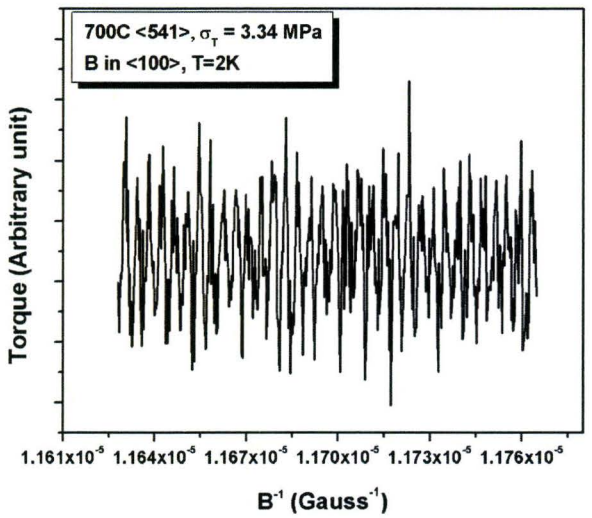

(a) Torque oscillations as a function of the inverse of the applied magnetic field, measured at temperature $T = 2K$ and orientation of the magnetic filed along $< 100 >$.

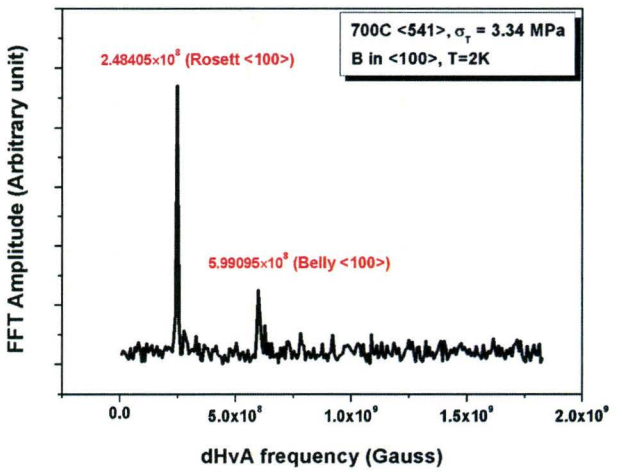

(b) Fourier spectrum of the torque as a function of B^{-1} from Figure 8.36(a), at $T = 2K$ and the magnetic field along $< 100 >$. The two peaks correspond to the dHvA oscillation frequencies of the four-cornered rosette and belly orbits normal to $< 100 >$ direction respectively

Figure 8.36: The dHvA effect and oscillatory frequency for $< 541 >$ sample 700C, deformed to 3.34 *MPa*, for the orientation of the magnetic field along $< 100 >$ direction.

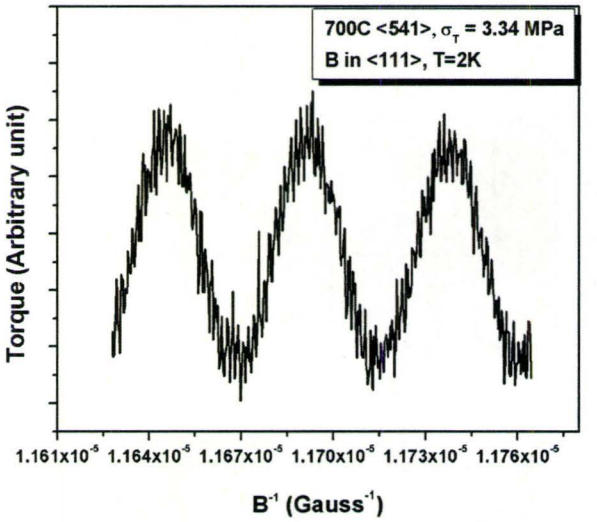

(a) Torque oscillations as a function of the inverse of the applied magnetic field, measured at temperature $T = 2K$ and orientation of the magnetic filed along $< 111 >$.

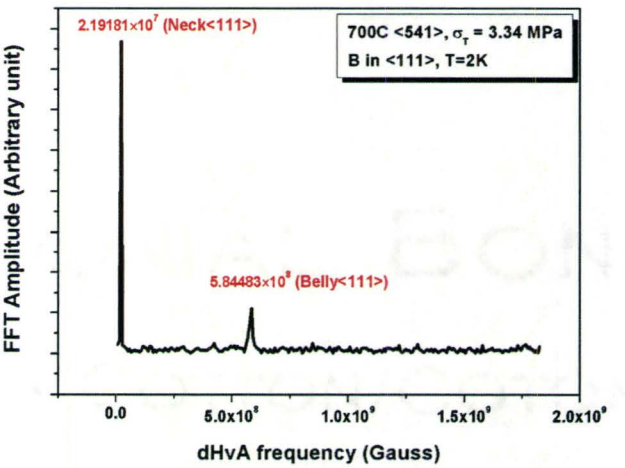

(b) Fourier spectrum of the torque as a function of B^{-1}, at $T = 2K$ and magnetic field along $< 111 >$ direction. The two peaks correspond to the dHvA oscillation frequencies of the neck and belly orbits normal to $< 111 >$ direction respectively

Figure 8.37: The dHvA effect and oscillatory frequency for $< 541 >$ sample 700C, deformed to 3.34 *MPa*, for the orientation of the magnetic field along $< 111 >$ direction.

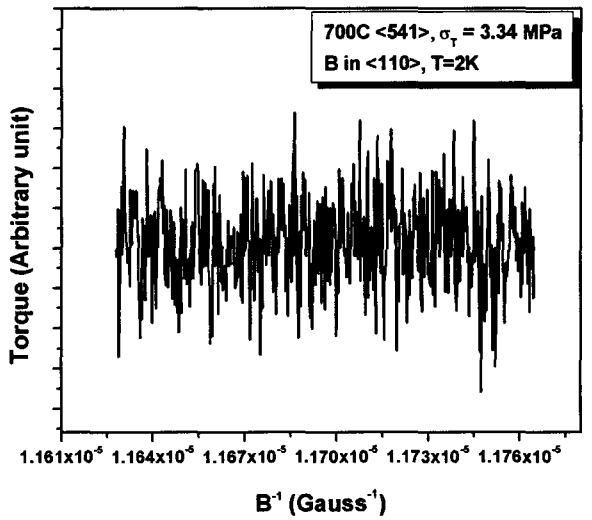

(a) Torque oscillations as a function of the inverse of the applied magnetic field, measured at temperature $T = 2K$ and orientation of the magnetic filed along $< 111 >$.

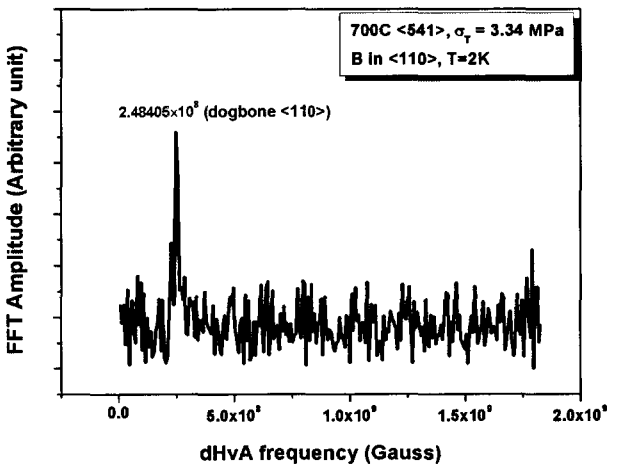

(b) Fourier spectrum of the torque as a function of B^{-1}, at $T = 2K$ and magnetic field along $< 110 >$ direction. The peak corresponds to the dHvA oscillation frequency of dog-bone orbits normal to $< 110 >$ direction

Figure 8.38: The dHvA effect and oscillatory frequency for $< 541 >$ sample 700C, deformed to 3.34 *MPa*, for the orientation of the magnetic field along $< 110 >$ direction.

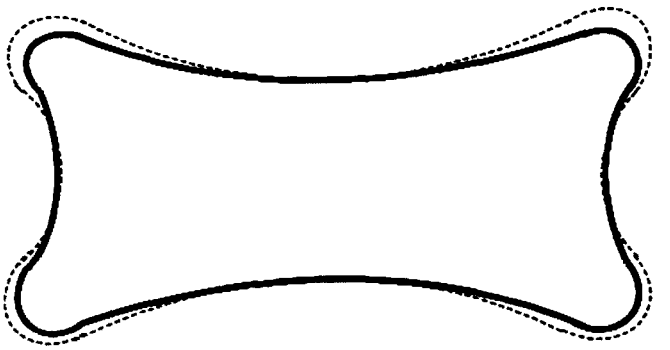

Figure 8.39: Solid curve shows the dog-bone orbit in copper sample containing dislocations for $< 110 >$ orientation of the magnetic field. The area of the orbit shrinks comparing to the dog-bone orbit of pure, undistorted copper (dash line)

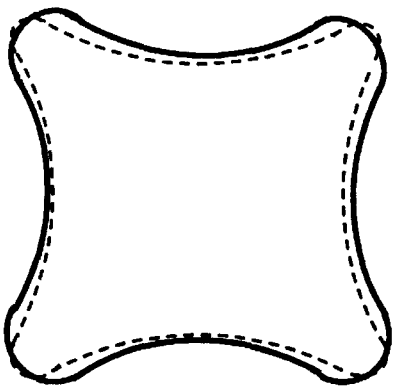

Figure 8.40: Solid curve shows the four-cornered rosette orbit in copper sample containing dislocations, for $< 100 >$ orientation of the magnetic field. The area of the orbit expands comparing to the orbit of pure, undistorted copper (dash line).

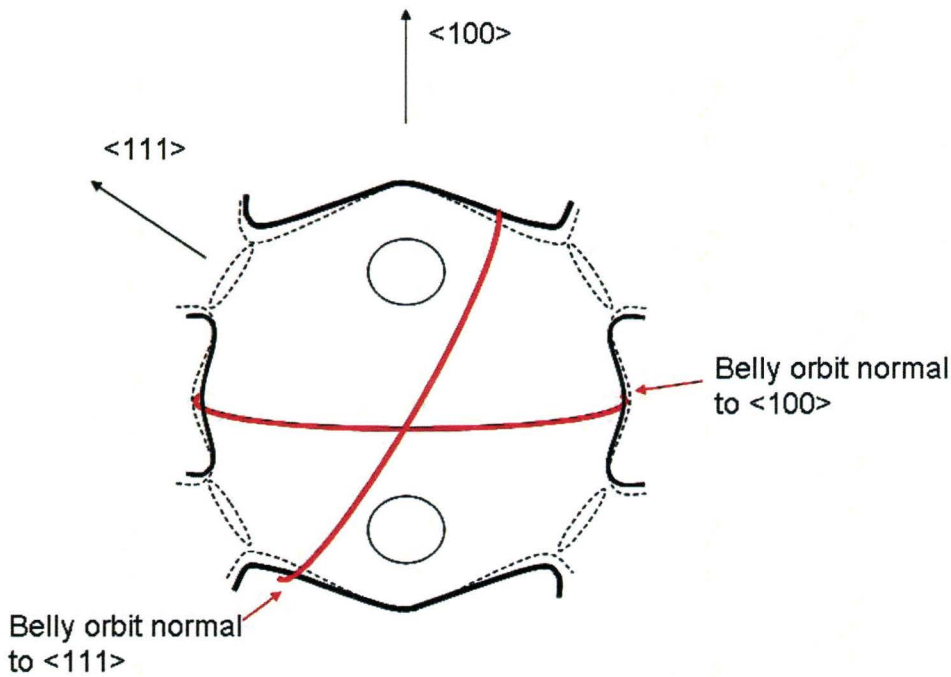

Figure 8.41: Schematic sketch of the distortion of the Fermi surface of copper containing dislocations in one Brillouin zone, along $< 110 >$ view direction. The black solid curves denotes the distorted contour of the Fermi surface due to dislocations in comparison to the undistorted Fermi surface of pure copper (dash curves). Two red solid curves show the belly orbits normal to $< 100 >$ and $< 111 >$ directions.

Chapter 9

Modeling of Transverse Magnetoresistivity

9.1 Solution to Green's Function in Free Space

Based on the theory of galvanomagnetic properties of metals discussed in chapter 3, the conductivity tensor of a single crystal in a magnetic field $\vec{B}$, is given by a general tensor

$$\overleftrightarrow{\sigma} = (\sigma_{ij}) = \begin{pmatrix} \sigma_{xx} & \sigma_{xy} & \sigma_{xz} \\ \sigma_{yx} & \sigma_{yy} & \sigma_{yz} \\ \sigma_{zx} & \sigma_{zy} & \sigma_{zz} \end{pmatrix}. \tag{9.1}$$

The nine elements in this conductivity tensor are not independent and must satisfy Onsager relation

$$\sigma_{ij}(\vec{B}) = \sigma_{ji}(-\vec{B}). \tag{9.2}$$

This yields

$$\sigma_{ij} = -\sigma_{ji}, \ \ (i \neq j), \tag{9.3}$$

Because the non-diagonal elements (Hall effect) are the linear function of the magnetic field, we may write the conductivity tensor as the sum of two parts, a symmetric tensor and an anti-symmetric tensor which are of the forms

$$\overleftrightarrow{\sigma} = \overleftrightarrow{\sigma}^S + \overleftrightarrow{\sigma}^A = \begin{pmatrix} \sigma_{xx} & 0 & 0 \\ 0 & \sigma_{yy} & 0 \\ 0 & 0 & \sigma_{zz} \end{pmatrix} + \begin{pmatrix} 0 & \sigma_{xy} & \sigma_{xz} \\ \sigma_{yx} & 0 & \sigma_{yz} \\ \sigma_{zx} & \sigma_{zy} & 0 \end{pmatrix}. \tag{9.4}$$

In order to compute the effective conductivity tensor of an inhomogeneous media within the effective medium approximation, we have to find either Green's function in the free space or we have to provide the solution to the boundary problem of equation (4.23). Suppose that the conductivity tensor of the uniform medium in which the randomly oriented grains are embedded has the same form as equation (9.4)

$$\overleftrightarrow{\sigma}_m = \overleftrightarrow{\sigma}^S_m + \overleftrightarrow{\sigma}^A_m \tag{9.5}$$

Using equation (9.5), we can change equation (4.23) into a well-known form for

Green's function

$$\left\{\sigma_{xx}\frac{\partial^2}{\partial x^2}+\sigma_{yy}\frac{\partial^2}{\partial y^2}+\sigma_{zz}\frac{\partial^2}{\partial z^2}\right\}G(\vec{r},\vec{r}')=-\delta(\vec{r}-\vec{r}'). \tag{9.6}$$

The detailed derivation of equation (9.6) is provided in Appendix A (A.2).

By means of a transformation

$$X=\frac{x}{\sqrt{\sigma_{xx}}},\ Y=\frac{y}{\sqrt{\sigma_{yy}}},\ Z=\frac{z}{\sqrt{\sigma_{zz}}}, \tag{9.7}$$

equation (9.6) can be simplified as

$$\left\{\frac{\partial^2}{\partial X^2}+\frac{\partial^2}{\partial Y^2}+\frac{\partial^2}{\partial X^2}\right\}G(\vec{R},\vec{R}')=-(\sigma_{xx}\sigma_{yy}\sigma_{zz})^{-1/2}\delta(\vec{R}-\vec{R}'), \tag{9.8}$$

where

$$\vec{R}=X\vec{e}_1+Y\vec{e}_2+Z\vec{e}_3. \tag{9.9}$$

and $\vec{e}_1$, $\vec{e}_2$ and $\vec{e}_3$ are unit vectors along x,y and z axes as mentioned in Appendix A (A.2).

The solution to equation (9.8) is

$$\begin{aligned} G(\vec{R},\vec{R}') &= \frac{1}{4\pi\sqrt{\sigma_{xx}\sigma_{yy}\sigma_{zz}}}\frac{1}{|\vec{R}-\vec{R}'|} \\ &= \frac{1}{4\pi\sqrt{\sigma_{xx}\sigma_{yy}\sigma_{zz}}}\frac{1}{\sqrt{(X-X')^2+(Y-Y')^2+(Z-Z')^2}}. \end{aligned} \tag{9.10}$$

Using equations 9.7, we can write the Green's function as

$$G(\vec{r},\vec{r}') = \frac{1}{4\pi\sqrt{\sigma_{xx}\sigma_{yy}\sigma_{zz}}} \frac{1}{\sqrt{\frac{(x-x')^2}{\sigma_{xx}} + \frac{(y-y')^2}{\sigma_{yy}} + \frac{(z-z')^2}{\sigma_{zz}}}}. \tag{9.11}$$

This solution satisfies the boundary condition

$$\lim_{|\vec{r}-\vec{r}'|\to\infty} G(\vec{r},\vec{r}') \longrightarrow 0 \tag{9.12}$$

Equations (9.11) and (9.12) are the solutions to the boundary problem of equation (4.23) which was first derived by Stroud and Pan (Stroud & Pan, 1979)

9.2 Magnetoconductivity Tensor for Open Orbits

It was discussed in chapter 3 that the variation of the magnetoresistance of a single crystal in the magnetic field depends on the topology of the Fermi surface in momentum space as well as the orientation of the magnetic field. If the energy band of the single crystal has a spherical structure which corresponds to the free-electron approximation, electrons always have closed orbits independent of the direction of the magnetic field. Assuming that the magnetic field is along z -axis, the magnetoresistivity tensor for such system is described by equation (3.31), which reads

$$\overleftrightarrow{\sigma}^{cl} = \begin{pmatrix} \sigma_{xx} & \sigma_{xy} & 0 \\ -\sigma_{xy} & \sigma_{yy} & 0 \\ 0 & 0 & \sigma_{zz} \end{pmatrix} = \sigma_0 \begin{pmatrix} 1/1+\lambda^2 & -\lambda/1+\lambda^2 & 0 \\ \lambda/1+\lambda^2 & 1/1+\lambda^2 & 0 \\ 0 & 0 & 1 \end{pmatrix}, \tag{9.13}$$

where $\lambda = w_c\tau$ and the other variables such as w_c and σ_0 are defined as before, i.e. $w_c = eB/m^*$ and $\sigma_0 = ne^2\tau/m^*$.

The inverse of the electrical conductivity tensor, equation (9.13), shows that the diagonal elements are independent of the magnetic field and they are saturated in the magnetic field. Nevertheless, if the single crystal has an open energy band structure in momentum space and the magnetic field is oriented along some direction in which an open orbit occurs, the variation of magnetoresistivity with the magnetic field shows a quadratic dependence, which was predicted by Lifshitz' theory and is described by equation (3.60). However, to derive the explicit expression for the magnetoresistivity tensor analytically is by no means trivial because not only the specific information about the topology of the Fermi surface, but also the dynamical details of electrons' movement are required. To avoid such complexity, we follow Overhauser's approach (Overhauser, 1971, 1974; Huberman & Overhauser, 1981) and assume that the crystal with the open orbits has two energy bands which do not overlap with each other. One band is in a form of a spherical Fermi surface, therefore the electrons in this band can move freely on the surface of constant energy. The other band is in a form of a cylindrical Fermi surface. The electrons in this band can not move freely along the cylindrical axis, since the electron velocity in a direction $\vec{v}$ is proportional to the directional derivative $\vec{\nabla}_{\vec{k}}E(\vec{k})$ of the constant energy surface along that direction in momentum space, but the value of this derivative is zero on the surface of constant energy along the direction of cylinder's axis. When an applied magnetic field is perpendicular to the direction of the cylindrical axis, the orbits of electron in a cylindrical band will be open.

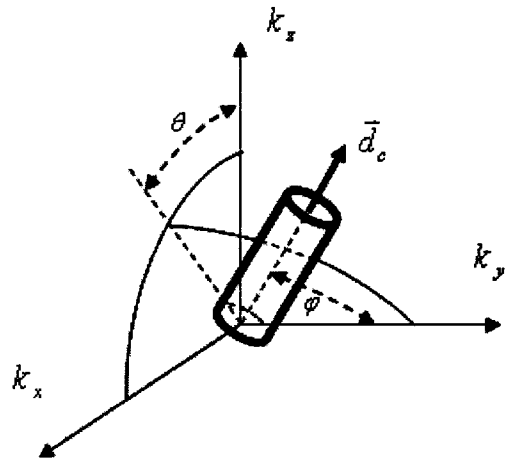

Figure 9.1: Cylindrical Shape of Fermi Surface. Axis direction $\vec{d}_c$ is determined by polar angles θ and φ

Let $\vec{d}_c$ be the axial direction of the cylindrical Fermi surface and its azimuthal angles are labeled in Figure 9.1. When a magnetic field is applied along z-axis, assuming the fraction of electrons in cylindrical band is f_e, the magnetoresistivity

tensor $\overleftrightarrow{\sigma}^{op}$ for such crystals can be written as

$$\sigma_{xx}^{op} = \frac{(1-f_e)\sigma_0}{1+\lambda^2} + \frac{f_e\sigma_0}{1+\Lambda^2}(1-\sin^2\varphi\sin^2\theta), \tag{9.14a}$$

$$\sigma_{xy}^{op} = \frac{-(1-f_e)\lambda\sigma_0}{1+\lambda^2} + \frac{f_e\sigma_0}{1+\Lambda^2}(-\sin\varphi\cos\varphi\sin\theta - \Lambda\sin\varphi\sin\theta), \tag{9.14b}$$

$$\sigma_{xz}^{op} = \frac{f_e\sigma_0}{1+\Lambda^2}(-\sin^2\varphi\sin\theta\cos\theta + \Lambda\cos\varphi), \tag{9.14c}$$

$$\sigma_{yx}^{op} = \frac{(1-f_e)\lambda\sigma_0}{1+\lambda^2} + \frac{f_e\sigma_0}{1+\Lambda^2}(-\sin\varphi\cos\varphi\sin\theta + \Lambda\sin\varphi\sin\theta), \tag{9.14d}$$

$$\sigma_{yy}^{op} = \frac{(1-f_e)\sigma_0}{1+\lambda^2} + \frac{f_e\sigma_0}{1+\Lambda^2}\sin^2\varphi, \tag{9.14e}$$

$$\sigma_{yz}^{op} = \frac{f_e\sigma_0}{1+\Lambda^2}(-\sin\varphi\cos\varphi\cos\theta - \Lambda\sin\varphi\sin\theta), \tag{9.14f}$$

$$\sigma_{zx}^{op} = \frac{f_e\sigma_0}{1+\Lambda^2}(-\sin^2\varphi\sin\theta\cos\theta - \Lambda\cos\varphi), \tag{9.14g}$$

$$\sigma_{zy}^{op} = \frac{f_e\sigma_0}{1+\Lambda^2}(-\sin\varphi\cos\varphi\cos\theta + \Lambda\sin\varphi\sin\theta), \tag{9.14h}$$

$$\sigma_{zz}^{op} = (1-f_e)\sigma_0 + \frac{f_e\sigma_0}{1+\Lambda^2}(1-\sin^2\varphi\sin^2\theta), \tag{9.14i}$$

where $\Lambda = w_c\tau\sin\varphi\cos\theta$. This expression assumes that the relaxation times in two bands are equal.

We apply the effective medium theory to model the electrical property of copper containing different density and distribution of dislocations in a magnetic field. During the plastic deformation of copper single crystals, dislocations arrange themselves in lower energy configurations and form the network of highly dislocated areas and the areas where there is almost no dislocations. Therefore, deformed sample can be viewed as a composite, composed of crystallites with different dislocation densities and orientations. When a magnetic field is applied in a certain direction, some crystallites have open electron orbits or long extended orbits, the

others have closed orbits. To simulate the behavior of magnetoresistance for such a complicated system, we employ the effective medium theory to view the deformed sample as a mixture of two types of oriented crystallites, in which one component with open electron orbits has the magnetoresistivity tensor described by equation (9.14) and the other component with closed electron orbits has the magnetoresistivity tensor denoted by equation (9.13). The effective conductivity tensor can be calculated through equation (4.37) by taking the component with closed electron orbits as a uniform medium and embedding the other component with open electron orbits in it. The details of computation are discussed in the next sections.

9.3 Construction of Depolarization Tensor

The firs step in calculating magnetoresistivity of copper single crystals containing dislocations using effective medium theory requires construction of depolarization tensor. Suppose that the applied magnetic field is applied along z-direction. We can take

$$\sigma_{xx} = \sigma_{yy} \tag{9.15}$$

in equation (9.11), which is used in this formulation because the embedding medium is uniform and crystallites are pure single crystals, then Green's function is given by

$$G(\vec{r},\vec{r}') = \frac{1}{4\pi\sigma_{xx}\sqrt{\sigma_{zz}}} \frac{1}{\sqrt{\frac{(x-x')^2}{\sigma_{xx}} + \frac{(y-y')^2}{\sigma_{xx}} + \frac{(z-z')^2}{\sigma_{zz}}}}. \tag{9.16}$$

Substituting above Green function into equation (4.33), we have

$$\begin{aligned}\Gamma_{ij} &= \oint_{S'}\left\{\frac{\partial}{\partial r_i'}G(\vec{r}')\right\}n_j' dS' \\ &= \oint_{S'}\left\{\frac{\partial}{\partial r_i'}\frac{1}{4\pi\sigma_{xx}\sqrt{\sigma_{zz}}}\frac{1}{\sqrt{\frac{x'^2}{\sigma_{xx}}+\frac{y'^2}{\sigma_{xx}}+\frac{z'^2}{\sigma_{zz}}}}\right\}n_j' dS' \\ &= \frac{-1}{4\pi\sigma_{xx}\sqrt{\sigma_{zz}}}\oint_{S'}\frac{r_i'/\sigma_{ii}}{\left\{\frac{x'^2}{\sigma_{xx}}+\frac{y'^2}{\sigma_{xx}}+\frac{z'^2}{\sigma_{zz}}\right\}^{3/2}}n_j' dS'. \end{aligned} \tag{9.17}$$

The above surface integral depends on the geometry of crystallites in inhomogeneous media. Under these conditions the depolarization tensor has following properties

a) If the geometry of crystallites is symmetric with respect to x,y and z axes, the integrand of equation (9.17) is odd when $i \neq j$, thus

$$\Gamma_{ij} \equiv 0, \quad i \neq j. \tag{9.18}$$

b) The elements of tensor $\overleftrightarrow{\Gamma}$ are not independent, and the diagonal elements satisfy following conditions

$$\sum_{i=1}^{3}\sigma_{ii}\Gamma_{ii} \equiv -1. \tag{9.19}$$

The above property can be easily proved by performing integration of both sides of equation (9.7).

Following Stroud and Pan (Stroud & Pan, 1979), we consider three types of crystallites: (I) sphere, (II) cylinder with the axis along y-direction perpendicular

to the magnetic field and, (III) cylinder with the axis along z-direction parallel to the magnetic field. The depolarization tensors with the accuracy to the first order for these three types of crystallites are calculated and summarized in the following. In derivation of the form of depolarization tensors, we have taken the size effect of crystallites into account and provide more precise values of the tensor components than those derived by Stroud and Pan (Stroud & Pan, 1979). The detailed derivation of these tensors is given in Appendix A.

Type I: Depolarization tensor for spherical crystallites (proof in Appendix A.3).

$$\Gamma_{zz} = \frac{1}{\chi\sigma_{zz}}\left\{\sqrt{1-\chi}\frac{\sin^{-1}\sqrt{\chi}}{\sqrt{\chi}} - 1\right\} \tag{9.20a}$$

$$\Gamma_{xx} = \Gamma_{yy} = -\frac{1}{2}\left\{\Gamma_{zz} + \frac{\sin^{-1}\sqrt{\chi}}{\sqrt{\chi\sigma_{xx}\sigma_{zz}}}\right\} \tag{9.20b}$$

$$\Gamma_{ij} \equiv 0, \quad (Otherwise), \tag{9.20c}$$

Type II: Depolarization tensor for cylinder with the axis along y-direction (proof in Appendix A.4).

$$\Gamma_{zz} = \frac{\sqrt{1-\chi}-1}{\sigma_{zz}\chi} + \frac{1}{4\sigma_{zz}}\frac{D^2}{L^2}\sqrt{1-\chi} \tag{9.21a}$$

$$\Gamma_{xx} = (1-\frac{1}{\sqrt{1-\chi}})\frac{1}{\sigma_{zz}\chi} + \frac{1}{4\sigma_{xx}}\frac{D^2}{L^2}\sqrt{1-\chi} \tag{9.21b}$$

$$\Gamma_{yy} = -\frac{1}{2\sigma_{xx}}\frac{D^2}{L^2}\sqrt{1-\chi} \tag{9.21c}$$

$$\Gamma_{ij} \equiv 0, \quad (Otherwise), \tag{9.21d}$$

Type III: Depolarization tensor for cylinder with the axis along z-direction (proof in Appendix A.5).

$$\Gamma_{xx} = \Gamma_{yy} = -\frac{1}{2\sigma_{xx}}\left\{1 - \frac{D^2}{2L^2(1-\chi)}\right\} \tag{9.22a}$$

$$\Gamma_{zz} = -\frac{D^2}{2L^2\sigma_{zz}(1-\chi)} \tag{9.22b}$$

$$\Gamma_{ij} \equiv 0, \quad (Otherwise). \tag{9.22c}$$

In the above expressions, $\chi = 1 - \sigma_{xx}/\sigma_{zz}$, D and L are the diameter and length of cylindrical crystallites.

We will use these three types of crystallites to simulate the field-dependent variation of magnetoresistance of dislocated copper samples with the different density and orientation of dislocations.

9.4 Theoretical Modeling of Transverse Magnetoresistivity

9.4.1 Magnetoresistivity of Samples with Low Dislocation Density

In this section we simulate transverse magnetoresistance of copper containing dislocation substructure. In the deformed copper single crystals, dislocation boundaries

are formed by accumulating dislocations of different slip systems, the density of dislocations depends on the magnitude and direction of the applied stress. Such a dislocated coper single crystal can be considered as a polycrystalline medium, but it is characterized by its own specific microstructure discussed in Chapter 2. We apply the effective medium theory to model the behavior of magnetoresistance after different deformation history, namely, after *stage I*, *stage II* and during the early *stage III*.

Copper single crystal samples deformed in *stage I*, accumulate approximately $10^{10} cm^{-2}$ density of dislocations (table 8.2). Electron microscopy studies (figures 2.7 and 2.8) indicate that dislocation arrangement at this stage is very inhomogeneous. One observes large areas completely free of dislocations, separated by edge dislocation bundles. Consequently, the deformed samples can be viewed as containing a large volume of dislocation-free crystallites with approximately the same crystallographic orientation and a very small volume of the crystal containing dislocations (lines of voids, see the model in reference (Bhatia & Gupta, 1970)) whose conductivity can be regarded as zero. We assume that all these crystallites have the same shape. Figure 9.2 schematically shows the model used in computation of effective magnetoresistivity ratio for slightly deformed samples which can be viewed as being comprised of cylindrical crystallites and dislocations.

To compute magnetoresistivity tensor for such system by using the effective medium theory, we suppose that these crystallites are embedded in a uniform medium with the conductivity tensor described by equation (9.13). When the magnetic field is oriented along z-direction, these crystallites have open orbits and the conductivity

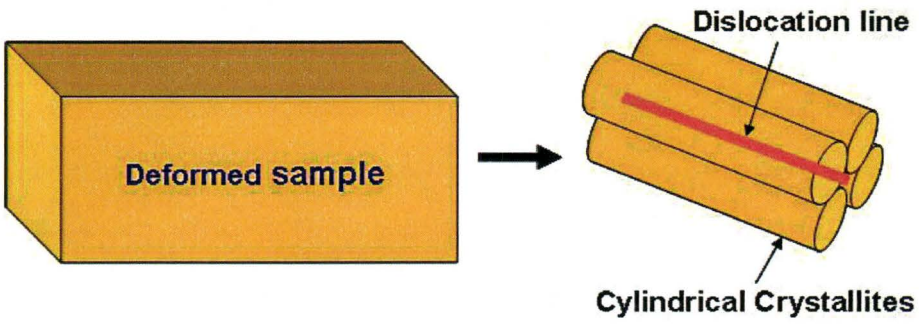

Figure 9.2: Geometrical illustration for the model of slightly deformed samples which can be viewed as being comprised of cylindrical crystallites and dislocations.

tensor is described by equation (9.14). Let the long side (current direction) of the rectangular parallelepiped sample be in x direction. Applying equation (4.37), we have

$$\begin{aligned}\overleftrightarrow{\sigma}_{eff} &= \overleftrightarrow{\sigma}_m + \\ &\left\{(1-f_v)(-\overleftrightarrow{\sigma}_m)\left[1+\overleftrightarrow{\Gamma}_1\cdot\overleftrightarrow{\sigma}_m\right]^{-1} + f_v\delta\overleftrightarrow{\sigma}\cdot\left[1-\overleftrightarrow{\Gamma}_2\cdot\delta\overleftrightarrow{\sigma}\right]\right\} \\ &\cdot\left\{(1-f_v)\left[1+\overleftrightarrow{\Gamma}_1\cdot\overleftrightarrow{\sigma}_m\right]^{-1} + f_v\left[1-\overleftrightarrow{\Gamma}_2\cdot\delta\overleftrightarrow{\sigma}\right]^{-1}\right\}^{-1}. \qquad (9.23)\end{aligned}$$

Where

$$\delta\overleftrightarrow{\sigma} = \overleftrightarrow{\sigma}^{op}(\varphi) - \overleftrightarrow{\sigma}_m, \qquad (9.24)$$

f_v is the volume fraction of the crystallites with open orbits and $\overleftrightarrow{\Gamma}_1$ and $\overleftrightarrow{\Gamma}_2$ are depolarization tensors of dislocations and crystallites whose forms depend on their configurations.

Equation (9.23) is complicated and numerical methods have to be applied to

find its solution. A FORTRAN program was written to calculate the effective conductivity tensor from equation (9.23) by iterations. The initial conductivity tensor for the medium is chosen to have the form of equation (9.13). After the solution to equation (9.23) is determined, taking the inverse of it yields magnetoresistivity tensor.

Three model configurations of crystallites, namely type I (sphere), type II and III (cylinder with its axis in y and z-direction respectively), are considered in calculation. First, we investigate the effect of volume fraction of open orbits f_e on magnetoresistance by plotting the effective magnetoresistivity ratio $(\rho_{xx}(B)-\rho_{xx}(0))/\rho_{xx}(0)$ as a function of the magnetic field for three types of crystallites (see Figures 9.3, 9.4 and 9.5). In calculation, φ in equation (9.14) is taken as 90 degrees. Details of computation (FORTRAN program) are given in Appendix B.1

Figures 9.3, 9.4 and 9.5 all show almost the same behavior that, the calculated effective magnetoresistivity ratio as a function of the magnetic field falls off as the fraction f_e of electrons occupying open-orbits decrease. Such feature implies that the geometry of crystallites is not particularly important in determination of galvanomagnetic property for slightly deformed crystals. This is because the size of the crystallites in slightly deformed samples are relatively large and they are oriented almost in the same direction, so the boundary shape between the crystallites is a neglectable factor in comparison to the volume fraction of dislocations contributing to magnetoresistivity.

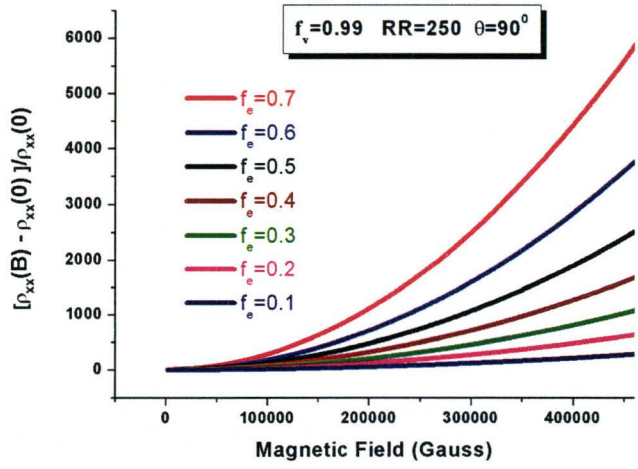

Figure 9.3: Effective magnetoresistivity ratio $(\rho_{xx}(B) - \rho_{xx}(0))/\rho_{xx}(0)$ against the magnetic field for different fraction of electrons in open orbits for the configuration of spherical crystallites. In calculation, $f_v = 0.99$ and $RR = 250$.

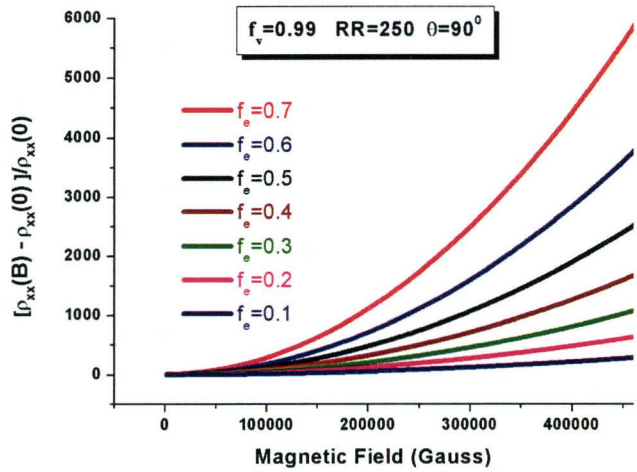

Figure 9.4: Effective magnetoresistivity ratio $(\rho_{xx}(B) - \rho_{xx}(0))/\rho_{xx}(0)$ against the magnetic field for different fraction of electrons in open orbits for the configuration of cylindrical crystallites parallel to y-direction. In calculation, $f_v = 0.99$ and $RR = 250$.

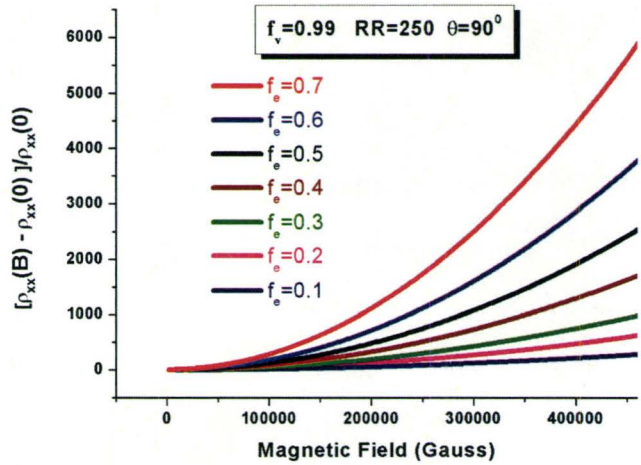

Figure 9.5: Effective magnetoresistivity ratio $(\rho_{xx}(B) - \rho_{xx}(0))/\rho_{xx}(0)$ against the magnetic field for different fraction of electrons in open orbits for the configuration of cylindrical crystallites parallel to z-direction. In calculation, $f_v = 0.99$ and $RR = 250$.

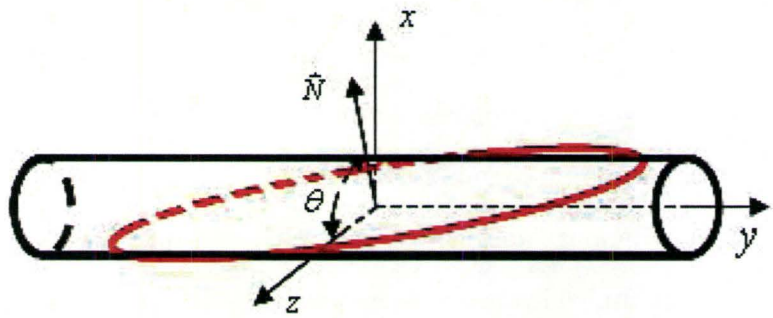

Figure 9.6: Schematic illustration of an extended orbit on cylindrical Fermi surface. Polar angle $\theta \neq \frac{\pi}{2}$

We have also investigated the influence of extended orbits on magnetoresistance in deformed samples by considering different polar angles in calculation. Figure

9.6 schematically shows an extended orbit on the cylindrical Fermi surface. Extended orbits are expected to have the same behavior as open orbits at sufficiently low fields, since cyclotron frequency is small at very low fields and the electrons moving on these orbits can not complete a full circuit before they are scattered out of the orbits. However, at high fields, electrons' cyclotron speed is much faster and they will act like moving on closed orbits. Based on the experimental results of magnetoresistivity for samples 733B2 and 749A2 deformed to strain of about $1 \sim 3\%$ (Table 8.2), we computed transverse effective magnetoresistivity ratio as a function of the field by taking different polar angles corresponding to different extended orbits. Figures 9.7, 9.8 and 9.9 are the plots of the computing results.

It can be seen from the Figures 9.7 - 9.9 that the effective magnetoresistivity ratio is significantly reduced as polar angle θ denoting the field direction, deviates from $\pi/2$ in which open-orbit occurs. Deviation by only a few degrees in θ causes substantial reduction in magnetoresistivity ratio. In addition, Figures 9.7, 9.8 and 9.9 retain similar pattern, which is consistent with the previous conclusion that the shape of crystallites in slightly deformed crystals is unimportant in determination of galvanomagnetic properties.

For comparison of the theory with experiment, we plot both the experimental and theoretical results in Figures 9.10 and 9.11. It is clear that theoretical simulations match very well with the experimental data.

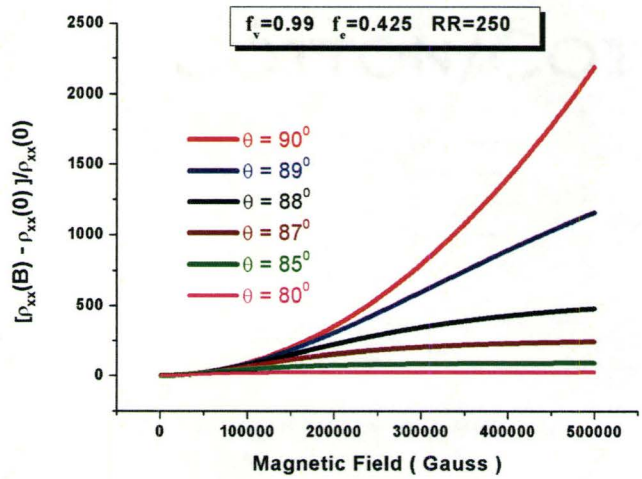

Figure 9.7: Effective magnetoresistivity ratio $(\rho_{xx}(B) - \rho_{xx}(0))/\rho_{xx}(0)$ against the magnetic field for different polar angles for the configuration of spherical crystallites. In calculation, $f_v = 0.99$, $f_e = 0.425$ and $RR = 250$.

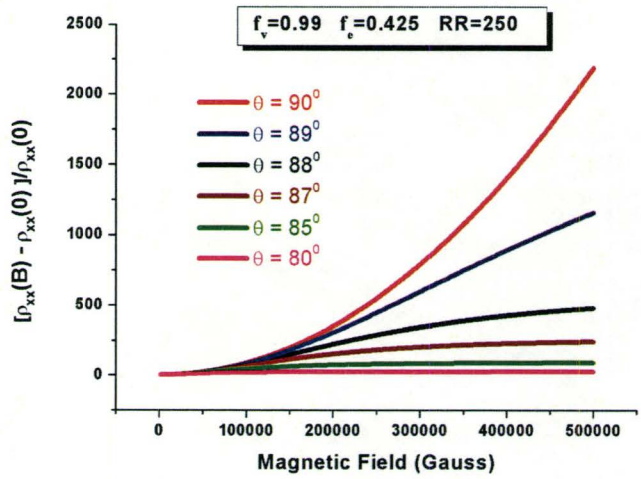

Figure 9.8: Effective magnetoresistivity ratio $(\rho_{xx}(B) - \rho_{xx}(0))/\rho_{xx}(0)$ against the magnetic field for different polar angles for the configuration of cylindrical crystallites parallel to y-direction. In calculation, $f_v = 0.99$, $f_e = 0.425$ and $RR = 250$.

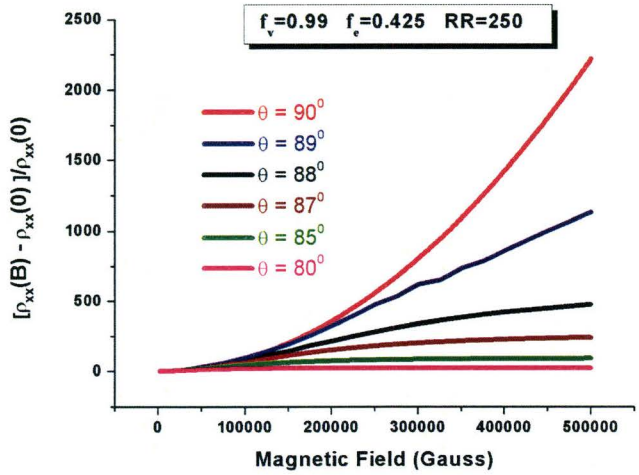

Figure 9.9: Effective magnetoresistivity ratio $(\rho_{xx}(B) - \rho_{xx}(0))/\rho_{xx}(0)$ against the magnetic field for different polar angles for the configuration of cylindrical crystallites parallel to z-direction. In calculation, $f_v = 0.99$, $f_e = 0.425$ and $RR = 250$.

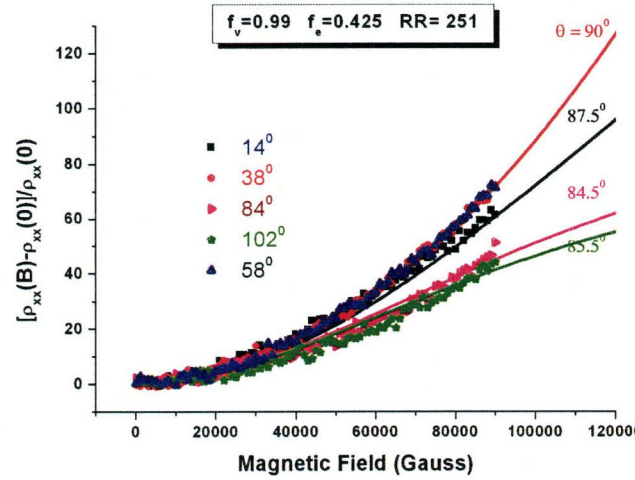

Figure 9.10: Solid lines are the field dependent effective magnetoresistivity ratio $(\rho_{xx}(B) - \rho_{xx}(0))/\rho_{xx}(0)$ for different polar angles for the configuration of cylindrical crystallites parallel to y-direction. In calculation, $f_v = 0.99$, $f_e = 0.425$ and $RR = 251$. Point curves are the experimental data for sample 733B2 plotted in Figure 8.19

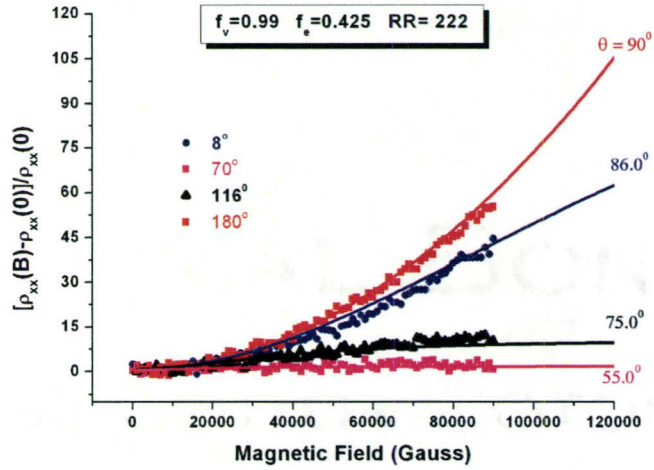

Figure 9.11: Solid lines are the field dependent effective magnetoresistivity ratio $(\rho_{xx}(B) - \rho_{xx}(0))/\rho_{xx}(0)$ for different polar angles for the configuration of cylindrical crystallites parallel to y-direction. In calculation, $f_v = 0.99$, $f_e = 0.425$ and $RR = 222$. Point curves are the experimental data for sample 749A2 plotted in Figure 8.24.

In order to study the angular dependence of magnetoresistance, we calculated the effective magnetoresistance ratio as a function of polar angle θ for the samples with different density of dislocations determined by the resistivity ratio RR. Figures 9.12, 9.13 and 9.14 are the plots of the theoretical results. All these figures indicate that for different resistivity ratio RR, the effective magnetoresistivity ratio reaches the maximum (the peak) at $\theta = \pi/2$ corresponding to open-orbit, whereas the height of the peaks reduces as the the density of dislocations in samples increases. Such theoretical consequence is consistent with the experimental measurements of magnetoresistance for samples 733B and 749A which are shown in Figures 8.18, 8.19, 8.20, 8.23, 8.24 and 8.25 . In calculation, the magnetic field is fixed at 9 Tesla for all three configurations. FORTRAN program for computation

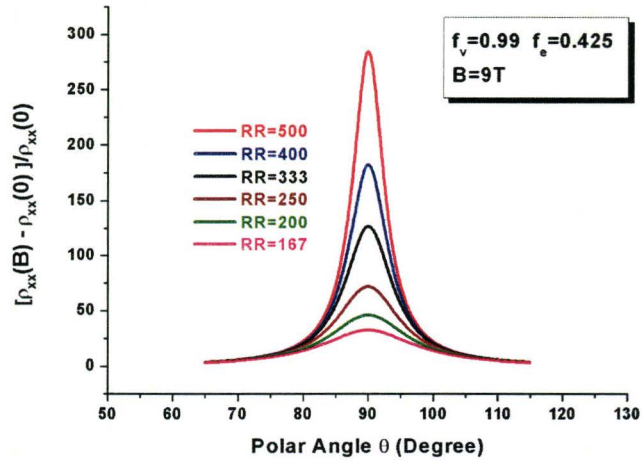

Figure 9.12: Effective magnetoresistivity ratio against polar angle for spherical crystallites with different density of dislocations given by resistivity ration *RR*. In calculation, $f_v = 0.99$ and $f_e = 0.425$.

of the angular dependence of magnetoresistance is given in Appendix B.2.

To understand the effect of dislocation density on transverse magnetoresistance for open-orbits, we calculated the effective magnetoresistivity ratio as a function of the magnetic field for different density of dislocations characterized by resistivity ratio *RR*, as shown in Figures 9.15, 9.16 and 9.17. All figures display a parabolic variation of effective magnetoresistivity ratio with the magnetic field and it is seen that effective magnetoresistivity ratio gets smaller as *RR* decreases. However, the parabolic dependence of the magnetoresistivity in the applied field is observed even for a somewhat smaller value of resistivity ratio such as $RR = 166$ corresponding to a density of dislocations $10^{11}/cm^2$.

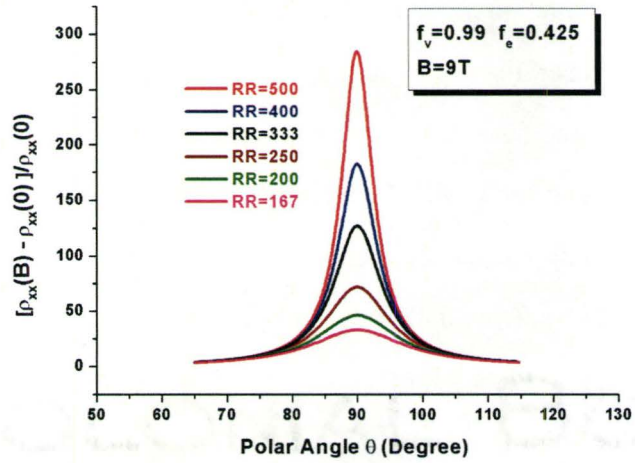

Figure 9.13: Effective magnetoresistivity ratio against polar angle for the cylindrical crystallites along y-direction with different density of dislocations given by resistivity ration RR. In calculation, $f_v = 0.99$ and $f_e = 0.425$.

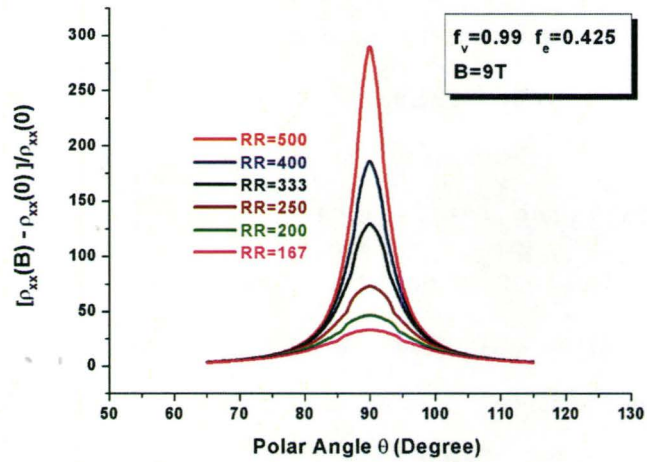

Figure 9.14: Effective magnetoresistivity ratio against polar angle for the cylindrical crystallites along z-direction with different density of dislocations given by resistivity ration RR. In calculation, $f_v = 0.99$ and $f_e = 0.425$.

In the above approach, the adjustable parameters of the model are volume fraction f_v and electron fraction f_e. As a further investigation, we want to examine whether there is a general set of f_v and f_e through which transverse magnetoresistivity ratio against the field can be calculated for any deformed sample with the density of dislocations given by *RR*. In order to fulfill this goal, we computed transverse magnetoresistivity ratio as a function of the magnetic field by choosing the parameters ($f_v = 0.99$ and $f_e = 0.425$) for best fit of the experimental data for sample 733B2 ($RR = 251$). Plots both theoretical and experimental results are given in Figure 9.18 (blue solid line and point curve). Based on these two parameters, we also calculated field-dependent transverse mangnetoresistivity ratio by taking different value of *RR* equal to 418, 400, 222, 166, 151 which corresponds to the density of dislocations in samples 733B and 749A measured experimentally. For comparison, we plot both modeling curve (solid lines) and experimental data (point curves) in Figure 9.18 for sample 733B and in Figure 9.19 for sample 749A. It is seen in Figure 9.19 that the modeling curve (blue solid line) and experimental data (blue points) match very well for sample 749A2 ($RR = 222$) but for *RR* values 400 and 166 , they show a big discrepancy. This is because the densities of dislocations in [100] sample 733B2 ($RR = 251$) and [541] sample 749A2 ($RR = 222$) are very close to each other and both samples have similar structure at this stage of deformation. Consequently, the set of parameters to fit one sample in simulation of field-dependent magnetoresistance will fit another having alike structure, characterized by similar value of *RR*. To make this point stronger, we recalculated field-dependent magnetoresistance for samples 733B3 ($RR = 166$) and 749A3 ($RR = 151$) by taking $f_e = 0.275$ for both samples and plotting them in Figures 9.18 and 9.19 (black dash lines). It is found that theoretical calculation is in very good agreement with

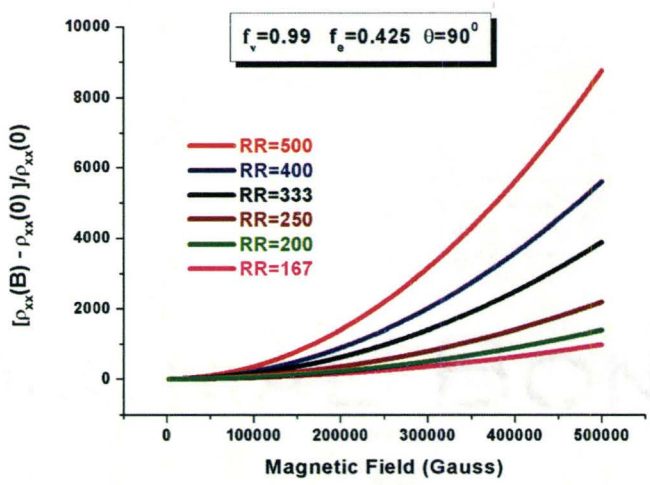

Figure 9.15: Field dependent effective magnetoresistivity ratio for different density of dislocations for the configuration of spherical crystallites. In calculation, $f_v = 0.99$ and $f_e = 0.425$.

experimental data for both samples. Such result imply that dislocations introduced to the crystals with different crystallographic orientation of the tensile axis make no difference in galvanomagnetic properties as long as the samples have the same density of dislocations.

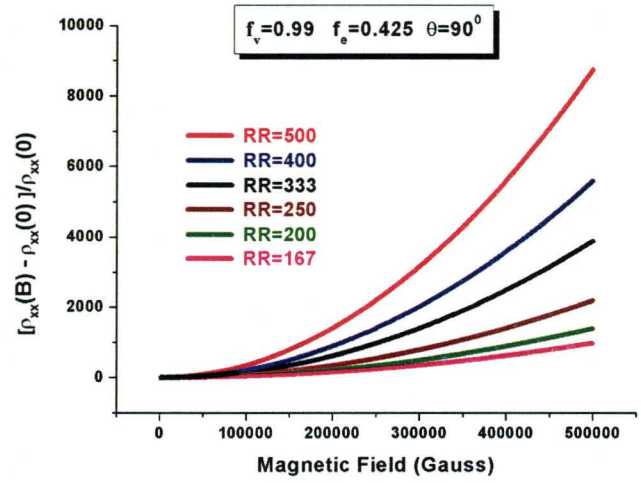

Figure 9.16: Field dependent effective magnetoresistivity ratio for different density of dislocations for the configuration of cylindrical crystallites parallel to y-direction. In calculation, $f_v = 0.99$ and $f_e = 0.425$.

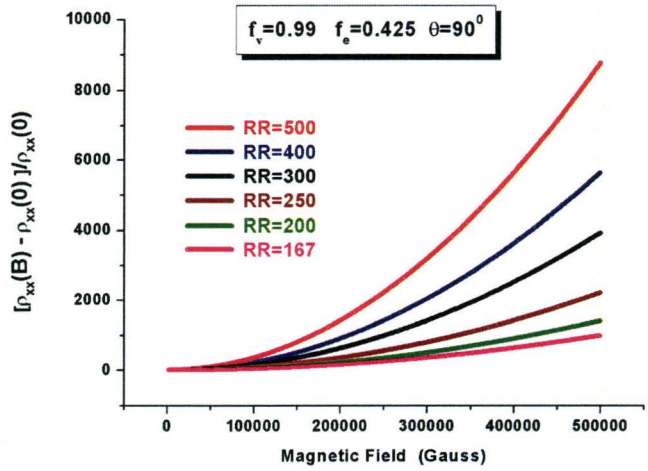

Figure 9.17: Field dependent effective magnetoresistivity ratio for different density of dislocations for the configuration of cylindrical crystallites parallel to z-direction. In calculation, $f_v = 0.99$ and $f_e = 0.425$.

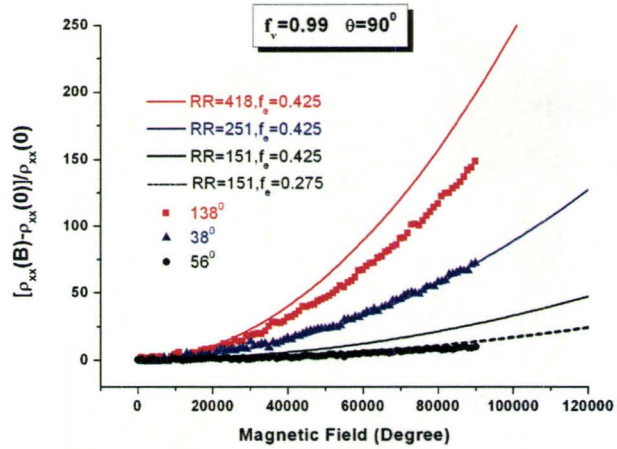

Figure 9.18: Field dependent effective magnetoresistivity ratio for different density of dislocations for the configuration of cylindrical crystallites parallel to y-direction. Solid and dash lines are the modeling curves. Point lines are the experimental data for open orbits for sample 733B1, 733B2 and 733B3 (given in Figures 8.18(b), 8.19(b) and 8.20(b)) respectively. In calculation, $f_v = 0.99$.

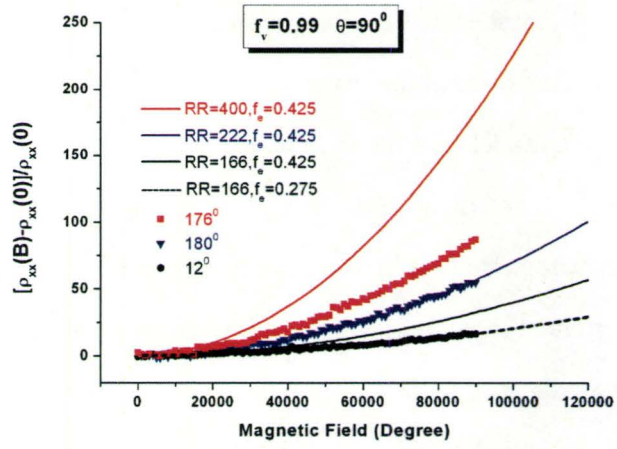

Figure 9.19: Field dependent effective magnetoresistivity ratio for different density of dislocations for the configuration of cylindrical crystallites parallel to y-direction. Solid and dash lines are the modeling curves. Point lines are the experimental data for open orbits for sample 749A1, 749A2 and 749A3 (given in Figures 8.23(b), 8.24(b) and 8.25(b)) respectively. In calculation, $f_v = 0.99$.

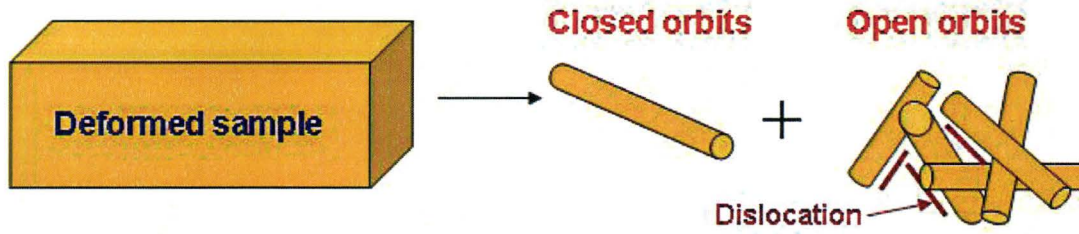

Figure 9.20: Geometrical illustration for the model of largely deformed samples which can be viewed as being comprised of cylindrical crystallites with closed and open orbits.

9.4.2 Magnetoresistivity of Samples with High Dislocation Density

In samples deformed to later stage *II* or early stage *III*, dislocations of various slip systems are accumulated in the substructure leading to the development of misoriented cells enclosed by higher dislocation density cell walls (see pictures 2.10, 2.11, 2.12 and 2.13). This form of the material substructure corresponds to misoriented crystallites in our model. For the time being, we assume that these misorientation of dislocation cells and dislocation arrangement in the cell walls are random. Such a structure can be regarded as consisting of two kinds of crystallites. First kind of crystallites are oriented in such a way that only closed orbits exist in the plane perpendicular to the magnetic field and they are assumed to have a free-electron conductivity tensor described by equation (9.13). Second kind of crystallites do have open orbits on the plane perpendicular to the magnetic field which is usually taken along z-direction. The conductivity tensor for these crystallites has the form of equation (9.14) when θ is taken 90^0. Figure 9.20 schematically represents the model that a deformed sample is comprised of cylindrical crystallites with closed

and open-orbits. Since all crystallites in the deformed sample are oriented randomly, this will result in a random distribution of the orientations of open orbits in momentum space. Mathematically, polar angle φ in equation (9.14) will take any value from 0 to 2π. Consequently, the orientations of open orbits have equal probability in each direction on the plane perpendicular to the magnetic field. For such a system, the effective conductivity tensor satisfies

$$\begin{aligned}\overleftrightarrow{\sigma}_{eff} &= \overleftrightarrow{\sigma}_m + \\ &\frac{1}{2\pi}\int_0^{2\pi}\left\{(1-f_v)\delta\overleftrightarrow{\sigma}_1\left[1-\overleftrightarrow{\Gamma}_1\cdot\delta\overleftrightarrow{\sigma}_1\right]^{-1}+f_v\delta\overleftrightarrow{\sigma}_2\cdot\left[1-\overleftrightarrow{\Gamma}_2\cdot\delta\overleftrightarrow{\sigma}_2\right]\right\} \\ &\cdot\left\{(1-f_v)\left[1-\overleftrightarrow{\Gamma}_1\cdot\delta\overleftrightarrow{\sigma}_1\right]^{-1}+f_v\left[1-\overleftrightarrow{\Gamma}_2\cdot\delta\overleftrightarrow{\sigma}_2\right]^{-1}\right\}^{-1}d\varphi \qquad (9.25)\end{aligned}$$

Where

$$\delta\overleftrightarrow{\sigma}_1 = \overleftrightarrow{\sigma}^{cl} - \overleftrightarrow{\sigma}_m, \qquad (9.26a)$$

$$\delta\overleftrightarrow{\sigma}_2 = \overleftrightarrow{\sigma}^{op}(\varphi) - \overleftrightarrow{\sigma}_m, \qquad (9.26b)$$

and $\overleftrightarrow{\sigma}^{cl}$ denotes the conductivity tensor of free-electrons. Γ_1 and Γ_2 represent depolarization tensor for crystallites with closed and open orbits respectively. f_v is the volume fraction of crystallites with open-orbit and f_e is electron fraction having the same definition as in equation (9.23).

By applying self-consistent method, we have calculated the effective conductivity tensor from equation (9.25) for the crystallites of type I and II. FORTRAN source code for these calculations is given in Appendix B.3. Figures 9.21 and 9.22 show effective magnetoresistivity ratio as a function of the magnetic field for dif-

ferent volume fraction f_v of spherical and cylindrical crystallites respectively, with open orbits. In these calculation, $RR = 118$ and $f_e = 0.5$. Figure 9.21 reveals a linear variation of magnetoresistance with the magnetic field in a field range above 2 *Tesla*, for f_v values from 0.1 to 0.6. It is seen that the slope of the lines decreases as f_v gets smaller, which means the number of electron moving on open orbits decreases. Figure 9.22 reveals similar features as seen previously in Figure 9.21, i.e., the effective magnetoresistance ratio decreases with decreasing volume fraction f_v. However, the linear variation of magnetoresistance occurs only at very large fields above 30 or 40 *Tesla*. It is seen that at lower fields, below 30 *Tesla*, the change of magnetoresistance with the field is not linear, but show more like parabolic behavior. Furthermore, it is seen that magnetoresistivity ratio is larger for the crystals with cylindrical than spherical crystallites, provided that other parameters such as f_e , f_v and RR remain the same. This suggest that the single crystals for which the magnetoresistivity behavior can be predicted with the model incorporating spherical crystallites have more random structure of dislocations than these with magnetoresistivity behavior described by the model using cylindrical crystallites.

We also investigated the effect of dislocation density on magnetoresistivity by plotting magnetoresistivity ratio as a function of the magnetic fields for different values of resistivity ratio RR (Figures 9.23 and 9.24). In these simulations $f_v = 0.5$ and $f_e = 0.5$. It is noted from the figures that the density of dislocations has a substantial effect on magnetoresistance of deformed samples and with more dislocations stored in the samples, effective magnetoresistivity ratio decreases. Moreover, the linear behavior of field-dependent magnetoresistivity appears in all curves for

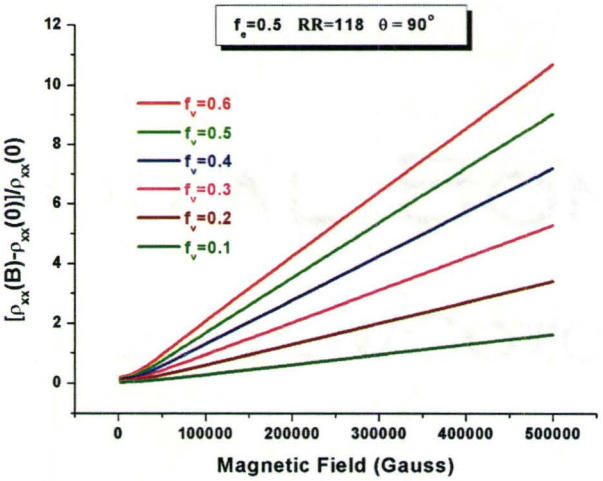

Figure 9.21: Effective magnetoresistivity ratio against the magnetic field for different volume fraction of crystallites having open orbits for the configuration of spherical crystallites. In calculation, $f_e = 0.5$ and $RR = 118$.

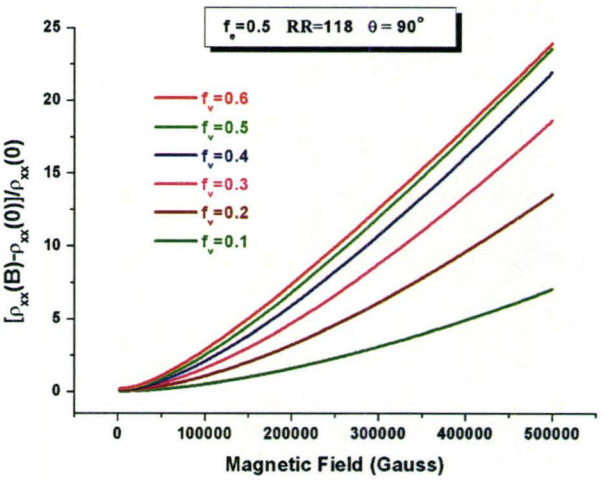

Figure 9.22: Effective magnetoresistivity ratio against the magnetic field for different volume fraction of crystallites having open orbits for the configuration of cylindrical crystallites parallel to y-direction.In calculation, $f_e = 0.5$ and $RR = 118$.

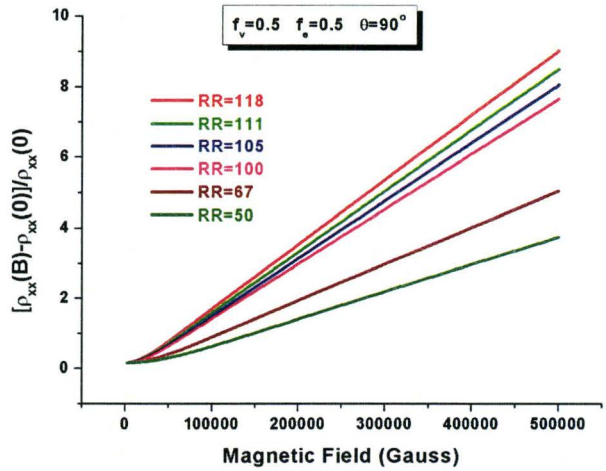

Figure 9.23: Effective magnetoresistivity ratio against the magnetic field for largely deformed samples with different density of dislocations for the configuration of spherical crystallites. In calculation, $f_e = 0.5$ and $f_v = 0.5$.

both types of crystallites, but for cylindrical crystallites, this linearity occurs at the higher applied filed. Similar to the previous case of magnetoresistivity behavior observed in Figure 9.22, one can argue that with more dislocations stored in the samples, magnetoresistivity considerably decreases and the linear behavior starts approximately from 4 *Tesla* for spherical crystallites but from about 20 *Tesla* for cylindrical crystallites.

Figure 9.25 show comparison of the magnetoresistivity behavior predicted theoretically using above discussed model against the experimental data. The field-dependent magnetoresistivity ratio has been calculated by taking $RR = 104$ and $RR = 67$ which corresponds to the experimentally measured resistivity ratio for highly deformed sample 700H ($RR = 104$) and polycrystalline copper sample Poly43-

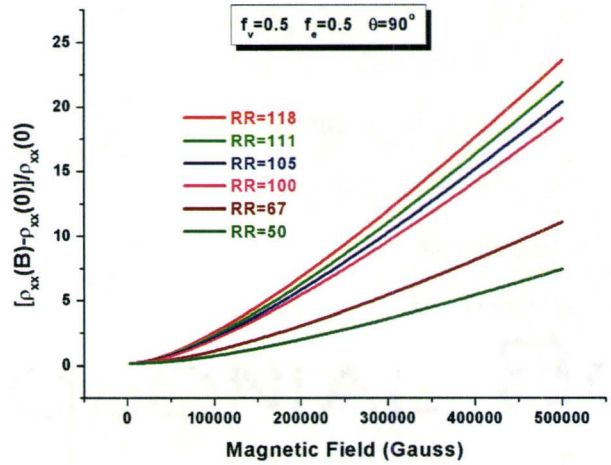

Figure 9.24: Effective magnetoresistivity ratio against the magnetic field for largely deformed samples with different density of dislocations for the configuration of cylindrical crystallites parallel to y-direction. In calculation, $f_e = 0.5$ and $f_v = 0.5$.

micron($RR = 67$) included in Figure 9.25. Adjustable parameters f_v and f_e are taken to be 0.6 and 0.95, which is based on the assumption that in highly deformed samples the crystallites are oriented randomly, so that the number of electrons moving on open-orbits is equal to the number of electrons circulating on closed orbits. Figure 9.25 shows that the modeling curve of magnetoresistivity against the magnetic field for polycrystalline sample (red line) has a very good agreement with the experimental data (red points). Such a good consistency between theory and experiment confirms the assumption that orientations of crystallites in a polycrystalline material should have a random distribution of dislocations and its electrical properties can be obtained by spatially averaging the physical quantities over all crystallites. However, there is a big discrepancy between the modeling curve (blue dash line) and the experimental data (blue points) for large deformed sam-

ple 700H ($RR = 104$). In reality, such a big difference can not be eliminated by only adjusting the parameters in theoretical calculation, for example, increasing the volume fraction of crystallites with open orbits or the fraction of electrons in the cylindrical band. Electron-microscopy observations of the dislocation substructure in plastically deformed copper single crystals show that the arrays of dislocations form small angle grain boundaries in the deformation *stage III* (see Figure 2.14). It may be reasonable to postulate that crystallites in largely deformed samples are not oriented randomly and they have some preferential crystallographic orientation. The distribution of orientations of crystallites will depend on the formation of the dislocation substructure which is developed under the applied stress. In general, the larger deformation, the higher angular distribution the crystallites in the sample. To investigate the influence of angular distribution of crystallites on magnetoresistivity, we have computed the effective conductivity tensor from equation (9.25) by taking different integral boundaries and plotted resistivity ratio as a function of the magnetic fields for the two types of crystallites in Figures 9.26 and 9.27. It is seen in both figures that the broadening integral regions lead to a significant decrease of the magnetoresistance but simulated curves show higher degree of linearity.

We have also studied the effect of extended orbits on the galvanomagnetic properties for largely deformed samples by taking different polar angle to calculate the effective conductivity from equation (9.25). Figures 9.28 and 9.29 show the effective resistivity ratio as a function of the magnetic fields for different polar angles which correspond to different extended orbits in largely deformed samples. It is seen in both figures that with electron orbits getting shorter (θ deviates from $\pi/2$),

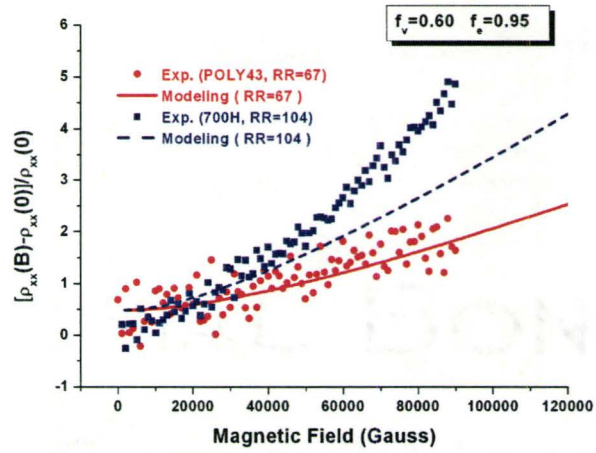

Figure 9.25: Effective magnetoresistivity ratio against the magnetic fields for the configuration of cylindrical crystallites parallel to y-direction. In calculation, the volume and electron fraction are taken as 0.60 and 0.95. The blue dashed line and red solid line are the modeling curves for $RR = 104$ and $RR = 67$ respectively. The solid square and circle points are the experimental data for samples 700H and poly43micron respectively shown previously in Figures 8.26(b) and 8.27(b)

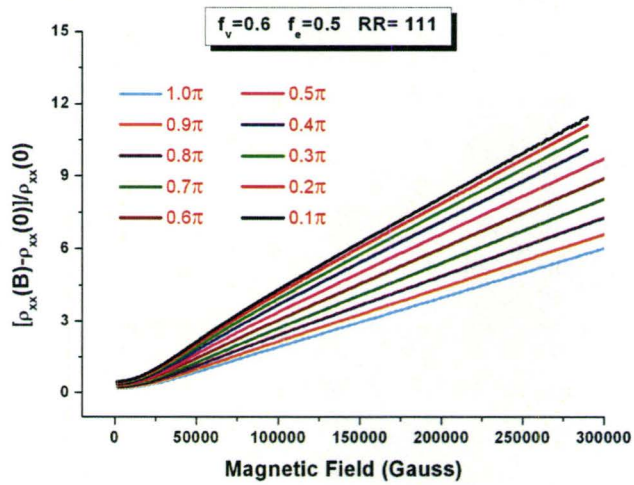

Figure 9.26: Effective magnetoresistivity ratio against the magnetic field for different integral regions for the configuration of spherical crystallites. In calculations $f_v = 0.6$, $f_e = 0.5$ and $RR = 111$ respectively.

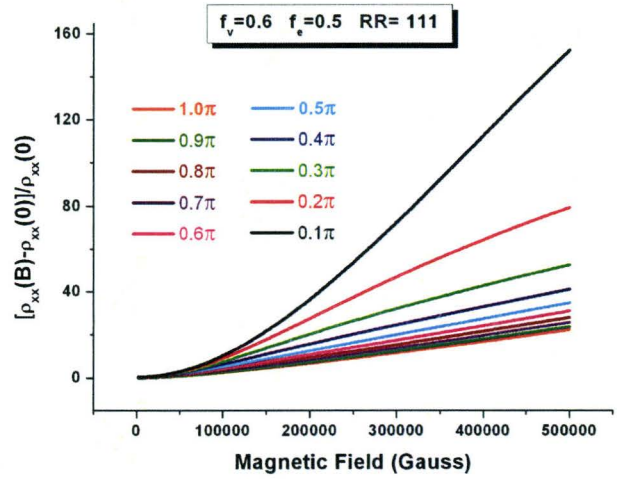

Figure 9.27: Effective magnetoresistivity ratio against the magnetic field for different integral regions for the configuration of cylindrical crystallites parallel to y-direction. In calculations $f_v = 0.6$, $f_e = 0.5$ and $RR = 111$ respectively.

effective magnetoresistance decreases considerably and shows saturating behavior at large magnetic filed.

To examine applications of the above-discussed theory to crystals containing high dislocations densities, we have simulated field-dependent magnetoresistance for highly deformed samples by taking the parameters based on their experimental data. Figures 9.30, 9.31 and 9.32 show modeling curves matching the experimental data for samples 700H ($RR = 104$), 733C ($RR = 138$) and 749A3 ($RR = 166$).

It is seen that Figures 9.30 and 9.31 demonstrate a very good agreement of

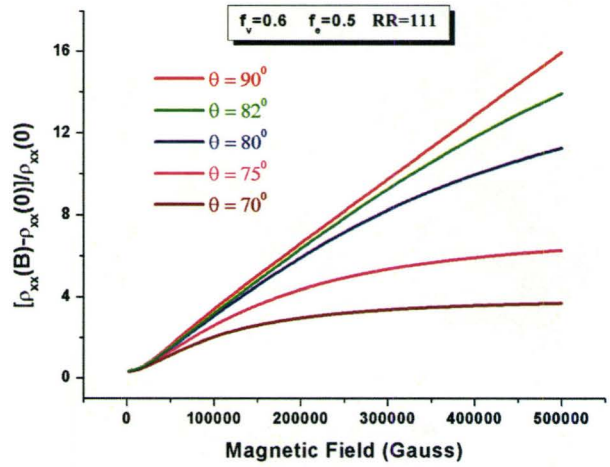

Figure 9.28: Effective magnetoresistivity ratio against the magnetic field for largely deformed samples with different density of dislocations for the configuration of spherical crystallites. In calculation, $f_e = 0.5$ and $f_v = 0.6$.

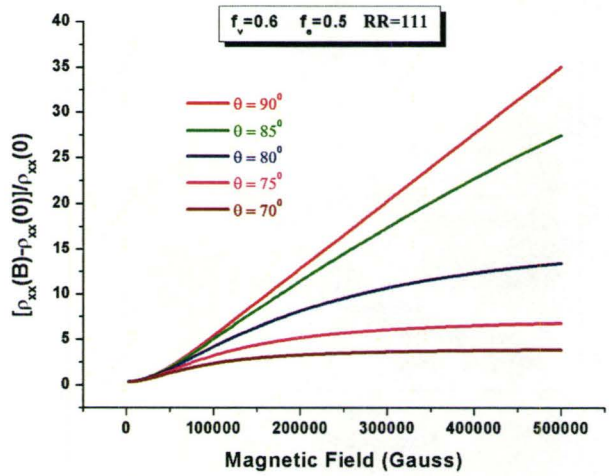

Figure 9.29: Effective magnetoresistivity ratio against the magnetic field for largely deformed samples with different density of dislocations for the configuration of cylindrical crystallites parallel to y-direction. In calculation, $f_e = 0.5$ and $f_v = 0.6$.

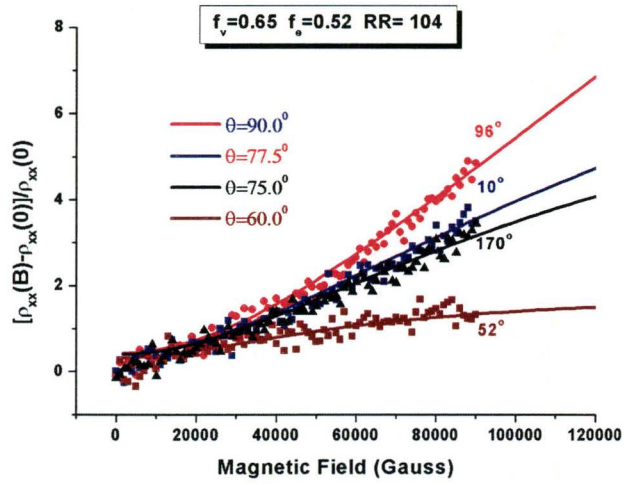

Figure 9.30: Field dependent effective magnetoresistivity ratio for the crystallites of type II. In calculation, the integral region is from -0.5π to 0.5π, f_v, f_e and RR are taken as 0.65, 0.52 and 104 respectively. The points are the experimental data for sample 700H ($RR = 104$) plotted in Figure 8.26(b).

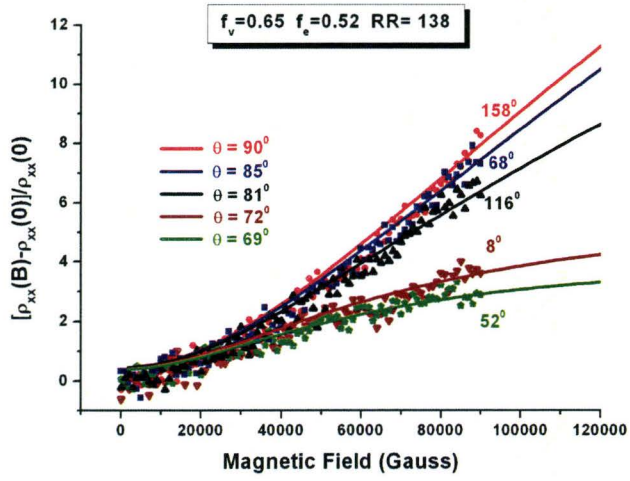

Figure 9.31: Field dependent effective magnetoresistivity ratio for the crystallites of type II. In calculation, the integral region is from -0.42π to 0.42π, f_v, f_e and RR are taken as 0.65, 0.52 and 138 respectively. The points are the experimental data for sample 733C ($RR = 138$) plotted in Figure 8.21(b).

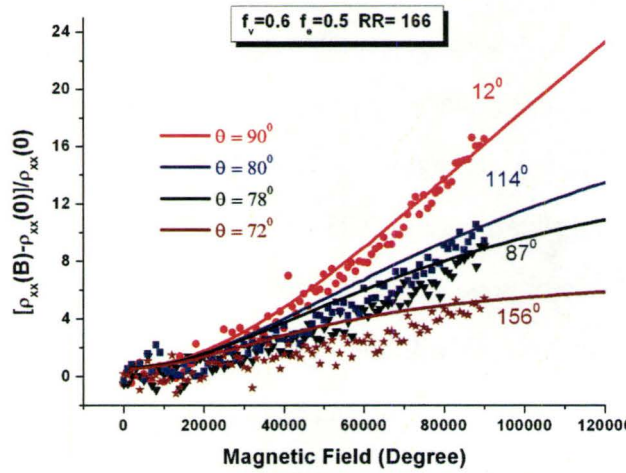

Figure 9.32: Field dependent effective magnetoresistivity ratio for the crystallites of type II. In calculation, the integral region is from -0.025π to 0.025π, f_v, f_e and RR are taken as 0.6, 0.5 and 166 respectively. The points are the experimental data for sample 749A3 ($RR = 166$) plotted in Figure 8.25(b).

the modeling results with the experimental data for samples 700H ($RR = 104$) and 733C ($RR = 138$). However, there is a substantial difference between the calculated magnetoresistivity values and experimental data for extended orbits for sample 7494A3 ($RR = 166$), although the modeling results for open orbits (red solid line) show fairly good agreement with experimental data (red points). After carefully examining the experimental data for extended orbits in Figure 9.32, we find that the curves bend slightly upright in a fairly large region of the magnetic fields. From the mathematical view-point this means that the derivative of the slopes for the curves is positive in this region. This implies that deformed sample must still retain the characteristics of the quadratic behavior of magnetoresistance against the magnetic fields. However, numerical calculation shows that the quadratic behavior of magnetoresistance with the magnetic field, characteristic for open orbits, is sub-

stantially reduced when taking the spatial average over all crystallites in calculation of magnetoresistance. The quadratic behavior may only appear within a small region of the field near the starting point. This can easily be checked by comparing Figures 9.15 and 9.16 with Figures 9.23 and 9.24. At large fields, the magnetoresistance of highly deformed samples in which the orientations of crystallites are random has a linear variation with the magnetic field, similar to the case of polycrystalline samples. Such conclusion can be obtained from Figures 9.23 and 9.24. In other words, sample 749A3 consists of crystallites which have preferential orientation of crystallite distribution rather than random distribution. Consequently, applying equation (9.25) to calculate magnetoconductivity for sample 749A3 will cause disparity between theory and experiment.

To simulate the behavior of magnetoresistance for deformed samples 733B3 ($RR = 151$) and 749A3 ($RR = 166$), we apply equation (9.23). It is found from Figures 9.33 and 9.34 that theoretical calculations agree very well with the experimental data.

9.4.3 Modeling of Magnetoresistance for Closed Orbits

The preceding discussion and the modeling of magnetoresistance of deformed samples focused on open or extended orbits. In the present section, we concentrate on the modeling of magnetoresistance for closed orbits and investigate how the density of dislocations stored in deformed samples affect the saturating behavior of magne-

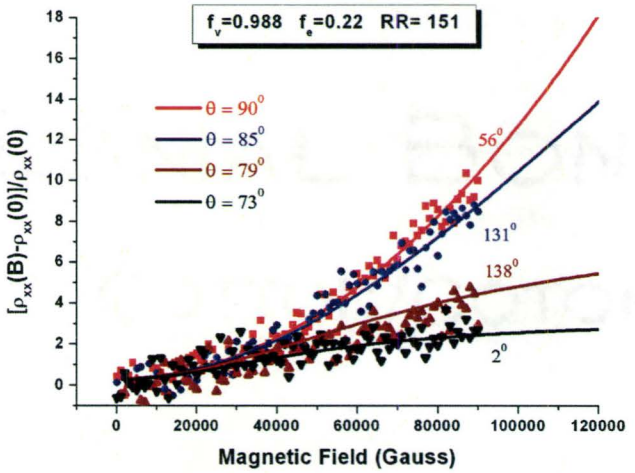

Figure 9.33: Field dependent magnetoresistivity ratio for different polar angles for the configuration of cylindrical crystallites parallel to y-direction. In calculations, equation (9.23) is used and f_v= 0.988, f_e=0.22 and RR=151. Color points are the experimental data of transverse magnetoresistance for sample 700B3 (RR=151) shown in Figure 8.20(b).

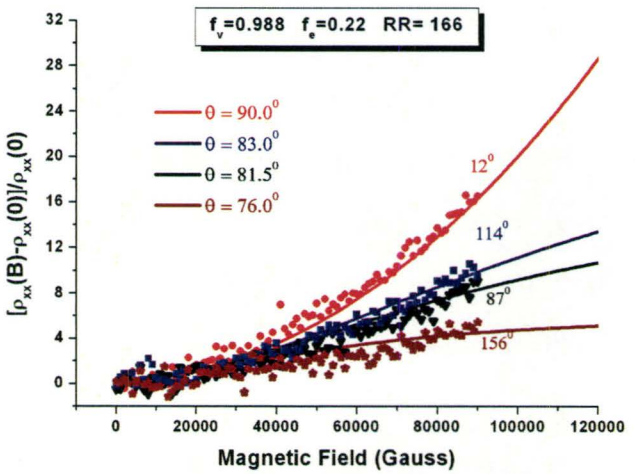

Figure 9.34: Field dependent magnetoresistivity ratio for different polar angles for the configuration of cylindrical crystallites parallel to y-direction. In calculations, equation (9.23) is used and f_v=0.988, f_e=0.22 and RR=166. Color points are the experimental data of transverse magnetoresistance for sample 749A3 (RR=166) shown in Figure 8.25(b) .

toresistance in samples by means of theoretical predictions (see section 3.3.3)

Closed orbits in deformed samples mean that for a given field direction, most of crystallites in deformed samples are oriented in such a way that only closed orbits exist in the plane perpendicular to the magnetic field and only small portion of crystallites is associated with the open orbits. Therefore, in predicting magnetoresistivity behavior for samples with closed orbits, we can employ exactly the same approach as used to predict magnetoresistivity of crystals containing low dislocation densities, discussed in section 9.4.1. The only change needed to be made is a smaller value for electron fraction f_e representing the portion of electrons moving on open orbits.

Following the same procedure as in section 9.4.1, we have computed effective magnetoresistivity ratio as a function of the magnetic field by applying self-consistent method to solve equation 9.23. Figure 9.35 shows field-dependent effective magnetoresistivity ratio for different values of electron fraction f_e. In simulations $f_v = 0.99$ and $RR = 400$ respectively. The figure reveals that with the decreasing electron fraction f_e, effective magnetoresistivity ratio falls off, but all curves show similar patterns. It is seen that the magnetoresistivity raises very quickly at small fields, whereas the rate of magnetoresistivity increase is lower at large fields and under certain conditions magnetoresistivity may even reach a saturation. Such phenomenon is a universal characteristics of magnetoresistance in metals containing closed Fermi surface, where the electrons are localized predominantly on closed orbits (Fickett, 1971; Beers *et al.*, 1978). It can be also seen that with f_e decreasing, magnetoresistivity slope at large fields is getting smaller, which is consistent

with the conclusion that in samples with closed orbits only ($f_e = 0$), magnetoresistance will saturate. Figure 9.36 shows the field dependence of effective magnetoresistivity ratio for various values of resistivity ratio *RR*. It is clear that as more dislocations are present in the samples, indicated by a smaller value of *RR*, the curves for each *RR* lose their universal characteristic of magnetoresistance for closed orbits. In this case it is observed that the magnetoresistivity slopes at low field decrease, whereas slopes of the magnetoresistivity curves at large fields increase and reach approximately the same value at $RR = 100$, corresponding to a straight line on the magnetoresistivity-field relationship. This indicates that dislocations present in the sample affect magnetoresistivity behavior in such a way that they bend field-dependent magnetoresistance curve upright from both sides of turning point and make it eventually straight. With increasing dislocation density (*RR* decreases), field-dependent magnetoresistance curve exhibits a linear behavior, but with a lower slope. There is no doubt that dislocations induced in deformed samples change the saturating characteristic of the field-dependent magnetoresistance for closed orbit and cause it to vary linearly at large applied magnetic field.

To examine the applicability of the above-discussed model for the prediction of the magnetoresistivity behavior of deformed copper single crystals, we have calculated effective magnetoresistance ratio as a function of the field for closed orbits by employing self-consistent method and solving equation 9.23. Theoretical results are plotted in Figure 9.37. In calculations $f_v = 0.99$ and $f_e = 0.075$ and these have been found to represent the best set of f_v and f_e values to simulate the experimental data for sample 733B1 ($RR = 418$) (solid blue curve). The family of magnetoresistivity

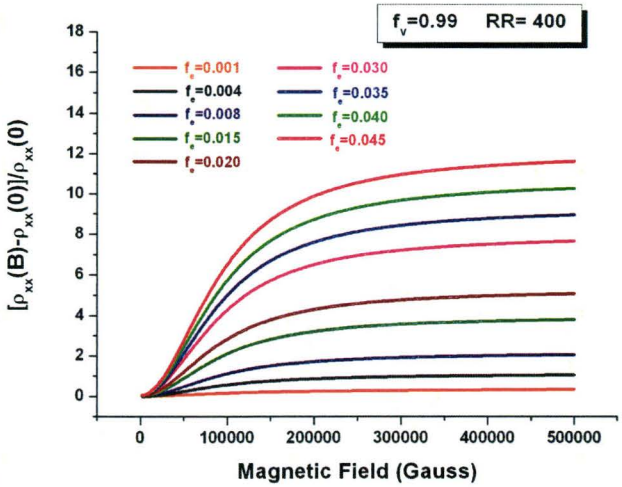

Figure 9.35: Field dependent effective magnetoresistivity ratio for different value of f_e for the configuration of cylindrical crystallites parallel to y-direction. In calculations, f_v= 0.99, $\theta = 90^0$ and RR=400.

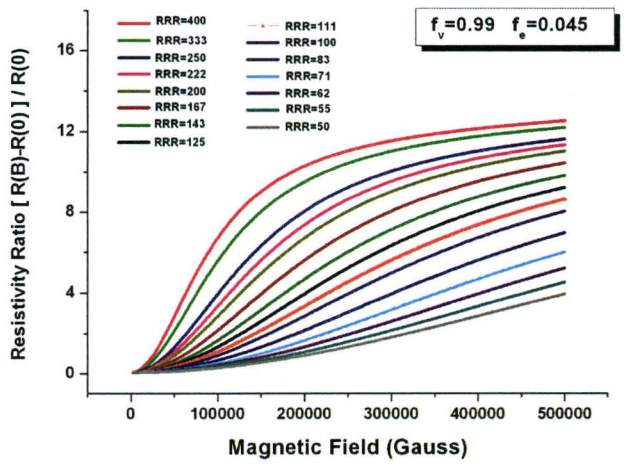

Figure 9.36: Field dependent effective magnetoresistivity ratio for different value of RR for the configuration of cylindrical crystallites parallel to y-direction. In calculations, f_v= 0.99, $f_e = 0.045$ and $\theta = 90^0$.

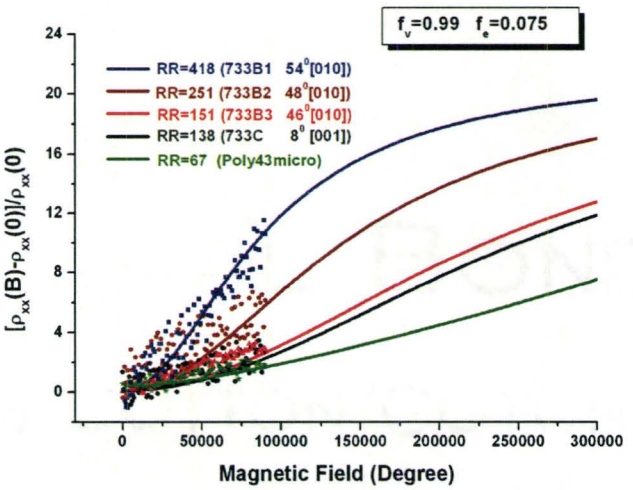

Figure 9.37: Solid lines are the modeling curves of field-dependent effective magnetoresistivity ratio for different value of *RR* for the configuration of cylindrical crystallites parallel to y-direction. In calculations, f_v= 0.99, $f_e = 0.075$. Solid points are the experimental data of the samples having the corresponding value of *RR* plotted in Figure 8.22

characteristics was subsequently calculated for other values of resistivity ratio *RR*. Figure 9.37 shows both theoretical and experimental data obtained in the course of the work. It is seen that theoretical calculations agrees with experimental data quite well for all samples except for the sample 733C with resistivity ratio $RR = 138$, where it is seen that the modeling curve (black solid line) deviates slightly from the experimental measurement points (black points). Such a deviation may be a result of the experimental error associated with determination of exact orientation of the crystallographic direction parallel to the applied magnetic filed rather than from modeling. For example, if the applied field deviates from [001] by only 2 degree, it will lead to substantial deviation of magnetoresistance from the minimum point (see Figure 8.21) and this error can easily account for observed discrepancy. One can argue however, that theoretical modeling of the magnetoresistivity can help to gain

better insight into the properties of dislocation substructure in deformed crystals.

Chapter 10

Summary and Conclusions

In the preceding chapters, we have presented detailed experimental and theoretical studies of the influence of dislocation structure on galvanomagnetic properties of plastically deformed copper single crystals in a high magnetic field, as well as on the de Hass-van Alphen effect of plastically deformed copper samples. In experiments, we measured the angle and field-dependent magnetoresistivity for copper crystal samples containing different density and distribution of dislocations in the crystallographic orientations in which open, extended and closed orbits occur. We also studied the induced torque of copper single crystals containing dislocations in the applied field and obtained oscillation frequencies for the extremal orbits normal to the principal crystallographic directions through Fourier transform of torque versus field characteristics. On the theory side, we have developed a model to calculate angle and field-dependent transverse magnetoresistivity of the samples containing different densities of dislocations for open, extended and closed orbits, using the ef-

fective medium approximation with the aid of Green's function to solve the boundary problem of crystallites in an electrical field. We have applied this theory to simulate the experimental data obtained in this work. Based on the results obtained following conclusions can be drawn.

(1) Calculated angle and field-dependent effective magnetoresistance using the effective medium approximation agree well with the experimental results. Theoretical results show that the linear behavior of magnetoresistance versus the magnetic field for open or long extended orbits is the consequence of the spatial average of this physical quantity over all crystallites. These are affected by dislocations (Figures 9.23 and 9.24). Theoretical calculations suggest that the orientation distribution of crystallites in the highly deformed samples whose density of dislocations is approaching $1.65 \times 10^{12} cm^{-2}$ show some anisotropy, so that the experimental results of magnetoresistivity are reproduced by taking spatial average over a certain integral region depending upon the density of dislocations. In general, a highly deformed sample has a larger volume fraction of crystallites with a broader angular distribution. Based on such assumption, the calculated magnetoresistivity through a self-consistent method shows good agreement with the experimental results, clearly seen in Figures 9.30 and 9.31 for highly deformed samples and Figures 9.33, 9.34, 9.10 and 9.11 for slightly deformed samples.

(2) The experimental measurements and theoretical calculations both show that dislocations accumulated in the volume of the material have a substantial effect on the galvanomagnetic properties of the samples. With the increasing dislocation density, magnetoresistivity ratios $(\rho(\vec{B}) - \rho(0))/\rho(0)$ corresponding to both open or long extended and closed orbits decrease substantially. Such feature can be clearly seen from the measurements of angle-dependent magnetoresistivity for

the samples with different densities of dislocations. For example, Figures 8.18(a), 8.19(a), 8.20(a) and 8.21(a) show the experimental measurements of transverse magnetoresistivity ratio as a function of sample orientation for different densities of dislocations, characterized by residual resistivity ratio *RR*. The amplitude of peaks corresponding to open or long extended orbits in the diagrams is significantly reduced with increasing dislocation density in the samples i.e., *RR* decreasing. Figure 8.22 shows that the same phenomenon is observed from the characteristics of the field-dependent transverse magnetoresistivity for closed orbits. Theoretical calculations shown in Figures 9.13, 9.16, 9.10, 9.33 and 9.37 agree with the experimental observations and suggest that decrease of the fraction of the open orbits in relation to close orbits caused by the presence of dislocations is responsible for the decrease of the magnetoresistivity of the samples. The theoretical modeling suggests that magnetoresistivity is strongly dependent upon the number of electrons moving on open orbits, which in turn is determined by the spatial distribution of dislocations in the crystal lattice. However, the nature of the dislocation substructure in our samples is such that after large deformations single crystals contain approximately random dislocation distribution and therefore the anisotropy of the magnetoresistivity in strongly suppressed.

(3) The quadratic variation of the transverse magnetoresistivity ratio with the magnetic field for open or long extended orbits changes to linear as the dislocation density increases. Figures 8.18(b), 8.19(b), 8.20(b) and 8.21(b) provide the experimental evidence of this phenomenon, which is also supported by theoretical modeling results shown in Figures 9.15, 9.16 and 9.17.

(4) The linear variation of magnetoresistivity with the magnetic field for open or long extended orbits occurs only in largely deformed samples containing high

dislocation densities. Figures 8.21(b) and 8.26(b) illustrate the linear behavior of field-dependent transverse magnetoresistivity for open or long extended orbits beyond the applied field of $B = 4\ Tesla$ in samples $733C$ and $700H$. This behavior is caused by the structure and orientation of dislocations stored in the samples, which can be approximated by the disordered crystallites in modeling magnetoresistivity. It is seen that more disordered crystallites produce flatter characteristics of field-dependent transverse magnetoresistance. This behavior was theoretically predicted by Guttal and Stroud (Guttal & Stroud, 2005). In this light, we should expect that transverse magnetoresistance in [100] samples deformed by tension be smaller than the transverse magnetoresistance in [541] samples, because the latter samples have relatively more ordered dislocation substructure than the former. However, we did not observe the apparent difference between these two sample orientations. This again indicates that both crystals have microscopically very similar dislocation substructure and galvanomagnetic properties are determined by the density of dislocations, characterized by residual resistivity ratio *RR*. The results suggest that magnetoresistance of the samples is similar as long as they have the same value of *RR*. Transmission electron microscopy observations of the dislocations substructure in both single crystal samples shown in Figures 2.15 and 2.16 agree with these conclusions.

(5) The saturating behavior of magnetoresistivity at large magnetic fields for closed-orbits changes into a linear dependence with a lower slope as the density of dislocations increases. This behavior has been shown in Figure 9.36 which exhibits the detailed evolution of magnetoresistivity as a function of applied field for different values of *RR*. It has been observed that the experimental measurements of filed-dependent magnetoresistance in the closed-orbit crystallographic orientation

have an excellent agreement with the modeling curves in the initial linear portion and in filed lower than 10 *Tasla*, (from Figure 9.37). Our experimental setup allow us to measure galvanomagnetic properties only in the range from 0 to 9 *Tesla*, the maximum intensity of the magnetic field achieved with the system. Thus, it would be interesting to investigate this effect at higher fields, beyond 9 *Tesla*, to determine if the theoretical predictions match the experimental results, which may be the task for the future studies.

(6) Experimental measurements of the magnetoresistivity in crystals oriented initially along [541] (Figure 8.26) indicate that in samples deformed to large strains transverse magnetoresistance is still anisotropic. Unlike in polycrystalline samples, the orientation of the crystallites in deformed single crystals containing $N_d \sim 1.5 \times 10^{12} cm^{-2}$ density of dislocations is not fully random and they have some preferential orientation, which results in anisotropy of magnetoresistance along different crystallographic directions. This feature is reproduced in modeling of the magnetoresistivity in the sample 700H deformed to large strains by considering smaller than 2π range of integration angles.

(7) The de Hass-van Alphen effect on plastically deformed copper single crystals have been investigated by torque magnetometer measurement technique. The maximum density of dislocations stored in deformed samples for the occurrence of the effect $N_d \sim 6.6 \times 10^{12} cm^{-2}$, has been estimated using free-electron approximation and has been found to be in good agreement with experimental observations. The oscillation frequencies for the extremal orbits normal to the principal crystallographic directions are obtained through Fourier transform of torque versus field characteristics and are listed in table 8.3. By comparing these frequencies with the analogous frequencies obtained for undeformed copper crystals, the changes of the

extremal cross-section areas corresponding to the extremal orbits are obtained and the shape of the Fermi surface of copper crystals with dislocations is qualitatively determined (Figures 8.39, 8.40 and 8.41). The results reveal that in general dislocations cause expansion of the Fermi surface with the exception of the dog-bone orbits and belly orbit normal to $< 100 >$, which undergo shrinkage. As discussed in chapter 8, the change of the Fermi surface caused by stress field for the dislocations stored in the sample is quite different from the effect caused by elastic strain field. To interpret the reasons for the difference more work is required, which may be carried out in the future.

Appendix A

Proofs of Equations

A.1 Proof of equation (4.24)

Integrating by parts, we can write equation (4.24) as

$$\begin{aligned}
\Phi(\vec{r}) &= \Phi_0(\vec{r}) + \int_V \vec{\nabla}' \cdot \left\{ G(\vec{r},\vec{r}') \left[\delta \overleftrightarrow{\sigma}(\vec{r}') \cdot \vec{\nabla}' \Phi(\vec{r}') \right] \right\} d\vec{r}' \\
&\quad - \int_V \left\{ \left[\delta \overleftrightarrow{\sigma}(\vec{r}') \cdot \vec{\nabla}' \Phi(\vec{r}') \right] \cdot \vec{\nabla}' \right\} G(\vec{r},\vec{r}') d\vec{r}' \\
&= \Phi_0(\vec{r}) + \int_S G(\vec{r},\vec{r}') \left[\delta \overleftrightarrow{\sigma}(\vec{r}') \cdot \vec{\nabla}' \Phi(\vec{r}') \right] \cdot \vec{n} dS \\
&\quad - \int_V \left[\delta \overleftrightarrow{\sigma}(\vec{r}') \cdot \vec{\nabla}' \Phi(\vec{r}') \right] \cdot \vec{\nabla}' G(\vec{r},\vec{r}') d\vec{r}' \\
&= \Phi_0(\vec{r}) - \int_V \left\{ \vec{\nabla}' G(\vec{r},\vec{r}') \right\} \cdot \delta \overleftrightarrow{\sigma}(\vec{r}') \cdot \vec{\nabla}' \Phi(\vec{r}') d\vec{r}', \qquad \text{(A.1)}
\end{aligned}$$

where $\vec{n}$ is an outward normal vector on the surface S at a point $\vec{r}'$. The surface integral in the above equation is zero because of the boundary condition for Green's

function. In derivation, we have used Gauss' theorem (or divergence theorem) which is stated as following

$$\int_V \vec{\nabla}\cdot\vec{F}(\vec{r})d\vec{r} = \int_S \vec{F}(\vec{r})\cdot\vec{n}dS$$

A.2 Proof of equation (9.6)

Substituting equation (9.5) into equation (4.23), we have

$$\vec{\nabla}\cdot\overleftrightarrow{\sigma}_m\cdot\vec{\nabla}G(\vec{r},\vec{r}') = \vec{\nabla}\cdot\overleftrightarrow{\sigma}^S_m\cdot\vec{\nabla}G(\vec{r},\vec{r}') + \vec{\nabla}\cdot\overleftrightarrow{\sigma}^A_m\cdot\vec{\nabla}G(\vec{r},\vec{r}') = -\delta(\vec{r}-\vec{r}'). \quad \text{(A.2)}$$

The second term in the above equations

$$\begin{aligned}
\vec{\nabla}\cdot\overleftrightarrow{\sigma}^A_m\cdot\vec{\nabla}G(\vec{r},\vec{r}') &= \sum_{i=1}^{3}\frac{\partial}{\partial r_i}\vec{e}_i\cdot\sum_{j,k=1}^{3}\sigma_{jk}(1-\delta_{jk})\vec{e}_j\vec{e}_k\cdot\sum_{j=1}^{3}\frac{\partial}{\partial r_j}G(\vec{r},\vec{r}')\vec{e}_j \\
&= \sum_{i=1}^{3}\frac{\partial}{\partial r_i}\vec{e}_i\cdot\sum_{j,k=1}^{3}(-\sigma_{kj})(1-\delta_{jk})\vec{e}_j\vec{e}_k\cdot\sum_{j=1}^{3}\frac{\partial}{\partial r_j}G(\vec{r},\vec{r}')\vec{e}_j \\
&= -\vec{\nabla}\cdot\overleftrightarrow{\sigma}^A_m\cdot\vec{\nabla}G(\vec{r},\vec{r}') \qquad \text{(A.3)}
\end{aligned}$$

where $\vec{e}_i$, $\vec{e}_j$,... are the unit vectors along r_i , r_j ,...respectively. It is clear that equation (A.3) gives

$$\vec{\nabla}\cdot\overleftrightarrow{\sigma}^A_m\cdot\vec{\nabla}G(\vec{r},\vec{r}') \equiv 0 \qquad \text{(A.4)}$$

The first term in equation (A.2)

$$\begin{aligned}
\vec{\nabla}\cdot\overleftrightarrow{\sigma}^{S}_{m}\cdot\vec{\nabla}G(\vec{r},\vec{r}') &= \sum_{i=1}^{3}\frac{\partial}{\partial r_i}\vec{e}_i\cdot\sum_{j=1}^{3}\sigma_{jj}\vec{e}_j\vec{e}_j\cdot\sum_{k=1}^{3}\frac{\partial}{\partial r_k}G(\vec{r},\vec{r}')\vec{e}_k \\
&= \sum_{i,j,k=1}^{3}\sigma_{jj}\frac{\partial}{\partial r_i}\frac{\partial}{\partial r_j}G(\vec{r},\vec{r}')\vec{e}_i\cdot\vec{e}_j\vec{e}_j\cdot\vec{e}_k \\
&= \sum_{i,j,k=1}^{3}\sigma_{jj}\frac{\partial}{\partial r_i}\frac{\partial}{\partial r_j}G(\vec{r},\vec{r}')\delta_{ij}\delta_{jk} \\
&= \sum_{i=1}^{3}\sigma_{ii}\frac{\partial}{\partial r_i}\frac{\partial}{\partial r_i}G(\vec{r},\vec{r}') \qquad \text{(A.5)}
\end{aligned}$$

Combining equations (A.2), (A.4) and (A.5) together gives

$$\sum_{i=1}^{3}\sigma_{ii}\frac{\partial}{\partial r_i}\frac{\partial}{\partial r_i}G(\vec{r},\vec{r}') = -\delta(\vec{r}-\vec{r}'), \qquad \text{(A.6)}$$

which is exactly equation (9.6).

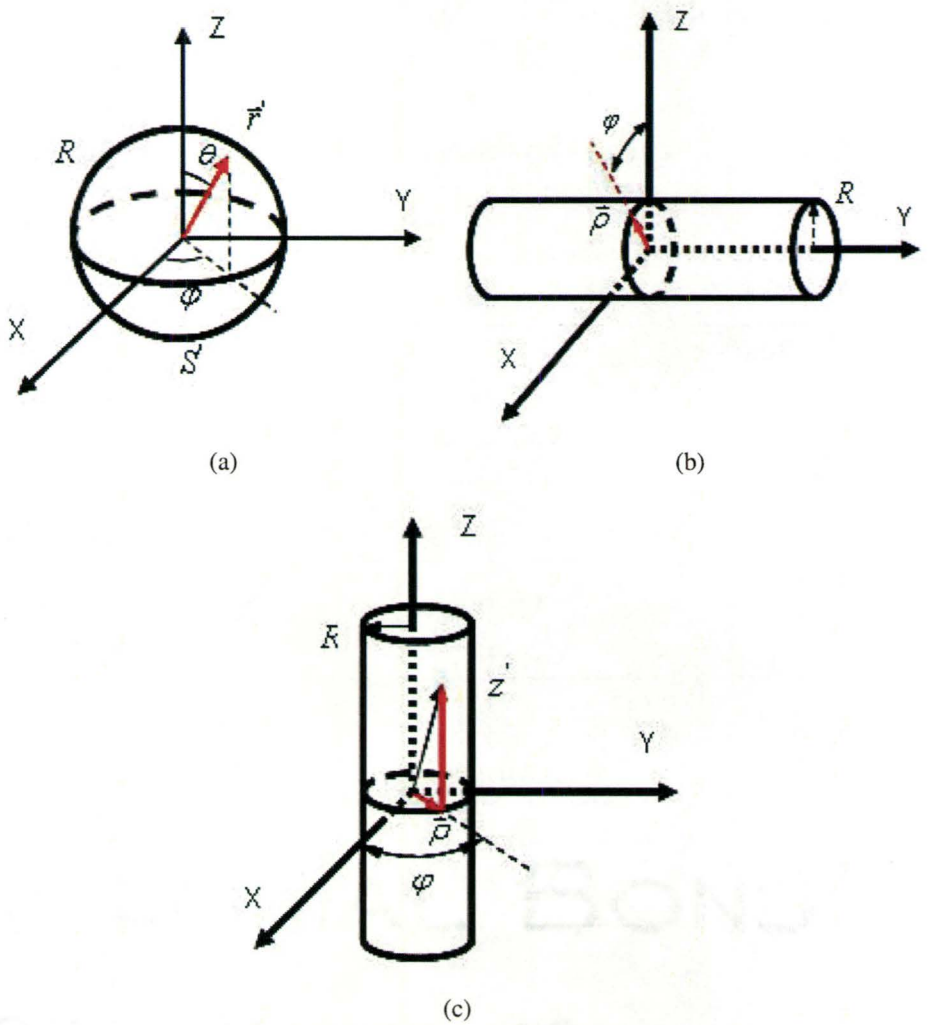

Figure A.1: Schematic illustration of the surface integral over different types of crystallites to compute depolarization tensor. (a) Type I (Sphere) (b) Type II (Cylinder with the axis along y-axis (c) Type III (Cylinder with the axis along z-axis)

A.3 Proof of equation (9.20)

Let R be the radius of spherical crystallites (see figure A.1(a)). From equation (9.17), we have

$$\begin{aligned}
\Gamma_{zz} &= \frac{-1}{4\pi\sigma_{xx}\sqrt{\sigma_{zz}}}\oint_{S'}\frac{z'/\sigma_{zz}}{\left\{\frac{x'^2}{\sigma_{xx}}+\frac{y'^2}{\sigma_{xx}}+\frac{z'^2}{\sigma_{zz}}\right\}^{3/2}}n'_z dS' \\
&= \frac{-1}{4\pi\sigma_{xx}\sigma_{zz}^{3/2}}\int_0^{\pi}\int_0^{2\pi}\frac{\cos^2\theta}{\left\{\frac{\sin^2\theta\cos^2\varphi}{\sigma_{xx}}+\frac{\sin^2\theta\sin^2\varphi}{\sigma_{xx}}+\frac{\cos^2\theta}{\sigma_{zz}}\right\}^{3/2}}\sin\theta d\theta d\varphi \\
&= \frac{-1}{4\pi\sigma_{xx}\sigma_{zz}^{3/2}}\int_0^{\pi}\int_0^{2\pi}\frac{\cos^2\theta}{\left\{\frac{\sin^2\theta}{\sigma_{xx}}+\frac{\cos^2\theta}{\sigma_{zz}}\right\}^{3/2}}\sin\theta d\theta d\varphi \\
&= \frac{1}{2\sigma_{xx}\sigma_{zz}^{3/2}}\int_{-1}^{1}\frac{\cos^2\theta}{\left\{\frac{1-\cos^2\theta}{\sigma_{xx}}+\frac{\cos^2\theta}{\sigma_{zz}}\right\}^{3/2}}d\cos\theta \\
&= \frac{1}{2}\frac{\sigma_{xx}^{1/2}}{\sigma_{zz}^{3/2}}\int_{-1}^{1}\frac{\cos^2\theta}{\left\{1-(1-\frac{\sigma_{xx}}{\sigma_{zz}})\cos^2\theta\right\}^{3/2}}d\cos\theta \\
&= \frac{1}{\chi\sigma_{zz}}\left\{\sqrt{1-\chi}\frac{\sin^{-1}\sqrt{\chi}}{\sqrt{\chi}}-1\right\} \qquad \text{(A.7)}
\end{aligned}$$

where χ is defined as $1-\sigma_{xx}/\sigma_{zz}$. Since the medium is symmetric along x and y directions ($\sigma_{xx}=\sigma_{yy}$), it can be shown

$$\Gamma_{xx}=\Gamma_{yy}. \qquad \text{(A.8)}$$

Combining equations (A.7) and (A.8) with equation (9.19) yields

$$\begin{aligned}
\Gamma_{xx} &= \Gamma_{yy} = -\frac{1}{2\sigma_{xx}}(1+\sigma_{zz}\Gamma_{zz}) \\
&= -\frac{1}{2}\left\{\frac{1}{\sigma_{xx}} + \frac{1}{\sigma_{xx}\chi}(\sqrt{1-\chi}\frac{\sin^{-1}\sqrt{\chi}}{\sqrt{\chi}} - 1)\right\} \\
&= -\frac{1}{2}\left\{\frac{1}{\sigma_{xx}} - \frac{1}{\sigma_{xx}\chi} + \frac{1}{\sigma_{xx}\chi}\sqrt{1-\chi}\frac{\sin^{-1}\sqrt{\chi}}{\sqrt{\chi}}\right\} \\
&= -\frac{1}{2}\left\{-\frac{1}{\sigma_{zz}\chi} + \frac{1}{\chi}\frac{\sin^{-1}\sqrt{\chi}}{\sqrt{\chi\sigma_{xx}\sigma_{zz}}}\right\} \\
&= -\frac{1}{2}\left\{-\frac{1}{\sigma_{zz}\chi} + (\frac{1}{\chi} - 1)\frac{\sin^{-1}\sqrt{\chi}}{\sqrt{\chi\sigma_{xx}\sigma_{zz}}} + \frac{\sin^{-1}\sqrt{\chi}}{\sqrt{\chi\sigma_{xx}\sigma_{zz}}}\right\} \\
&= -\frac{1}{2}\left\{-\frac{1}{\sigma_{zz}\chi} + (\frac{\sqrt{1-\chi}}{\sqrt{\chi}})\frac{\sin^{-1}\sqrt{\chi}}{\chi\sigma_{zz}} + \frac{\sin^{-1}\sqrt{\chi}}{\sqrt{\chi\sigma_{xx}\sigma_{zz}}}\right\} \\
&= -\frac{1}{2}\left\{\Gamma_{zz} + \frac{\sin^{-1}\sqrt{\chi}}{\sqrt{\chi\sigma_{xx}\sigma_{zz}}}\right\}
\end{aligned} \tag{A.9}$$

A.4 Proof of equation (9.21)

We use cylindrical coordinates shown in Figure A.1(b) and assume that the length L of the cylinder is much larger than its diameter $D = 2R$ ($L \gg D$). Starting from

the definition of of depolarization tensor , we have

$$
\begin{aligned}
\Gamma_{zz} &= \frac{-1}{4\pi\sigma_{xx}\sqrt{\sigma_{zz}}}\oint_{S'}\frac{z'/\sigma_{zz}}{\left\{\frac{x'^2}{\sigma_{xx}}+\frac{y'^2}{\sigma_{xx}}+\frac{z'^2}{\sigma_{zz}}\right\}^{3/2}}n'_z dS' \\
&= \frac{-1}{4\pi\sigma_{xx}\sqrt{\sigma_{zz}}}\int_0^{2\pi}\int_{-L/2}^{L/2}\frac{R\cos\varphi/\sigma_{zz}}{\left\{\frac{R^2\sin^2\varphi}{\sigma_{xx}}+\frac{y'^2}{\sigma_{xx}}+\frac{R^2\cos^2\varphi}{\sigma_{zz}}\right\}^{3/2}}R\cos\varphi d\varphi dy' \\
&= \frac{-R^2}{4\pi\sigma_{xx}\sigma_{zz}^{3/2}}\int_0^{2\pi}\cos^2\varphi d\varphi \\
&\times \left.\frac{\sqrt{\sigma_{xx}}y'/\sqrt{\sigma_{xx}}}{(\frac{R^2\sin^2\varphi}{\sigma_{xx}}+\frac{R^2\cos^2\varphi}{\sigma_{zz}})(\frac{R^2\sin^2\varphi}{\sigma_{xx}}+\frac{y'^2}{\sigma_{xx}}+\frac{R^2\cos^2\varphi}{\sigma_{zz}})^{1/2}}\right|_{y'=-L/2}^{L/2} \\
&\approx \frac{-R^2}{4\pi\sigma_{xx}\sigma_{zz}^{3/2}}\int_0^{2\pi}\cos^2\varphi d\varphi \\
&\quad \frac{2\sqrt{\sigma_{xx}}}{(\frac{R^2\sin^2\varphi}{\sigma_{xx}}+\frac{R^2\cos^2\varphi}{\sigma_{zz}})}\left\{1-\frac{1}{2}\frac{\sigma_{xx}(2R)^2}{L^2}(\frac{\sin^2\varphi}{\sigma_{xx}}+\frac{\cos^2\varphi}{\sigma_{zz}})\right\} \\
&= \frac{-2\sqrt{\sigma_{xx}}}{4\pi\sigma_{xx}\sigma_{zz}^{3/2}}\left\{\int_0^{2\pi}\frac{\cos^2\varphi}{\sin^2\varphi(\frac{1}{\sigma_{xx}}-\frac{1}{\sigma_{zz}})+\frac{1}{\sigma_{zz}}}d\varphi-\frac{\sigma_{xx}}{2}\frac{D^2}{L^2}\int_0^{2\pi}\cos^2\varphi d\varphi\right\} \\
&= \frac{-2\sqrt{\sigma_{xx}}}{4\pi\sigma_{xx}\sigma_{zz}^{3/2}}\times\left\{\frac{2\pi(-1+\sqrt{\frac{\sigma_{zz}}{\sigma_{xx}}})}{\frac{1}{\sigma_{xx}}-\frac{1}{\sigma_{zz}}}-\frac{\sigma_{xx}\pi}{2}\frac{D^2}{L^2}\right\} \\
&= \frac{1}{\sigma_{zz}-\sigma_{xx}}(\frac{\sqrt{\sigma_{xx}}}{\sqrt{\sigma_{zz}}}-1)+\frac{D^2}{4L^2}\frac{\sqrt{\sigma_{xx}}}{\sqrt{\sigma_{zz}}\sigma_{zz}} \\
&= \frac{\sqrt{1-\chi}-1}{\sigma_{zz}\chi}+\frac{1}{4}\frac{D^2}{L^2}\frac{\sqrt{1-\chi}}{\sigma_{zz}}.
\end{aligned}
\tag{A.10}
$$

Here the result is of the first order of D^2/L^2. Using the same procedure but on the different integral surface, we obtain

$$\begin{aligned}
\Gamma_{yy} &= \frac{-1}{4\pi\sigma_{xx}\sqrt{\sigma_{zz}}}\oint_{S'}\frac{y'/\sigma_{yy}}{\left\{\frac{x'^2}{\sigma_{xx}}+\frac{y'^2}{\sigma_{xx}}+\frac{z'^2}{\sigma_{zz}}\right\}^{3/2}}n'_y dS' \\
&= 2\times\frac{-1}{4\pi\sigma_{xx}\sqrt{\sigma_{zz}}}\int_0^{2\pi}\int_0^R\frac{L/2\sigma_{xx}}{\left\{\rho^2(\frac{\sin^2\varphi}{\sigma_{xx}}+\frac{\cos^2\varphi}{\sigma_{zz}})+\frac{L^2}{4\sigma_{xx}}\right\}^{3/2}}\rho d\rho d\varphi \\
&= 2\times\frac{-1}{4\pi\sigma_{xx}\sqrt{\sigma_{zz}}}\int_0^{2\pi}\int_0^R\frac{L/2\sigma_{xx}}{(\frac{\sin^2\varphi}{\sigma_{xx}}+\frac{\cos^2\varphi}{\sigma_{zz}})\left\{\rho^2(\frac{\sin^2\varphi}{\sigma_{xx}}+\frac{\cos^2\varphi}{\sigma_{zz}})+\frac{L^2}{4\sigma_{xx}}\right\}^{3/2}} \\
&\quad\times\frac{1}{2}d\left\{\rho^2(\frac{\sin^2\varphi}{\sigma_{xx}}+\frac{\cos^2\varphi}{\sigma_{zz}})\right\}d\varphi \\
&= \frac{-1}{4\pi\sigma_{xx}\sqrt{\sigma_{zz}}}\int_0^{2\pi}\frac{1}{1-3/2}\frac{1}{(\frac{\sin^2\varphi}{\sigma_{xx}}+\frac{\cos^2\varphi}{\sigma_{zz}})} \\
&\quad\times\left\{\frac{L/2\sigma_{xx}}{\left[R^2(\frac{\sin^2\varphi}{\sigma_{xx}}+\frac{\cos^2\varphi}{\sigma_{zz}})+\frac{L^2}{4\sigma_{xx}}\right]^{1/2}}-\frac{1}{\sqrt{\sigma_{xx}}}\right\}d\varphi \\
&= 2\times\frac{1}{4\pi\sigma_{xx}\sqrt{\sigma_{zz}}}\int_0^{2\pi}\frac{1}{(\frac{\sin^2\varphi}{\sigma_{xx}}+\frac{\cos^2\varphi}{\sigma_{zz}})} \\
&\quad\times\left\{\frac{1}{\sqrt{\sigma_{xx}}}\left[1-\frac{1}{2}\frac{(2R)^2\sigma_{xx}}{L^2}(\frac{\sin^2\varphi}{\sigma_{xx}}+\frac{\cos^2\varphi}{\sigma_{zz}})\right]-\frac{1}{\sqrt{\sigma_{xx}}}\right\}d\varphi \\
&= 2\times\frac{1}{4\pi\sigma_{xx}\sqrt{\sigma_{zz}}}\times\frac{-1}{2}\frac{D^2\sigma_{xx}}{L^2\sqrt{\sigma_{xx}}}\int_0^{2\pi}d\varphi \\
&= 2\times\frac{1}{4\pi\sigma_{xx}\sqrt{\sigma_{zz}}}\times\frac{-1}{2}\frac{D^2\sigma_{xx}}{L^2\sqrt{\sigma_{xx}}}\times 2\pi \\
&= -\frac{1}{2}\frac{D^2}{L^2}\sqrt{1-\chi}/\sigma_{xx} \qquad \text{(A.11)}
\end{aligned}$$

As a proof of equation (9.18), we do the tedious job to calculate Γ_{xx} which is of

the form

$$
\begin{aligned}
\Gamma_{xx} &= \frac{-1}{4\pi\sigma_{xx}\sqrt{\sigma_{zz}}}\oint_{S'}\frac{x'/\sigma_{xx}}{\left\{\frac{x'^2}{\sigma_{xx}}+\frac{y'^2}{\sigma_{xx}}+\frac{z'^2}{\sigma_{zz}}\right\}^{3/2}}n'_x dS' \\
&= \frac{-1}{4\pi\sigma_{xx}\sqrt{\sigma_{zz}}}\int_0^{2\pi}\int_{-L/2}^{L/2}\frac{R\sin\varphi/\sigma_{xx}}{\left\{\frac{R^2\sin^2\varphi}{\sigma_{xx}}+\frac{y'^2}{\sigma_{xx}}+\frac{R^2\cos^2\varphi}{\sigma_{zz}})\right\}^{3/2}}R\sin\varphi d\varphi dy' \\
&= \frac{-1}{4\pi\sigma_{xx}\sqrt{\sigma_{zz}}}\frac{R^2}{\sigma_{xx}}\int_0^{2\pi}\sin^2\varphi d\varphi \\
&\quad \times\frac{\sqrt{\sigma_{xx}}y'/\sqrt{\sigma_{xx}}}{(\frac{R^2\sin^2\varphi}{\sigma_{xx}}+\frac{R^2\cos^2\varphi}{\sigma_{zz}})(\frac{R^2\sin^2\varphi}{\sigma_{xx}}+\frac{y'^2}{\sigma_{xx}}+\frac{R^2\cos^2\varphi}{\sigma_{zz}})^{1/2}}\Bigg|_{y'=-L/2}^{L/2} \\
&\approx \frac{-1}{4\pi\sigma_{xx}\sqrt{\sigma_{zz}}}\frac{R^2}{\sigma_{xx}}\int_0^{2\pi}\sin^2\varphi d\varphi \\
&\quad \frac{2\sqrt{\sigma_{xx}}}{(\frac{R^2\sin^2\varphi}{\sigma_{xx}}+\frac{R^2\cos^2\varphi}{\sigma_{zz}})}\left\{1-\frac{1}{2}\frac{\sigma_{xx}(2R)^2}{L^2}(\frac{\sin^2\varphi}{\sigma_{xx}}+\frac{\cos^2\varphi}{\sigma_{zz}})\right\} \\
&= \frac{-1}{4\pi\sigma_{xx}\sqrt{\sigma_{zz}}}\frac{2}{\sqrt{\sigma_{xx}}}\left\{\int_0^{2\pi}\frac{\sin^2\varphi}{(\frac{\sin^2\varphi}{\sigma_{xx}}+\frac{\cos^2\varphi}{\sigma_{zz}})}d\varphi-\frac{\sigma_{xx}}{2}\frac{D^2}{L^2}\int_0^{2\pi}\sin^2\varphi d\varphi\right\} \\
&= \frac{-1}{4\pi\sigma_{xx}\sqrt{\sigma_{zz}}}\frac{2}{\sqrt{\sigma_{xx}}}\left\{\frac{-2\pi(1-\sqrt{\frac{\sigma_{xx}}{\sigma_{zz}}})}{\frac{1}{\sigma_{zz}}-\frac{1}{\sigma_{xx}}}-\frac{\sigma_{xx}\pi}{2}\frac{D^2}{L^2}\right\} \\
&= \frac{\sqrt{\sigma_{zz}}}{\sqrt{\sigma_{xx}}}\frac{1-\sqrt{\frac{\sigma_{xx}}{\sigma_{zz}}}}{\sigma_{xx}-\sigma_{zz}}+\frac{1}{4}\frac{\sqrt{\sigma_{xx}}}{\sigma_{xx}\sqrt{\sigma_{zz}}}\frac{D^2}{L^2} \\
&= (1-\frac{1}{\sqrt{1-\chi}})\frac{1}{\sigma_{zz}\chi}+\frac{1}{4}\frac{D^2}{L^2}\sqrt{1-\chi}/\sigma_{xx} \qquad \text{(A.12)}
\end{aligned}
$$

Combining equations (A.10), (A.11) and (A.12) will directly give the identity of equation (9.19).

A.5 Proof of equation (9.22)

In cylindrical coordinate system shown in Figure A.1(c), with the same integral as equation (A.10) but y and z interchanged, we can write

$$\begin{aligned}
\Gamma_{xx} &= \frac{-1}{4\pi\sigma_{xx}\sqrt{\sigma_{zz}}}\oint_{S'}\frac{x'/\sigma_{xx}}{\left\{\frac{x'^2}{\sigma_{xx}}+\frac{y'^2}{\sigma_{xx}}+\frac{z'^2}{\sigma_{zz}}\right\}^{3/2}}n'_x dS' \\
&= \frac{-1}{4\pi\sigma_{xx}\sqrt{\sigma_{zz}}}\int_0^{2\pi}\int_{-L/2}^{L/2}\frac{R\cos\varphi/\sigma_{xx}}{\left\{\frac{R^2}{\sigma_{xx}}+\frac{z'^2}{\sigma_{xx}}\right\}^{3/2}}R\cos\varphi d\varphi dz' \\
&= \frac{-1}{4\pi\sigma_{xx}\sqrt{\sigma_{zz}}}\frac{R^2}{\sigma_{xx}}\frac{L\pi/\sqrt{\sigma_{zz}}}{\frac{R^2}{\sigma_{xx}}\left\{\frac{R^2}{\sigma_{xx}}+\frac{L^2}{4\sigma_{zz}}\right\}^{1/2}} \\
&= \frac{-1}{2\sigma_{xx}}\times\frac{1}{\left\{1+\frac{4R^2\sigma_{zz}}{L^2\sigma_{xx}}\right\}^{1/2}} \\
&\approx \frac{-1}{2\sigma_{xx}}\left\{1-\frac{D^2}{2L^2(1-\chi)}\right\}
\end{aligned} \tag{A.13}$$

From the symmetry, we know

$$\Gamma_{xx}=\Gamma_{yy}=\frac{-1}{2\sigma_{xx}}\left\{1-\frac{D^2}{2L^2(1-\chi)}\right\} \tag{A.14}$$

Since n_z is not zero only on the top and bottom surface of the cylinder, it is

straightforward that

$$\begin{aligned}
\Gamma_{zz} &= \frac{-1}{4\pi\sigma_{xx}\sqrt{\sigma_{zz}}} \oint_{S'} \frac{z'/\sigma_{zz}}{\left\{\frac{x'^2}{\sigma_{xx}} + \frac{y'^2}{\sigma_{xx}} + \frac{z'^2}{\sigma_{zz}}\right\}^{3/2}} n'_z dS' \\
&= 2 \times \frac{-1}{4\pi\sigma_{xx}\sqrt{\sigma_{zz}}} \int_0^R \frac{L/2\sigma_{zz}}{\left\{\frac{\rho^2}{\sigma_{xx}} + \frac{L^2}{4\sigma_{zz}}\right\}^{3/2}} 2\pi\rho d\rho \\
&= \frac{1}{\sqrt{\sigma_{zz}}} \frac{L}{2\sigma_{zz}} \left\{ \frac{1}{(\frac{R^2}{\sigma_{xx}} + \frac{L^2}{4\sigma_{zz}})^{1/2}} - \frac{1}{\frac{L}{2\sqrt{\sigma_{zz}}}} \right\} \\
&= \frac{1}{\sigma_{zz}\left\{1 + \frac{4R^2\sigma_{zz}}{L^2\sigma_{xx}}\right\}^{1/2}} - \frac{1}{\sigma_{zz}} \\
&= -\frac{D^2}{2L^2\sigma_{zz}(1-\chi)}
\end{aligned} \tag{A.15}$$

Appendix B

FORTRAN Programs

B.1 Program for computation of field dependent magnetoresistivity through equation (9.23)

```
      PARAMETER (KNR=400,KNI=3)
      IMPLICIT DOUBLE PRECISION (A-H, O-Z)
      DIMENSION CON(KNI,KNI), GAMA(KNI,KNI), RESIS(KNI,KNI),
     1    CONOP(KNI,KNI),DCON1(KNI,KNI),PCG1(KNI,KNI),CB(KNI,KNI),
     1    CBIV1(KNI,KNI),TA(KNI,KNI),TB(KNI,KNI),TC1(KNI,KNI),
     1    CONE(KNI,KNI),TD(KNI,KNI),TE(KNI,KNI),TF(KNI,KNI),COM(KNI,KNI),
     1    TC2(KNI,KNI),DCON2(KNI,KNI),CBIV2(KNI,KNI),PCG2(KNI,KNI),
     1    RED1(KNR),RED2(KNR),TH(KNS),UI(KNI,KNI)
```

```
C
      OPEN (1,FILE='INPUT')
      OPEN (2,FILE='OUTPUT')
      READ (1,*) BM, RRR, DEN
      READ (1,*) LO, DOL, FV,FE
      CLOSE (1)
C
C      COMPUTE CONDUCTIVITY TENSOR FOR CLOSE ORBIT
C
      EMS=9.10938D-31
      ECH=1.602176D-19
      PI=3.141592654D0
      CC=5.90D+7
      FAI=PI/2.0D0
      THTA=PI/2.0D0
C
      DO N=1,KNR
        DO I=1,3
          DO J=1,3
            CON(I,J)=0.0
            CONOP(I,J)=0.0
            DCON1(I,J)=0.0
            CB(I,J)=0.0
            CBIV1(I,J)=0.0
            TA(I,J)=0.0
```

```
            TB(I,J)=0.0
            TC1(I,J)=0.0
          ENDDO
        ENDDO
        B=N*BM/KNR
        A=CC/(DEN*ECH*RRR)
        WT=B*A
C         WRITE (2,('(4H N= I2, 4D14.5)')) N,BM,TAO,DEN
C
C     THIS IS TO CUMPUTE CONDUCTIVITY TENSOR FOR CLOSE
C    ORBIT
C
        CON(1,1)=1.0D0/(1.0D0+WT**2)
        CON(2,2)=CON(1,1)
        CON(3,3)=1.0D0
        CON(1,2)=-WT/(1.0D0+WT**2)
        CON(1,3)=0.0D0
        CON(2,1)=WT/(1.0D0+WT**2)
        CON(2,3)=0.0D0
        CON(3,1)=0.0D0
        CON(3,2)=0.0D0
        AKAI=1.0-CON(1,1)/CON(3,3)
        DO J=1,3
C         WRITE (2,('(4E14.5)')) CON(J,1),CON(J,2), CON(J,3),WT
        ENDDO
```

```
C
C       THIS IS TO COMPUTE GAMA TENSOR FOR DIFFERENT
C       CONFIGURATIONS
C
100      IF (LO.EQ.1) THEN
           AA=SQRT(1-AKAI)
           GAMA(1,1)=(1-1.0/AA)/(CON(3,3)*AKAI)+0.25*DOL*AA/CON(1,1)
           GAMA(2,2)=-0.5*DOL*AA/CON(1,1)
           GAMA(3,3)=(AA-1)/(CON(3,3)*AKAI)+ 0.25*DOL*AA/CON(1,1)
           GAMA(1,2)=0
           GAMA(1,3)=0
           GAMA(2,1)=0
           GAMA(2,3)=0
           GAMA(3,1)=0
           GAMA(3,2)=0
         ENDIF
C
         IF (LO.EQ.2) THEN
           GAMA(1,1)=-0.5*(1-0.5D0*DOL/(1-AKAI))/CON(1,1)
           GAMA(2,2)=GAMA(1,1)
           GAMA(3,3)=-0.5*DOL/(CON(3,3)*(1-AKAI))
           GAMA(1,2)=0
           GAMA(1,3)=0
           GAMA(2,1)=0
           GAMA(2,3)=0
```

```
          GAMA(3,1)=0
          GAMA(3,2)=0
        ENDIF
C
        IF (LO.EQ.3) THEN
          AA=SQRT(1-AKAI)*ASIN(SQRT(AKAI))/SQRT(AKAI)
          BB=ASIN(SQRT(AKAI))/SQRT(AKAI*CON(1,1)*CON(3,3))
          GAMA(3,3)=(AA-1)/(AKAI*CON(3,3))
          GAMA(1,1)=-0.5*(GAMA(3,3)+BB)
          GAMA(2,2)=GAMA(1,1)
          GAMA(1,2)=0
          GAMA(1,3)=0
          GAMA(2,1)=0
          GAMA(2,3)=0
          GAMA(3,1)=0
          GAMA(3,2)=0
        ENDIF
C
C
C       THIS IS TO COMPUTE CONDUCTICITY TENSOR FOR OPEN ORBIT
C
C       KH LOOP IS TO COMPUTE CONDUCTIVITY TENSOR FOR
C       EXTEND ORBIT
C
        KH=(KNS-1)/2
```

```
      DO K=1,KNS
        TH(KNS)=0.0
        THTA=0.5*PI+(K-KH-1)*50.0*PI/((KNS-1)*180.0)
        AB=SIN(FAI)*SIN(THTA)
        AC=SIN(FAI)*COS(THTA)
        ANTA=WT*AC
        DD=1+ANTA**2
        CONOP(1,1)=(1-FE)*CON(1,1)+FE*(1-AB**2)/DD
        CONOP(1,2)=(1-FE)*CON(1,2)+FE*(-AB*COS(FAI)-ANTA*AC)/DD
        CONOP(1,3)=FE*(-AB*AC+ANTA*COS(FAI))/DD
        CONOP(2,1)=(1-FE)*CON(2,1)+FE*(-AB*COS(FAI)+ANTA*AC)/DD
        CONOP(2,2)=(1-FE)*CON(2,2)+FE*SIN(FAI)**2/DD
        CONOP(2,3)=FE*(-AC*COS(FAI)-ANTA*AB)/DD
        CONOP(3,1)=FE*(-AB*AC-ANTA*COS(FAI))/DD
        CONOP(3,2)=FE*(-AC*COS(FAI)+ANTA*AB)/DD
        CONOP(3,3)=(1-FE)+FE*(1-AC**2)/DD
C
C         CALL RINV(CONOP,TF)
C
        DO J=1,3
C         WRITE (2,('(3E14.5)')) (1-FE)*con(2,1),
C  1        FE*(-AB*COS(FAI)+ANTA*AB)/DD
C         WRITE (2,('(3E14.5)')) CONOP(J,1),CONOP(J,2), CONOP(J,3)
      ENDDO
C
```

```
C       THIS IS THE TENSOR DIFFERENCE OF CLOSE AND OPEN ORBIT
C
          DO I=1,3
            DO J=1,3
              COM(I,J)=CON(I,J)
              IF (I.EQ.J) THEN
                UI(I,J)=1.0
              ELSE
                UI(I,J)=0.0
              ENDIF
            ENDDO
          ENDDO
          M=0
  200     DO I=1,3
            DO J=1,3
              DCON2(I,J)=CONOP(I,J)-COM(I,J)
              DCON1(I,J)=-COM(I,J)
            ENDDO
          ENDDO
          DO J=1,3
C             WRITE (2,('(3E14.5)')) AB, AC, DD
C             WRITE (2,('(3E14.5)')) DCON2(J,1),DCON2(J,2), DCON2(J,3)
          ENDDO
C
C       THIS IS TO CALCULATE THE PRODUCT OF TWO MATRIXES
```

```
C
      CALL PRODM (GAMA,DCON1,PCG1)
      CALL PRODM (GAMA,DCON2,PCG2)
C
      DO I=1,3
        DO J=1,3
          AA=UI(I,J)-PCG1(I,J)
          BB=UI(I,J)-PCG2(I,J)
          PCG1(I,J)=AA
          PCG2(I,J)=BB
        ENDDO
      ENDDO
      DO I=1,3
C       WRITE (2,('(3E14.5)')) PCG(I,1),PCG(I,2), PCG(I,3)
      ENDDO
C       WRITE (2,*) ' '
      CALL RINV(PCG1,CBIV1)
      CALL RINV(PCG2,CBIV2)
      DO I=1,3
C       WRITE (2,('(3E14.5)')) CBIV(I,1),CBIV(I,2), CBIV(I,3)
      ENDDO
C
      CALL PRODM(DCON1,CBIV1,TC1)
      CALL PRODM(DCON2,CBIV2,TC2)
C
```

```
      DO I=1,3
        DO J=1,3
          TB(I,J)=(1-FV)*TC1(I,J)+FV*TC2(I,J)
          TE(I,J)=(1-FV)*CBIV1(I,J)+FV*CBIV2(I,J)
        ENDDO
      ENDDO
      CALL RINV(TE,TD)
      CALL PRODM(TB,TD,TA)
C
      DO I=1,3
        DO J=1,3
          CONE(I,J)=COM(I,J)+TA(I,J)
        ENDDO
C         WRITE (2,('(3E14.5)')) CONE(I,1),CONE(I,2), CONE(I,3)
      ENDDO
C
      DD=ABS(CONE(1,1)-COM(1,1))
      IF (DD.GE.1.0E-8) THEN
        M=M+1
C         WRITE (2,('(I3, 2E14.7)')) M,cone(1,1),com(1,1)
        DO I=1,3
          DO J=1,3
C             BB=COM(I,J)
            AA=CONE(I,J)
            COM(I,J)=AA
```

```
            ENDDO
          ENDDO
          GO TO 200
        ENDIF
C
        CALL RINV(CONE,RESIS)
      DD=RESIS(1,1)-1.0D0
      RED1(N)=DD
      WRITE (2,('(3E14.5)')) B*1.0E+4,RED1(N)
    ENDDO
    END
C
   SUBROUTINE PRODM(AM,BM,CM)
   DIMENSION AM(3,3),BM(3,3),CM(3,3)
   DOUBLE PRECISION AM,BM,CM
   DO I=1,3
      DO J=1,3
        CM(I,J)=0.0
        DO L=1,3
          CM(I,J)=CM(I,J)+AM(I,L)*BM(L,J)
        ENDDO
      ENDDO
   ENDDO
   RETURN
   END
```

```
C
C
      SUBROUTINE RINV(RR,RI)
      DIMENSION RR(3,3),RI(3,3)
      DOUBLE PRECISION RR,RI
      DET=RR(1,1)*RR(2,2)*RR(3,3)+RR(2,1)*RR(3,2)*RR(1,3)
     1     +RR(3,1)*RR(1,2)*RR(2,3)-RR(1,1)*RR(3,2)*RR(2,3)
     1     -RR(3,1)*RR(2,2)*RR(1,3)-RR(2,1)*RR(1,2)*RR(3,3)
      IF (DET.NE.0.0) THEN
      RI(1,1)=(RR(2,2)*RR(3,3)-RR(2,3)*RR(3,2))/DET
      RI(1,2)=(RR(1,3)*RR(3,2)-RR(1,2)*RR(3,3))/DET
      RI(1,3)=(RR(1,2)*RR(2,3)-RR(1,3)*RR(2,2))/DET
      RI(2,1)=(RR(2,3)*RR(3,1)-RR(2,1)*RR(3,3))/DET
      RI(2,2)=(RR(1,1)*RR(3,3)-RR(1,3)*RR(3,1))/DET
      RI(2,3)=(RR(1,3)*RR(2,1)-RR(1,1)*RR(2,3))/DET
      RI(3,1)=(RR(2,1)*RR(3,2)-RR(2,2)*RR(3,1))/DET
      RI(3,2)=(RR(1,2)*RR(3,1)-RR(1,1)*RR(3,2))/DET
      RI(3,3)=(RR(1,1)*RR(2,2)-RR(1,2)*RR(2,1))/DET
      ELSE
      WRITE (*,*) 'ERR STOP'
      ENDIF
      RETURN
      END
```

B.2 Program for computation of magnetoresistivity against polar angle θ

```
      PARAMETER (KNR=400,KNI=3,KNS=271)
      IMPLICIT DOUBLE PRECISION (A-H, O-Z)
      DIMENSION CON(KNI,KNI), GAMA(KNI,KNI), RESIS(KNI,KNI),
     1    CONOP(KNI,KNI),DCON1(KNI,KNI),PCG1(KNI,KNI),CB(KNI,KNI),
     1    CBIV1(KNI,KNI),TA(KNI,KNI),TB(KNI,KNI),TC1(KNI,KNI),
     1    CONE(KNI,KNI),TD(KNI,KNI),TE(KNI,KNI),TF(KNI,KNI),COM(KNI,KNI),
     1    TC2(KNI,KNI),DCON2(KNI,KNI),CBIV2(KNI,KNI),PCG2(KNI,KNI),
     1    RED1(KNR),RED2(KNR),TH(KNS),UI(KNI,KNI)
C
      OPEN (1,FILE='INPUT')
      OPEN (2,FILE='OUTPUT')
      READ (1,*) BM, RRR, DEN
      READ (1,*) LO, DOL, FV,FE
      CLOSE (1)
C
C     COMPUTE CONDUCTIVITY TENSOR FOR CLOSE ORBIT
C
      EMS=9.10938D-31
      ECH=1.602176D-19
      PI=3.141592654D0
      CC=5.90D+7
```

```
      FAI=PI/2.0D0
      THTA=PI/2.0D0
C
      DO N=72,73
        DO I=1,3
          DO J=1,3
            CON(I,J)=0.0
            CONOP(I,J)=0.0
            DCON1(I,J)=0.0
            CB(I,J)=0.0
            CBIV1(I,J)=0.0
            TA(I,J)=0.0
            TB(I,J)=0.0
            TC1(I,J)=0.0
          ENDDO
        ENDDO
        B=N*BM/KNR
        A=CC/(DEN*ECH*RRR)
        WT=B*A
C         WRITE (2,('(4H N= I2, 4D14.5)')) N,BM,TAO,DEN
C
C     THIS IS TO CUMPUTE CONDUCTIVITY TENSOR FOR CLOSE
C     ORBIT
C
        CON(1,1)=1.0D0/(1.0D0+WT**2)
```

```
      CON(2,2)=CON(1,1)
      CON(3,3)=1.0D0
      CON(1,2)=-WT/(1.0D0+WT**2)
      CON(1,3)=0.0D0
      CON(2,1)=WT/(1.0D0+WT**2)
      CON(2,3)=0.0D0
      CON(3,1)=0.0D0
      CON(3,2)=0.0D0
      AKAI=1.0-CON(1,1)/CON(3,3)
      DO J=1,3
C        WRITE (2,('(4E14.5)')) CON(J,1),CON(J,2), CON(J,3),WT
      ENDDO
C
C     THIS IS TO COMPUTE GAMA TENSOR FOR DIFFERENT
C     CONFIGURATIONS
C
100   IF (LO.EQ.1) THEN
        AA=SQRT(1-AKAI)
        GAMA(1,1)=(1-1.0/AA)/(CON(3,3)*AKAI)+0.25*DOL*AA/CON(1,1)
        GAMA(2,2)=-0.5*DOL*AA/CON(1,1)
        GAMA(3,3)=(AA-1)/(CON(3,3)*AKAI)+ 0.25*DOL*AA/CON(1,1)
        GAMA(1,2)=0
        GAMA(1,3)=0
        GAMA(2,1)=0
        GAMA(2,3)=0
```

```
      GAMA(3,1)=0
      GAMA(3,2)=0
    ENDIF
C
    IF (LO.EQ.2) THEN
      GAMA(1,1)=-0.5*(1-0.5D0*DOL/(1-AKAI))/CON(1,1)
      GAMA(2,2)=GAMA(1,1)
      GAMA(3,3)=-0.5*DOL/(CON(3,3)*(1-AKAI))
      GAMA(1,2)=0
      GAMA(1,3)=0
      GAMA(2,1)=0
      GAMA(2,3)=0
      GAMA(3,1)=0
      GAMA(3,2)=0
    ENDIF
C
    IF (LO.EQ.3) THEN
       AA=SQRT(1-AKAI)*ASIN(SQRT(AKAI))/SQRT(AKAI)
       BB=ASIN(SQRT(AKAI))/SQRT(AKAI*CON(1,1)*CON(3,3))
       GAMA(3,3)=(AA-1)/(AKAI*CON(3,3))
      GAMA(1,1)=-0.5*(GAMA(3,3)+BB)
      GAMA(2,2)=GAMA(1,1)
      GAMA(1,2)=0
      GAMA(1,3)=0
      GAMA(2,1)=0
```

```
          GAMA(2,3)=0
          GAMA(3,1)=0
          GAMA(3,2)=0
        ENDIF
C       WRITE (2,*) 'GAMA'
C       WRITE (2,('(3E14.5)')) 1.0/SQRT(1-AKAI),SQRT(1-AKAI),AKAI
C       WRITE (2,*) ' '
      DO J=1,3
C       WRITE (2,('(3E14.5)')) GAMA(J,1),GAMA(J,2), GAMA(J,3)
      ENDDO
C
C     THIS IS TO COMPUTE CONDUCTICITY TENSOR FOR OPEN ORBIT
C
C     KH LOOP IS TO COMPUTE CONDUCTIVITY TENSOR FOR
C     EXTEND ORBIT
C
       KH=(KNS-1)/2
       DO K=1,KNS
          TH(KNS)=0.0
          THTA=0.5*PI+(K-KH-1)*50.0*PI/((KNS-1)*180.0)
          AB=SIN(FAI)*SIN(THTA)
          AC=SIN(FAI)*COS(THTA)
          ANTA=WT*AC
          DD=1+ANTA**2
          CONOP(1,1)=(1-FE)*CON(1,1)+FE*(1-AB**2)/DD
```

```
            CONOP(1,2)=(1-FE)*CON(1,2)+FE*(-AB*COS(FAI)-ANTA*AC)/DD
            CONOP(1,3)=FE*(-AB*AC+ANTA*COS(FAI))/DD
            CONOP(2,1)=(1-FE)*CON(2,1)+FE*(-AB*COS(FAI)+ANTA*AC)/DD
            CONOP(2,2)=(1-FE)*CON(2,2)+FE*SIN(FAI)**2/DD
            CONOP(2,3)=FE*(-AC*COS(FAI)-ANTA*AB)/DD
            CONOP(3,1)=FE*(-AB*AC-ANTA*COS(FAI))/DD
            CONOP(3,2)=FE*(-AC*COS(FAI)+ANTA*AB)/DD
            CONOP(3,3)=(1-FE)+FE*(1-AC**2)/DD
C
C             CALL RINV(CONOP,TF)
C
            DO J=1,3
C             WRITE (2,('(3E14.5)')) (1-FE)*con(2,1),
C  1            FE*(-AB*COS(FAI)+ANTA*AB)/DD
C             WRITE (2,('(3E14.5)')) CONOP(J,1),CONOP(J,2), CONOP(J,3)
          ENDDO
C
C       THIS IS THE TENSOR DIFFERENCE OF CLOSE AND OPEN
C
          DO I=1,3
            DO J=1,3
              COM(I,J)=CON(I,J)
              IF (I.EQ.J) THEN
                UI(I,J)=1.0
              ELSE
```

```
                UI(I,J)=0.0
              ENDIF
            ENDDO
          ENDDO
          M=0
200       DO I=1,3
            DO J=1,3
              DCON2(I,J)=CONOP(I,J)-COM(I,J)
              DCON1(I,J)=-COM(I,J)
            ENDDO
          ENDDO
          DO J=1,3
C             WRITE (2,('(3E14.5)')) AB, AC, DD
C             WRITE (2,('(3E14.5)')) DCON2(J,1),DCON2(J,2), DCON2(J,3)
          ENDDO
C
C       THIS IS TO CALCULATE THE PRODUCT OF TWO MATRIXES
C
          CALL PRODM (GAMA,DCON1,PCG1)
          CALL PRODM (GAMA,DCON2,PCG2)
C
          DO I=1,3
            DO J=1,3
              AA=UI(I,J)-PCG1(I,J)
              BB=UI(I,J)-PCG2(I,J)
```

```
            PCG1(I,J)=AA
            PCG2(I,J)=BB
          ENDDO
        ENDDO
        DO I=1,3
C         WRITE (2,('(3E14.5)')) PCG(I,1),PCG(I,2), PCG(I,3)
        ENDDO
C         WRITE (2,*) ' '
        CALL RINV(PCG1,CBIV1)
        CALL RINV(PCG2,CBIV2)
        DO I=1,3
C         WRITE (2,('(3E14.5)')) CBIV(I,1),CBIV(I,2), CBIV(I,3)
        ENDDO
C
        CALL PRODM(DCON1,CBIV1,TC1)
        CALL PRODM(DCON2,CBIV2,TC2)
C
        DO I=1,3
          DO J=1,3
            TB(I,J)=(1-FV)*TC1(I,J)+FV*TC2(I,J)
            TE(I,J)=(1-FV)*CBIV1(I,J)+FV*CBIV2(I,J)
          ENDDO
        ENDDO
        CALL RINV(TE,TD)
        CALL PRODM(TB,TD,TA)
```

```
C
      DO I=1,3
        DO J=1,3
          CONE(I,J)=COM(I,J)+TA(I,J)
        ENDDO
C         WRITE (2,('(3E14.5)')) CONE(I,1),CONE(I,2), CONE(I,3)
      ENDDO
C
      DD=ABS(CONE(1,1)-COM(1,1))
      IF (DD.GE.1.0E-8) THEN
        M=M+1
C         WRITE (2,('(I3, 2E14.7)')) M,cone(1,1),com(1,1)
        DO I=1,3
          DO J=1,3
C             BB=COM(I,J)
            AA=CONE(I,J)
            COM(I,J)=AA
          ENDDO
        ENDDO
        GO TO 200
      ENDIF
C       DO J=1,3
C         WRITE (2,('(3e17.9)')) CONE(J,1),CONE(J,2),CONE(J,3)
C         WRITE (2,('(3e17.9)')) COM(J,1),COM(J,2),COM(J,3)
C       ENDDO
```

```
C
        CALL RINV(CONE,RESIS)
        IF (N.EQ.72) THEN
          A1=RESIS(1,1)-1.0
          TH(K)=A1
C           WRITE (2,('(I5)')) N
          WRITE (2,('(3E14.5)')) 180.0*THTA/PI,TH(K)
        ENDIF
      ENDDO
      IF (N.EQ.72) THEN
        A=TH(1)
          DO K=1,KNS
          THTA=0.5*PI+(K-KH-1)*50.0*PI/((KNS-1)*180.0)
          IF (K+2.LT.KH+1) then
            B1=0.5*(TH(K)+TH(k+2))
            TH(1)=A
            TH(k+1)=B1
            TH(KNS-K)=B1
          ENDIF
C           WRITE (2,('(2E14.5)')) 180.0*THTA/PI,TH(K)
        ENDDO
      ENDIF
      DD=RESIS(1,1)-1.0D0
      RED1(N)=DD
C     WRITE (2,('(3E14.5)')) B*1.0E+4,RED1(N)
```

```
      ENDDO
C     DO N=1,KNR
C        B=N*BM/KNR
C        AA1=RED1(1)
C        RED2(1)=AA1
C        AA2=RED1(KNR)
C        RED2(KNR)=AA2
C        IF ((N.NE.1).AND.(N.NE.KNR)) THEN
C           AA3=0.5D0*(RED1(N-1)+RED1(N+1))
C           RED2(N)=AA3
C        ENDIF
         WRITE (2,('(3E14.5)')) B*1.0E+4,RED2(N)
C     ENDDO
C
      END
C
      SUBROUTINE PRODM(AM,BM,CM)
      DIMENSION AM(3,3),BM(3,3),CM(3,3)
      DOUBLE PRECISION AM,BM,CM
      DO I=1,3
         DO J=1,3
            CM(I,J)=0.0
            DO L=1,3
               CM(I,J)=CM(I,J)+AM(I,L)*BM(L,J)
            ENDDO
```

```
      ENDDO
    ENDDO
    RETURN
    END
C
C
    SUBROUTINE RINV(RR,RI)
    DIMENSION RR(3,3),RI(3,3)
    DOUBLE PRECISION RR,RI
    DET=RR(1,1)*RR(2,2)*RR(3,3)+RR(2,1)*RR(3,2)*RR(1,3)
   1      +RR(3,1)*RR(1,2)*RR(2,3)-RR(1,1)*RR(3,2)*RR(2,3)
   1      -RR(3,1)*RR(2,2)*RR(1,3)-RR(2,1)*RR(1,2)*RR(3,3)
    IF (DET.NE.0.0) THEN
    RI(1,1)=(RR(2,2)*RR(3,3)-RR(2,3)*RR(3,2))/DET
    RI(1,2)=(RR(1,3)*RR(3,2)-RR(1,2)*RR(3,3))/DET
    RI(1,3)=(RR(1,2)*RR(2,3)-RR(1,3)*RR(2,2))/DET
    RI(2,1)=(RR(2,3)*RR(3,1)-RR(2,1)*RR(3,3))/DET
    RI(2,2)=(RR(1,1)*RR(3,3)-RR(1,3)*RR(3,1))/DET
    RI(2,3)=(RR(1,3)*RR(2,1)-RR(1,1)*RR(2,3))/DET
    RI(3,1)=(RR(2,1)*RR(3,2)-RR(2,2)*RR(3,1))/DET
    RI(3,2)=(RR(1,2)*RR(3,1)-RR(1,1)*RR(3,2))/DET
    RI(3,3)=(RR(1,1)*RR(2,2)-RR(1,2)*RR(2,1))/DET
    ELSE
    WRITE (*,*) 'ERR STOP'
    ENDIF
```

```
      RETURN
      END
```

B.3 Program for computation of field dependent magnetoresistivity through equation (9.25)

```
      PARAMETER (KNR=400,KNI=3,KNS=271,KNP=4000)
      IMPLICIT DOUBLE PRECISION (A-H, O-Z)
      DIMENSION CON(KNI,KNI), GAMA(KNI,KNI), RESIS(KNI,KNI),UI(KNI,KNI)
     1    CONOP(KNI,KNI),DCON1(KNI,KNI),PCG1(KNI,KNI),CB(KNI,KNI),
     1    CBIV1(KNI,KNI),TA(KNI,KNI),TB(KNI,KNI),TC1(KNI,KNI),
     1    CONE(KNI,KNI),TD(KNI,KNI),TE(KNI,KNI),TF(KNI,KNI),COM(KNI,KNI),
     1    TC2(KNI,KNI),DCON2(KNI,KNI),CBIV2(KNI,KNI),PCG2(KNI,KNI),
     1    TT(KNS,KNI,KNI),CONS(KNS, KNI,KNI)
C
      OPEN (1,FILE='INPUT')
      OPEN (2,FILE='OUTPUT')
      READ (1,*) BM, RRR, DEN
      READ (1,*) LO, DOL, FV,FE
      CLOSE (1)
C
C     COMPUTE CONDUCTIVITY TENSOR FOR CLOSE ORBIT
```

```
C
      EMS=9.10938D-31
      ECH=1.602176D-19
      PI=3.141592654D0
      CC=5.90D+7
      FAI=PI/2.0D0
      THTA=PI/2.0D0
C
      DO N=1,KNR
        DO I=1,3
          DO J=1,3
            CON(I,J)=0.0
            CONOP(I,J)=0.0
            DCON1(I,J)=0.0
            CB(I,J)=0.0
            CBIV1(I,J)=0.0
            TA(I,J)=0.0
            TB(I,J)=0.0
            TC1(I,J)=0.0
          ENDDO
        ENDDO
        B=N*BM/KNR
        A=CC/(DEN*ECH*RRR)
        WT=B*A
C         WRITE (2,('(4H N= I2, 4D14.5)')) N,BM,TAO,DEN
```

```
C
C       THIS IS TO CUMPUTE CONDUCTIVITY TENSOR FOR CLOSE
C       ORBIT
C
          CON(1,1)=1.0D0/(1.0D0+WT**2)
          CON(2,2)=CON(1,1)
          CON(3,3)=1.0D0
          CON(1,2)=-WT/(1.0D0+WT**2)
          CON(1,3)=0.0D0
          CON(2,1)=WT/(1.0D0+WT**2)
          CON(2,3)=0.0D0
          CON(3,1)=0.0D0
          CON(3,2)=0.0D0
          AKAI=1.0-CON(1,1)/CON(3,3)
          DO J=1,3
C           WRITE (2,('(4E14.5)')) CON(J,1),CON(J,2), CON(J,3),WT
          ENDDO
C
C       THIS IS TO COMPUTE GAMA TENSOR FOR DIFFERENT
C       CONFIGURATIONS
C
100       IF (LO.EQ.1) THEN
            AA=SQRT(1-AKAI)
            GAMA(1,1)=(1-1.0/AA)/(CON(3,3)*AKAI)+0.25*DOL*AA/CON(1,1)
            GAMA(2,2)=-0.5*DOL*AA/CON(1,1)
```

```
      GAMA(3,3)=(AA-1)/(CON(3,3)*AKAI)+ 0.25*DOL*AA/CON(1,1)
      GAMA(1,2)=0
      GAMA(1,3)=0
      GAMA(2,1)=0
      GAMA(2,3)=0
      GAMA(3,1)=0
      GAMA(3,2)=0
    ENDIF
C
    IF (LO.EQ.2) THEN
      GAMA(1,1)=-0.5*(1-0.5D0*DOL/(1-AKAI))/CON(1,1)
      GAMA(2,2)=GAMA(1,1)
      GAMA(3,3)=-0.5*DOL/(CON(3,3)*(1-AKAI))
      GAMA(1,2)=0
      GAMA(1,3)=0
      GAMA(2,1)=0
      GAMA(2,3)=0
      GAMA(3,1)=0
      GAMA(3,2)=0
    ENDIF
C
    IF (LO.EQ.3) THEN
      AA=SQRT(1-AKAI)*ASIN(SQRT(AKAI))/SQRT(AKAI)
      BB=ASIN(SQRT(AKAI))/SQRT(AKAI*CON(1,1)*CON(3,3))
      GAMA(3,3)=(AA-1)/(AKAI*CON(3,3))
```

```
            GAMA(1,1)=-0.5*(GAMA(3,3)+BB)
            GAMA(2,2)=GAMA(1,1)
            GAMA(1,2)=0
            GAMA(1,3)=0
            GAMA(2,1)=0
            GAMA(2,3)=0
            GAMA(3,1)=0
            GAMA(3,2)=0
          ENDIF
C         WRITE (2,*) 'GAMA'
C         WRITE (2,('(3E14.5)')) 1.0/SQRT(1-AKAI),SQRT(1-AKAI),AKAI
C         WRITE (2,*) ' '
        DO J=1,3
C         WRITE (2,('(3E14.5)')) GAMA(J,1),GAMA(J,2), GAMA(J,3)
        ENDDO
        DO I=1,3
          DO J=1,3
            COM(I,J)=CON(I,J)
            IF (I.EQ.J) THEN
              UI(I,J)=1.0
            ELSE
              UI(I,J)=0.0
            ENDIF
          ENDDO
        ENDDO
```

```
C
C       THIS IS TO COMPUTE CONDUCTICITY TENSOR FOR OPEN ORBIT
C
C         DO K=1,KNP
        THTA=0.5*PI-(135.0-K)*PI/180.0
C
        II=0
        SS=0.0
        M=0
200     DO KK=1,KNS+1
          DO I=1,3
            DO J=1,3
              TT(KK,I,J)=0.0
            ENDDO
          ENDDO
          FAI=0.5*PI+0.42*(KK-2001)*PI/(1.0*KNS)
          DFAI=0.42*PI/KNS
          AB=SIN(FAI)*SIN(THTA)
          AC=SIN(FAI)*COS(THTA)
          ANTA=WT*AC
          DD=1+ANTA**2
          CONOP(1,1)=(1-FE)*CON(1,1)+FE*(1-AB**2)/DD
          CONOP(1,2)=(1-FE)*CON(1,2)+FE*(-AB*COS(FAI)-ANTA*AC)/DD
          CONOP(1,3)=FE*(-AB*AC+ANTA*COS(FAI))/DD
          CONOP(2,1)=(1-FE)*CON(2,1)+FE*(-AB*COS(FAI)+ANTA*AC)/DD
```

```
      CONOP(2,2)=(1-FE)*CON(2,2)+FE*SIN(FAI)**2/DD
      CONOP(2,3)=FE*(-AC*COS(FAI)-ANTA*AB)/DD
      CONOP(3,1)=FE*(-AB*AC-ANTA*COS(FAI))/DD
      CONOP(3,2)=FE*(-AC*COS(FAI)+ANTA*AB)/DD
      CONOP(3,3)=(1-FE)+FE*(1-AC**2)/DD
C
C       CALL RINV(CONOP,TF)
C
C     THIS IS THE TENSOR DIFFERENCE OF CLOSE AND OPEN
C
      DO I=1,3
        DO J=1,3
          DCON2(I,J)=CONOP(I,J)-COM(I,J)
          DCON1(I,J)=CON(I,J)-COM(I,J)
        ENDDO
      ENDDO
      DO J=1,3
C         WRITE (2,('(3E14.5)')) AB, AC, DD
C         WRITE (2,('(3E14.5)')) DCON2(J,1),DCON2(J,2), DCON2(J,3)
      ENDDO
C
C     THIS IS TO CALCULATE THE PRODUCT OF TWO MATRIXES
C
      CALL PRODM (GAMA,DCON1,PCG1)
      CALL PRODM (GAMA,DCON2,PCG2)
```

```
C
      DO I=1,3
        DO J=1,3
          AA=UI(I,J)-PCG1(I,J)
          BB=UI(I,J)-PCG2(I,J)
          PCG1(I,J)=AA
          PCG2(I,J)=BB
        ENDDO
      ENDDO
      DO I=1,3
C       WRITE (2,('(3E14.5)')) PCG(I,1),PCG(I,2), PCG(I,3)
      ENDDO
C     write (2,*) ' '
      CALL RINV(PCG1,CBIV1)
      CALL RINV(PCG2,CBIV2)
      DO I=1,3
C       WRITE (2,('(3E14.5)')) CBIV(I,1),CBIV(I,2), CBIV(I,3)
      ENDDO
C
      CALL PRODM(DCON1,CBIV1,TC1)
      CALL PRODM(DCON2,CBIV2,TC2)
C
      DO I=1,3
        DO J=1,3
          TB(I,J)=(1-FV)*TC1(I,J)+FV*TC2(I,J)
```

```
            TE(I,J)=(1-FV)*CBIV1(I,J)+FV*CBIV2(I,J)
          ENDDO
        ENDDO
        CALL RINV(TE,TD)
        CALL PRODM(TB,TD,TA)
C         WRITE (2,('(2i4)')) KK
        DO I=1,3
          DO j=1,3
            TT(KK,I,J)=DFAI*TA(I,J)
          ENDDO
C           WRITE (2,('(3e14.5)')) TT(KK,I,1), TT(KK,I,2),TT(KK,I,3)
        ENDDO
      ENDDO
      DO I=1,3
        DO J=1,3
          SS=0.0
          DO KK=1,KNS
            SS=SS+TT(KK,I,J)
          ENDDO
          TA(I,J)=SS
          CONE(I,J)=COM(I,J)+SS/(0.84*PI)
        ENDDO
C         WRITE (2,('(i3, 3E14.5)')) II, TA(I,1),TA(I,2), TA(I,3)
      ENDDO
      DD=ABS(CONE(1,1)-COM(1,1))
```

```
      IF (DD.GE.1.0E-6) THEN
        M=M+1
C         WRITE (2,('(I3, 2E14.7)')) M,CONE(1,1),COM(1,1)
        DO I=1,3
          DO J=1,3
C             BB=COM(I,J)
            AA=CONE(I,J)
            COM(I,J)=AA
          ENDDO
        ENDDO
C
        GO TO 200
      ENDIF
      CALL RINV(CONE,RESIS)
C       IF (N.EQ.72) THEN
C         WRITE (2,('(i5)')) N
C         WRITE (2,('(3E14.5)')) 180.0*THTA/PI,RESIS(1,1)-1.0
C       ENDIF
C     ENDDO
    WRITE (2,('(3E14.5)')) B*1.0E+4,RESIS(1,1)-1.0
  ENDDO
  END
C
  SUBROUTINE PRODM(AM,BM,CM)
  DIMENSION AM(3,3),BM(3,3),CM(3,3)
```

```
      DOUBLE PRECISION AM,BM,CM
      DO I=1,3
         DO J=1,3
            CM(I,J)=0.0
            DO L=1,3
               CM(I,J)=CM(I,J)+AM(I,L)*BM(L,J)
            ENDDO
         ENDDO
      ENDDO
      RETURN
      END
C
C
      SUBROUTINE RINV(RR,RI)
      DIMENSION RR(3,3),RI(3,3)
      DOUBLE PRECISION RR,RI
      DET=RR(1,1)*RR(2,2)*RR(3,3)+RR(2,1)*RR(3,2)*RR(1,3)
     1     +RR(3,1)*RR(1,2)*RR(2,3)-RR(1,1)*RR(3,2)*RR(2,3)
     1     -RR(3,1)*RR(2,2)*RR(1,3)-RR(2,1)*RR(1,2)*RR(3,3)
      IF (DET.NE.0.0) THEN
      RI(1,1)=(RR(2,2)*RR(3,3)-RR(2,3)*RR(3,2))/DET
      RI(1,2)=(RR(1,3)*RR(3,2)-RR(1,2)*RR(3,3))/DET
      RI(1,3)=(RR(1,2)*RR(2,3)-RR(1,3)*RR(2,2))/DET
      RI(2,1)=(RR(2,3)*RR(3,1)-RR(2,1)*RR(3,3))/DET
      RI(2,2)=(RR(1,1)*RR(3,3)-RR(1,3)*RR(3,1))/DET
```

```
RI(2,3)=(RR(1,3)*RR(2,1)-RR(1,1)*RR(2,3))/DET
RI(3,1)=(RR(2,1)*RR(3,2)-RR(2,2)*RR(3,1))/DET
RI(3,2)=(RR(1,2)*RR(3,1)-RR(1,1)*RR(3,2))/DET
RI(3,3)=(RR(1,1)*RR(2,2)-RR(1,2)*RR(2,1))/DET
ELSE
WRITE (*,*) 'ERR STOP'
ENDIF
RETURN
END
```

References

Abrikosov, A. A. 1972. *Introduction to the theory of normal metals.* Solid State Physics: Advances in Research and Applications, vol. 12. ACADEMIC PRESS INC. New York and London.

Ackerman, M. W., & Klemens, P. G. 1971. Lattice Thermal Resistivity due to Dense Arrays of Dislocations. *Physical Review B*, **3**(8), 2375–2379.

Alekseyevsky, N. E., & Gaidukov, Yu. P. 1959. *Zh. Eksp. Teor. Fiz.*, **37**, 672.

Altshuler, B., Khmelnitskii, D., Karkin, A., & Lee, P. 1980. Magnetoresistance and Hall effect in a disordered two-dimensional electron gas. *Physical Review B*, **22**, 5142–5153.

Amelinckx, S. 1964. *The Direct Obervation of Dislocations.* Solid State Physics (Supplement 6): Advances in Research and Application. Academic Press Inc., New York.

Amundsen, T., & Jerstad, P. 1974. Linear Magnetoresistance of Aluminum. *Journal of Low Temperature Physics*, **15**, 459.

Aron, P. R. 1972. Oscillatory Magnetostriction in the noble metals. *Journal of Low Temperature Physics*, **9**, 67–72.

Ashcroft, N. W., & Mermin, N. David. 1976. *Solid State Physics.* HOT, RINEHART AND WINSTON, New York Chicago San Francisco Atlanta Dallas Montreal Toronto London Sydney.

Babiskin, J., & Siebenmann, P.G. 1971. Model for the Analysis of the Magnetoresistance in Potassium. *Physical Review Letter*, **27**, 1361–1364.

Bacon, D.J., Barnett, D.M., & Scattergood, R. O. 1980. Anisotropic continuum theory of lattice defects. *Progress in Materials Science*, **23**, 51–262.

Barabash, Sergey V., & Stroud, D. 2001. Negative Magnetoresistance Produced by Hall Fluctuations in Ferromagnetic Domain Structure. *Applied Physics Letters*, **79**, 979–980.

Bardeen, J., & Shockley, W. 1950. Deformation Potentials and Mobilities in Non-Polar Crystals. *Physical Review*, **80**, 72–80.

Basinski, Z. S. 1964. Dislocation distribution in deformed copper single crystals. *Discussions of Faraday Society*, 93–102.

Basinski, Z. S., & Basinski, S. J. 1964. Dislocation distributions in deformed copper single crystals. *Philosophical Magazine*, **9**, 51–80.

Basinski, Z. S., & Dugdale, J. S. 1985. Electrical Resistivity due to Dislocations in Highly Purified Copper. *Physical Review B*, **32**, 2149 – 2155.

Bausch, Richard, Schmitz, Rudi, & Turski, Lukasz A. 1999. Scattering of Electrons on Screw Dislocations. *Physical Review B*, **52**, 13491–13493.

Beers, C. J., van Dongen, J. C. M., van Kempen, H., & Wyder, P. 1978. nfluence of Voids on the Linear Magnetoresistance of Indium. *Physical Review Letter*, **40**(18), 1194–1197.

Bergman, D. J., & Stroud, D. 2000. High-Field Magneto transport in Composite Conductors: Effective-Medium Approximation. *Physical Review B*, **62**, 6603–6613.

Bhatia, A. B., & Gupta, O. P. 1970. Electrical Resistivity due To Dislocations. *Physical Review B*, **1**(12), 4577–4584.

Blatt, F. J. 1968. *Physics of Electronic Conduction in Solids.* McGraw-Hill, Maidenhead, McGraw-Hill Book Co., New York.

Boltzmann, W. L. 1872. *Sitz.-Ber. Akad. Wiss. (Wien)*, **66**, 275. also in *Vorlesungen üer Gastheorie (Translated as: Lectures on Gas Theory. Cambridge University Press, 1964).*

Bross, Helmut, & Häerlen, Oliver. 1993. The Scattering of Electrons by Edge Dislocations in Al. *Journal of Physics : Condensed Matter*, **5**, 7687–7700.

Brown, R. A. 1977a. Dislocation Electrical Resistivity and Resonance Scattering. *Journal of Physics F:Metal Physics*, **7**, L95–L97.

Brown, R. A. 1977b. Electrical Resistivity of Dislocations in Metals. *Journal of Physics F: Metal Physics*, **7**, 1283–1295.

Brown, R. A. 1977c. Scattering Theory for Crystal Dislocation. *Journal of Physics F: Metal Physics*, **7**, 1269–1281.

Brown, R. A. 1978. Dislocation Scattering and de Haas-van Alphen Amplitudes. *Journal of Physics F: Metal Physics*, **8**, 1159–1168.

Brown, R. A. 1982. The Interaction of Conduction Electrons With Dislocations and Grain Boundaries in Metals. *Canadian Journal of Physics*, **60**, 766–778.

Bruggeman, D.A.G. 1935. Berechnung verschiedener physikalischer Konstantenvon heterogenen Substanzen. *Annalen der Physik*, **(Leipzig) 24**, 636–679.

Bruls, G. J. C. L., Bass, J., van Gelder, A. P., Kempen, H. van, & P., Wyder. 1981. Linear Magnetoresistance Caused by Sample Thickness Variations. *Physical Review Letters*, **46**(8), 553–555.

Burgers, J. M. 1939. *Proc. Kon. Ned. Akad. Wetenschap.*, **42**, 293–, 378–.

Callaway, J. 1991. *Quantum Theory of the Solid State*. Second edition edn. Academic Press, INC.

Chang, Y. K., & Higgins, R. J. 1975. de Haas-van Alphen effect Study of dislocations in Copper. *Physical Review*, **12**, 4261–4282.

Choy, T. S. 2007. *http://www.phys.ufl.edu/ tschoy/Welcome.html*.

Choy, Tuck C. 1999. *Effective Medium Theory: Principles and Applications*. Oxford University Press Inc., New York.

Coleridge, P. T., Croxon, A. A. M., Scott, G. B., & Templeton, I. M. 1971. High precision absolute measurement of de Haas van Alphen frequencies. *Journal of Physics E*, **4**, 414–416.

Conwell, E. M. 1967. *Solid State Physics (Suppliment 9)*. New York Academic.

Crachnell, A. P., & Wong, K. C. 1973. *The Fermi surface*. Oxford Univesity Press, Ely house, London W. 1.

Cracknell, A. P. 1971. *The Fermi Surface of Metals*. Taylor and Francis Ltd., London ; Barnes & Noble, New York.

Datars, W. R. 1969. Open-Orbit Induced Torque in Copper. *Physics Letters*, **29A**(11), 700–701.

Datars, W. R. 1970. Induced Galvanomagnetic Effects in Copper. *Canadian Journal of Physics*, **48**, 1806–1816.

de Hass, W. J., & van Alphen, P. M. 1930. *Proceedings of the Royal Netherlands Academy of Arts and Sciences*, **33**, 1106.

Dexter, D. L. 1952a. Conductivity of Cold-Worked Metals. *Physical Review*, **85**, 936–937.

Dexter, D. L. 1952b. Scattering of Electrons from Point Singularities in Metals. *Physical Review*, **87**, 768–777.

Dexter, D. L. 1952c. Scattering of Electrons in Metals by Dislocations. *Physical Review*, **86**, 770–774.

Esposito, F. Paul, Newrock, R. S., & Loeffler, K. 1978. Effects of Voids on the Thermal Magnetoresistivity of Metals. *Physical Review Letters*, **41**(12), 818–821.

Ewing, A., & Rosenhain, W. 1898. The Crystalline Structure of Metals. *Philosophical Transactions of the Royal Society (London)*, **A193**, 353–375.

Falicov, L. M., & Smith, H. 1972. Linear Magnetoresistance and Anisotropic Quantum Fluctuations. *Physical Review Letters*, **29**, 124–127.

Fickett, F. R. 1971. Magnetoresistance of Very Pure Polycrystalline Aluminum. *Physical Review B*, **3**, 1941–1952.

Fisher, K. D., & Stroud, D. 1997. Conductivity and Magnetoresistance of a Periodic Composite by Network Discretization. *Physical Review B*, **56**, 14366–14373.

Gamble, D., & Watts, B. R. 1973. Changes in the Fermi surfaces of zinc and cadmium subjected to uniaxial compression. *Journal of Physics F: Metal Physics*, **3**, 98–108.

Garland, James C., & Bowers, R. 1969. High-Field Galvanomagnetic Properties of Indium. *Physical Review*, **188**, 1121–129.

Gerstein, I.I., & Elbaum, C. 1973. Uniaxial stress dependence of the fermi surface of zinc. *Physica Status Solidi. (b)*, **57**, 157–166.

Green, B. A., & Chandrasekhar, B. S. 1963. Observation of Oscillatory Magnetostriction in Bismuth at 4.2K. *Physical Review Letters*, **11**, 331–332.

Griessen, R., & Kündiga, A. 1972. The stress dependence of the fermi surface of zinc. *Solid State Communications*, **11**, 295–298.

Griessen, R., & Olsen, J. L. 1971. The oscillatory magnetostriction in aluminum. *Solid State Communications*, **9**, 1655–1658.

Griessen, R., & Sorbello, R. S. 1972. Oscillatory Magnetostriction and the Stress Dependence of the Fermi Surface of Aluminum. *Physical Review B*, **6**, 2198–2208.

Griessen, R., Lee, M. J. G., & Stanley, D. J. 1976. Homogeneous strain response of the Fermi surface of molybdenum. *Physical Review B*, **16**, 4385–4399.

Guttal, V, & Stroud, D. 2005. Model for a Macroscopically Disordered Conductor with an Exactly Linear High-Field Magnetoresistance, , 201304 (2005). *Physical Review B*, **71**, 201304–1–4.

Halse, M. R. 1969. The Fermi Surfaces of the Noble Metals. *Philosophical Transactions of the Royal Society A*, **265**, 507–532.

Harrison, W. A. 1958. Resistivity due to dislocations in copper. *Journal of Physics and Chemistry of Solids*, **5**, 44–46.

Hedges, J. M., & Mitchell, J. W. 1953. *Philosophical Magazine*, **44**(7), 223–, 357–.

Herring, Conyers. 1960. Effect of Random Inhomogeneities on Electrical and Galvanomagnetic Measurements. *Jouranl of Applied Physics*, **31**(11), 1939–1953.

Hirth, John Price, & Lothe, Jens. 1968. *Theory of Dislocation*. McGraw-Hill, Inc.

Huberman, M., & Overhauser, A. W. 1981. Effective-Medium Theory of Open-orbit Inclusion. *Physical Review B*, **23**, 6294–6300.

Hunter, S. C., & Nabarro, F. R. N. 1953. The Propagation of Electrons in a Strained Metallic Lattice. *Proceedings of the Royal Society of London*, **A220**, 542–561.

Jan, J-P, & Templeton, I.M. 1966. Precision Measurements of $< 111 >$ de Haas-van Alphen Frequencies in Copper, Silver, and Gold. *Physical Review*, **161**, 556–558.

Jones, H., & Zener, C. 1934. The Theory of the Change in Resistance in a Magnetic Field. *Proceedings of the Royal Society of London. Series A*, **145**, 268–277.

Kapitza, P. L. 1929. The Change of Electrical Conductivity in Strong Magnetic Fields. Part I-Experimental Results. *Proceedings of the Royal Society of London*, **A123**, 292–372.

Kesternich, W., & Ullmaier, H. 1971. Linear high field magnetoresistance in aluminum: Dependence on defect structure and crystal orientation. *physics Letter*, **A36**(5), 411–412.

Kittel, C. 1986. *Introduction to Solid State Physics*. John Wiley and Sons, Inc. New.

Klauder, J. R., Reed, W. A., Brennert, G. F., & Kunzler, J. E. 1966. Study of the Fine Structure in the High-Field Galvanomagnetic Properties and the Fermi Surface of Copper. *Physical Review*, **141**(12), 592–603.

Koehler, J. S. 1941. On the Dislocation Theory of Plastic Deformation. *Physical Review*, **60**, 397–410.

Koehler, J. S. 1949. A Calculation of the Changes in the Conductivity of Metals Produced by Cold-Work. *Physical Review*, **75**, 106–117.

Koss, R. S., & Stroud, D. 1985. Applications of the Effective-Medium Approximation to Cubic Geometries. *Physical Review B*, **32**, 3456–3461.

Kovács, I., & Zsoldos, L. 1973. *Dislocation and Plastic Deformation.* Pergamon Press, Oxford, New York , Toronto, Sydney, Braunschweig.

Kubo, R. 1957. Statistical-Mechanical Theory of Irreversible Processes. I. General Theory and Simple Applications to Magnetic and Conduction Problems. *Journal of the Physical Society of Japan*, **12**, 570–586.

Kunin, I. A., & Sosnina, E. G. 1971. *Dokl. Akad. Nauk SSSR[(Sov. Phys. CDokl. 16, (1972))*, **199**, 571.

Landau, L. D., Lifshitz, E. M., & Pitaevskii, L. P. 1984. *Electrodynamics of Continuous Media (in Course of Theoretical Physics)*. Vol. 8. Pergamon Press, Oxford.

Landauer, R. 1951. Conductivity of Cold-Worked Metals. *Physical Review*, **82**, 520–521.

Landauer, R. 1952. The Electrical Resistance of Binary Metallic Mixtures. *Journal of Applied Physics*, **23**, 779–784.

Landauer, R. 1977. Electrical conductivity in Inhomogeneous media,. *In:* Garland, J. C., & Tanner, D. B. (eds), *Electrical Transport and Optical Properties of Inhomogeneous media*. Ohio State University.

Lee, M. J. G., Perz, J. M., & Stanley, D. J. 1976. Angular-Shear Deformation of the Fermi Surface of Tungsten. *Physical Review Letters*, **37**, 537–539.

Lee, Martin J. G. 1969. Phase-Shift Analysis of the Fermi Surface of Copper. *Physical Review*, **187**, 901–911.

Lifshitz, I. M., & Kosevich, A. M. 1956. *Soviet Physics -JETP*, **2**, 636.

Lifshitz, I. M., & Peschanski, V. G. 1959. English Translation: Galvanomagnetic Characteristics of Metals with Open Fermi Surfaces. *Soviet Physics-JETP*, **8**, 875–883. Originally published in: J. Exper. Theoret. Phys. (U.S.S.R.) 35, p: 1251-1264 (1958).

Lifshitz, I. M., Azbel, M. I., & KaGONOV., M. I. 1957. English Translation: On the Theory of Galvanomagnetic Effects in Metals. *Soviet Physics -JETP*, **4**, 143–145. Originally published in: J. Exper. Theoret. Phys. (U.S.S.R.) 30, p: 220-222 (1956).

Lifshitz, I. M., Azbel', M. Ya., & Kaganov, M. I. 1973. *Electron Theory of Metals*. Consultants Bureau, New York-London. Translated from Russian by Albin Tybulewicz.

Lüthi, B. 1960. *Helvetica Physica Acta*, **33**, 161.

Mackenzie, J. K., & Sondheimer, E. H. 1950. The Theory of the Change in the Conductivity of Metals Produced by Cold Work. *Physical Review*, **77**, 264–270.

Martin, J. W., & Ziman, J. M. 1970. Dislocation Resistivity of Aluminum. *Journal of Physics: Condensed Matter*, **3**, L75– L77.

Mavroides, J. G., Lax, B., Button, K. J., & Shapira, Y. 1962. Oscillatory Quantum Effects

in the Ultrasonic Velocity in Bismuth. *Physical Review Letters*, **9**, 451–453.

Maxwell-Garnett, J. C. 1904. Colours in metal glasses and in metallic films. *Philosophical Transactions of the Royal Society, Series A*, **203**, 385–420.

Mayers, J., & Watts, B. R. 1978. Changes in the Fermi surfaces of magnesium, zinc and cadmium under uniaxial compression. *Journal of Physics. F: Metal Physics.*, **8**, 799–806.

Messiah, A. 1961. *Quantum Mechanics*. North-Holland Pub. Co., Amsterdam ; Interscience Publishers, New York:.

Milton, G. W. 1985. The Coherent potential Approximation is a Realizable Effective Medium Scheme. *Communications in Mathematical Physics*, **99**, 463–500.

Moon, P. W. 1986. *Field Theory Handbook*. Springer-Verlag, Berlin.

Mügge, O. 1883. *Neues Jahrb. Min.*, **13**.

Niewczas, M. 2002. Transmission Electron Microscopy Observations of Debris Structure in Deformed Copper Single Crystals. *Philosophical Magazine A*, **82**, 393–414.

Niewczas, M. 2003. *Unpublished*.

Niewczas, M., Basinski, Z. S., & Embury, J. D. 2001. Deformation of copper single crystals to large strains at 4.2 K. II. Transmission electron microscopy observations of defect structure. *Philosophical Magazine A*, **81**, 1143–1159.

Onager, L. 1952. Interpretation of the de Haas-van Alphen effect. *Philosophical Magazine*, **43**, 1006–1008.

Orowan, E. 1934. *Z. Physics*, **89**, 605 and 634.

O'Sullivan, W. J., & Schirber, J. E. 1967. Accurate de Haas-van Alphen periods for calibration of magnetic fields at low temperatures. *Cryogenics*, **7**, 118–119.

O'Sullivan, W. J., & Schirber, J. E. 1968. Addendum to Experimental Determination of the Effect of Hydrostatic Pressure on the Fermi Surface of Copper: Zero-Pressure de Haas-Van Alphen Frequencies. *Physical Review*, **181**, 1367–1367.

Overhauser, A. W. 1971. Observability of Charge-Density Waves by Neutron Diffraction.

Physical Review, **B3**(10), 3173–3182.

Overhauser, A. W. 1974. Magnetoflicker noise in Na and K. *Physical Review B*, 2441–2447.

Overhauser, A. W. 1978. Charge-density waves and isotropic metals. *Advances in Physics*, **27**, 343–346.

Pippard, A. B. 1965. Magnetic Breakdown in a Dislocated Lattice. *Proceedings of the Royal Society of London*, **A287**, 165–182.

Polanyi, M. 1934. *Z. Physics*, **89**, 660.

Posternak, M., Waeber, W. B., Griessen, R., W. Joss, W., van der Mark, W., & Wejgaard, W. 1975. The stress dependence of the fermi surface of molybdenum. I. The electron lenses. *Journal of Low Temperature Physics*, **21**, 47–74.

Reed-Hill, Robert E., & Abbaschian, Reza. 1992. *Physical Metallurgy Principles*. PWS-KENT PUBLISHING COMPANY.

Rodberg, L. S., & Thaler, R. N. 1976. *Introduction to the Quantum Theory of Scattering*. Academic Press, NY.

Ruesink, D. W., & Perz, J. M. 1983. Uniaxial strain derivatives of the Fermi surface of copper. *Canadian Journal of Physics*, **61**, 177–187.

Sacks, R. A., & Robinson, J. E. 1976. Electrical resistivity of dislocation arrays. *Physical Review B*, **13**(2), 611?20.

Schiff, L.I. 1968. *Quantum Mechanics (3rd ed.)*. McGraw-Hill, New York.

Schmid, M, & Boas, W. 1950. *Kristalplasticzitat*. Springer-Verlag, Berlin.

Schmid, M, & Siebel, G. 1931. *Z. Elektrochem*, **37**, 447.

Seeger, Karlheinz. 1991. *Semiconductor Physics: An Introduction*. Springer-Verlag.

Shoenberg, D. 1959. The De HaasCVan Alphen Effect in Copper. *Nature*, **183**, 171–171.

Shoenberg, D. 1960. The de Hass-van Alphen effect. *In:* Harrison, W. A., & Webb, M. B. (eds), *The Fermi Surface*. John Wiley & Sons, Inc. , New York , London.

Shoenberg, D. 1965. The de Hass-van Alphen effect. *Pages 665–675 of:* Daunt, J. G.,

Edwards, D. O., Milford, F. J., & Yaqub, M. (eds), *Low temperature physics LT9 : (Proceedings of the 9th International Conference on Low temperature physics).* Plenum Press, New York.

Shoenberg, D, & Stiles, P. J. 1964. The de Haas-Van Alphen Effect in Alkali Metals. *Proceedings of the Royal Society of London. Series A, Mathematical and Physical Sciences*, **281**, 62–91.

Shoenberg, D., & Watts, B. R. 1964. The effect of tension on the Fermi surface of the noble metals. *Pages 831–834 of:* Daunt, J. G., Edwards, D. O., Milford, F. J., & Yaqub, M. (eds), *Low temperature physics LT9 : (Proceedings of the 9th International Conference on Low temperature physics).* Plenum Press, New York.

Shoenberg, D., & Watts, B. R. 1967. The effect of tension on the Fermi surfaces of the noble metals. *Philosophical Magazine*, **15**, 1275–1288.

Shoenberg, David. 1984. *Magnetic Oscillations in Metals.* Cambridge University Press.

Sirenko, V., Gasparini, A., de Visser, A., Eremenko, V., Ibulaev, V., & Bruk, V. 2009. New details of the Fermi surface of 2H-$NbSe_2$ revealed by quantum oscillations in the magnetostriction. *In: Proceedings of the 25th International Conference on Low Temperature Physics (LT25).*

Slavin, A. J. 1973. Osillatory Magnetostriction in the noble metals. *Philosophical Magazine*, **27**, 65–80.

Smith, Arthur C., Janak, James F., & Adler, Richard B. 1967. *Electronic Conduction in Solids.* McGraw-Hill Book Company, New York St. Louis San Francisco Toronto London Sydney.

Stachowiak, H. 1964. On Certain Boundary Problems in the Theory of Galvanomagnetic Processes in High Magnetic Fields. *Acta Physica Polonica*, **26**, 217–228.

Stachowiak, H. 1967a. On the Effective Conductivity of Polycrystalline Mixtures. *Bull. Acad. Polon. Sci. sr. math. phys. astr.*, **15**, 631–635.

Stachowiak, H. 1967b. On the Magnetoresistance of Polycrystals at High Magnetic Fields, 15, 631 (1967). *Bull. Acad. Polon. Sci. sér. math. phys. astr.*, **15**, 637–642.

Stachowiak, H. 1970. Effective Electric Conductivity Tensor of polycrystalline Metals in

High Magnetic Fields. *Physica (Utrecht)*, **45**, 481–499.

Stachowiak, H. 1973. Calculation of the Magnetoresistance of Polycrystalline Metals. *physica status solidi (a)*, **20**, 707–716.

Steeds, J. W. 1966. Dislocation arragnement in copper single crystals as a function of strain. *Proceedings of the Royal Society of London*, **A292**, 343–373.

Stroud, D. 1975. Generalized Effective-Medium approach to the Conductivity of an Inhomogeneous Material. *Physical Review*, **B12**, 3368–3373.

Stroud, D. 1998. The effective medium approximations: Some recent developments. *Superlat-tices and Microstructure*, **23**, 567–574.

Stroud, D., & Pan, F. P. 1976. Effect of isolated inhomogeneities on the galvanomagnetic properties of solids. *Physical Review*, **B13**(4), 1434–1438.

Stroud, D., & Pan, F. P. 1978. Self-Consistent Approach to Electromagnetic Wave Propagation in Composite Media Application to Model Granular Metals. *Physical Review*, **B17**, 1602–1610.

Stroud, D., & Pan, F. P. 1979. Magnetoresistance and Hall Coefficient of Inhomogeneous Metals. *Physical Review*, **B20**, 455–465.

Taylor, G. I. 1934a. The Mechanism of Plastic Deformation of Crystals. Part I. Theoretical. *Proceedings of the Royal Society of London*, **A145**, 362–387.

Taylor, G. I. 1934b. The Mechanism of Plastic Deformation of Crystals. Part II. Comparison with Observations. *Proceedings of the Royal Society of London*, **A145**, 388–404.

Templeton, I. M. 1974. The Effect of Hydrostatic Pressure on the Fermi Surfaces of Copper, Silver, and Gold. II. High Precision Studies. *Canadian Journal of Physics*, **52**, 1628–1634.

Terwilliger, D. W., & Higgins, R. J. 1973. Dislocations and the de Haas-van Alphen Effect in Copper. *Physical Review B*, **7**(2), 667–673.

Testardi, L. R., & Condon, J. H. 1970. Landau Quantum Oscillations of the Velocity of Sound in Be: The Strain Dependence of the Fermi Surface. *Physical Review B 3928C3942*, **1**, 3928–3942.

Verkin, B. I., Dmitrenko, I. M., & G., Lazarev. B. 1956. *Zh. Eksp. Teor. Fiz.*, **31**, 538. Soviet Phys. -JETP, 4, 432 (1957).

Veyssiére, P., Chiu, Y., & Niewczas, M. 2006. Dislocation Micromechanisms under single slip conditions. *International Jouranl of Materials Research*, **97**, 189–199.

Volterra, V. 1907. *Ann. Éc. Norm. Sup.*, **24**, 400.

Watts, B. R. 1987. The Structure Factor of a Dislocated Metal and Why its Electrical Resistivity May be Approximately Isotropic. *Journal of Physics F: Metal Physics*, **17**, 1703–1716.

Watts, B.R. 1988. Calculation of electrical resistivity produced by dislocations in various metals. *Journal of Physics F: Metal Physics*, **18**, 1197–1210.

Watts, B.R. 1989. *Conduction Electron Scattering in Dislocated Metals, (Dislocation in Solids)*. Vol. 8. North-Holland Publishing Company, Amsterdam, New York, Oxford.

Ziman, J. M. 1958. Galvanomagnetic properties of cylindrical fermi surfaces. *Philosophical Magazine*, **3**, 1117–1127.

Ziman, J. M. 1960. *Electrons and Phonons*. Oxford University, New York.